LEABHARLANN CHOLÁISTE NA TRÍONÓIDE, BAILE ÁTHA CLIATH | TRINITY COLLEGE LIBRARY DUBLIN
Ollscoil Átha Cliath | The University of Dublin

Terms and Conditions of Use of Digitised Theses from Trinity College Library Dublin

Copyright statement

All material supplied by Trinity College Library is protected by copyright (under the Copyright and Related Rights Act, 2000 as amended) and other relevant Intellectual Property Rights. By accessing and using a Digitised Thesis from Trinity College Library you acknowledge that all Intellectual Property Rights in any Works supplied are the sole and exclusive property of the copyright and/or other IPR holder. Specific copyright holders may not be explicitly identified. Use of materials from other sources within a thesis should not be construed as a claim over them.

A non-exclusive, non-transferable licence is hereby granted to those using or reproducing, in whole or in part, the material for valid purposes, providing the copyright owners are acknowledged using the normal conventions. Where specific permission to use material is required, this is identified and such permission must be sought from the copyright holder or agency cited.

Liability statement

By using a Digitised Thesis, I accept that Trinity College Dublin bears no legal responsibility for the accuracy, legality or comprehensiveness of materials contained within the thesis, and that Trinity College Dublin accepts no liability for indirect, consequential, or incidental, damages or losses arising from use of the thesis for whatever reason. Information located in a thesis may be subject to specific use constraints, details of which may not be explicitly described. It is the responsibility of potential and actual users to be aware of such constraints and to abide by them. By making use of material from a digitised thesis, you accept these copyright and disclaimer provisions. Where it is brought to the attention of Trinity College Library that there may be a breach of copyright or other restraint, it is the policy to withdraw or take down access to a thesis while the issue is being resolved.

Access Agreement

By using a Digitised Thesis from Trinity College Library you are bound by the following Terms & Conditions. Please read them carefully.

I have read and I understand the following statement: All material supplied via a Digitised Thesis from Trinity College Library is protected by copyright and other intellectual property rights, and duplication or sale of all or part of any of a thesis is not permitted, except that material may be duplicated by you for your research use or for educational purposes in electronic or print form providing the copyright owners are acknowledged using the normal conventions. You must obtain permission for any other use. Electronic or print copies may not be offered, whether for sale or otherwise to anyone. This copy has been supplied on the understanding that it is copyright material and that no quotation from the thesis may be published without proper acknowledgement.

Investigation of Electronic Structure and Optical Properties of Organic Molecular Semiconductor Materials by X-ray Spectroscopies

A thesis submitted to
THE UNIVERSITY OF DUBLIN
for the degree of
Doctor in Philosophy

Nikolaos Peltekis
School of Physics
University of Dublin
Trinity College
Dublin 2, Ireland
August 2009

Declaration

I declare that:

(a) This thesis has not been submitted as an excercise for a degree to Trinity College Dublin or any other university.

(b) This thesis is entirely my own work, with the exception of the assistance noted in the acknowledgements.

(c) I agree that the library may lend or copy this thesis on request.

Contents:

Acknowledgements.

Many people have helped/supported me during the course of this work. I would like to express my sincere gratitude to all of you for being source of encouragement during these years. I am especially indebted to the following persons:

My supervisor, Dr. Cormac McGuinness, who trusted me and gave me the opportunity to join him on this high end experimental (synchrotron) world. Inspired by his scientific knowledge, ambitions and positive atitude on dealing with problems (things opposite to my character) and challenged by new scientific developments, I feel grateful that I met and join him on this tour.

All my colleagues from the School of Physics (with chronological order):
Lee Carroll: Good friend. Infinite hours spent in the lab together; helping me and advising me with any scientific or UHV related problem. Also, he makes good cocktails.
Brendan Holland: Good friend. Infinite hours spent together in our labs and on the synchroton tours. I am very greateful for his help on collecting data. Thanks for any lab related or scientific advice. Many thanks for proof reading my thesis. After so many hours working together you would be the only one that could understand my syntax and my spelling mistakes. We had a very good match working together. We were talking hours about everything (missed that).
The surface group:
Julie (thanks for the infinite after 17:00 hours spending on the lab talking or joking about everthing). John thanks for all the cigarettes and the drinks we had all these years and of course for all help you gave me. Niall thanks for helping me repair Lucia. Lina thanks for your presence. A female presence make the rest of us in the group behave better. Satheesh, Brian, Brendan, Declan and Daniel the older and newer members of my group thanks for all these years.
Chris Smith: What can I say here? I remember all these long nights out hitting the night life down town. Probably you don't remember because most of the time you were hammered.

Karsten: Many thanks for any scientific and experimental help and advice. Thanks also for any personal advice and pushing through my thesis progression. Real friendships have to be like this.

Sandhya: I haven't forgotten you. I wish I knew you earlier. Thanks for any personal help and support. I really enjoy any of our nights out here, in Berlin or even in Manaous.

External collaborators: I am really grateful to Kevin Smith's (Boston University) group for all help and assistance on my experiments. Also, I would like to thank Dr. James Downes (Macquarie University Australia) for his help on collecting parts of data and setting up a a new optical probe method on the X1B end station. Further, I would like to thank Dr. Nigel Poolton (University of Wales Aberystwyth) who assisted me with the optical spectroscopy measurements in Daresbury laboratories. Nigel inspired and implanted in me, his passion for the synchrotron based optical spectroscopies.

Staff members: Mick, Pat, Ken, Nigel, Joe thanks for all the assistance that you provided to me all these years and the patience you had with me.

Barbara: I am grateful that with a lot of patience and devotion you share most of this trip with me. Because "the ex-love(r)s go to paradise" (taken form *Maro Vanvounaki's* book).

Tim, Motohiro, Simone, Shawn, Said, Mychio, Antony, Josie, Megan, Petra, Fiona, Heather, Myriam just because a person's uniqueness defined through his name. Dublin is an interesting place to meet interesting people.

Haris, Vasiliki my Greek "fat" friends here in Dublin. It's good (in a small portion) that we hang together all these years. Eleftheria thanks for being part of my life.

All the friends and enemies, new and old ones: the friends, for their company and help and the enemies that they haven't managed to take me down yet. (I need to have this in case I am forgetting someone)

My brother and his family: Thanks for all the support and trust on me. I don't think I am going to find the way to pay back to them all this support in this life.

Mana I still haven't found the strength to say something about you. I'll try on the next step.

Abstract

The electronic structure of thin films of several members of the metal phthalocyanine (MPc) and metal chelate families of organic molecular semiconductors have been studied using resonant soft x-ray emission spectroscopy, x-ray absorption spectroscopy, photoemission spectroscopy and x-ray excited optical luminescence spectroscopy. Prolonged exposure of any organic molecule to ultraviolet or x-ray light induces damage in the molecular structure, typically referred to as beam damage. This is the case even for robust molecules such as the phthalocyanine family. Due to this, a degradation of the measured spectrum occurs with time, a particular problem with the long acquisition times of x-ray emission spectra. The influence of beam damage on non-panar (SnPc, PbPc) and planar phthalocyanine films (MgPc) was studied by core-level photoemission and x-ray absorption studies and the evolution of the fitted core-level spectra with exposure is discussed. Analysis of these spectra revealed two processes of damage: crystalline degradation and molecular decay. This helps set limits to allow for accurate measurements of resonant soft x-ray emission spectra by minimizing beam damage through a continuous translation of the film during data acquisition.

The comparison of resonant soft x-ray emission spectra with photoemission spectra is of general importance for confirming the electronic structure especially for the chemically active valence electrons of these organic semiconductors. A first experimental presentation of atomic site partial density of states (PDOS) based on the x-ray emission spectroscopy (XES) is presented here for a selection of examples from the aforementioned organic molecular semiconductor families. Atomic angular momentum resolved PDOS based on DFT calculations that are presented here show good agreement with the experimental XES spectra and help further the understanding of the nature of their electronic structure.

Finally an attempt to reveal luminescence chromophore centres in the atomic sites of magnesium phthalocyanine (MgPc) and Zinc(II) bis(8-hydroxyquinoline) (Znq_2) molecular films presented here are based on the synchrotron x-ray excited optical luminescence and optically detected x-ray absorption spectroscopy. Results from MgPc indicate that a non-bonding nitrogen state is actively involved in the main optical luminescence

band of this molecule. Furthermore, the intermolecular interference appears to play a large role in transitions on such solid films.

Keywords/Glossary

AES	Auger Electron Spectroscopy
ARPES	Angle Resolved Photoemission Spectoscopy
DFT	Density Functional Theory
EA	Electron Affinity
EL	Electroluminescence
ETM	Electron Transport material
EXAFS	Extended X-ray Absorption Fine Structure
FWHM	Full Width Half Maximum
HOMO	Highest Occupied Molecular Orbital
HTM	Hole Transport material
IP	Ionization Potential
IR	Infrared
LPDOS	Local Partial Density Of States
LUMO	Lowest Unoccupied Molecular Orbital
MO	Molecular Orbital
M-Pc	Metal Phthalocyanine
NEXAFS	Near-Edge X-ray Absorption Fine Structure
NXES	Normal X-ray Emission Spectroscopy
OD-XAS	Optically Detected X-ray Absorption Spectroscopy
OFETS	Organic Field Effect Transistor
OLED	Organic Light Emitting Diode
OMBD/E	Organic Molecular Beam Deposition/Evaporation
OMC	Organic Molecular Crystal
OTFT	Organic Thin Film Transistors
PCI	Post Collision Interaction

PDOS	Partial Density Of States
PES	Photoemission Spectroscopy
PFY	Partial Fluorescent Yield
PL	Photoluminescence
PLY	Partial Luminescence Yield
QE	Quasi-epitaxial
RIXS	Resonant Inelastic X-ray Scattering
RSXE	Resonant Soft X-ray Emission
RXES	Resonant X-ray Emission Spectroscopy
RXRS	Raman X-ray Scattering
SXA	Soft X-ray Absorption
SXE	Soft X-ray Emission
SXPS	Soft X-ray Photoelectron Spectroscopy
TEY	Total Electron Yield
TFY	Total Fluorescence Yield
UHV	Ultra High Vacuum
UPS	Ultraviolet Photoemission Spectroscopy
UV	Ultra Violet
vdW	Van der Waals
vdWE	Van der Waals epitaxy
VUV	Vacuum Ultra-Violet
XANES	X-ray Absorption Near Edge Structure
XAS	X-ray Absorption Spectroscopy
XEOL	X-ray Excited Optical Luminescence
XES	X-ray Emission Spectroscopy
XPS	X-ray Photoemission Spectroscopy

1. Introduction

Organic molecular semiconductor materials are of increasing scientific and technological importance and have attracted interest for applications in optoelectronics and the semiconductor industry. The ability to deposit organic films on a variety of low-cost substrates such as glass, plastic or metal foils, and their relative ease of processing sets them on top priority for the above mentioned applications. Due to the low cost and ease of processing, new innovative fabrication of devices on inexpensive, large-area substrates are currently being engineered by hundreds of chemists/physicists and huge progress on materials development, device design, deposition processes, and modelling has been achieved in the last decade[1,2].

They are already the basis of newer generations of electronic and optoelectronic devices, most notably the high efficiency, very bright and colourful thin displays of several mobile electronic appliances based on organic light-emitting devices (OLEDs)[4,5], amplifiers and switching devices for these displays and other devices, including organic thin film transistors (OTFTs)[6-11] and thin film organic photovoltaic cells[12-16]. Furthermore, thin films of epitaxially grown hybrid organic-inorganic devices are being widely studied[17], for example they have to shown to alter the I-V behaviour of Schottky interfaces[18].

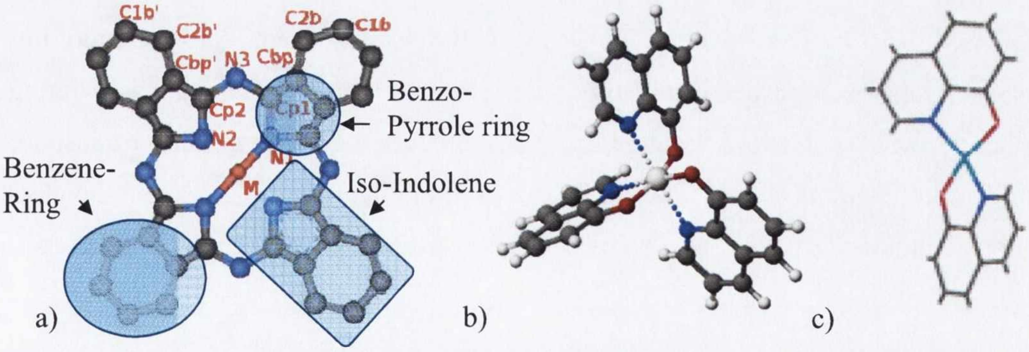

Figure 1 Molecular structure of organic material families commonly used in opto-electronic applications: a) Metal Phthalocyanine (Notation Alfredsson et al[3]) Metal chelates: b) Metal-tris (8-hydroxy quinoline) and c) Metal- bis (8-hydroxy quinoline) respectively.

1.1 Organic semiconductors as Materials

There are two major classes of organic semiconductors: low molecular weight materials and polymers. Both have in common a conjugated π-electron system being formed by the p_z-orbitals of sp^2-hybridized C-atoms in the molecules. As compared to the σ-bonds forming the backbone of the molecules, the π-bonding is significantly weaker. Therefore, the lowest electronic excitations of conjugated molecules are the π-π^*-transitions with the energy gap typically between 1.5 and 3 eV leading to light absorption or emission in the visible spectral range. The energy gap can be controlled by the degree of conjugation in a molecule. Thus, chemistry offers a wide range of possibilities to tune the optoelectronic properties of organic semiconducting materials.

An important difference between these two classes of materials lies in the way they are processed to form thin films. Whereas small molecules are usually deposited from the gas phase by sublimation or evaporation, conjugated polymers can only be processed from solution e.g by spin-coating or printing techniques. Additionally, a number of low-weight molecular materials can be grown as single crystals allowing intrinsic electronic properties to be studied on such model systems. The controlled growth of highly ordered thin films either by vacuum deposition or solution processing is still subject of ongoing research, but will be crucial for many applications.

The nature of bonding in organic semiconductors is fundamentally different from their inorganic counterparts. Organic molecular crystals are van der Waals bonded solids implying a considerably weaker intermolecular bonding as compared to covalently bonded semiconductors like Si or GaAs. The consequences are seen in mechanical and thermodynamic properties like reduced hardness or lower power melting point, but even more importantly in a much weaker delocalization of electronic wavefuctions among neighbouring molecules, which has direct implications for optical properties and charge carrier transport. The bonding in polymers chains can lead to improved mechanical properties, but the electronic interaction between adjacent chains is usually still weak in this class of materials[19].

1.2 Organic light emitting diodes (OLEDs)

Since the molecular systems that will be studied in this thesis are strongly related to OLED applications a brief description of such devices is given here. Emission of electromagnetic radiation in the UV, visible and infrared (IR) is called luminescence and it is the result of a recombination of excited electrons from lowest unoccupied molecular orbital (LUMO) to the highest occupied molecular orbital (HOMO). The electron can be excited by photon injection (laser, soft x-rays) resulting in photoluminescence (PL) or by applying voltage to an organic semiconductor material, as first discovered in anthracence single crystals[21-23], resulting in electroluminescence (EL). Typical OLEDs are double charge injection devices, requiring the simultaneous supply of both electrons and holes to the electroluminescent material which is sandwiched between two electrodes (Fig. 2a). To achieve an efficient OLED with the single-layer configuration shown in Figure 2a, the organic EL material would ideally have a high luminescence quantum yield and be able to facilitate injection and transport of electrons and holes. This demand of multifunctional capabilities from a single organic material is rarely met by current materials[20]. Most highly fluorescent or phosphorescent organic materials of interest in OLEDs tend to have either p-type (hole-transport) or n-type (electron transport) charge transport characteristics and as result poor

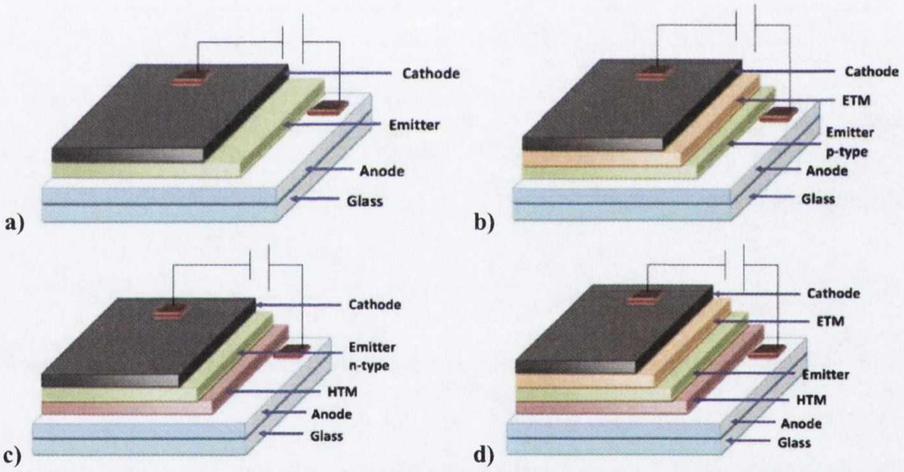

Figure 2 a) Typical structure of single layer OLED. b) Structure of OLED with multi-layer structure comprising a p-type emitter and electron transport material (ETM). c) Multi-layer structure comprising a n-type emitter as hole transport material (HTM). d) Multi-layer structure comprising emitter layer with deferent electron and hole transport material layers[20].

efficiency and brightness from the single organic layer configuration have been observed[24-26]. Using two or more layers of different organic materials, efficient light emission, good electron and hole injection and effective charge transport can be achieved. Examples of these increasingly complex OLEDs architectures are shown in Figure 2b-d. The multilayer configurations also give the opportunity of tuning and optimizing the light emission, injection and transport properties of the devices independently. Two of the key parameters for the performance of the OLED devices are the electron affinity (EA) and the ionization potential (IP); these are the energy of the LUMO and the HOMO relative to the vacuum level, respectively. The offset of these levels to the cathode and anode work functions (Φ_c and Φ_a) determine the electron and hole injection into the diode. Large mismatches, thus large barriers for hole injection at the anode ($\Delta E_h = \Phi_a$ - IP) and electron injection at the cathode ($\Delta E_e = \Phi_c$ - EA), lead to poor OLED performance.

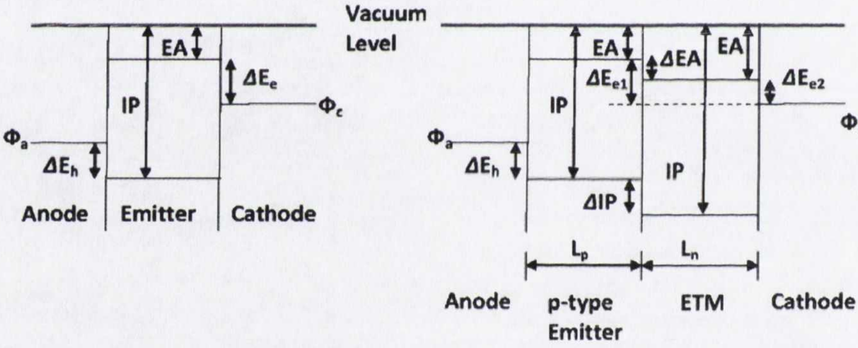

Figure 3 Energy-level diagrams of (a) a single-layer OLED and (b) a two-layer OLED based on a p-type emitter and an ETM[20].

Thus by choosing the proper cathode electrode with low work function (Φ_c) and anode with high work function (Φ_a) and including layers of electron transport materials (ETM) (as demonstrated on Fig. 3) or hole transport materials (HTM) the barrier mismatches can be minimized.

Furthermore, the difference between the electron and hole mobilities on the device can lead to a shifting of their recombination towards the electrodes (away from the emissive layer) where recombination take place by a non-radiative decay. By using the multilayer architecture with extra HTM and ETM layers, with the potential of different thicknesses, the recombination of the charge carriers could be shifted towards the emissive layer[20].

OLED display devices typically have low power consumption, broad temperature ranges and wide viewing angles. HTM and ETM layers on typical OLED sandwich structures has resulted in the concentration in research and development of organic thin films of planar molecules where mobility seems to get enhanced[27,28] . One of the foremost classes of planar organic molecular semiconductors is that of the family of metal phthalocyanines (MPc). Metal phthalocyanines, $MC_{32}H_{16}N_8$, are symmetric macrocycle molecules composed of four units of benzene rings bonded to pyrrole rings (isoindoline groups) connected together by four meso-bridging aza nitrogens (as shown in Figure 1).

The structure has a central cavity that can accommodate various metal ions, bonded via the pyrrole nitrogens. There are currently upwards of 70 M-Pcs reported, though many have axial ligands of the central metal ion. These exhibit aromatic behaviour due to the delocalised electron density of the π-bonds above and below the plane of the molecules. The central metal atom is usually in a 2+ oxidation state with the macrocycle backbone existing as a di-anion (Pc^{-2}). The central metal atom determines many of the physical properties of the material including the luminescence[29]. Their structural similarity to the active sites of chlorophyll and haemoglobin (porphyrin compounds), makes them also interesting for biomimetic applications as catalysts for oxidation reactions in heterogeneous catalysis[30-33] . They have attracted much attention as the important building blocks in molecular electronics, e.g organic field effects transistors (OFETs)[34] , OLEDs[35] and resistive chemical sensors[36-39] . In OLED devices M-Pcs or metal free-Pcs are mainly used as hole transport material (HTM) improving substantially the hole charge transfer mobility[40-42].

Another organic family that gained great interest for OLED applications, especially after Tang *et al.*[5] reported efficient electroluminescence from thin films of tris (*-hydroxyquinoline) Aluminium (Alq_3), is that of the metal chelates. Metal chelates are based on 8-hydroxyquinoline (C_9H_6ON) molecule bonded with either trivalent (Al, Ga, In) or divalent metals (Be, Zn). They are mainly used as emissive and electron transport materials[26,43-45]. Alq_3 is the most wide studied chelate mainly due to its superior characteristics such as good EA and IP values, good thermal stability, good film growth behaviour with sublimation in vacuum conditions (pinhole-free) and the highest fluorescence efficiency among the chelates (Kulkarni *et al.* and references therein[20]). The divalent metal chelate Znq_2 is also of interest due to similar EA and IP characteristics to Alq_3, but it is a yellow emitter with better brightness and better electron transport mobilities than Alq_3[20]. This results from the fact that Znq_2 appears as a tetramer in solid films and has crystal structure with overlapping intra- and inter-molecular atomic states, which make it a better ETM, which can operate at lower voltages[46].

1.3 Growth and Structure of Organic Thin Films

Since the structure has a strong impact on the functional properties, understanding the structure formation i.e., the growth process, and finding ways to optimise the structural definition is a prerequisite for technological progress.

As discussed at Forrest's review[47] organic molecular beam deposition (OMBD) (also known as OMBE) under ultra-high vacuum (UHV) has been demonstrated as a well-suited technique for preparing organic films of high structural quality[48]. It has the advantage of providing both layer thickness control and an atomically clean environment and substrate. Typically, growth occurs by the sublimation in a background vacuum ranging from 10^{-7} to 10^{-11} Torr of a highly purified powder from a temperature-controlled oven or Knudsen cell[49].

While the properties of organic molecular crystals (OMCs) have been studied for over 50 years, it has only recently been observed that excellent structural ordering can be achieved by deposition on a wide range of substrates, sometimes without regard for the degree of strain between the film and the substrate[50-52]. There has been considerable experimental and theoretical investigation of OMBD growth resulting in ordered thin films, although currently there is no detailed understanding of the range of materials (both film and substrate), and conditions under which long-range structural ordering can be achieved. The varied nature of the substrate/adsorbed layer interaction in such van der Waals (vdW) bonded systems has led researchers to term ordered growth of OMCs variously as "epitaxy",[51] "quasiepitaxy",[53] and "van der Waals epitaxy".[54]

Epitaxy, as in the case of inorganic materials, refers to systems where there is a one-to-one commensurate relationship between the molecular positions in the deposited layer and the substrate. For OMCs, there are two types of epitaxy: conventional epitaxy where the molecules are chemisorbed onto the substrate surface[55] and van der Waals epitaxy (vdWE) where physisorption involving only vdW bonding dominates[56]. Slight mis-

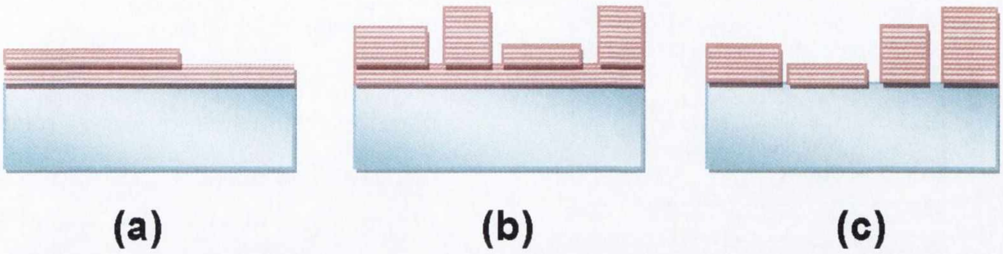

Figure 4 Various modes of epitaxial growth: (a) layer-by-layer (Frank-van der Merwe), (b) layer-plus-island (Stranski-Krastanov), and (c) island (Volmer-Weber). The horizontal lines on the epitaxial layers schematically represent individual atomic or molecular layers[47,57].

matches between the substrate and film lattices results in "strained vdWE", although for highly strained growth, epitaxial structures tend to relax at a critical thickness (d_c), thereby generating defects. Epitaxy tends to occur as a result of equilibrium growth conditions, and depending on the relative strengths of the adsorbate-adsorbate, and adsorbate-substrate interactions, the layer grows via one of three modes[57] illustrated in Figure 4: layer-by layer (Frank-van der Merwe), layer-plus-islands (Stranski-Krastanov), and island growth (Volmer-Weber). Due to the requirement for commensurability, it is difficult to find OMC/substrate combinations leading to unstrained vdWE, in which case Stranski-Krastanov growth tends to be the most frequently observed mode.

In contrast, quasiepitaxial (QE) structures are those in which the substrate and film are incommensurate over any meaningful lattice length scale. Nevertheless, there can be a well-defined orientational relationship between the film and substrate lattices resulting in azimuthal order and in some cases residual stress develops in the film as it conforms to the substrate lattice (strained QE). The most interesting feature of strained QE films is that they can be distorted from their bulk lattice structure with no significant relaxation of this distortion with film thickness (i.e., $d_c \rightarrow \infty$). Instead, it has been proposed that strain relaxation in QE films results from periodic variations in the degrees of freedom internal to the adsorbate molecules and their unit cells[58]. This property of vdW bonded OMCs is a direct result of their very small elastic constants. In contrast to vdWE, QE is primarily achieved under non-equilibrium growth conditions, and since strain relief can occur without inducing disorder, Frank-van der Merwe as well as Stranski-Krastonov growth modes have been observed[59-61].

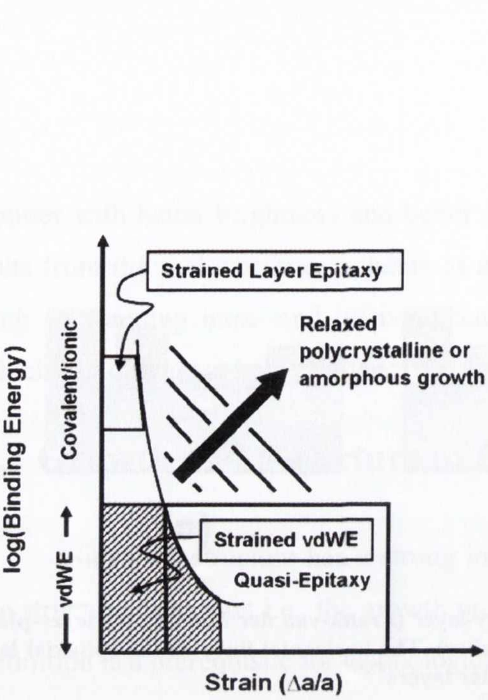

Figure 5 Schematic diagram of modes of epitaxy. Epitaxial growth occurs for commensurate lattices while QE growth occurs for vdW bonded incommensurate thin films. The left-hand axis corresponds to unstrained growth. The curved line represents the boundary between ordered and disordered growth assuming a particular value of critical thickness, d_c. The lower the binding energy is, the larger the strain allowed to achieve unrelaxed growth of a given thickness, $d < d_c$[47,62].

Figure 5 is a diagram placing these several growth modes in relative context[62].The vertical axis shows the logarithm of the bond energy to the substrate, where vdW bonds are typically in the range of 1-10 meV/atom[63] (although the binding energy per molecule can exceed 1 eV), whereas for covalent or ionic bonding, the energies range from 100 meV to 5eV/atom[64]. Unstrained, epitaxial growth corresponds to $\Delta a/a = 0$ ($\Delta a/a = \Delta a/a_s$ where a_s is the substrate lattice constant, $\Delta a=|a_f-a_s|$, and a_f is the lattice constant of the thin film). The curved line schematically indicates the strain for a constant critical layer thickness:[65] as the bond energy increases, strain must decrease if d_c is to be maintained at a constant value. At higher strains, relaxed polycrystalline or amorphous growth occurs. While different regions of this energy/strain plot are occupied by strained vdWE and QE, there are also areas of significant overlap. That is, for a particular strain energy, strained vdWE or QE structures can be attained, depending on the growth conditions employed[47].

From Forrest's review it is clear that the growth of molecular semiconductor is very complex.

1.3.1 Crystalline structures of phthalocyanines

The most extensive studies of epitaxial growth of OMC films have concentrated on the phthalocyanines (Pc) layered on ionic substrates such as the alkali halides[66-73], metals[74], and on passivated surfaces[75-77] of Si(111) and GaAs(111). Typical conditions leading to epitaxial growth of planar molecules include low growth rates (<0.001 to 0.01ML/s) and high substrate temperatures (~100-200 °C, depending on the sublimation temperature of the organic molecule). These conditions result in the growth of equilibrium thin film structures, where the incident molecules have sufficient thermal energy after deposition to arrange themselves into their minimum energy configuration.

Epitaxial molecular thin films are typically grown into structures which are determined by the substrate lattice rather than by the bulk structure of the organic molecular solid itself. Since the substrates used are typically inorganic crystals whose structure is considerably different than the OMC, neither the lattice constant nor the lattice symmetry of these two contacting layers are matched. This has two consequences: due to the flexible nature of the vdW force responsible for the cohesion of the organic layers, the structure of the thin film can be substantially distorted from bulk. This severe lattice distortion, however, results in a large stress within the film, thereby creating disorder after the growth of only a few monolayers[55,73]. In effect, the mismatched film relaxes to its bulk structure within 2-5 ML, resulting in a rough columnar surface morphology (corresponding to Stranski-Krastanov growth[57]). The film relaxation prevents the growth of molecularly flat films with thicknesses beyond only a few monolayers[47].

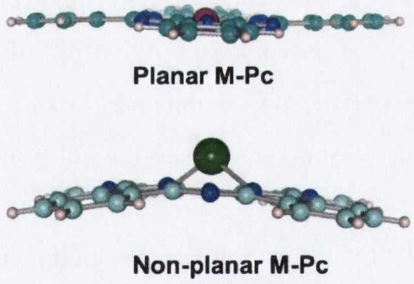

Figure 6 A side view of the difference between planar and non-planar phthalocyanines (M-Pcs).

There is extensive literature describing the various crystal structures of most of the molecules in the family M-Pcs which is best summarised by the reviews of Kadish[78] and Engel[79]. Both distinguish the phthalocyanines in two main categories, based on the planarity of the molecule, where distinct differences in the crystal structures have been observed. Planar phthalocyanines are those that can fully accommodate the metal ion in the central cavity of the molecule. These are two dimensional and follow the D_{4h} point group symmetry. The non-planar have the metal ion protruding out of plane because it is too big to be accommodated in the central cavity. These are three dimensional molecules with C_{4v} point group symmetry (Fig. 6).

Increasing attention is being paid to the phenomenon of polymorphism[80]. If a crystal may be looked at as a giant supramolecule, polymorphs are the corresponding su-

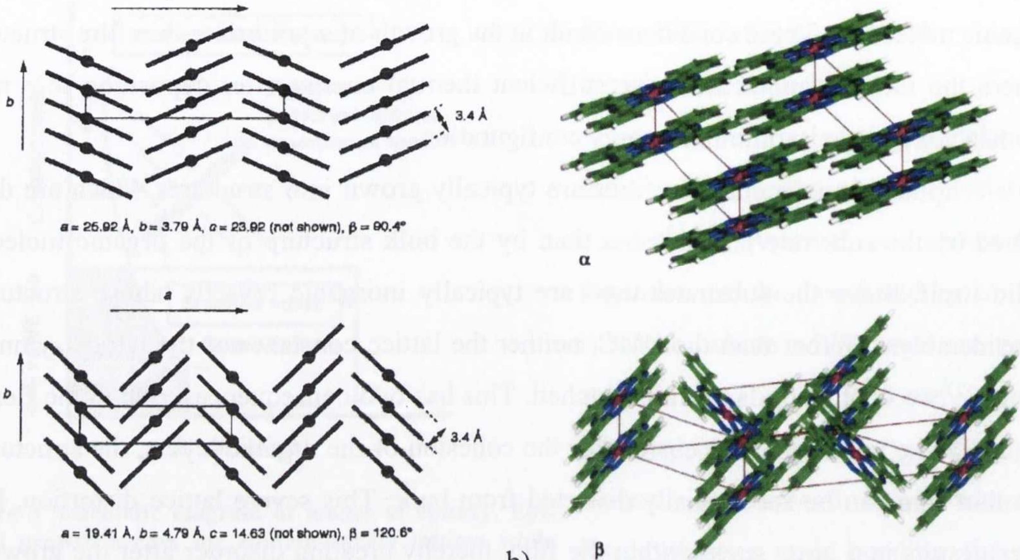

a) b)

Figure 7 Schematic showing the herringbone columnar packings of *α*-phase (top) and the *β*-phase (bottom) of planar MPcs[78]. a) shows both polymorphic forms contain stacks of the molecule which are titled with respect the *b*-axis of the crystal (the column axis) with intermolecular average distance of *d*≈3.4Å. b) Three dimensional depiction of the of *α*-phase (top) and the *β*-phase (bottom) of planar MPcs[86]

pramolecular isomers[81]. As for chemically bonded isomers, polymorphs differ in properties related to the solid state, such as melting point, colour, hardness, conductivity, photoconductivity[82-86] etc. For example during the 76 years since its discovery, 10 polymorphs of the planar CuPc have been identified[86]. Crystal structure polymorphism depends largely on factors such as pressure, temperature, deposition rate and epitaxial/quasi-epitaxial growth (matching with substrate)[78].

Of the planar Pcs there are two dominant crystal structures, both are monoclinic and are labelled *α*- and *β*- forms. The molecular packing in both polymorphs is depicted schematically in Figure 7, with data shown for CuPc[78]. Both polymorphic forms contain stacks of phthalocyanine molecules, which are tilted with respect to the *b*-axis of the crystal (the column axis). The tilts are reversed from one column to the next column to generate the so-called "herringbone" structure. The tilt angle *θ*, the angle between the normal to the ring and the column axis, is smaller in the *α*-form than the *β*-form. Typical angles for the *α*-form and *β*-form are *θ*≈25° and *θ*≈47°, respectively. An intermolecular distance of *d*≈3.4 Å occurs between neighbour molecules on the stacking axis.

The non-planar phthalocyanines adopt a "shuttlecock" shape that defines two molecular sides: A "phthalocyanine-only" side and a side dominated by the central atom, called "concave" and "convex" sides, respectively. They come with two main crystal structures, the monoclinic and the triclinic phase. This is based on X-ray single crystal structure determinations of both PbPc[87,88] and SnPc[89]. The first structural determination of PbPc was of the monoclinic form in which the molecules stack linearly to form a column whose axis is along the direction of the crystal *c*-axis (Fig.8a). Intermolecular repeat spacing within a column is 3.73 Å[87]. Molecules in the next-nearest neighbour are arranged in the opposite sense, i.e. the column is inverted. In the triclinic structure, grown at a higher temperature, the molecules stack along the crystal α-axis with an alternating arrangement within a column[88]. In this form the Pb atom is further out of the plane of the central nitrogen atoms than in the monoclinic form. In this triclinic phase adjacent rows of molecules are almost perpendicular to each other (Fig.8b).

Mason and co-workers have reported a triclinic structure in their structure determi-

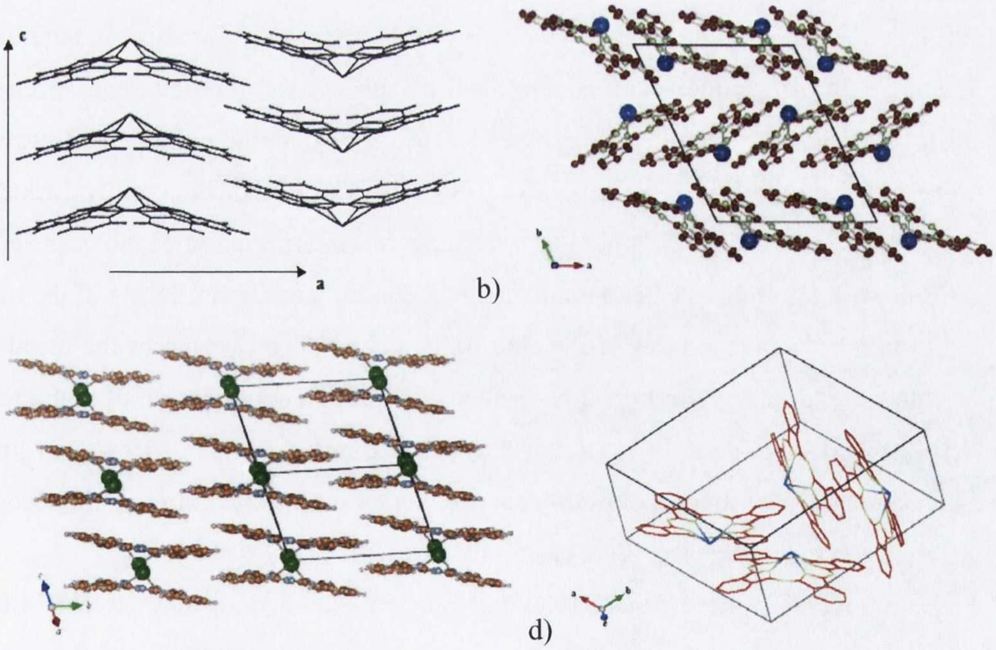

Figure 8 Crystal structures of non-planar MPcs. a) The crystal structure of the monoclinic PbPc. Molecules in the next-nearest neighbour are arranged in the opposite sense, i.e the column is inverted (after Ukei et al[87]). b)The crystal stracture of triclinic PbPc. Adjacent rows of molecules are almost perpendicular to each other c) The crystal structure of the triclinic SnPc. Adjacent rows of molecules are parallel to each other. d) The projection of concave and convex type arrangement where molecules stack along the crystal α-axis with an alternating arrangement within a column.

nation of SnPc[89], confirmed later by Kubiak[90]. Its crystal structure is similar to that of PbPc, but differs in that the adjacent rows of molecules are parallel to each other[90] (Fig. 8c). In his extensive review on phthalocyanine crystal structures, Engel also reports that SnPc could be crystallized in the monoclinic phase, however, no publication or crystallographic data is presented[79].

1.4 Electronic Structure

The chemical, mechanical, thermal, optical, and electrical properties of a material fundamentally are ultimately determined by its electronic structure.

Moreover, the transport of electrons and holes across the interface of layers on OLEDs depends sensitively on the electronic structure, and hence on the composition, structure and impurity levels of materials on either side of the junction. Because of this, the 'energetics' of an organic-inorganic semiconductor interface are of critical importance. Energetics is the term used to describe the important electrical parameters governing charge transport across semiconductor interfaces; these parameters include valence band offset, interface dipole, bandbending, etc. The energetics of inorganic semiconductor interfaces has been principally determined with a great deal of success by photoelectron spectroscopy, and this method has recently been extended to organic semiconductors. However, recent RXES work by the Downes *et al.*, has raised doubts as to the accuracy and general application of this method[91]. Their argument was that a full interpretation of the near Fermi edge electronic structure of CuPc is complicated by the particular energy levels of the transition metal ion (Cu^{2+}) attached to the phthalocyanine ligand. The overlap of the metal *3d* electronic states (d_{xy} orbital) with ligand N *2p* states produces a combination of both localized and delocalized states near the Fermi level as detailed by Liao *et al.*.[92] However, since then it has been suggested that a possibility for an exciton energy breaking could account for the difference in the near Fermi level electron states.

Furthermore, the valence band (HOMO) spectra obtained through RXES differ from XPS spectra because XPS is an ionizing spectroscopy, while RXES is not. As a consequence RXES more closely reflects the ground state molecule as the excited core electron can effectively screen the empty core-hole state in large delocalized molecular systems[93]. This difference can be clearly seen in CuPc for which the state nearest the Fermi level is a half-filled state of b_{1g} symmetry, 0.5 eV below which lies a filled state of a_{1u} symmetry; yet ionization from the b_{1g} state requires 0.7 eV more than from the a_{1u} state as indicated in Figure 9[92]. The resulting UPS spectrum is that of the final state, i.e. the ionized molecule as shown in Figure 10, and highlighted in the inset.

Accurate determination of this electronic structure near the Fermi level is of general importance in establishing accurately the energetics of organic semiconductor interfaces.

It was proposed that this RXES work be extended to other members of the phthalocyanine family; copper as the end-of-row transition metal may prove quite different from other metal types. This should provide a more accurate description electronic structure and precise values of energetics, upon which interface models can be based.

However, as the application of X-ray emission spectroscopy to organic molecules requires significant exposure of the material to the synchrotron radiation beam, it is imperative that beam damage must be accounted for when making any measurement. Where this

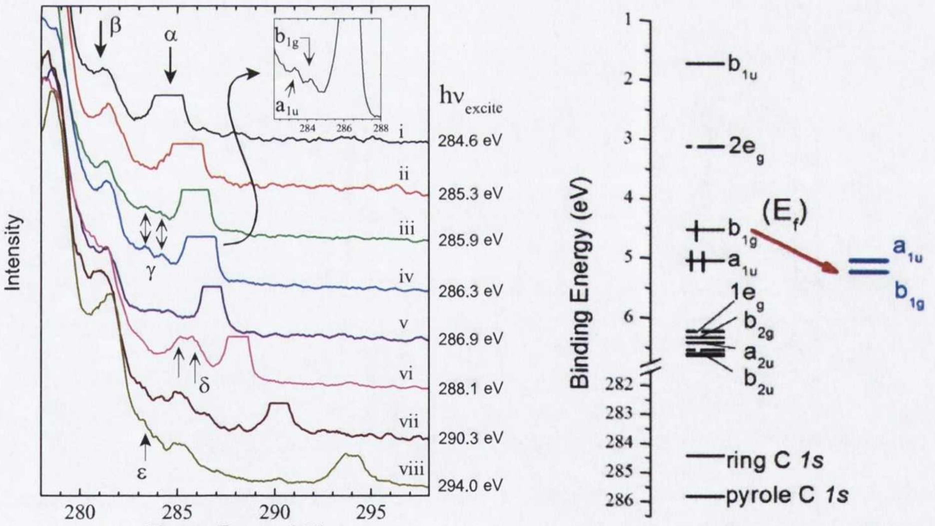

Figure 9 Left: Resonant x-ray emission spectra at the C 1s level of CuPc showing the details of the spectra near the HOMO band from Downes et al[91]. Right: Electronic structure of CuPc as calculated by Liao et al[92] with experimentally observed ring and pyrole C 1s binding energies. Observation of two discrete states near E_F labelled γ and δ (shown for clarity in the inset), which differs from published photoemission results, but is in excellent agreement with density functional calculations as shown on the right side. Strong final state effects modify the binding energy of the b_{1g} state, as observed by UPS, and photoemission from this state overlaps in energy that from the a_{1u} state producing a broad asymmetric photoemission feature that is identified in UPS spectra as the HOMO (see also Fig. 10).

is not specifically accounted for an erroneous picture of the electronic structure may emerge[91,94]. Even though phthalocyanines are known to be robust molecules the effect of beam or radiation damage on these has also been noted [95,96]. Recently obtained spectra of undamaged CuPc by Downes et al.[91] are startling in their clarity compared to previously published damaged spectra by Kurmaev *et al.*[97] (Fig. 11).

These beam damaged measurements similarly took place at a high flux undulator beamline but without taking into account the damage that occurs with long exposure. The earliest XES measurement of an organic molecular phthalocyanine semiconductor by Tegeler *et al.* was also likewise beam damaged[98]. Even though these measurements were made at a low intensity bending magnet beamline, the long spectrum accumulation time resulted in beam damage.

Recent results by McGovern and collaborators has also highlighted similar effects in photoemission, showing the effect of beam damage on the HOMO, with implications for the establishment of the energetics as described above. Moreover, this group has observed an additional effect in core-level SXPS of SnPc; the exposure-related growth of a "high binding energy" satellite is interpreted as the flux-induced conversion of Sn-II to Sn-IV

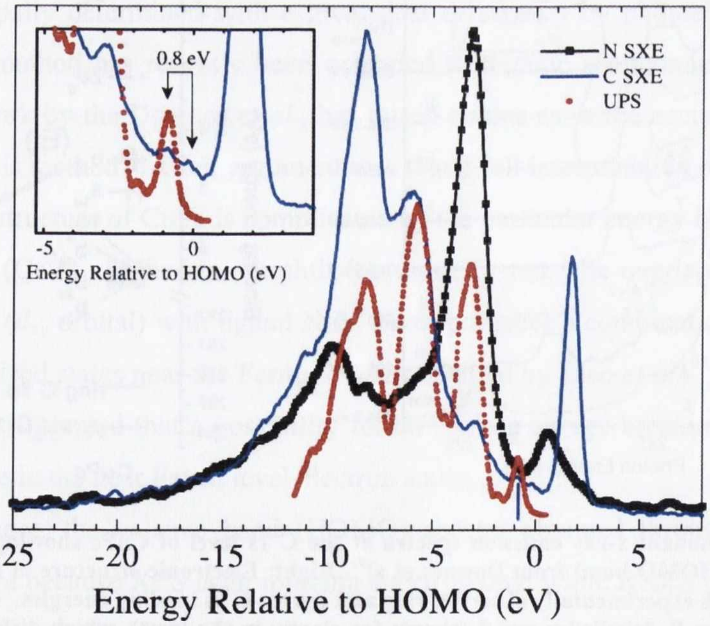

Figure 10 The N Kα RXES and C Kα RXES of CuPc compared to UPS spectrum of CuPc (from Downes et al.[91]). Detail shows difference between ionizing (UPS) and non-ionizing spectroscopy (RXES) for the a_{1u} and b_{1g} states. Peaks appeared above 0eV are due to x-ray scattering (Rayleigh scattering) in XES process, where the core hole filling occurs from the same excited electron.

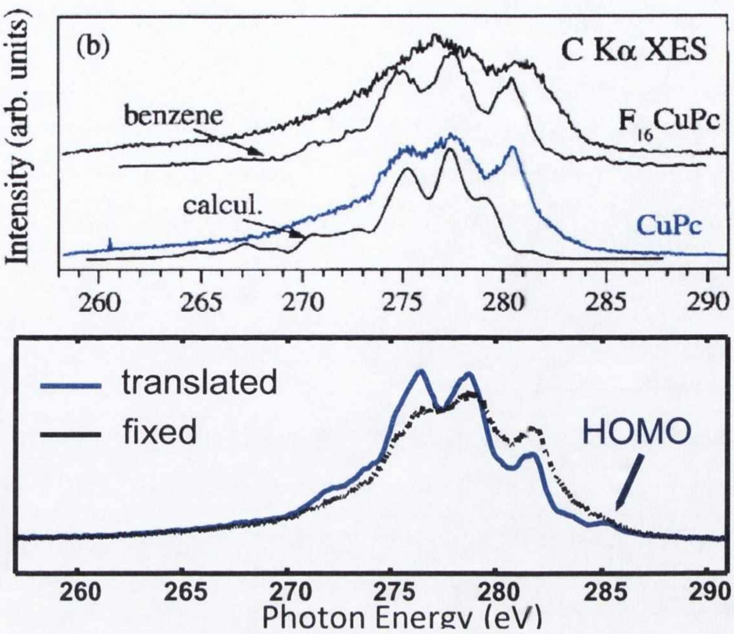

Figure 11 Top: Published spectrum of CuPc (Kurmaev *et al*[97]). Bottom: Contrast of beam damaged SXE spectrum and non-damaged SXE spectrum.[Downes et al[91]]

charge state[99].

In this thesis these observations are extended to other members of the metal-phthalocyanine family, in particular the equivalent Group IV SnPc and PbPc. The aim is to further clarify the nature of beam damage in these materials, particularly as this potentially also limits the precision of the determination of interface energetics. Furthermore, accurate exposure limits of radiation is needed in order to successfully apply resonant x-ray emission spectroscopy to a wide spectrum of phthalocyanines.

Summarizing up the aims and the purposes of this project are:

- The study of the electronic structure of organic molecular semiconductors, specifically metal phthalocyanines (M-Pc) and metal chelates through means of X-ray photoemission spectroscopy (XPS) and X-ray emission spectroscopy (XES), with straight forward comparison of the accuracy of the first technique and the role of the final state effects in the precise determination of the electronic structure of these materials. The ultimate purpose is to provide an insight into the role that these spectroscopies can play into a study of the "energetics" on interfaces with these materials.

- An in depth investigation of the radiation damage that occurs to the robust metal phthalocyanines at their exposure to the synchrotron light, which would help in the interpretation of damage effects in measurements to many other aromatic organic molecules.
- An attempt to connect specific core sites to luminescence centres of these materials using x-ray excited optical luminescence (XEOL). This is a synchrotron based spectroscopy where exciting at site specific core levels we get the optical luminescence response dependent on where the luminescence centres are located within the molecule. This could also shed light on how the chemical bonding involved on the luminescence process.

Experiments followed two parallel themes of investigation. These were firstly: beam damage in phthalocyanines and secondly: the spectroscopic characterization of organic semiconductors by XPS, NEXAFS, RXES and XEOL.

2. Experimental techniques

2.1 X-ray spectroscopies

Core level spectroscopies are important to obtain information about the chemical state, local geometric structure, nature of chemical bonding and dynamics in electron transfer processes. The core electrons are localized to one atom. They are characterised by the binding energy which describes the coulomb interaction with the nucleus, which is the energy needed for them to be removed from the atom. Different nuclei (elements) have different binding energies, e.g the 1*s* (most tightly bound) core level energy for C and N are different, this makes the spectroscopies elementally specific. The core levels can be used to determine information about valence electrons in two different ways. First, the binding energy of the core level is affected by the valence electrons, in a process called screening, principally used to determine the chemical valence of the atom. Secondly, we can have transitions between core and valence levels proving a direct probe of valence electronic structure. Since the core electrons are localized to one atom the valence electrons can be studied in an atom-specific way. This provides a tool to look into the nature of the surface chemical bond by disentangling the contributions from different atoms. Furthermore, the valence electrons will be sensitive to the local geometry or bonding environment and we can expect that the core levels are chemically shifted depending on absorption sites and molecular orientations. The excitation process involving the core electrons will also cause some dynamical response to the system involving electron transfer processes and vibrational excitations[100].

There are different core level spectroscopies which are based on the same function: creation and decay of core holes though absorption of incoming light. If the photon energy is sufficient to ionize core level electrons, we are talking about X-ray photoelectron spectroscopy (XPS) where we measure the distribution of energies of the outgoing photoelectrons. If the excitation energy is not high enough to reach the ionization continuum, we can populate bound states above the Fermi level, where this method is generally denoted X-ray Absorption Spectroscopy (XAS). It is divided into two regimes; Near Edge X-ray Absorption Fine Structure or X-ray Absorption Near Edge Spectroscopy (NEXAFS or XANES) for bound states and low energy resonances in the continuum (these shape resonances can extend to 40eV above threshold), and the Extended X-ray Absorption Fine Structure (EXAFS) when the outgoing electron is well into the ionization continuum. In the NEXAFS regime the spectroscopy provides information about the empty molecular electronic states.

The core-hole can decay through two different mechanisms involving non-radiant and radiant processes. The first process involves an electronic rearrangement and will lead to electron emission, denoted Auger decay. The second set of processes will lead to luminescence emission of X-rays or optical light. In the radiant process the core-hole is filled with an outer shell electron and the excess energy is emitted in the form of a photon. For all core-levels both types of process contribute to the decay. In order to obtain information about the bonding of the electrons we are primarily interested in decay processes involving the valence states. The analysis of the emitted electrons is the basis for Auger Electron Spectroscopy (AES) and on photons Optically Detected X-ray Absorption spectroscopy (OD-XAS), X-ray Excited Optical Luminescence (XEOL) and X-ray Emission Spectroscopy (XES). For the XEOL and OD-XAS, the emitted photons may arise from a secondary process, where the primary core-hole decays through a non-radiant process, and the subsequent shallow core hole decays radiatively. However, XES is the direct radiative emission process in which the primary core hole created will be filled by dipole-allowed transitions. In XES the valence electron states projected on the absorbing atom are observed. This contrasts with valence band photoemission where the electronic structure of the whole system is measured [100].

2.2 Synchrotron light source radiation.

These spectroscopies require a tunable, high brilliance radiation sources to probe the varied binding energies of the elements. Synchrotron radiation provides this. It is generated when a charged particle (electron), moving at relativistic speeds is accelerated in a magnetic field as shown schematically in Fig. 12a. This causes emission of electromagnetic radiation in a broad spectral range from the infrared region though the visible, ultraviolet, and into the x-ray region up to energies of many tens of kilovolts. The acceleration can be achieved either by bending magnets (circular motion) or by periodic magnetic structures

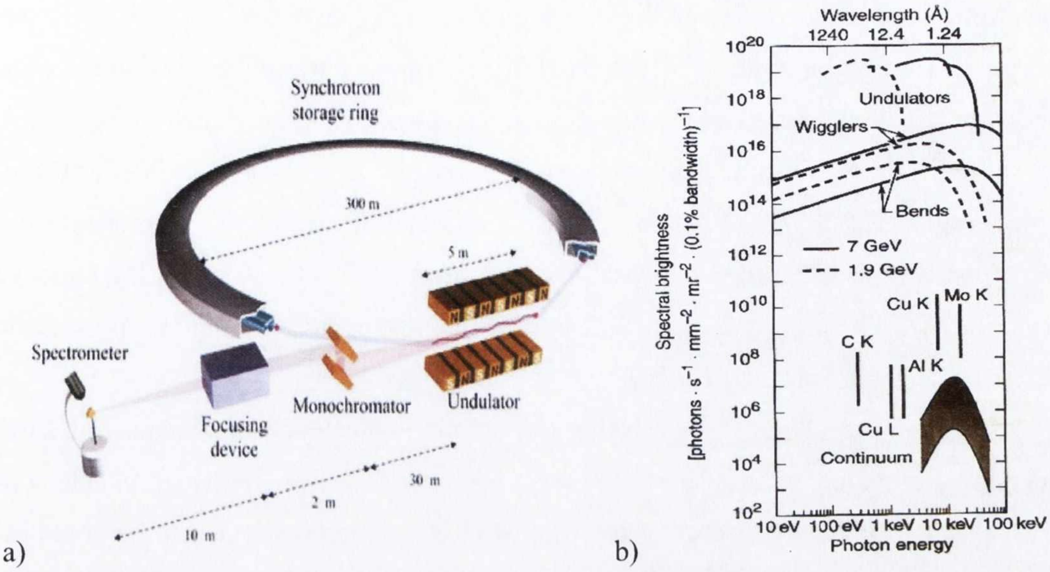

Figure 12 a) Outline of a synchrotron storage ring and typical beamline set up[101]. b) Spectral brightness for several synchrotron radiation sources and conventional x-ray sources[102]

(sinusoidal motion). Synchrotron radiation provides a bright, polarized photon beam as the excitation source. In general, synchrotron radiation is several orders of magnitude more intense, more site selective (through its tunability) and covers a much broader energy range than conventional X-ray sources, as well as being polarised.

Three types of radiation sources on a "typical" storage ring are common: bending magnets, wigglers and undulators, with increasing brightness respectively. Figure 12 b shows the spectral brightness for several synchrotron radiation sources and conventional x-rays sources.

2.2.1 Why is Synchrotron Radiation required?

High intensity X-ray sources, such as 3rd generation synchrotron sources, are required for XES studies in order to compensate for the low probability of radiative vs. non-radiative de-excitation of the core hole (Fig. 13) for light ele-

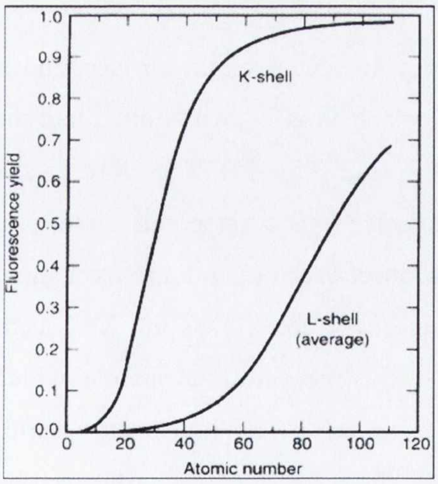

Figure 13 Fluorescence yield emission depending on atomic number[102,103].

ments. More importantly, the tunability of synchrotron radiation allows for selectively creating a core hole on an atom in a compound. This is particularly useful in organic compounds where the core levels of inequivalent carbon atoms are usually chemically shifted. Thus, different atomic (chemical) sites in a molecule can be easily probed by X-ray absorption near edge spectroscopy (XANES or NEXAFS), which then can drive a resonant excitation of the core level of these different chemical sites to unoccupied states, the radiative decay of them (XES) may produce significantly different spectra reflecting the site-specific local partial density of states (LPDOS).

Synchrotron radiation has also transformed the photoelectron techniques of ultraviolet and x-ray photoemission spectroscopes (UPS/XPS). The availability of tunable photons means that the kinetic energy of the emitted electron can be selected to be at the escape depth minimum, i.e. greatly enhancing the surface-sensitivity of these techniques; this is usually described as soft x-ray photoelectron spectroscopy (SXPS).

Absorption spectroscopy (NEXAFS/XANES) is a tool to probe the empty states below the vacuum level, and is traditionally obtained with secondary electron yield from synchrotron polarized light also can be probed by photon emission. Thus also the polarization geometry of absorption provides state selectivity in the measured x-ray emission spectrum.

2.3 X-ray photoelectron spectroscopy (XPS)

XPS is in principle a simple process. A photon of energy *hν* penetrates the surface, and is absorbed by an electron with a binding energy of E_B. This electron is then emitted into the vacuum with a kinetic energy: $E_{kin} = h\nu - E_B - (E_{vac} - E_{Fermi})$ (Fig. 14). Therefore, in the simplest approximation, the energy distribution of photoelectrons corresponds directly to the energy distribution of electron states in the solid surface. With a good approximation, this formula gives the binding energy of the emitted electron, and allows the XPS technique to be used as a probe to identify the chemical elements present in the sample, which show dramatically different spectral “fingerprints”. Moreover, the binding energy varies even for electrons in the same elemental core level since this is considerably influenced by factors like the valence of the atom, the local chemical and physical environment. These variations in energy for a given elemental level are known as chemical shifts, and provide the XPS technique the ability to distinguish atoms of the same species in different environments. This constitutes the basis of the property of site selectivity.

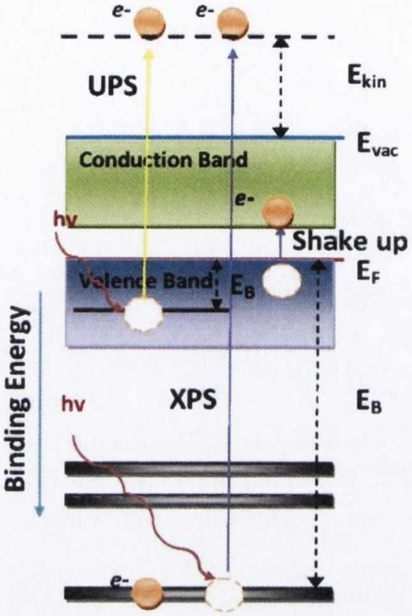

Figure 14 Sketch representing photoemission processes (XPS and UPS).

In ultraviolet photoemission spectroscopy the same principal applies. However, in this case only the shallow (valence) level electrons can be excited. The distribution of energies of the photoemitted electrons is then recorded with an electron energy analyser. The recorded spectrum of energies reflects the valence or HOMO band density of states. This is valence band XPS or UPS.

2.3.1 The shake-up process

This description, although very useful for the immediate interpretation of the main spectral lines, does not account for the complexity of the XPS satellite lines and spectral shapes, which are found in experiments.

The photoemission process involves a transition from an initial state *i* of wave function ψ_i to a final state *f* of wave function ψ_f. (This brief treatment is similar to any introductory text on photoemission such as Spectrophysics: Principles and Applications by A. Thorne, U. Litzen,S. Johansson[104]). This transition is induced by the photon field. The transition probability may be calculated by use of Fermi's Golden Rule, which in the dipole approximation gives:

$$w = \frac{4\pi^2}{h} \left|\langle \Psi_f | r | \Psi_i \rangle\right|^2 \delta(E_f - E_i - h\nu) \quad (1)$$

where ***r*** is the dipole operator and E_i, E_f the initial and final energy states, respectively. In order to discuss the transition matrix element certain assumptions about the wave functions have to be made. The simplest approximation is to assume that the initial and final states may be described in terms of single electron wave functions. In addition, the final states involves a free electron of kinetic energy E_{kin}. We can then write the initial state wave function as a product of the orbital $\varphi_{i,k}$ from which the electron was excited and which represents the *N-1* remaining electrons:

$$\psi_i(N) = C\varphi_{i.k}\psi^k_{i,R}(N-1) \quad (2)$$

where *R* means remaining, with the kth electron excluded, and C is a constant

In a similar fashion the final state wave function may be written as:

$$\psi_f(N) = C\varphi_{f.E_{kin}}\psi^k_{f,R}(N-1) \quad (3)$$

Therefore the transition matrix element may be written as:

$$\langle\psi_f|r|\psi_i\rangle = \langle\varphi_{f,E_{kin}}|r|\varphi_{i,k}\rangle\langle\psi^k_{f,R}(N-1)|\psi^k_{i,R}(N-1)\rangle \quad (4)$$

If the *N-1* remaining electrons are unaltered by the photoemission process the final factor in the above expression $\langle\psi^k_{f,R}(N-1)|\psi^k_{i,R}(N-1)\rangle = 1$, and the transition matrix element reduces to the simple expression that contains two one-electron wave functions:

$$\langle\psi_f|r|\psi_i\rangle = \langle\varphi_{f,E_{kin}}|r|\varphi_{i,k}\rangle \quad (5)$$

This is often denoted "the frozen orbital approximation".

However, this approximation fails to accurately describe the spectra in most cases since after the excitation of the electron from orbital *k*, the remaining *N-1* electrons readjust in such a way to minimize its energy. This is called relaxation.

To account for relaxation we now assume that the final state of *N-1* electrons has *m* excited states with the corresponding wave function: $\psi^k_{f,m}(N-1)$ and energy $E_m(N-1)$. The expression for the transition matrix element becomes:

$$\langle\psi_f|r|\psi_i\rangle = \langle\varphi_{f,E_{kin}}|r|\varphi_{i,k}\rangle \Sigma_m C_m \quad (6)$$

where C_m is given by:

$$C_m = \langle\psi^k_{f,m}(N-1)|r|\psi^k_{i,R}(N-1)\rangle \quad (7)$$

Here $|C_m|^2$ is the probability that the removal of an electron in orbital φ_k of the *N*-electron ground state leaves the system in the excited state *m* of the *N-1* electron system. For strongly correlated systems many of the C_m are non-zero. In the photoemission spectrum this means that for *m=k* one obtains the "main" photoemission peak, and for the other non-zero C_m one gets "satellite" peaks. If electron-electron correlations are weak, the C_m are zero for $m \neq k$ and $|C_m|^2=1$, only the "main" photoemission peak remains.

Such satellites play an important role in various areas in solid state physics. Satellite peaks which stem from relaxation, shake-up (excitation to a bound state) and shake-off (excitation to the continuum) processes are many-electron or many body effects, and are in principle complicated to describe in a comprehensive way.

The electron correlation and relaxation have considerable effect on the photoelectron spectra, for example asymmetry of the shape of the peaks due to post collision interaction (PCI) in metals[105,106] or extra features close to the spectroscopic main lines (shake-up, shake-off). The shake-up excitations are experimentally observable as satellite lines, lying at higher perceived binding energies than the main peak, as shown in the example in Figure 15.

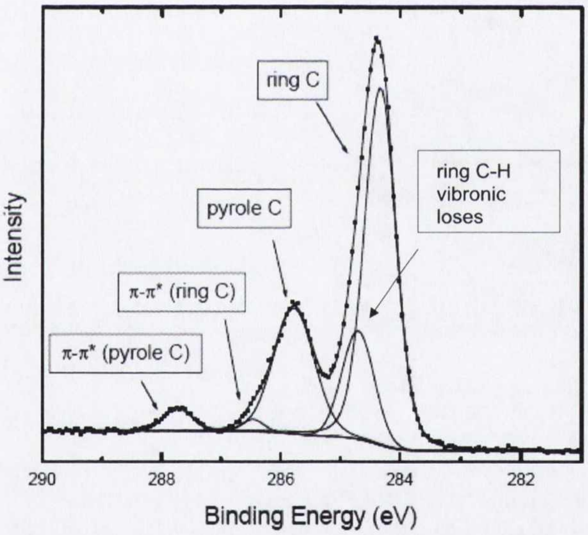

Figure 15 X-ray photoelectron spectrum of C *1s* and from CuPc[107]. Excitation of secondary electrons from π state on HOMO to π* LUMO state caused by electrons of high kinetic energy of the main peaks appear as the "shake up" features at apparently higher binding energy due to a non-ground state molecule remaining after photoelectron emission. The energy difference between the shake up features and the main peaks in a good approximation measures the optical bad gap of this organic semiconductor.

2.4 X-ray absorption spectroscopy (XAS)

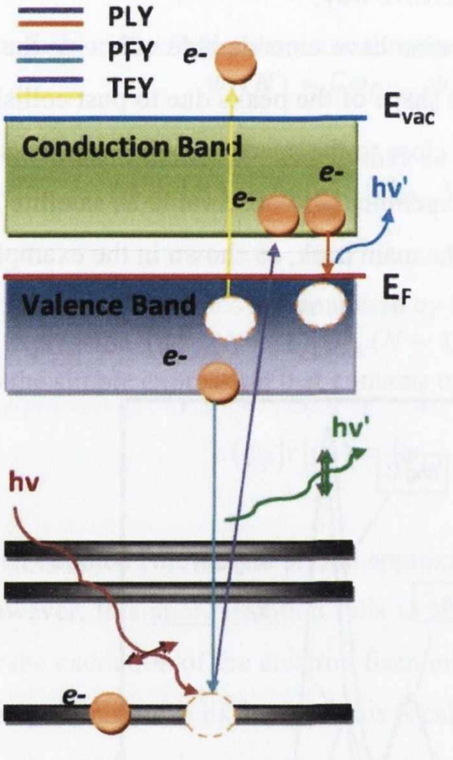

Figure 16 Sketch presents three different ways of probing NEXAFS through total electron yield (TEY), partial fluorescent yield (PFY) and photoluminescence yield (PLY). Colour sheme: violet describes initial excitation of e$^-$, in compination with: yellow describes TEY, cyan describes PFY and orange describes PLY.

The X-ray absorption process is shown schematically in Fig. 16. A photon is absorbed by an electron in a core level which is excited into an unoccupied state above the Fermi level. The final state in the absorption process is therefore a neutral excited state. The key assumption when doing soft X-ray absorption, is that the yield of electrons or photons from the decay of the excited state is proportional to the probability of exciting an electron from a core level to a given electron energy level above the Fermi level. Soft X-ray absorption requires the photon energy to be varied and thus requires the use of synchrotron radiation. However, the detection system is simple, and the experiment is in principle relatively simple to perform. Stöhr provides a complete review of NEXAFS spectroscopy [108].

The acronym NEXAFS (near-edge X-ray absorption fine structure) is used primarily in connection with studies of adsorbed molecules on crystal surfaces, where the polarized nature of the synchrotron radiation is utilized. This provides a sensitive experimental tool in determining molecular orientations on surfaces. The near edge x-ray absorption fine structure (NEXAFS) is dedicated to the study of the near edge region of the absorption spectra. It is a probe of the unoccupied energy levels, and provides information on the

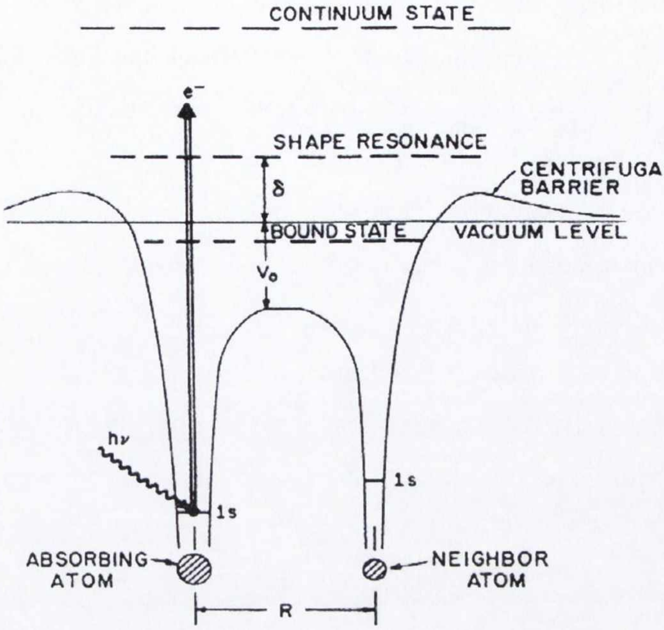

Figure 17 Figure shows schematic pictures of the various regions in a NEXAFS spectrum of a molecule [after [109]].

chemical bonding, as well as the geometrical orientation of a molecule. For a large class of molecules, ranging from di- to poly-atomic sizes, there exists a region around the *1s* absorption threshold that is dominated by resonance structures of varying energy position and intensities. The positions of the most pronounced resonances correspond to excitation energies that are about 5 to 10 eV below the *1s* ionization energy (IP). Such bound-state resonances originate from transitions to partially filled molecular orbitals or to unfilled orbitals that are pulled below the vacuum level by the Coulomb interaction with the created core hole. Above the ionization threshold (IP) other wider resonances exist. These are called shape-resonances and are assigned to relative increases in the amplitude of continuum states of σ-symmetry within the molecule near the atomic site.

In Fig. 17. is shown a schematic diagram of the potential wells in a diatomic molecule. In molecules with unoccupied π^* orbitals the lowest energy molecular resonance occurs at an excitation which is less than the *1s* IP and is a transition to the lowest unoccupied molecular orbital (LUMO) in molecular systems. It corresponds to a transition of a *1s* electron into an empty or partially filled antibonding π^* orbital. The σ shape resonance (typically observed at 5-20 eV higher energy) corresponds to a transition from *1s* into a σ^* state located immediately above the vacuum level. This resonance may be viewed as the result of the photoelectron wave being scattered resonantly back and forth along the inter-nuclear axis between the absorbing atom and its neighbour[109] or by a quasi bonded electronic state due to the potential barrier.

The dipole approximation introduces restrictions about which transitions are allowed for the atomic/molecular electrons. The dipole approximation is based on the fact that the function $e^{ik \cdot r}$ describing the special behavior of the electromagnetic field (of x-rays) is at a first approximation $e^{ik \cdot r} = 1$ because λ ($|k| = 2\pi/\lambda$) for soft x-rays transitions is of order 20-250 Å and $|r|$ (electron-nuclear distance) of the order of 0.5-1.0 Å. The dipole operator that describes the interaction of the x-rays with an electron creating the transition is:

$$\langle f|r|i\rangle = \int \Psi_f^* r \Psi_i dr. \quad (8)$$

Since r changes sign by inversion at the origin, the contributions from all values of r to the integral will cancel, unless $\Psi_f^* \Psi_i$ also changes sign, i.e. the product of the two wave functions has odd parity. That means that the initial and the final states must have opposite parities. As parity depends on $\sum l$ (where l is the orbital angular momentum quantum number), it follows that l of the electron making the transition must change by ±1, ±3,… . A detailed investigation of the angular part of the wave functions shows that only a change of ±1 is allowed, and we have the selection rule $\Delta l = \pm 1$. Similarly the magnetic quantum number (m_l) gives the selection rule $m_{ll} = 0, \pm 1$.

Thus, if the transition involves a K-shell, for example a C *1s* electron, then only transitions to p character unoccupied states are allowed, and it is in-fact this angular momentum specific partial density of states (PDOS) of a material that NEXAFS measures, e.g the local *2p* PDOS on the specific atomic site of the excitation.

The excited state or core hole and LUMO electron, generated by the x-ray absorption process can decay via several channels (Fig. 16). Typically, the dominant mechanism is via Auger decay, or the related Coster-Kronig process. Two different decay channels of the excited system are possible within the Auger process: (1) An electron in a lower energy level may decay into the deep core hole, while the initially excited electron remains in its state (called "spectator" decay) or (2) the electron that was initially excited may decay into the core hole. This is called "participator" decay. In both cases a second electron is ejected from the system. As an example, after excitation of the C *1s* core level to the LUMO, the core hole is filled by an electron of *2p* states and another electron from the same state emitted to conserve energy. This is the *KLL* Auger transition process, involving only transitions from the two first quantum energy levels (*K,L*). Typically lifetime for this transition is in the order of ten femtoseconds (~10 fsec). Both these decay channels ultimately excite large numbers of low energy electrons from the surface of the sample. As the number electrons that is produced is directly connected to the number of x-rays absorbed, this provides a means by which the x-ray absorption transition probability may be measured experimentally. This is referred to as the total electron yield (TEY) or sample drain current method. A secondary channel involves the radiative decay of a valence electron into the core hole. If the flux of x-ray photons emitted by the sample is measured, then this provides another means to indirectly observe the underlying x-ray absorption process. This is called the partial fluorescent yield (PFY) method[108].

A third channel involves radiative decay through optical light, a photoluminescence procedure named as Optically Detected XAS. OD-XAS is essentially an energy transfer event in which the absorption of the X-ray photon produces a large number of energetic electrons (photoelectron and Auger). These electrons in turn cause further ionization and excitation. The energy is transferred to luminescent centres through inelastic processes which lead to creation of holes in the valence band and electrons in conduction band in semiconductor nanostructures, for example, or holes and electrons in the occupied and unoccupied molecular orbital (MO) of organic molecules, respectively. The radiative recombination of holes and electrons will emit light. In that way this can probe the core electronic structure which caused this emission of photons. This is the well-known scintillation process. OD-XAS is also a photon in – photon out technique and is called partial luminescence yield (PLY) method[110,111]. Measuring the PFY and the PLY simultaneously is referred to as the total fluorescence yield (TFY).

One important property of the NEXAFS technique is the polarization dependence which is commonly exploited to determine the orientation of ordered molecules. The angular dependency is contained in the dipole transition matrix element. The molecular and atomic electrons are described by wave functions that are characterized by a well defined spatial orientation. The orientation of the transition matrix element depends on the relative orientations of the electronic wave functions and the electromagnetic field. The intensity of a particular resonance depends on the relative orientations of the matrix element with respect to the polarization vector of the photon electric field $\hat{E}$. The polarization dependence can be expressed as a function of the angle (ϑ) between the direction of maximum amplitude of the resulting vector matrix here discussed, and the polarization vector of the photons. The σ^* bond lies along the molecular internuclear axis (defined as z for the following discussion). The π^* bonds, for a homonuclear diatomic molecule, are aligned perpendicular to this axis (defined as x and y for the following discussion). The resonance intensities for the transition from the *1s* to the σ^* and, respectively, π^* levels are:

$$I_{f,i}(\sigma) \propto |\hat{E}| * |\hat{z}|^2 \propto \cos^2 \vartheta \quad (9)$$

$$I_{f,i}(\pi) \propto |\hat{E}| * |\hat{x}|^2 + |\hat{E}| * |\hat{y}|^2 \propto \sin^2 \vartheta \quad (10)$$

where ϑ is the polar angle between $\hat{E}$ and the internuclear axis (along z). The polarization dependences for σ^* and π^* have opposite behaviour. $I_{f,i}(\sigma)$ is at its maximum when the polarization vector is aligned with the internuclear axis, while $I_{f,i}(\pi)$ reaches its maximum when the polarization vector is normal to the internuclear direction. This offers a very useful and simple thumb rule for the determination of molecular orientations and also for the study of the molecular bonds provided we can distinguish between σ^* and π^*absorption features[112]. In general σ and π orbitals (and in this case σ^* and π^*) can be distinguished due to their energy separation which Hückel[113] introduced as one of the fundamental concepts of quantum chemistry, where σ orbitals are symmetric with respect on the reflection in the plane of the molecule and π orbitals are antisymmetric. The most tightly bound orbitals are thus bonding σ, bonding π, antibonding $\pi^*$and antibonding σ^* respectively. In general below a certain energy threshold the π^* states are probed and above that σ^* are probed. However, for some molecules, such as CuPc, there may be an energy overlap between transitions to in-plane orbitals and out-of-plane π^* orbitals[114].

2.5 X-ray Emission Spectroscopy (XES)

Soft X-ray emission (SXE) occurs (soft X-rays generally defined as spanning the range ~100-1000 eV) when the resultant core-hole is then filled by another electron through a radiative transition, where the most probable radiative process is a dipole transition (selection rule $\Delta l = \pm 1$ applies). The emitted photon has an energy which is equal to the difference in binding energies of the two states involved and the final state is also an ionized one. When the valence band electrons participate in filling the core hole, then the width and shape of the emitted spectrum of photon energies reflects the dipole-selected angular-momentum component of the valence band or occupied molecular orbital partial density of states (PDOS). Thus, when probing organic molecular systems the creation of a carbon *1s* core hole results in fluorescence yield or x-ray emission involving dipole transitions from the carbon *2p* states that contribute to the valence band or occupied molecular orbitals of the material. The emitted spectrum then corresponds to the carbon *2p* occupied PDOS. The binding energy of the carbon *1s* level (285 eV) is in the soft x-ray region of the spectrum as is the consequent SXE spectrum. Recording the SXE spectrum is more commonly referred to as X-ray Emission Spectroscopy.

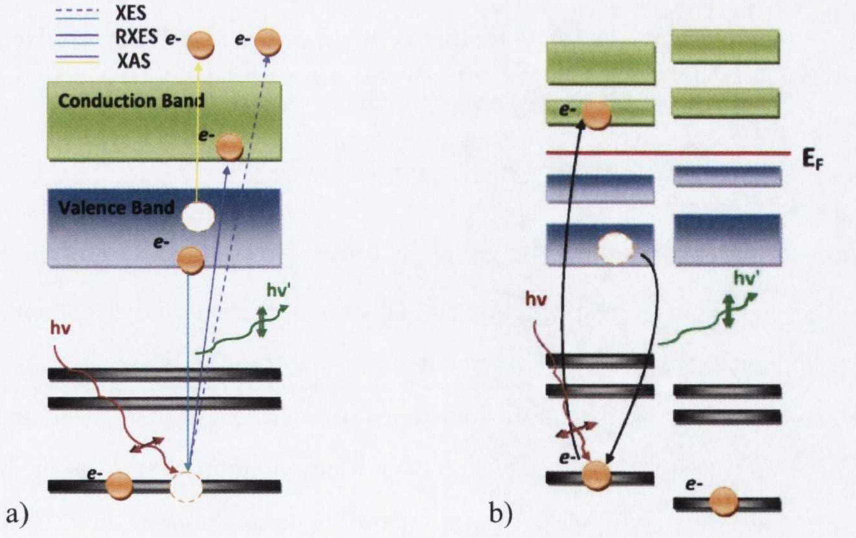

Figure 18 a) schematic of X-ray Emission Spectroscopy (XES) or Soft X-ray Emission (SXE) when x-rays ≤1000 eV as demonstrated along with the Resonant X-ray Emission (RXES) where the first step is Soft X-ray Absorption (XAS) and b) Schematic of resonant X-ray Emission Spectroscopy (RXES) from a molecule in which the core site of the same element in different chemical environment can be independently excited. The resultant RXES could be a projection of the local partial density of states (LPDOS) of that site on the valence band (site selective).

Different XES techniques have emerged, depending on the information that can be obtained from the experiment and the energy of the incident photons: (i) If the core electron is resonantly excited to the absorption threshold by the incident photon (as in X-ray absorption spectroscopy), the resulting emission spectrum depends strongly on the incident photon energy; this technique is denoted as Resonant X-ray Emission spectroscopy (RXES) as shown in Fig. 18. (ii) If the core electron is excited well above the absorption threshold i.e. non-resonant, the XES spectroscopy is called NXES (Normal X-ray Emission Spectroscopy) Fig.18a. In this case, the emission spectrum does not depend on the energy of the incident photons. The difference between RXES and NXES is that the intermediate state of RXES is the same as the final state of an X-ray absorption spectrum, where an electron is promoted to an empty bound level. Whereas that of NXES is the same as the final state of X-ray photoemission from the core level. Sometimes RXES is denoted as RIXS (resonant inelastic X-ray scattering) or RXRS (Resonant X-ray Raman Scattering) because it can be described as an inelastic process due to the fact that the energy of the emitted photon is different from the energy of the incident photon. On the other hand, NXES is also called "x-ray fluorescence spectroscopy".

RIXS describes the inelastic scattering of x-rays, with the photon energy tuned to the x-ray-absorption resonance of the scatterer, where the resonant inelastic scattering cross section is given in perturbational treatment by the modified Kramers-Heisenberg formula:[115,116]

$$I_{RIXS}(\omega',\omega) \propto \sum_F \left| \sum_M \frac{\langle F|\vec{D}\cdot\overrightarrow{E'}|M\rangle\langle M|\vec{D}\cdot\vec{E}|G\rangle}{\hbar\omega-(E_M-E_F)+i\Gamma_M/2} \right|^2 \times \delta(\hbar\omega-\hbar\omega'+E_G-E_F) \quad (11)$$

The energy of the incoming and outgoing photons is given by $\hbar\omega$ and $\hbar\omega'$, with the electric-field vectors $\vec{E}$ and $\overrightarrow{E'}$, respectively, and $\vec{D}$ is the transition dipole moment. The scattering process consists of x-ray absorption from the ground state $|G\rangle$ to intermediate states $|M\rangle$, and x-ray emission to all final states $|F\rangle$ with energies E_G, E_M, and E_F, respectively. The core-hole intermediate states have a lifetime broadening Γ_M. For different core-hole intermediate states with an energetic separation comparable to their lifetime broadening Γ_M, the multiple-scattering channels interfere, making the x-ray absorption and x-ray emission inseparable[115]. The interfering intermediate states are due to closely spaced absorption resonances or vibrational excitations. In the RIXS process the initial and final states transform according to the same irreducible representation (final states of same parity as the initial state), where the total nuclear and electronic symmetry of the scatterer has to be considered, since the nuclear and electronic motion is coupled[117]. A full RIXS description is necessary for many periodic systems, i.e. crystals. Here the atomic symmetry-selection rules transform to *k*-selection rules, and the energy dependence of the RIXS spectral distribution contains band-structure information on the joint density of states as momentum is conserved in the coupled absorption and emission steps as is shown in Figure 19[115,117].

In the case where different core-hole intermediate states with an energetic separation larger than their lifetime broadening Γ_M only a single core-hole intermediate state $|M\rangle$ is possible to be reached and the RIXS can be described in a two-step approximation, an independent =X-ray absorption step and subsequent radiative decay of the core-hole state. This case is denoted as resonant x-ray emission (RXES) and the x-ray emission spectrum is then given by Fermi's golden rule[117]:

$$I_{RXES}(\omega') \propto \sum_F (E_M - E_F)^3 \left|\langle F|\vec{D}\cdot\vec{E'}|M\rangle\right|^2 \times \delta(E_M - E_F - \hbar\omega') \quad \text{(XII)}$$

This will most likely occur in the case of a narrow band organic molecular solid where if the organic molecule contains several atoms of the same type but with differing chemical environments, then the energies of their core-level states may be sufficiently separated that transitions between these chemically shifted core levels and unoccupied states may be excited independently, as is illustrated in Fig. 18b.

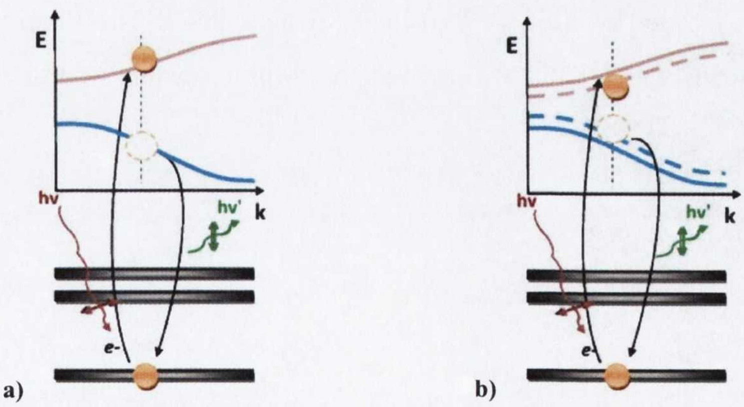

a) b)

Figure 19 a) The core electron is resonantly excited into an unoccupied band close to the Fermi level. Crystal momentum as well as energy and angular momentum are conserved and the emission spectrum contains information on the band structure of the crystal. This is the non-relaxing, or frozen orbital, approximation. b) The interaction between the core-hole state and the valence and conduction states modifies the band structure, resulting in excitonic bands in the band gap.

In some cases dynamical effects require the scattering process to be considered as a three-step process rather than the two-step process described above. In the case where the intermediate state may undergo a transition in the time interval between the excitation and the emission of the X-ray photon e.g an electron or a phonon could be emitted or absorbed. The excited molecular system in the resonant case with an electron populating specific unoccupied states could also create excitonic states due to electrostatic, relaxation and correlation contributions[118], which can have significant effect in the energy of the bound electrons (screening effect). In these cases the sudden approximation and frozen orbital approximation may be invalid (Fig. 19b).

As has been mentioned, in the soft x-ray region the dipole approximation applies, and for systems with inversion symmetry, like homonuclear diatomic molecules, each dipole transition changes the parity, from even (gerade) to odd (ungerade) or vice versa. As such when an electron is excited into an unoccupied molecular orbital state of a given symmetry, this places a further restriction on the occupied levels that are allowed to fill the core-hole.

Dipole selection rules are important also in systems with lower symmetry where this can be seen in the angular dependence of the scattering. Thus, exciting a linear C-C-N bond with linearly polarized soft x-rays, at the central C site as demonstrated in Fig. 20, parallel to the internuclear axis it is possible to record emission, at 90º to the incident beam. This can be either normal to the internuclear axis (and normal to the polarization) or emitted along the internuclear axis (and parallel to the polarization). In each case light from the occupied C 2p states with different spatial orientation due to selection rules will be detected. In the first instance, radiative decay or XES from the atomic p states in the plane

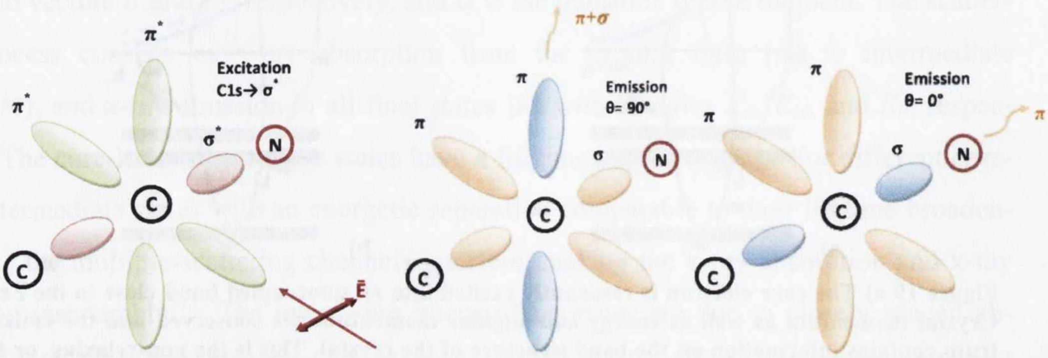

Figure 20 Sketch illustrating the origin of angular dependence in RSXE in the case of excitation to a σ bond from linear polarized x-rays where the symmetry of the core excited states drives the emission anisotropically.

normal to the emission axis, are selected and are from molecular σ and π states. In the second instance, XES from atomic *p* states in the plane normal to the emission axis are detected and are from molecular π states only.

Because radiative decay in the soft x-ray region is orders of magnitude smaller than non-radiative decay and because spectra are recorded within a narrow band of energies, only third generation synchrotron radiation sources and undulator insertion device beam lines provide the flux and brightness needed for these experiments.

2.5.1 Why XES or specifically RXES?

If the photon energy is close to the absorption threshold as in RXES, then the excited electron resides in a conduction band state. Therefore, RXES can be considered as a non-ionizing spectroscopy. In this case, features due to both conventional emission processes and due to resonant inelastic x-ray scattering (RIXS) become visible. In RXES the resulting spectrum may differ considerably from that obtained far above threshold. These differences can occur due to either site selectivity or state selectivity via RXES. In phthalocyanine based organic semiconductors there is a chemical shift between the ring carbon *1s* binding energies and the pyrrole carbon *1s* binding energies (Figs. 4 and 15). This shift means that on resonance with the absorption threshold one can only create core holes and observe x-ray emission exclusively from those sites with the lowest binding energy (ring sites). Hence the emission spectrum is the site specific carbon *2p* valence band PDOS or local partial density of states (LPDOS) of the ring site. With increasing photon energy core-holes are created on all carbon sites, in proportion to the XAS intensity associated with each site, and the XES spectra will contain an LPDOS contribution from the pyrrole sites.

Using RXES, core hole lifetime effects, specifically broadening, can be side stepped. The resolution of the experiment is limited not by the lifetime of the intermediate state (final state of XAS with core hole) but by the longer lifetime of the RXES final state (HOMO hole)[119], thus allowing higher resolution determination of the HOMO states than with NXES.

Furthermore, in RXES near threshold the molecule is not ionized and the core hole on the atomic site will be better screened due to the electron in the LUMO levels and by the delocalized states. As a result the RXES spectrum should give a better representation of the PDOS of the neutral molecule than ionizing spectroscopies like photoemission spectroscopy [119].

2.6 X-ray Excited Optical Luminescence (XEOL)

The excitation of electrons involves the absorption of an X-ray photon to excited or ionized states resulting in emission of photoelectrons, Auger electrons and further secondary electrons; typically detected by total electron yield (TEY) methods. The decay of these core-hole excited states may, through interactions of the Auger or secondary electrons with the valence states result in energy being transferred to luminescent centres or chromophores through inelastic or shake-up processes. This can result in creation of holes

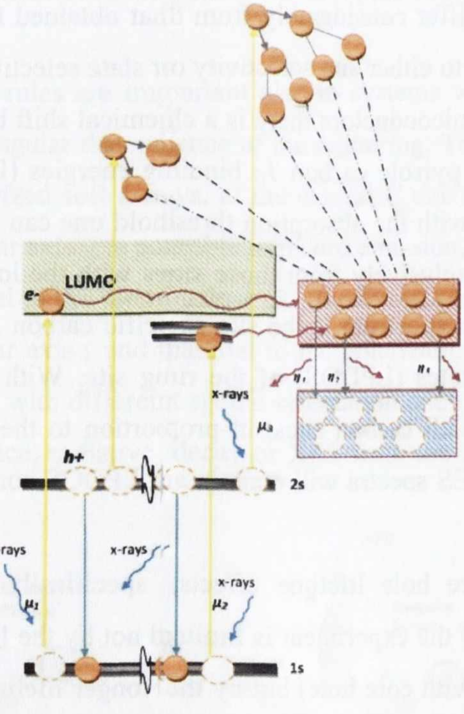

Figure 21 A schematic diagram of the excitation-luminescence cycles. Three different excitations are shown: From a *1s* state (absorption coefficient μ_1) to a continuum state, a *1s* state (μ_2) *to* a bound state, and a *2s* (μ_3) to a continuum state, each give rise to luminescence with the respective luminescence yields η_1, η_2, and η_3. The different pathways to luminescence of X-ray fluorescence, KLL Auger electron multiscattering, a non-radiative decay due to electron-phonon scattering, and radiative transitions are schematically depicted. (after[120])

in valence band and electrons in conduction band for example in semiconductors, or in the occupied and unoccupied molecular orbital (MO) of organic molecular semiconductors. In OD-XAS the radiative recombination of these holes and electrons is measured as a function of photon energy. In XEOL the spectral distribution of these optical photons is measured and both spectroscopies can be a probe of the core electronic structure that is related to luminescence. Both of these spectroscopies target the optical transitions from the ultra violet (UV), to visible and infrared (IR) range, though this is dependent upon the detector system used.

There are three different excitation pathways that can give rise to a single luminescence and these have been described by Emura et al[120](Fig. 16). Excitations from a *1s* state to a continuum state, a *1s* state to a bound state, and a *2s* to a continuum state-give rise to a single luminescence with different luminescence yields (η). A simple model has been put forward to explain the essential processes that result in an XEOL spectrum. The proposed simple model has a sample with thickness *t* that is irradiated with incoming photons of intensity I_o. This leads to the intensity of optical luminescence due to the *L*-shell and *K*-shell excitations as[120]:

$$P_L = \int_0^t dP = I_o \frac{\mu}{\mu+\mu'} \eta_L \left[1 - e^{\{-(\mu+\mu')t\}}\right] \quad (13)$$

and

$$P_K = \int_0^t dP' = I_o \frac{\mu'}{\mu+\mu'} \eta_K \left[1 - e^{\{-(\mu+\mu')t\}}\right] \quad (14)$$

respectively: μ and μ' are the absorption coefficients for the *L*-shell and *K*-shell excitations and are dependent on the excitation energy *E*; η_L and η_K are total yields of the optical luminescence due to the *L*-shell and the *K*-shell excitations. The total intensity is the sum $P_L + P_K$. As $\mu' = 0$ for $E < E_K$, where E_K is the *K*-edge excitation energy, the ratio *R* between the total intensity to P_L is defined as:

$$R = \frac{P_L + P_K}{P_L} = \frac{\overbrace{\left[1-e^{\{-(\mu+\mu')t\}}\right]}^{H1}}{[1-e^{-\mu t}]} \frac{\overbrace{\mu+\mu' B}^{H2}}{\mu+\mu'} \quad (15)$$

where $B \equiv \frac{\eta_K}{\eta_L} > 1$ ($R > 1$). $R < 1$ means a negative jump in the OD-XAS spectrum and a quenching of luminescence in the XEOL spectrum when $E > E_K$. When $B > 1$, the yield spectrum or OD-XAS spectrum will be a normal one for any arbitrary sample thickness. Here normal indicates that the observed luminescence across the optical spectrum increases as the photon energy passes the threshold for *K*-shell excitation. This is denominated as a positive jump. By contrast a negative jump would result in an inverted optically detected x-ray absorption spectrum. For a sufficiently thick ($t \rightarrow \infty$) and transparent specimen, a negative jump OD-XAS spectrum and quenching of the emission (XEOL) spectrum will be observed under the condition of B < 1. On the other hand, a thinner specimen ($t \rightarrow 0$) will also exhibit a normal spectrum. When B $\longrightarrow 0$ ($\eta_K \rightarrow 0$) means that there is no contribution from the *K*-shell excitation to the optical luminescence and an inverted OD-XAS spectrum and quenched emission (XEOL) spectrum results for an arbitrary sample thickness. The factor *H1* in the equation XV contributes to a positive jump and significant emission while the factor *H2* is associated with the negative jump, or quenching of the optical emission under the condition B < 1. A balance between the two terms determines the nature of the spectrum. The same model can be easily extended to the case of three component parts with the absorption coefficients and the yields corresponding to a compound *AX* consisting of the atoms *A* and *X*.

3. Beam damage in organic molecular semiconductors

Methods used to probe the electronic structure and optical properties of organic molecules/crystals usually tend to alter the pristine molecule or the crystal structure. This is observable in some of the common characterisation techniques such as XPS[121], NEXAFS[122,123], scanning electron microscope (SEM)[124-126], x-ray diffraction (XRD)[125,127,128], optical absorption/ reflection spectroscopies[129] etc., where observable changes on the collected initial spectrum or image occurs after prolonged exposure to electromagnetic, electron and ion irradiation. It is not always clear if the observable changes are due to molecular fragmentation, atom displacement or crystal degradation but at this point beam damage would be defined as any observable change that occurs after exposure to any irradiated characterisation technique.

In the case of ion or electron irradiation the main interaction occurs through energy transfer from these high kinetic energy particles with the organic target. A similar picture occurs with electromagnetic radiation where photons with sufficient energy can excite many high kinetic energy electrons, which interact with the organic molecules. For very high flux photon densities, heating of the crystals might also occur. Following the arguments given by Helliwell[130], even crystals of low-Z elements absorb a considerable amount of the energy of the incident beam. Assuming that a large fraction of the absorbed energy is converted to heat, a local heating rate of 2.4 K/s has been estimated for low-Z compounds for 10^{14} photons s^{-1} mm^{-2} of wavelength λ = 1.0 Å [127]. These are conditions comparable with high-brilliance focused undulator beamlines at third-generation synchrotron radiation sources.

A proportion of an incident electron beam on a specimen undergoes inelastic interactions with the specimen, and energy is transferred from the electron to the target atom. The amount of energy transferred can vary between a fraction of an electron volt, sufficient to cause fluorescence, and the total energy of the electron, which may be able to displace the atom from its lattice position. The process is extremely rapid (10^{-14} s) and normally results in a series of chemical processes by the atom, as it sheds the absorbed energy[126,131]. A suitable beam damage threshold might be considered to be 1 electron/molecule[131]. In the process it can cause bond rupture. For aromatic organic compounds there is a low-energy process of activation energy 30-40 kJ mol^{-1} (approximately 0.4 eV/molecule) corresponding to single-bond breakage, and a higher-energy process of 820 kJ mol^{-1} (approximately 8.5 eV/molecule) corresponding to multiple-bond scission[132]. The rates of these chemical reactions, and their effect upon the molecular and crystal structure of the specimen depend on the chemical identity of the specimen[133].

As stated earlier in chapter 1, one of the themes of investigation is that of beam induced damage to phthalocyanines. This chapter explores the experimental results of these investigations.

The following beam damage investigation is based mainly on XPS and NEXAFS measurements, taken in MAX-lab, the Swedish National Electron Accelerator Laboratory for Synchrotron Radiation Research (Lund University, Sweden) at beam line I511. It consist of two branches: The bulk branch (I511-3) and the surface branch (I511-1). These both use the light of the same undulator with a mirror to switch the light between the two branches (Fig. 22). The following work is based at the I511-1 branch with two different high resolution photoelectron spectrometers; the Scienta SES-200 and Scienta R4000, relating to measurements before and after July 2006, respectively. Details of this beamline and its optimal layout are available in the literature[134], as are details of the endstation[135].

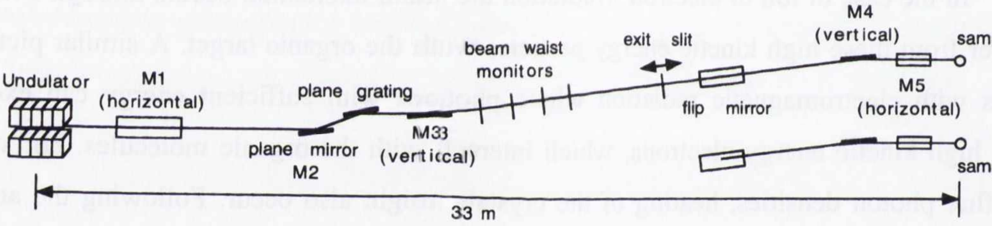

Figure 22 Schematic overview of BL I511 (not to scale). Shown is a side view with the two branch lines offset [134].

Even though phthalocyanines are known to be robust molecules the effect of beam or radiation damage on these has been previously noted[95,96]. This study is a preliminary one seeking to quantify and understand further the beam damage within these materials. The purposes of this are threefold: first, to apply the right thresholds of radiation exposure time in studies with x-ray spectroscopies like XES; second, to extract conclusions for a broad range of similar organic molecules; and third, to justify possible applications that may arise as a result of radiation exposure.

First, the C1s and N1s core level XPS spectra were measured with increasing exposure time, at specific excitation energy for SnPc. This gives an idea of the radiation exposure time limits with the use of an undulator. Secondly, an extensive investigation and analysis of the effects of radiation to thick and thin films of non-planar phthalocyanine (PbPc) are presented. Thirdly a comparison of the effects of synchrotron radiation on thick and thin films of planar phthalocyanine (MgPc) is presented. The principal parameters influencing the radiation beam damage such as temperature and excitation energy are discussed.

3.1 Non-planar phthalocyanine beam damage effects

3.1.1 Tin phthalocyanine (SnPc) thick film beam damage studied by XPS core level spectroscopies

The influence of beam damage on tin (II) phthalocyanine (SnPc) is reported here, as studied by core-level N *1s* and C *1s* photoemission. Beam damage in SnPc thick films has previously been observed to result in a conversion of Sn^{2+} to Sn^{4+} oxidation state as measured at the Sn 4d core level[99,136]. Furthermore, changes in the valence band (VB) were observed, in particular at the critical region of the HOMO levels[136]. These latter observations have been confirmed by our studies but will not be presented in this work.

The SnPc used was obtained commercially from Sensient Syntec GMBH and evaporated onto a clean Ge (001) substrate *in situ*. The Ge substrate was cleaned by Ar^+ 500eV energy ions sputtering with 45° incline angle for 2 hours at RT, annealed to 550°C for 30min and cooled down slowly (10°C/min) in order to regain the 2×1 surface reconstruction as verified by LEED. The clean substrate was checked with photoemission at C 1s, N 1s and O 1s edges for any remaining contamination. SnPc was deposited by organic molecular beam deposition (OMBD) using a Knudsen cell under ultra high vacuum (UHV) conditions. Before deposition the SnPc was purified in UHV by degassing the evaporator for several hours at just under the evaporation temperature. A thick film (~300 Å) of SnPc was sublimated (at ~390 °C K-cell temperature) onto the Ge substrate held at room temperature with an evaporation rate (~0.3 nm/min) as monitored by a quartz thickness crystal monitor.

Once grown, the surface of the as grown film is exposed to the synchrotron radiation beam, which has a Gaussian width of ~ 200 μm and height of ~50 μm which gives a footprint on the sample surface of 200 μm width and a length of ~360 μm(50 μm/sin8°). The length of the footprint arises as the synchrotron radiation beam has an angle of 8° incidence onto the surface of the sample, where the manipulator is coaxial with the beam direction (lying down).

The evolution of the core level spectra with exposure time to the radiation is shown in Fig. 23a for C 1s and in Fig. 24a for N 1s core levels. The spectra are shown in calibrated binding energy to the Fermi level. Exposure to the X-ray photon energy of 525 eV well above the excitation energies for the C 1s and N 1s core levels have been used. The

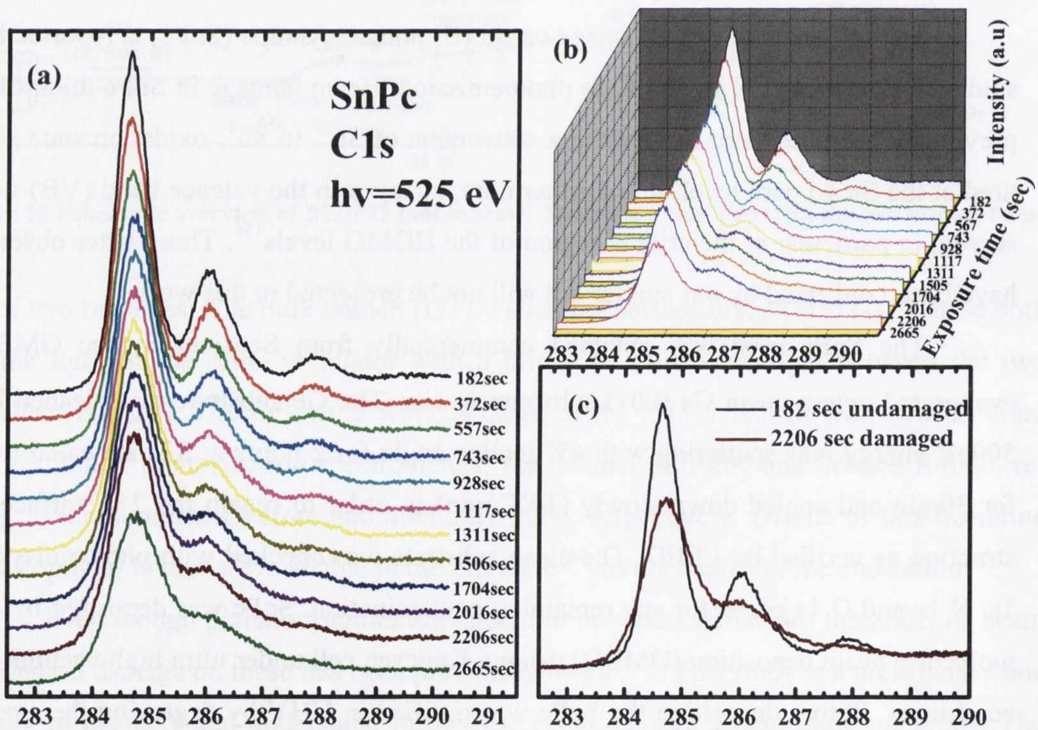

Figure 23 (a) C *1s* core level from SnPc as afunction of exposure to a beam of 525eV photon energy with a monochromator resolution of 0.1eV, and a flux of 1.4×10^{15} *photons·sec^{-1}·mm^{-2}*. (b) Change to the peak intensity with exposure time. (c) Comparison between undamaged and severely damaged SnPc C *1s*.

flux at the I511 for the photon energy used is approximately 2.8×10^{13}*photons·sec*$^{-1}$ *per 0.1%BW*[1]*per 100 mA*[134] where the typical beam current ranges at MAX-lab II from 200 mA to 90 mA. The monochromator resolution used here is 0.1 eV. Thus, the flux is estimated at 1.4×10^{15}*photons·sec*$^{-1}$*·mm*$^{-2}$.

Photoemission spectra were recorded with a nominal combined instrumental resolution of 0.2 eV. In figures Fig 23b and Fig 24b the evolution of the C 1s and N 1s core levels XPS spectrum with increased time exposure is shown. The intensity of the spectra presented exhibits a monotonic decrease, while a broadening of the features can also be observed. This becomes more obvious in Fig 23c and Fig 24c where direct comparisons between an undamaged C 1s (182 sec exposure) and N 1s (193 sec exposure) and the final damaged ones (C1s 2206 sec and N1s 2262 sec exposure) are given. The spectra become less intense, broadened and featureless. Small shifts and new features also arise which will

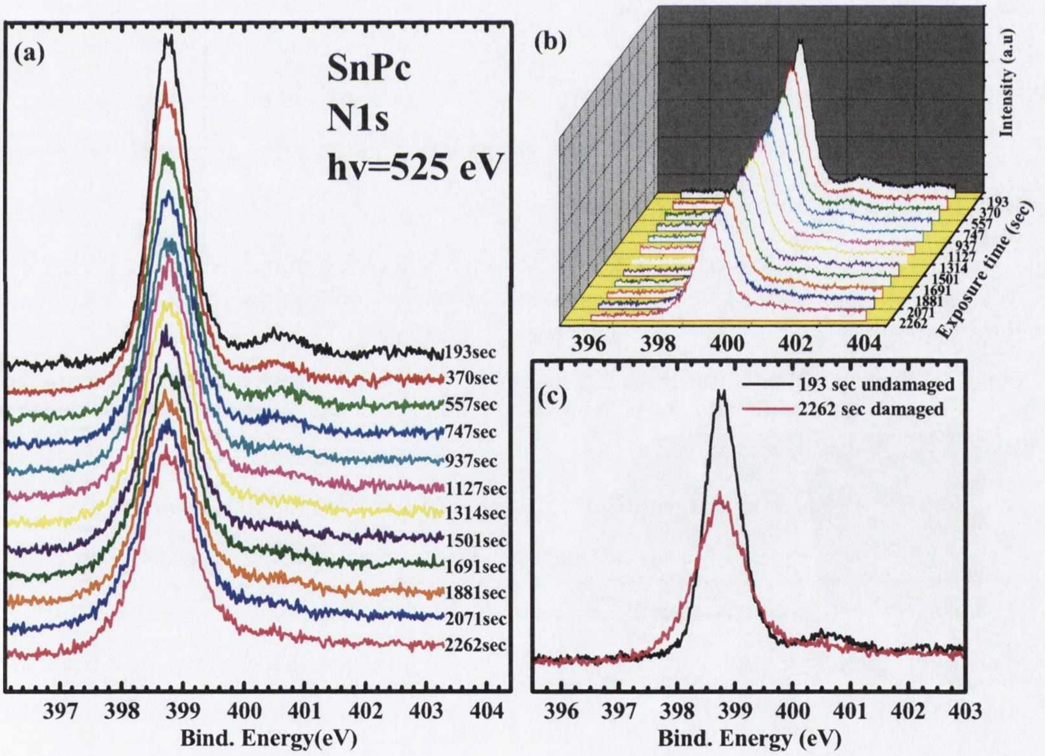

Figure 24 (a) N1s core level from SnPc as function of exposure to beam; (b) Change to peak intensity as evolution of the time; (c) Comparison between undamaged and severely damaged of SnPc C1s

---

[1] BW is monochromator's band width

form part of the qualitative analysis with results from PbPc presented in the next section. It should be noted that the general trend of the damaged spectra for most of the MPcs presented here are the same. Thus the approach to the analysis will be a general one and will include information extracted from the various MPc measurements.

Following the general description above, the integrated area of the SnPc C 1s and N 1s spectra with exposure time is presented in Fig. 25. The values related to the total integrated area under the curve, adjusted to the beam ring current as an indicator of the photon flux. The error bars come from the uncertainly on the ring current measurement. The integrated values presented are normalized to a value of 1 for the maximum intensity.

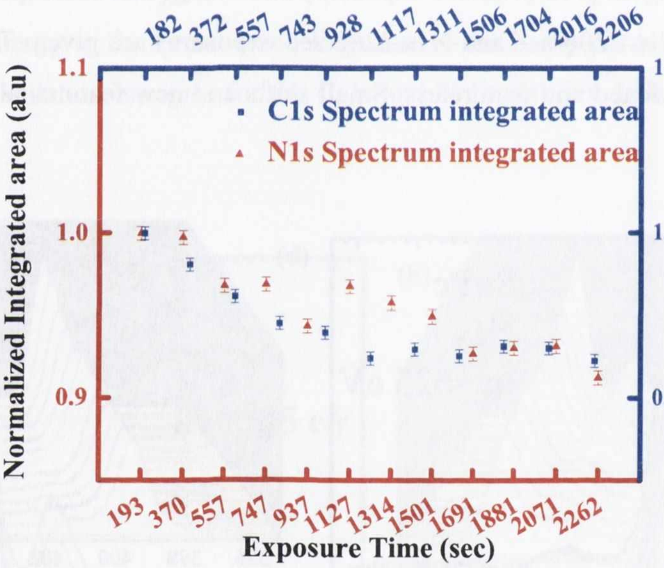

Figure 25 The progression of the integrated areas under C1s (blue) and N1s (red) spectra to the radiation exposure time. Both C 1s and N 1s spectra appear to face a loss of mass, probably due to scissoring.

The C 1s spectral area decreases with increasing exposure by approximately 7.7±0.1%, indicative of mass loss. The same picture is seen for the N 1s spectra for which the area is reduced by approximately 8.8±0.1 %. In this case the scenario of a MPc desorption is unlikely. This is possibly due to a scissioning in the molecule, where some of the C and N atoms are removed while the rest of the molecule remains stable. The rate of C and N atom desorption appears to be different with C desorption happening faster.

3.1.2 Lead phthalocyanine (PbPc) thick film beam damage studied by XPS core level.

The influence of beam damage on lead (II) phthalocyanine (PbPc) is reported here, as studied by core-level N *1s*, C *1s*, Pb *5d* and VB PES and NEXAFS. A qualitative analysis of the beam damage effects on thick films of MPc follows.

The PbPc used was obtained commercially from Sensient Systec GMBH and evaporated onto a clean Ge (001), substrate *in situ*. The same procedures of cleaning and preparation of the Ge (001) substrate are used. A thick film of ~70 Å of PbPc was prepared under similar evaporation conditions for the SnPc measurements.

High resolution XPS of undamaged C *1s* and N *1s* core levels spectra are presented in Fig. 26, including the best fit describing the different features and accounting for the different chemical environments. The spectra were taken at MAX-lab, beamline I511-1 with the Scienta R4000 electron analyser. The nominal combined instrumental resolution is 0.08-0.1 eV. Spectra were fitted using mixed Lorentzian-Gaussian (pseudo Voigt: linear combination of a Gaussian and a Lorentzian profile) doublets, with the same width for each component (winspec v3.4 software was used). This was chosen to best reproduce the lifetime and instrumental broadening. This procedure was followed for the fitting of all core level XPS spectra. The doublet accounts for the significant shake-up present for MPcs.

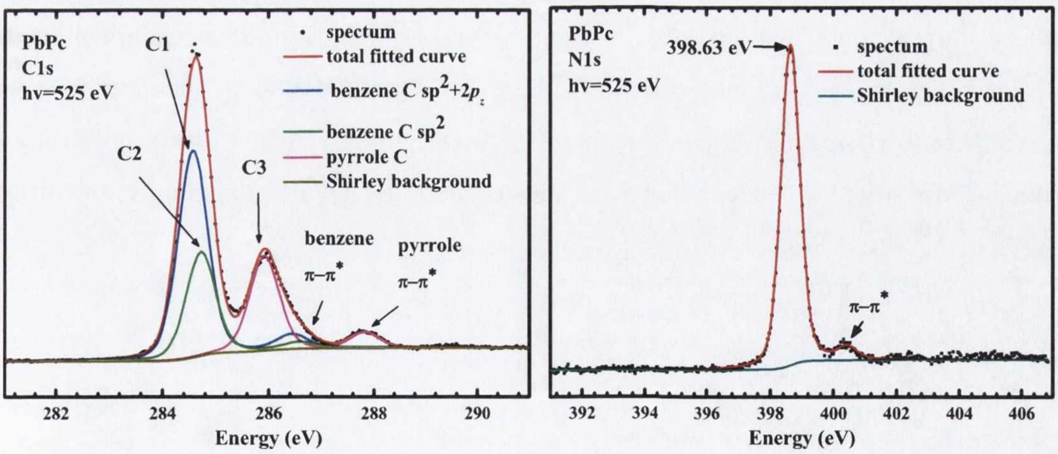

Figure 26 C 1s and N 1s core levels spectra of undamaged PbPc at RT. Spectra accompanied with fitted peaks that best describing the different chemical environments (bonds). In case of the C 1s there are benzene ring C (C1) sp^2+2p_z, benzene ring C (C2) sp^2, pyrrole C (C3) bonds with their individual π-π^* resonances.

The N 1s spectrum has been fitted with only one peak that accounts for both the aza (bridging) and inner nitrogens. The peak appears at 398.63 eV with a FWHM of 0.71 eV at room temperature. Using two peaks (inner & aza N) did not substantially improve the fit.

Extensive attention is given here to the C 1s undamaged spectrum in an attempt to determine in detail the different environments through fitting to the XPS spectra. Comparison with the fit to a damaged spectrum will help to reveal aspects of the damage process. Previously, high resolution XPS by Papageorgiou et al.,[137] Evagelista et al.[138] and Downes et al.[107] at C 1s have specified in these core level fitting peaks, benzene ring carbons, pyrrole carbons, their respective shake-up peaks and a fifth located in the valley between the benzene and pyrrole, accounting for the asymmetry of the main C1s peak. It has been postulated as a photoelectron energy loss peak associated with excitation of C-H vibrations[137].

A new approach is presented here based mainly on the interpretation of the best fit concerning the valley and asymmetry of the benzene peak. In Fig. 26 the C1s core level XPS spectrum of PbPc is shown where this is fitted with pseudo-voigt doublets for benzene ring carbon bonds and pyrrole carbon bonds where the doublet describes the individual shake up resonances (π-π^*). The fifth peak is considered unlikely to occur due to vibrational losses because a comparison between gas and solid phase of the CuPc C 1s XPS spectra as presented by Evangelista et al.[138] shows the same asymmetry on the main C 1s peak. However, in this case different vibrational modes would be expected.

The new approach to fitting the benzene C 1s component is based on the screening effect of the π-conjugated $2p_z$ atomic orbitals of the sp^2 hybridisation as occurs on the benzene carbons on the MPc molecule. In the benzene ring of MPc, in all instances four out of six carbons participate in a π-conjugated ($2p_z$) HOMO orbital which is not uniformly distributed across the benzene ring, as determined by DFT calculations of different

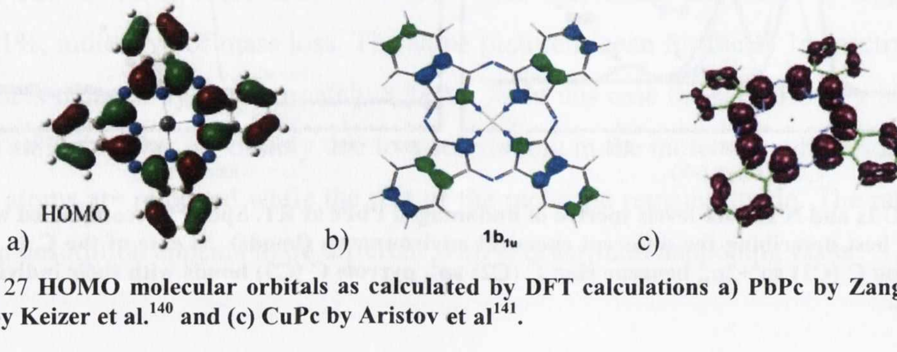

Figure 27 HOMO molecular orbitals as calculated by DFT calculations a) PbPc by Zang et al.[139], b) ZnPc by Keizer et al.[140] and (c) CuPc by Aristov et al[141].

MPcs[139,140], shown in Fig. 27.

Thus, an alternative is that the four benzene carbons with significant HOMO density of states (C1) screen the C 1s hole better than the two without high PDOS (C2) and as a result the C 1s binding energy is expected to occur to lower binding energy in comparison to the other two (unscreened). As such, a fitting of PbPc C 1s presented in Fig. 26 with two peaks on the benzene ring feature at binding energies of 284.55 eV and 284.79 eV with integrated areas matching perfectly the stoichiometric ratio of 2:1. Furthermore, the accompanying shake up peaks allow the pyrrole related peak (C3 at 285.87 eV) to have an integrated area that matches perfectly the stoichiometric ratio 1:3 to the benzene peaks (C1+C2), whereas this was only approximate in the previous fitting attempts.

Table 1 Fitting parameters of C 1s and N1s core levels of pristine PbPc thick film.

	E_{bind} (eV)	FWHM	% shake up	E_{split} (shake up) (eV)	Intergated Area
C1: benzene ring C 1s sp^2+2p$_z$	284.57	0.66	6.6	1.88	394.8
C2: benzene ring C 1s sp^2	284.72	0.66	5.8	1.88	195.9
C3: pyrrole C 1s	285.92	0.66	16.3	1.90	197.3
N 1s	398.63	0.71	3.7	1.81	223.4

The core-level and shake-up spectra of bulk-like H_2Pc has been theoretically well described by Brena et al.[142-144]. In this work it was shown that shake-up satellites from both pyrrole and benzene carbons are necessary, where the benzene-like shakeup is close to the pyrrole main line. It should be noted that although this justifies the use of four components in the fit, the situation is a little more complex as on each of the inequivalent benzene-like carbons the shake-up spectrum has been calculated to be different. That is the energies and intensities of the shakeup satellites differ from one benzene like carbon to another and can involve not just HOMO-LUMO transitions, but also to the LUMO+1. In most instances of MPc C 1s PES spectra it appears sufficient to express the shakeup fit feature at a fixed separation from the main line, for which doublets have been used here.

The progression of the core level XPS spectrum at room temperature (RT) to prolonged exposure to synchrotron radiation is presented in Fig. 28 for the same film of PbPc. A comparison of the XPS core levels spectra of C 1s, N 1s, Pb 5d and VB photoemission are given for different exposure time, radiation flux and energy of the incoming photons where the degradation of the spectrum could be considered beam damage. Here the black spectra represent undamaged PbPc, the red one represents exposure to synchrotron radiation for 10 min with energy of the photons at 525 eV and flux of approximately 2.8×10^{13} *photons*$\cdot$*sec*$^{-1}\cdot$*mm*$^{-2}$, the green represents 15 min total exposure, where the first 10 min is that of the red plus a 5 min exposure with 100 eV photons and flux approximately 1.4×10^{15} *photons*$\cdot$*sec*$^{-1}\cdot$*mm*$^{-2}$. Finally, the blue curve relates to a 10 min exposure to the x-rays with photon energy of 270 eV, just below the threshold of the C 1s core binding energy excitation in a fresh spot with approximately flux 5.6×10^{13} *photons*$\cdot$*sec*$^{-1}\cdot$*mm*$^{-2}$.

Looking at Fig. 28a and Fig. 28b where the progression of C 1s and N 1s of PbPc is shown (taken with excitation energy of 525 eV) and compared with the same core levels of the SnPc (Fig23 c and Fig24 c) it is obvious that a similar degradation process occurs. The

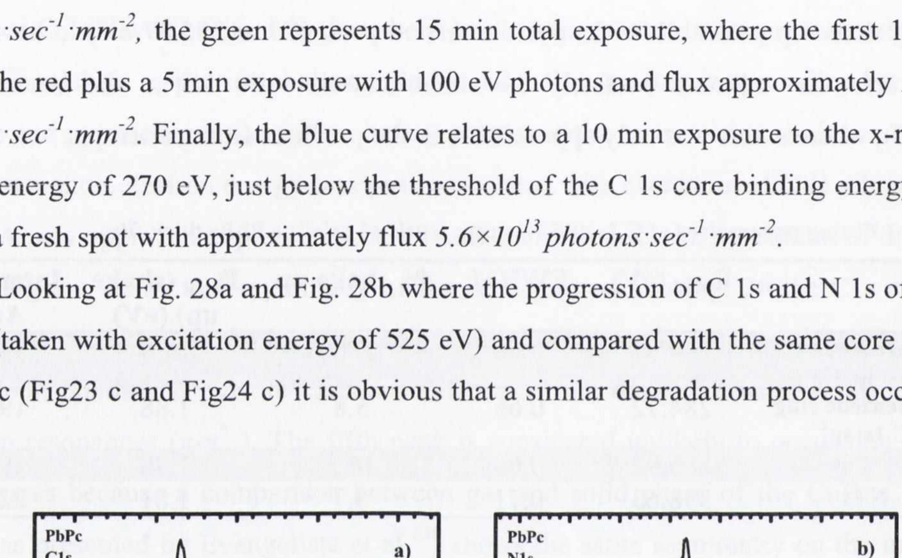

Figure 28 The effect on PbPc (~ 70 Å thick fim) of exposure to X-rays radiation at RT. XPS of: a) C 1s b) N 1s c) VB and d) Pb 5d at different exposure time, radiation flux and energy of the incoming photons.

C 1s spectrum becomes featureless and broader and follows a reduction to the intensity which is the same for the N 1s. The VB spectra taken with excitation energy of 100 eV follows similar trend with a substantial broadening of the HOMO levels which is similar to that previously reported by Cabailh et al[136] for both SnPc and PbPc. The Pb 5d core level taken with 100 eV excitation energy, follows a broadening probably due to various intermolecular and intramolecular rearrangements. However, it doesn't change the oxidation state as observed in the Sn 4d core level of SnPc[136,145].

The changes of these spectra are irreversible. The 10 min exposure (red) spectra illuminated with 525 eV photon energy, are almost identical to the spectra of 10 min exposure to 270 eV, just below the threshold of C 1s excitation energy. This indicates that the damage is not a result of the creation of 1s core holes, rather that it occurs from the amount of secondary electrons produced under this flux as previously reported [146]. Although the kinetic energy of the excited electrons is higher with higher excitation energy photons and the mean free path of these electrons are longer creating more ionisation events, there is no fundamental difference in the damage progress compared to the lower excitation energy.

A similar series of core level and VB photoemission was undertaken at low temperatures. The progression of the spectra at liquid nitrogen temperature (~79 K) with prolonged exposure to synchrotron radiation is presented in Fig. 29 for the same thick film of PbPc. This time the comparison of the C 1s, N 1s, Pb 5d and VB photoemission spectra, at different exposure time of the same radiation flux is given. The black curves represent undamaged spectra. The red represent exposure to synchrotron radiation for 5 min with photon energy of 100 eV and flux of approximately $1.4 \times 10^{15} photons \cdot sec^{-1} \cdot mm^{-2}$ and the green represent 10 min exposure with the same photon energy and flux on a fresh spot.

The core level and the VB spectra appear to exhibit a similar progression with exposure time to the synchrotron radiation as at RT spectra. However, the low temperature (~79 K) seems to slow down the damage progression of C 1s and N 1s as seen in Fig 29a and Fig. 29b. The degradation of the VB and Pb 5d spectra is observable even from the first 5 min exposure with mainly a broadening and reduction of intensity and in particular a broadening of HOMO for the VB and a shift to lower binding energy for the Pb 5d.

The degradation in the observed spectra with exposure may be analysed by fitting the photoemission spectra. In doing so, we can make a first attempt at understanding this process which may be called beam damage.

The advantage of the T~79 K spectra is that it makes it easier to see that two different processes are taking place. The first one is best observed in the low exposure time (5 min) spectra and mainly appears as a shift to the lower binding energy for all the core levels that have been measured. In fact a part of the film seems to have been modified, peaks labelled as B in Fig. 30 represent this modification, whereas the peaks that are labelled as A appear at the same positions and FWHM, as these obtained from the fit to the undamaged spectra. It should be noted that in fitting the spectra the same width and mixing ratio (Gaussian - Lorentzian) for A and B have been consistently applied for C 1s, N 1s and VB HOMO whereas a slight broadening on the Pb 5d has been applied (0.73→0.93 eV). The C 1s core level is fitted with the stoichiometric model that has been previously presented in Fig. 26. The shift to lower binding energy is in the range of 0.2-0.3 eV for the C 1s and N

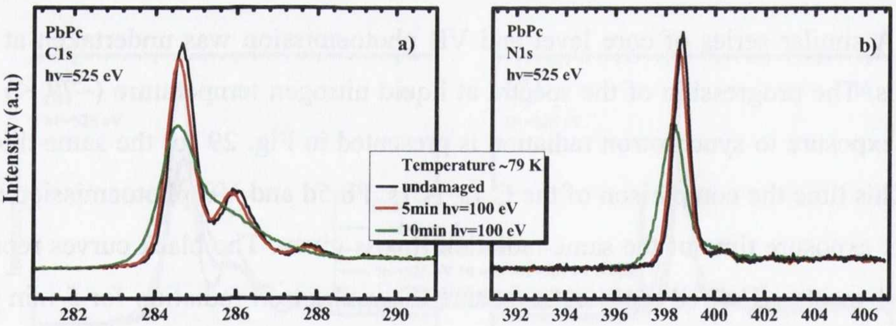

Figure 29 The effect of exposure of PbPc (~70 Å thick fim) to X-ray radiation with a sample temperature of 79 K. Photoemission spectra of a) C 1s b) N 1s c) VB and d) Pb 5d are given for different exposure time

1s core levels whereas on Pb 5d and the VB HOMO level, it is in the range of 0.3-0.55 eV (Fitting parameters are included in Appendix I).

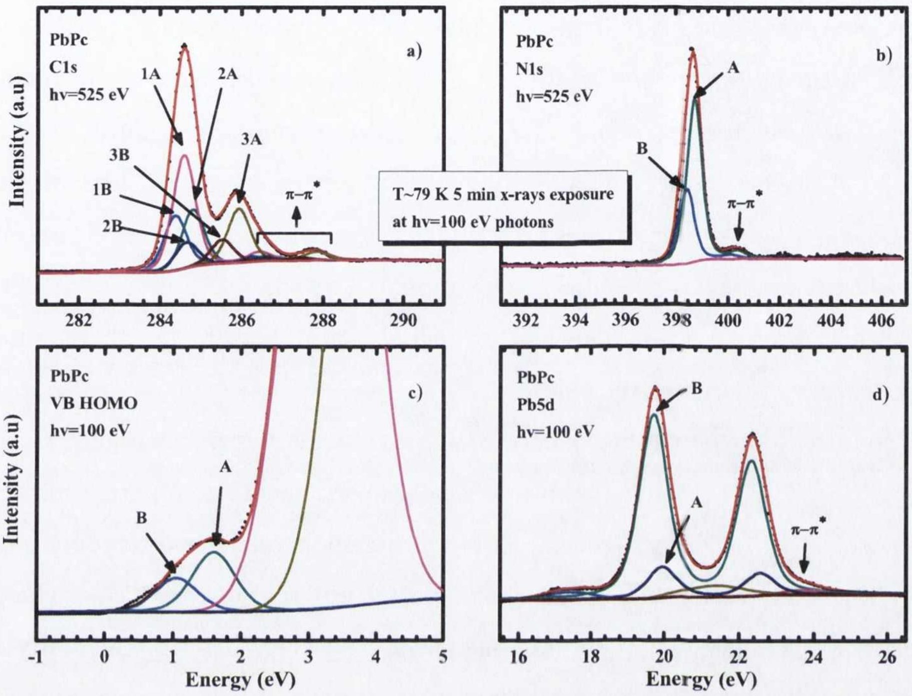

Figure 30 Fitted spectra of a) C 1s, b) N 1s, c) VB HOMO and d) Pb 5d that have been exposed to hv = 100 eV photons for 5min at T ~ 79 K. Fitted curves have been labelled with A and B, describing the still undamaged part of the film and the crystal damaged (or modified) part, respectively.

The fact that all the core levels and the HOMO VB shift in the same direction (to lower binding energy), one can conclude that an overall change applies to the electronic system. This most likely originates from a modification of the crystal structure. The difference in the shift between the C 1s, N 1s and Pb 5d and the VB HOMO could be attributed to the better screening of these core levels. Crystal structure modifications, such as an increase of the *d* spacing and changes of the intermolecular distances upon exposure to synchrotron radiation have been reported before[125,127,146]. Muller et al.[127] showed experimentally that sample heating is unlikely to occur ($\Delta T<2K$) under bending magnet synchrotron radiation source (10^{12} photons$\cdot s^{-1} \cdot mm^{-2}$) exposure. However, changes in the crystal structure of small organic molecules are still present, occurring simply at a different rate at low temperatures.

The source of the crystal modifications most probably relies on electrostatic rearrangements. The extensive excitation process (direct and secondary processes) that keeps the molecule ionized for a substantial time in combination with the different mobilities of hole and electron intermolecular transport and also the creation of some radicals such as H^+ could well create an ionized and electrically polarized molecule. It should be noted that the hopping process which is one of the main processes of intermolecular transport of electrons in this type of organic molecular semiconductors is suppressed at low temperatures. Furthermore, the low temperature makes difficult the movement of radicals and also eliminates the thermal activation energy needed in a creation of a new bond[127]. In this manner it is believed that the observed beam "damage" or degradation of spectra seen here is mainly attributable to a crystal structure changes.

The effect of electronic polarization on charge transfer parameters including changes on the VB HOMO have been extensively investigated and reported for several organic molecules[147-149]. Different stacking of such organic molecules depending on overlapping of orbitals due to electronic polarization creates different intermolecular charge transfer properties and a substantial spitting of the VB HOMO. There is potentially co-facial polarised interference within columnar molecular arrays and face to edge polarised interference between neighbouring stacks of molecules. The stronger electronic interaction between co-facial dimers, the larger the splitting of the HOMO and a better charge transfer might be expected[150] This has proved to be the case upon rotation of inter-columnar dimer triphenylene molecules around the stacking axis[148]. Even in the case of face to edge interaction which means that the dimer molecules are almost perpendicular to each other, a lowering in the energy of the HOMO have been observed in the case of ethylene based on the fact that the positive charge H of C-H bond interfere upon electronic polarization with the π-type HOMO of the face ethylene molecule[149]. Thus these observations are in good agreement with the observable changes in the HOMO of the damaged VB photoemission spectra (Fig. 30c), where broadening perhaps due to splitting or lowering of energy might occur due to closer intermolecular interaction.

It should be noted that growth of thin films of MPcs (and other organics) can result in quite different crystal structures for the film dependent upon substrate temperature, deposition rate, and the organic molecules interaction with the substrate itself. This is also the case for PbPc[151]. Two different crystal structures have been reported so far for PbPc, monoclinic[87] and triclinic[88](Fig. 26). The PbPc film under investigation here is believed to be a mixture between triclinic and monoclinic with the triclinic crystal structure to be the dominant one based on work by Cabailh[136], where the angular dependence of the π^* intensity peak as measured with NEXAFS suggest a mixture of molecular orientation due to different crystal structures. The films presented here have been prepared with exactly the same procedure and conditions as Cabailh[136].

At this first step of radiation damage the crystal deformation of the film structure is expected, with expansion and contraction of interplanar spacing along with cross linking between neighbour columnar molecules across the *b* axis (Fig. 31a) for example. This is well supported by electron micrographs and optical diffraction patterns taken from copper hexadecachlorophthalocyanine ($CuCl_{16}Pc$) films upon electron beam radiation exposure by Murata et al[125]. In this work the predominant feature of the *e*-beam radiation exposure is the degradation of crystallinity, whereas damage to the individual molecular structure is also seen but does not dominate. It is believed that molecule damage occurs mainly by Cl scissioning. Cross linking of molecules was also observed and it is believed to happened after some scissoring of C-Cl bonds or potentially with the chlorines of neighbouring molecules in specific molecular orientations, where the intermolecular distance is at a minimum. Furthermore, curving, coiling and helical structuring of MPc (CuPc, CoPc, NiPc, FePc, ZnPc and $F_{16}CuPc$) nanoribbons and nanowires upon electron beam radiation exposure have been reported by Tong et al[152]. This has been observed by scanning electron

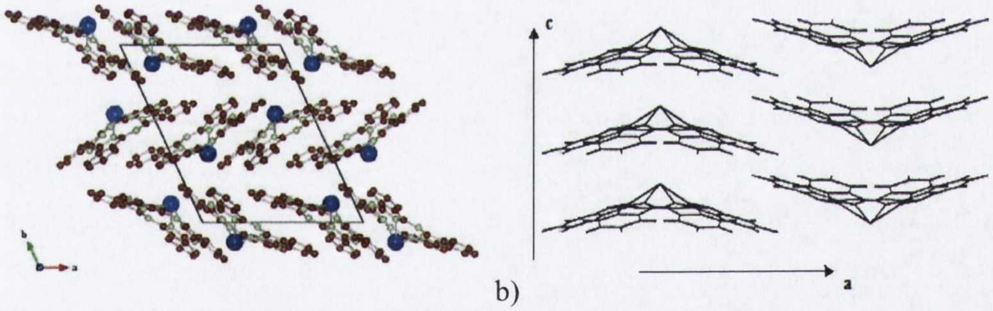

a) b)

Figure 31 a) Illustration of the columnar stack across the a-axis for the triclinic crystal structure of PbPc films after Iyechika et al[88]. b) Illustration of columnar stack across the c axis for the monoclinic crystal structure of PbPc films after Ukei et al[87] .

microscope (SEM) and transmission electron microscope (TEM) investigations, supporting the idea that a crystal rearrangement occurs.

The crystal rearrangements with co-facial linking across the columnar stack and face to edge linking through neighbouring columns of molecules are expected to enhance the intermolecular charge transfer. As a result, a better screening across the crystal lattice is expected through enhancing or creation of a band like electronic structure. Better screening would have an effect on the core level binding energies shifting them towards lower values as is observed through the fitting as presented in Figure 30.

Molecular relaxation in a new energetically favourable optimised geometry can not be excluded. In fact it seems that the ratio of the two fitted peaks on the Pb 5d doesn't quite follow the trend for those of C 1s and N 1s core levels. A new molecular geometry on the Pb atom, perhaps new atomic distance to the bonded nitrogens could be possible after the whole molecule gets excited and rearranged in a manner where more intermolecular interference occurs. This has already been the case for the two known different crystal structure monoclinic and triclinic where different distances to Pb atom from the bonded nitrogens have been observed[78,79,87,88].

After 10 min exposure at the same temperature (T~79 K) the degradation or damage becomes more obvious, especially at the C 1s and N 1s core levels. In Fig. 32 the fitted C 1s, N 1s, Pb 5d core levels and VB HOMO spectra are presented. These fits are presented consistent with two mechanisms of damage: 1) The crystal degradation as discussed above and 2) molecular changes like breaking of bonds and scissioning that creates radicals with new atomic chemical environments. Following the first mechanism the C1s and N1s spectra have been fitted similar to the previous discussion at 5 min exposure with fitting curves labelled B which previously described the crystal modification. Fitting curves labelled B appeared to be the dominant feature, and they come almost on the same energy positions as the 5 min exposure ones. Fitting curves labelled A are in the same positions as those labelled A after the 5 min exposure (Fig. 30). In this case they don't match exactly the pristine molecular spectrum, rather a change which relates only to the breaking of the π-conjugated $2p_z$ bonds, this implies that delocalization of the π-bonded electrons no longer occurs. In turn this leads to less well screened core holes and an increase in intensity of the peak labelled 2A as designated as C2 in the molecular spectrum (Fig. 26).

In these spectra a second damage process becomes observable which it is believed to be a scissioning of the molecular structure. This is described by the peak C on the C 1s and the peaks C and D on the N 1s spectrum. These peaks could arise from the remaining ligands of the MPc macromolecule or they could well be new chemical bondings from free radicals that have been created through the beam damage. For the N 1s and VB HOMO spectra, the same width and mixing ratio between Lorentzian and Gaussian as before has been applied. For the C 1s and Pb 5d a slight broadening was required, possible given the potential inhomogeneity of intermolecular interference or molecular relaxation caused from the surrounding environment. In the C 1s fitting as presented in Fig. 32a the increase in intensity of the peak labelled as 2A, where 1A is decreased is of interest (Fitting parameters are included in Appendix I Tab.3). As explanation of the peak labelled 2A has already been given, an interpretation of the change on the ratio between peaks 1A and 2A is that a sub-

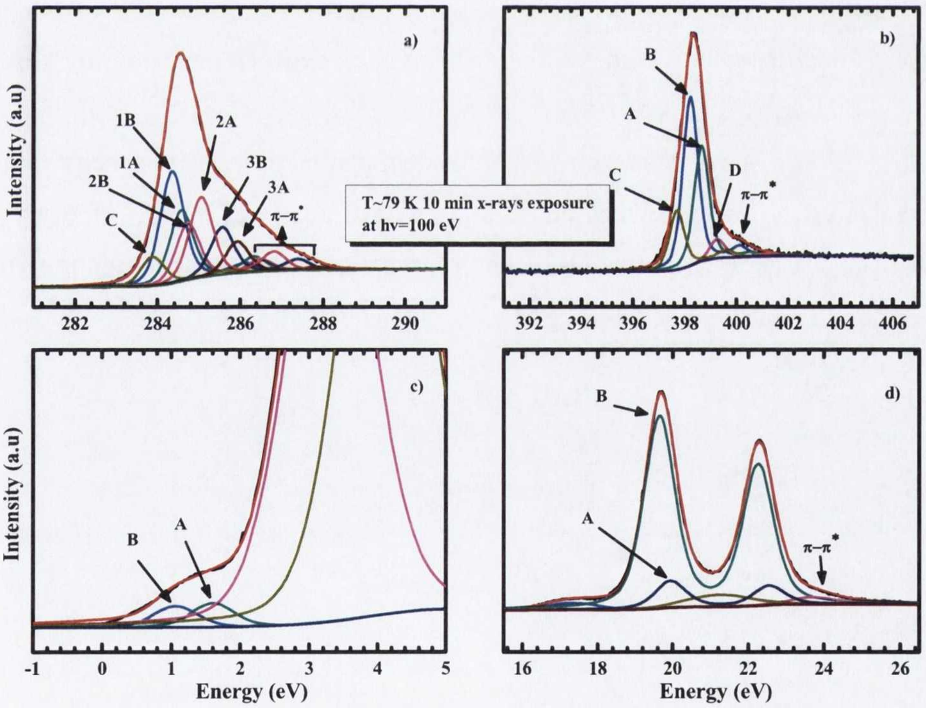

Figure 32 Fitted spectra of a) C 1s, b) N 1s, c) VB HOMO and d) Pb 5d photoemission spectra that have been exposed at hv=100 eV photons for 10 min at T~79 K. Fitting curves have been labelled with A and B describing the molecular modified part of the film and the crystal modified part, respectively. Peaks C and D describe molecular damage (or modification) through scissioning process.

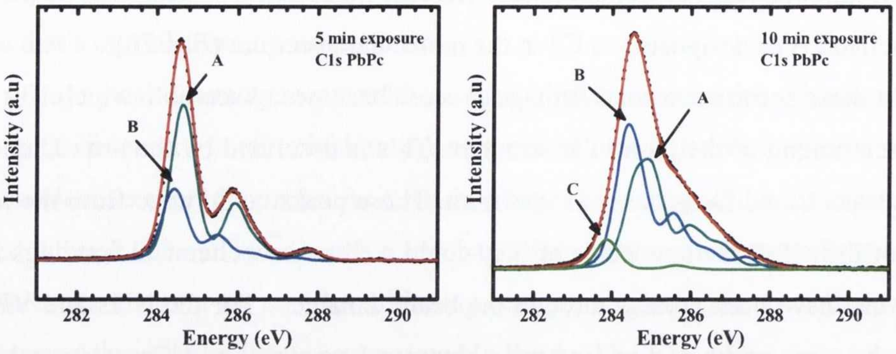

Figure 33 Left: demonstration of damage progression of C 1s XPS spectra with the fitted peaks grouped as crystal modified (B) and unmodified (A) crystal structure in the case of 5 min exposure. Right: more extensive crystal (B) and molecular degradation (A and C) on the 10 min exposure with curve C describing a scissioning process (See Appendix I Tab.2) .

stantial number of these π bondings have been broken, most likely through interaction with π orbitals of the neighbouring column of molecules.

The breaking of π-($2p_z$) conjugation between C atoms has reported before by Pakhomov et al.[121] and Ji et al.[153] where MPcs ($Cl_{16}CuPc$ and CuPc, respectively) have been damaged with ion irradiation and C1s XPS spectra appeared similar to the ones presented here, that is broadened and with a filling of the valley between benzene ring C peaks (C1 and C2) and the pyrrole C peak (C3).

In Fig. 33 a better demonstration of the degradation of the C 1s spectra is presented, where the fitted curves have been added and grouped together in terms of A and B processes as has been described previously. The 10 min exposure C 1s spectrum presented here also describes a molecular scissioning process.

3.1.3 NEXAFS beam damage studies of thick PbPc film.

The effects of exposure to synchrotron radiation on the unoccupied partial density of states (PDOS) of thick PbPc films will be presented here as obtained through near edge x-ray absorption spectroscopy (NEXAFS) measurements.

The NEXAFS measurements took place on the same I511-1 surface branch beamline at MAX-lab II measuring the total electron yield by the drain current method, and in some instances the secondary electrons with the photoemission analyser. Instrumental resolution was 0.09-0.1 eV. The beam line, is an undulator beamline with linearly polarised synchrotron light.

Figure 34 shows the N *K* edge NEXAFS of the same PbPc thick films, taken at room temperature (RT). The "damage" spectra have been taken after exposure to the high flux with hv = 100 eV for 10 min. The NEXAFS spectra have been taken with two different orientations of the substrate to the linearly polarised light. In Fig. 34a the electrical field

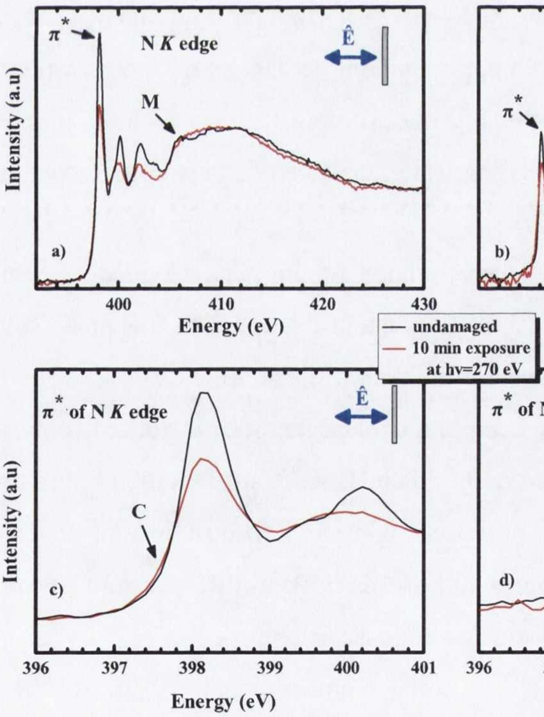

Figure 34 N *K* edge NEXAFS of PbPc thick film at RT with the polarization: a) normal to substrate and b) parallel to substrate of undamaged and damaged film. On graphs c) and d) the π^* orbital peak of these spectra presented in detail. The features labelled C and M shows observable changes that are discussed in the text.

vector of the polarised light is perpendicular to the substrate and the undamaged spectrum shows a pronounced dominant π^* orbital spectrum. This indicates that the light excites preferentially the out of the molecular plane π^* orbitals and that the molecules are probably lying down, with a small inclination angle to the substrate. More detailed work on the NEXAFS of PbPc monolayer and thick films has been presented by Holland[114]. Fig. 34b shows the spectra when the electrical field vector is parallel to the substrate and this preferentially excites σ^* orbitals, which are seen above 405eV.

The main changes in both polarisations between undamaged and damaged spectra appeared to be a reduction of the π^* orbital peak and that the σ^* shape resonances that becomes featureless, but with no substantial reduction in intensity. This seems to exclude the possibility of a change in molecular tilt, as this would cause a reduction of the intensity of the π^* peaks with a parallel increase in the intensity of the σ^* peaks, as has been described in section 2.4.

In Fig. 34c and 34d the π^* orbital of the N *K* edge is shown in finer detail for both polarisations of the light. Due to the fact that the π^* orbital is more isolated than the others and the lifetime width makes it sharp it becomes easier to identify shifts or changes. As can be seen there is a shoulder (labelled C) appearing on the damaged spectra which may indicate a new chemical environment probably due to molecular scissioning. There is also a substantial broadening of the main peak. Further analysis of this will be given for the following low temperature spectra.

Another noticeable change is the reduction of the peak labelled M which lies at 406.1 eV. In the literature there is a controversy about the origin of this peak. It is believed to be related to either σ^* resonance or a multi electron shake up excitation, or both overlapping[108,154,155] as has been reported by experimental and theoretical studied of pyridine[154,155] and experimental N_2 gas phase[108] spectra. In this instance it appears to be more pronounced in the undamaged spectrum with the polarised light parallel to molecular plane which excites σ^*states preferentially. The suppression of this peak in the spectrum of the damaged film could possibly indicate the breaking of bonds (scissioning).

NEXAFS spectra at the N *K*-edge were also obtained at T ~ 79 K are shown in Fig. 35a where again the film has been exposed for 10 min in high flux of hv = 100 eV photons to measure the effect of beam damage. The main change again is the reduction of π^* orbitals. It should be noted that this time the total electron yield is measured by secondary electrons with the XPS analyser; that is electrons that have been created by the Auger process of the core hole filling upon de-excitation. The reason for this was that during the cooling process with open cycle liquid nitrogen cooling, the sample holder was shaking giving spikes and noise to the drain current measured. The spectra have been taken with the Ê vector of the synchrotron light polarised perpendicular to the substrate.

A comparison between the undamaged spectrum at RT and at T ~ 79 K is shown in Fig. 35b. It appears that the low temperature spectrum comes with a slight enhancement of the σ^* resonances. Since the π^* states do not appear to change it is postulated that the lower temperature deforms the molecular structure in a way that allows N atoms (inner or aza) to bend out of the molecular plane more. The deformation could be result by contraction of the crystal lattice due to low temperature which could cause enhanced repulsions or attractions of atoms. One dimensional conductivity in the monoclinic form of PbPc at liquid helium temperatures have been reported by Ukei et al.[156] for this reason.

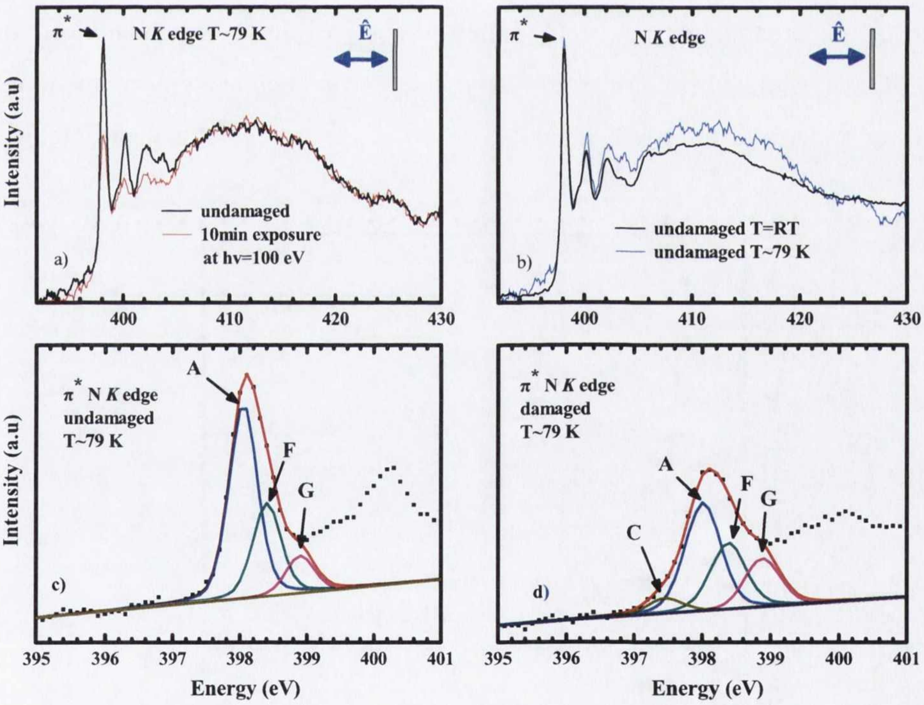

Figure 35 N *K* edge NEXAFS of PbPc thick film at T~79 K with the polarization normal to substrate of a) undamaged and damaged film. On graph b) comparison between undamaged spectrum on the two different temperatures c) π^* orbital peak of the undamaged spectrum at T~79 K fitted with three components A, F,and G d) the π^* orbital peak of the damaged spectra at T~79 K fitted with four components C, A, F and G.

In Fig. 35c the π^* peak of the undamaged spectrum is shown in detail. It has been fitted with three components, all with the same width and mixing ratio of pseudo-Voigt. The peak A describes the π^* unoccupied state. The NEXAFS π^* feature appears to have an asymmetry at higher photon energy, requiring peak F to provide a good fit. This asymmetry has been noticed before in the case of pyridine[154,155] and has been assigned through calculations to in-plane intra-molecular vibrations[155]. The comparison between the undamaged NEXAFS spectrum at RT and at T~79 K seems to support this argument since the observed asymmetry reduces in the case of the T~79K spectrum (Fig. 36). In the work on pyridine a weak peak, similar to the one labelled here with G, was been assigned as an N $1s \rightarrow 2\pi^*$ transition, which although dipole forbidden obtains some intensity through vibronic coupling[155]. Although uncertain it is that this is the case here, this peak is required for a good fit.

Thus, in Fig. 35d the π^* peak of the damaged spectrum is shown in detail, and has been fitted with the same components A, F and G plus one more at the lower photon energy which is labelled C. All peaks have been fitted with the same width and mixing ratio. This time substantial broadening has been applied in comparison to the undamaged spectrum The peak C is postulated to arise from a completely new chemical environment and is the result of molecular scissioning. The peak G occurs at the same photon energy (shift: -0.001

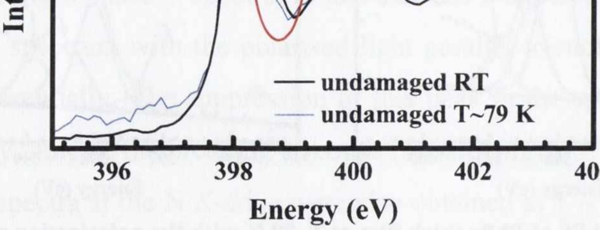

Figure 36 N *K* edge NEXAFS of PbPc thick film with the polarization normal to substrate comparison between undamaged spectra on the two different temperatures (RT and T~79 K). The red circle points out that the low temperature spectrum has slightly less asymmetric peak. The asymmetry may arise from in plane intra molecular vibrations.

eV) and appears to be slightly enhanced. The peaks A (shift: -0.005 eV) and F (shift: -0.03 eV) also occur at almost identical photon energies as the undamaged ones but broadened. It is believed that on the broadening of peak A, a new modified part (peak) with small shift towards lower photon energy is hidden. Previously the first step of the damage has been assigned on intermolecular interaction which causes splitting to the HOMO of 0.55 eV, as has been shown after Fig. 30c at 5 min exposure to 100 eV photons. Cornil et al[148] reports that in these kind of interactions where overlapping of electronic wavefunctions occurs, the splitting for the LUMO is expected to be half or even less than that observed for the HOMO. Taking this in to account the splitting for the LUMO here it should be 0.23 eV or less to lower photon energy. This could well be one of the reasons for the observed broadening of these peaks.

3.1.3 Lead phthalocyanine (PbPc) thin film (1 ML) beam damage studied by XPS.

The effects of synchrotron radiation exposure of a thin film of PbPc deposited on a Ge (001) substrate will be presented here. A monolayer of PbPc was deposited in situ by vapour deposition on a clean and well reconstructed (2x1) Ge (001) substrate, at room temperature. XPS measurements took place at the I511-1 beamline at MAXLAB II, using the same end station and electron analyser as in the case of the thick film.

The XPS core levels spectra of C 1s, N 1s, Pb 5d and VB photoemission from an undamaged film, are compared with a film exposed for the 10 min to X-rays of 100 eV photon energy as shown in Fig. 37. The nominal combined instrumental resolution used for the XPS measurements is 0.1 eV. In the case of the Pb 5d core level, a polynomial background subtraction has been applied in order to remove the signal that is attributable to the Ge substrate.

The C 1s spectrum (Fig. 37a) after exposure to the beam appears to be shifted towards lower binding energy with a loss of intensity on the pyrrole C peak. Both N 1s spectra (Fig. 37b) are very noisy and it is difficult to discern observable differences. For the valence band (Fig. 37c) there are observable changes especially on the HOMO and HOMO-1 states, similar to the thick film with a shoulder arising between these two levels. A reduction in intensity of the more tightly bound states (4-8 eV) is also observable. A clean Ge VB photoemission spectrum is presented here for comparison with the substrate background. The Pb 5d core level photoemission spectrum (Fig. 37d) shows an increased intensity on the higher binding energy side upon exposure. Further interpretation of the beam damage in the 1ML PbPc film will be based on consideration of this core level.

In the top row of Fig. 38 the undamaged and damaged Pb 5d photoemission spectra are shown fitted with two pseudo-Voigt doublets. The doublet accounts for the spin orbit $5d_{3/2}$ and $5d_{5/2}$ spitting of the orbitals. The spectra must be fitted with two such doublets which account for the different way that this non-planar molecule is facing the substrate (the so-called shuttlecock up and down orientation), in agreement with what has been previously reported for this system by Cabaith et al[136,157].

The spitting between the two doublets in the undamaged spectrum is found to be 0.75 eV in close agreement with the 0.8 eV been reported by Cabaith et al[136,157]. The ratio

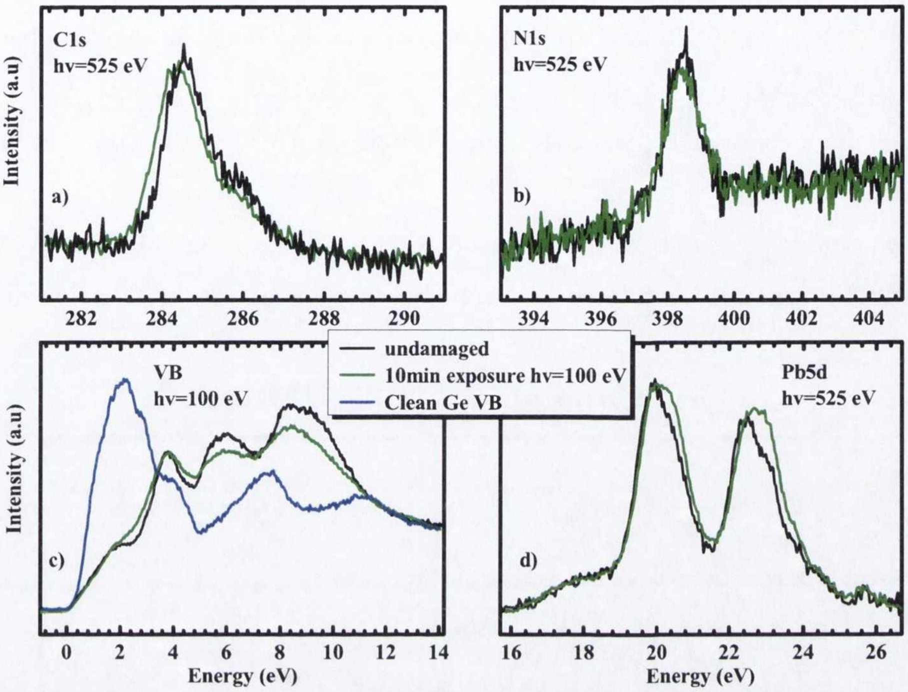

Figure 37 The effect on a PbPc 1 ML film to 10 min (hv=100 eV) X-rays radiation exposure at RT: a) C 1s b) N 1s c) VB and d) Pb 5d. Black - undamaged, green - 10 min exposure, blue - clean Ge.

between the integrated areas of the two doublets for the undamaged spectrum is 1.7 with the peak labelled D having Pb facing down.

After exposure the ratio of the two peaks D and U changes to 1.2. This perhaps indicates a substantial flipping from the face-down molecules to facing-up. It needs to be mentioned that further broadening had to be applied on the peaks which could account for various inhomogeneous small chemical shifts due to vibronic, molecular distortion and scissioning processes.

In the middle row of Fig. 38 the undamaged and the damaged spectra of the C 1s core level are presented; again fitted with two sets of pseudo-Voigt peaks labelled D and U. The same procedure for each of these two C 1s has been applied as reported earlier for the pristine thick film (section 3.1.2). In brief, the peak labelled 1 (C1) is assigned to the benzene ring carbons that have $\pi(2p_z)$-conjugation (double bond), peak labelled 2 (C2) is assigned to the benzene ring carbons without $\pi(2p_z)$-conjugation (double bond) and peak labelled 3 (C3) is assigned to the pyrrole carbons (fitting parameters are shown in Appendix I Tab.4&5).

Speaking for the undamaged spectrum it appears that the shuttlecock shape of the PbPc when the Pb facing down forbids a chemical interaction and substantial charge transfer between carbons and Ge substrate. This can be concluded from the fitted peaks (labelled D) which maintain the same stoichoimetric ratio as the thick pristine one and essentially the same binding energies.

On the other hand there is an interaction when the Pb atom is facing up. As can be seen from the fitting of the C1s peaks labelled U there is almost an inversion in the ratio

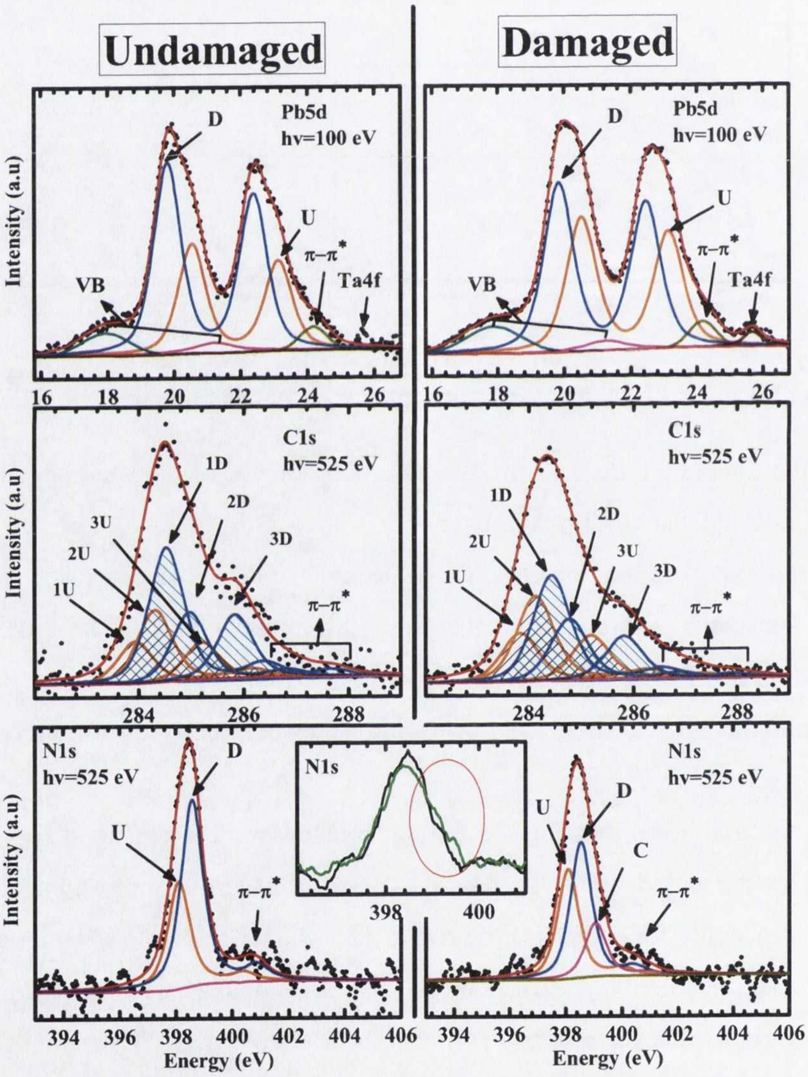

Figure 38 PbPc 1ML fitted graphs of undamaged and damaged spectra of Pb5d, C1s and N1s core levels. Peaks labelled D represent molecules with the Pb facing down and U Pb facing up. Peak C describes a scissioning (damage) of molecular structure. Inset compares undamaged and damage N1s core level which has been smoothed with a 2 point averaged smoothing. Fitting parameters are included in appendix I.

between 1U and 2U, compared to the 1D and 2D. That may indicate that less benzene ring carbons maintain the double bond due to possible sp^3 bonding formation to the Ge substrate. Recent unpublished work with STM imaging shows that the PbPc has a preferential orientation to the Ge substrate with two out of the four isoindolines sitting closer to the up dimers across the row of the Ge substrate[114]. An extensive interaction of two out of four benzene rings perhaps could explain the inversion of the ratio between 1U and 2U.

For the damaged C 1s spectrum there is an overall increase of the intensity for the set of peaks labelled U in coincidence with that observed from damaged Pb 5d core level which further supports the flipping of some molecules from down to up. In both undamaged and damaged spectra the ratio of integrated areas between the two fitted sets of peaks (D and U) follows the ratio of the fitted peaks D and U for the Pb 5d (1.7 undamaged to 1.2 damaged. See appendix1 Tab.4&5). Broadening of the peaks is also necessary which may arise from inhomogeneity in molecular distortion and scissioning processes. A very important observation is that the pyrrole to benzene ring integrated fitted areas for both set of peaks does not maintain the stoichoimetric ratio of 1:3 as for the undamaged spectrum, but increases. This may indicate that some of the pyrrole carbons have gone, perhaps due to scissioning process. A siminar indication is coming from the fitting of the severely damaged thick film, presented previously (Fig. 32), where the benzene ring C peaks and pyrrole C peaks do not maintain the stoichoimetric ratio 3:1, either. Furthermore, this is in agreement the C 1s spectra of SnPc discussed in section 3.1.1 where the integrated areas of C 1s have been reduced upon radiation damage (Fig. 25). This would result from the breaking of the bond between the pyrrole carbon and the bridging N. The breaking of the bond with the bridging N upon UV radiation exposure of a MPc has been reported by Slota et al.[129] based on FT-IR and optical absorption measurements of several MPc in solution, including PbPc.

Lastly the bottom row of Fig. 38 shows the undamaged and the damaged spectra for the N1s core level in a similar fashion. Both spectra have been smoothed with adjacent averaging of two points either side of each point. A direct comparison of the two is presented in the inset in the middle of the row. From this, a broadening on the higher binding energy side can be observed in the damaged spectrum. This could be as a result of the scissioning process. This appears as the peak C on the fitted damaged spectrum where the peaks D and U follow the trend as has been described before for Pb 5d and C 1s core levels.

3.2 Planar phthalocyanine beam damage effects

3.2.1 Magnesium phthalocyanine (MgPc) thick film beam damage studied by XPS core level and NEXAFS spectroscopies.

The influence of beam damage on magnesium phthalocyanine (MgPc) is reported here, studied by N *1s,* C *1s* and VB PES and NEXAFS. This gives a comparison to the non-planar phthalocyanines discussed above.

A thick film of ~100 Å prepared by sublimation onto a clean and well reconstructed substrate of Ge (001) in the same fashion as above for PbPc. XPS and NEXAFS measurements were conducted at the same beamline with the same experimental parameters as for the PbPc data. NEXAFS was measured via the drain current.

The progression of damage at room temperature to the X-rays radiation is presented in Fig. 39 for the thick film of MgPc. This involves the comparison of the XPS spectra of C 1s, N 1s, VB and HOMO. Different exposure time, radiation flux and energy of the incoming photons have been applied for the C 1s and N 1s core level spectra in comparison to the VB and VB HOMO photoemission spectra. The black coloured spectrum represents an undamaged spectrum. In the case of C 1s and N 1s core levels, the red one represents exposure to synchrotron radiation for 2235 sec (~37 min) with photon energy of 525eV and flux of approximately $2.8 \times 10^{13}\ photons \cdot sec^{-1} \cdot mm^{-2}$. The green spectrum represents a longer exposure to the same synchrotron radiation for 3510 sec (~1 hour). In the case of the VB and HOMO the magenta coloured spectrum represents 1032 sec (~17 min) exposure with 130 eV photons and flux approximately of $1.3 \times 10^{15}\ photons \cdot sec^{-1} \cdot mm^{-2}$, which is the around the maximum flux that this beamline could achieve.

A meaningful comparison of C 1s and N 1s red spectra with those from of SnPc that are shown in Fig. 23c and Fig. 24c is possible since in both cases the same exposure time, flux and energy of photons have been used. It is clear that although the changes in these core levels follow the same trend (broadening, disappearing of the valleys), this time it is much less and even after almost one hour exposure (green colour spectrum), the spectrum looks closer to the undamaged than SnPc.

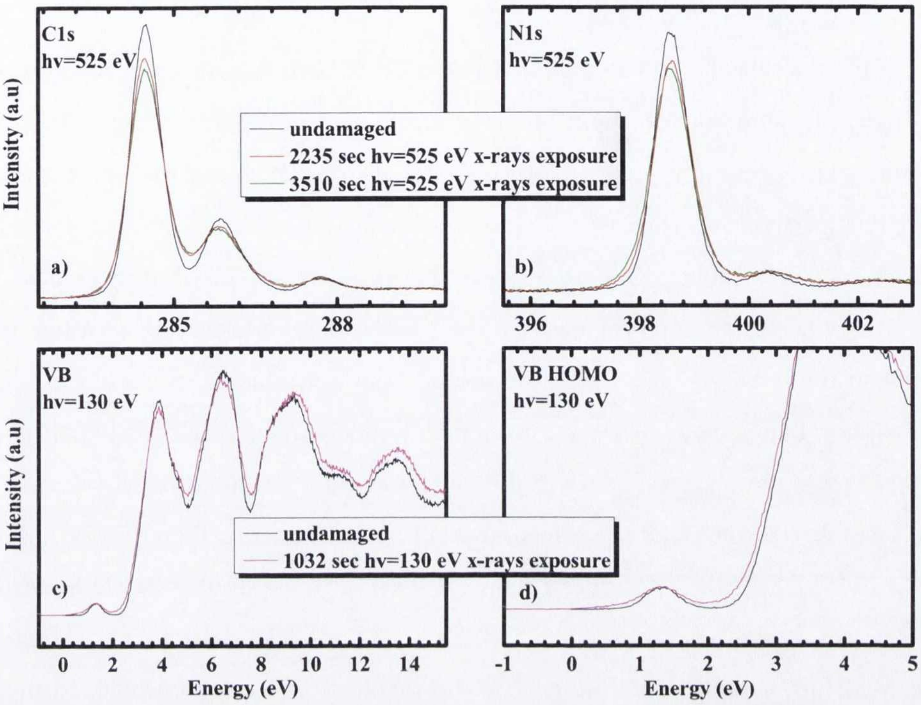

Figure 39 The effect of MgPc's (~100 Å thick fim) x-rays radiation exposure at RT to the core levels: a) C 1s b) N 1s c) VB and d) VB HOMO photoemission spectra. Different: exposure time, radiation flux and energy of the incoming photons have been applied for the C 1s and N 1s corel level to the VB and VB HOMO.

The VB and HOMO spectra are comparable with those of PbPc shown in Fig. 28c and Fig. 32c as they have been exposed to a similar radiation dose, although with a different time scale. As an aside it should be noted that the highest flux of the undulator is at hv=100 eV photon energy where slightly less flux occurs for the hv=130 eV photon energy. The damage follows the same trend (broadening of the HOMO and a shoulder between HOMO and HOMO-1) as in the case of PbPc but to a lesser degree.

3.2.2 NEXAFS beam damage studies of thick MgPc film.

Similar to the XPS spectra, N *K* edge NEXAFS spectra of a severely damaged MgPc thick film is compared with an undamaged one shown in the Fig. 40. It is evident that much longer exposure is needed to be applied in order to see the same degree of observable changes as in the case of PbPc as presented in Fig. 34.

The features labelled C and M describe a molecular scissioning process which is believed to be the same as in the case of PbPc with the main effect being a loss of pyrrole carbons and the breaking of the bond to the bridging nitrogen as discussed in section 3.1. Also a slight enhancement of the σ^* resonance region can be observed which is probably most likely to do with a changed tilt of the molecule in the crystal.

The fact that the planar MgPc is more robust than the non planar PbPc has also been observed by Slota et al[129]. This work suggests that the strength of the C-N bonds coupling the four benzopyrole (isoindoline) rings of the Pc macrocycle depends on the degree of polarization of the π-electronic cloud inside the macrocycle by the complexed metal anion and is related to the metal electronegativity (e.n.). If one considers that durability of the phthalocyanine macrocycle is determined by the distribution of the π-electrons engaged in the bonding system and the fact that Pb (e.n: 2.33) has almost double the elecrtonegativity of Mg (e.n: 1.31), this could easily favour a reduced electronic density across these C-N bonds which reduces further upon the photo-excitation at these atomic sites.

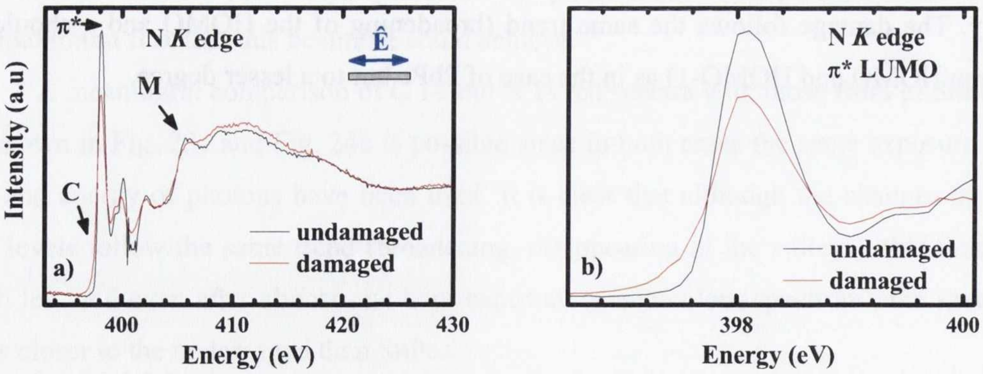

Figure 40 N *K* edge NEXAFS of MgPc thick film at RT with the polarization parallel to substrate of undamaged and damaged film. On graph b) the π^* orbital peak of these spectra presented in detail. The C and M features show observable changes.

3.2.3 Magnesioum phthalocyanine (MgPc) thin film beam damage studied by XPS.

To continue the comparison with the non planar phthalocyanines, the effects of exposure to the synchrotron radiation of a thin film of the planar MgPc on Ge (001) substrate are presented here. Approximately ~1½ML of MgPc was deposited in situ by vapour deposition on a clean and well reconstructed (2x1) Ge (001) substrate at room temperature. XPS measurements took place again at the I511-1 beamline at MAX-lab II, using the same end station and electron analyser as in the case of the thick film.

The comparison of the XPS of the undamaged spectra of C 1s, N 1s, Mg 2p and VB, compared with 23 min (red) and 100 min (green) exposure to 525 eV X-ray beam (flux: $2.8\times10^{13}\,photons\cdot sec^{-1}\cdot mm^{-2}$) is shown in Fig. 36. The nominal combined instrumental resolution used for the XPS measurements is 0.1 eV. In the case of the Mg 2p core level, a polynomial background subtraction has been applied in order to extract the signal to that which is attributed to the substrate. All spectra are presented with intensity normalised to a maximum of 1.

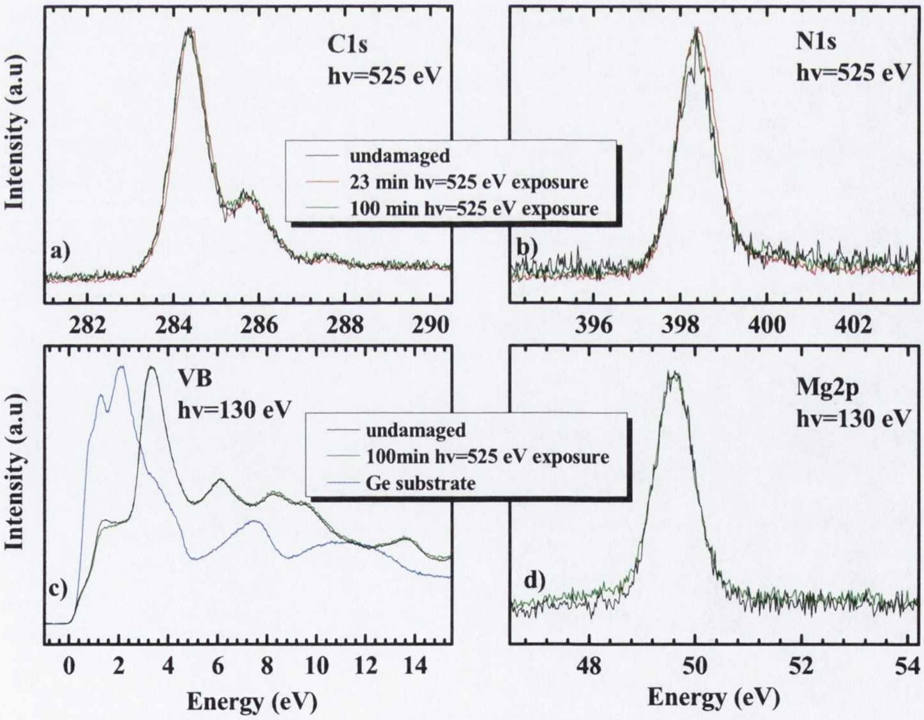

Figure 41 The effect on ~1½ ML MgPc of 525 eV X-rays radiation at RT. XPS of a) C1s b) N1s c) VB and d) Mg2p are given. Black: undamaged film. Red: 23 min exposure. Green: 100 min exposure. Blue: clean Ge VB spectrum.

Little change is observed in the core level spectra (C 1s, N 1s and Mg 2p) even after ~1½ hours exposure. In the VB spectrum the only observable difference is seen at the HOMO-1 level of the interface which seems to have been suppressed. The fact that the core levels are unaffected most likely indicates that the molecular structure remains intact (no scissioning). This enhances the argument that planar MgPc has a robust molecular structure. Perhaps this screening could be enhanced by the substrate interaction by distributing more electron charge across the molecule from the substrate.

3.3 Summary

Synchrotron radiation induced damaged to the organic semiconductor family of metal phthalocyanines solid films has been under investigation through photoemission and NEXAFS spectroscopies. A comparison between non-planar and planar phthalocyanines has been given, with discussions of the influence of temperature, and the difference between the damage effects of bulk in comparison to ML films.

Two major damage processes have been identified: a) Degradation or alteration of the crystal structure of the films and b) molecular damage (scissioning).

At low temperature these two processes occur at a lower rate as demonstrated by liquid nitrogen temperature XPS studies of a thick film of PbPc.

Comparison of non-planar (PbPc) and planar (MgPc) phthalocyanines under the same exposure time, energy and flux shows that the planar MgPc is more robust to damage than the non-planar PbPc.

Similarly, between thin films (~1 ML) of non-planar PbPc and planar MgPc, as investigated through core level and VB photoemission spectroscopy, the MgPc remains intact after significantly greater radation exposure in comparison to PbPc.

In the case of the PbPc ML film, prolonged exposure seems to alter the orientation of the non-planar molecule with respect to the substrate. The molecule is sitting flat with the Pb atom facing towards the substrate and away from the substrate in ratio 1:7. Synchrotron radiation seems to flip a substantial number of molecules and alters the ratio to 1:2.

4. Electronic structure of Organic Semiconductors

The electronic structure of phthalocyanine organic semiconductors is the second theme of investigation in this thesis. These investigations have proceeded by synchrotron radiation based x-ray spectroscopic measurements of thick (bulk-like) and thin phthalocyanine films. The results presented here are primarily XPS, NEXAFS and XES measurements taken at beamline X1B from the National Synchrotron Light Source (Brookhaven National Laboratory, USA). X1B is an undulator beamline with a flux in the energy range of the C and N *K*-edge of $\sim 4.7\times10^{14}$ *phs/sec/mm*^{2}*/0.1%BW/400 mA.* The monochromator in use at X1B has a number of gratings of which the 300 mm^{-1} and 600 mm^{-1} grating were used as flux or resolution necessitated at the C and N *K*-edges. More details of beamline X1B are available in the literature[158].

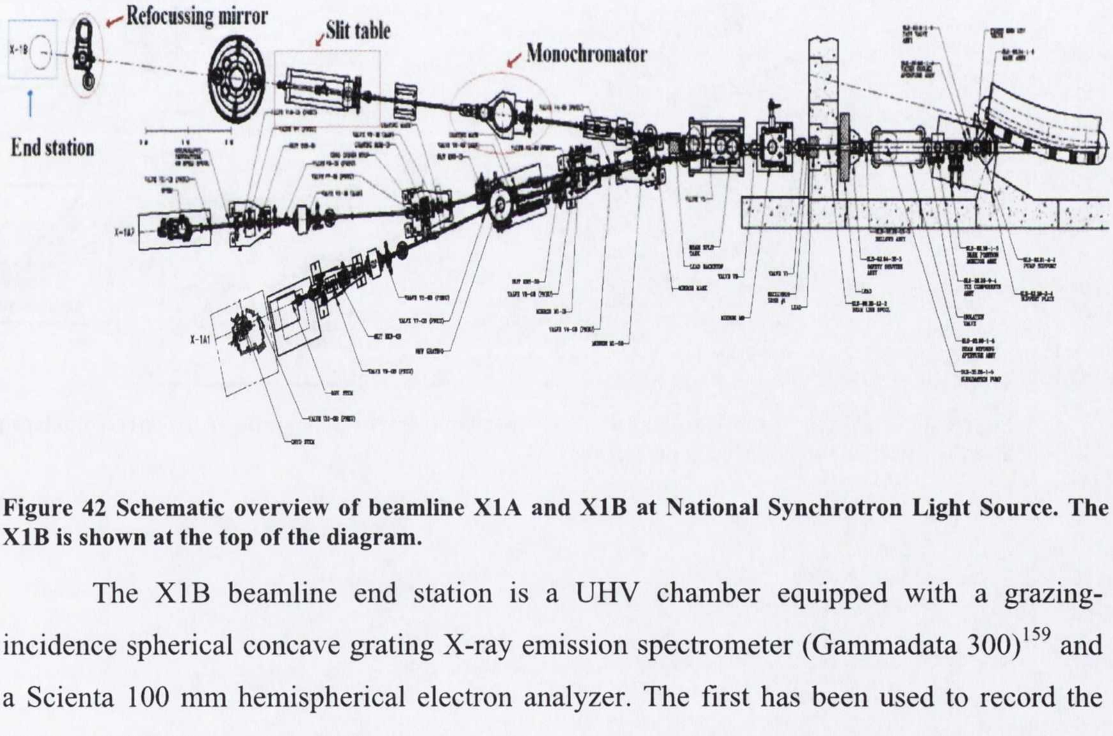

Figure 42 Schematic overview of beamline X1A and X1B at National Synchrotron Light Source. The X1B is shown at the top of the diagram.

The X1B beamline end station is a UHV chamber equipped with a grazing-incidence spherical concave grating X-ray emission spectrometer (Gammadata 300)[159] and a Scienta 100 mm hemispherical electron analyzer. The first has been used to record the XES and RXES spectra, while the second has been used to record core level and valence band photoemission spectra.

The XES300 Gammadata spectrometer is equipped with three different gratings as shown in Fig. 43. C *K*-edge spectra have been obtained using the 2nd grating of 400 l/mm, R=5000 mm and in 1st order, typically with a 10 μm spectrometer entrance slit, which gives

~0.3 eV resolution. N and O *K*-edge spectra have been obtained using the 1st grating of 1200 l/mm, R=5000 mm and in the 1st order typically with a 10 or 13 μm entrance slit, giving resolutions of 0.2-0.3 eV and 0.4-0.5 eV, respectively. NEXAFS spectra were also recorded at X1B via the electron drain current.

The use of these different spectroscopies is an attempt at a comprehensive investigation the electronic structure of these solid organic films. This includes different chemical environments (core level XPS), total and partial density of occupied states (VB XPS and XES respectively) and density of unoccupied states (NEXAFS). A comparison between different probing methods and theoretical calculated electronic densities of states is used to strengthen the conclusions.

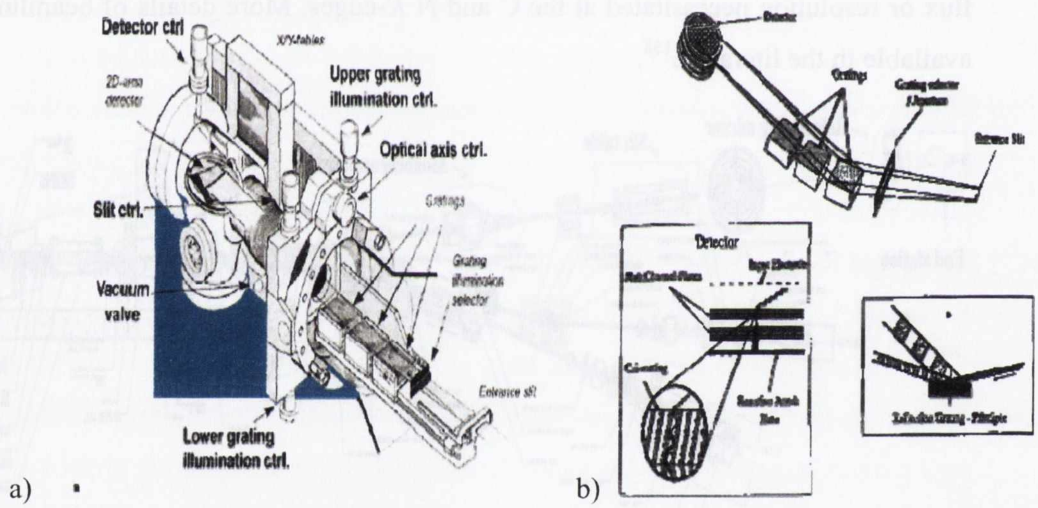

Figure 43 a) Sketch of the Gammadata XES spectrometer. b) Schematic of the spectrometers gratings and the microchannel plate 2D detectror.

4.1 XPS, NEXAFS, and RXES measurements of the electronic structure of metal phthalocyanines

4.1.1 Tin phthalocyanine (SnPc) solid film studied by XPS, RXES and NEXAFS.

The first phthalocyanine to be considered is tin (II) phthalocyanine (SnPc). All RXES spectra were obtained using a Nordgren-type grazing incidence x-ray emission spectrometer positioned in the horizontal plane at 90° to the beam[160]. NEXAFS spectra were obtained at C and N *K* edges with monochromator resolution of 0.11 eV for both edges and were obtained in total electron yield (TEY) by the current drain method. RXES spectra of the excited C and N *K* edges were obtained with nominal combined monochromator and x-rays emission spectrometer instrumental resolutions of 0.5-0.8 eV and 0.45 eV, respectively. Valence band XPS were taken from a thin (~10 ML) film grown on a Ag (111) substrate at the I511-1 surface branch beamline at MAX-lab using a Scienta R4000 electron analyzer with an estimated total instrumental resolution of 0.08 eV. For the RXES spectra, a SnPc film of ~1000 Å thickness was deposited by sublimating from a Knudsen cell at $<1 \times 10^{-7}$ Torr onto the native oxide of a Si (100) substrate held at room temperature. The deposition rate was of the order of 5 Å/minute. The substrate had been degassed for 6 hours at 200 °C in the chamber which had a base pressure of 5×10^{-9} Torr. The thickness was estimated by a quartz crystal monitor placed in front of the substrate. As RXES measurements require long accumulation times, sample exposure was limited to avoid beam damage by vertically translating the sample every 300 ms by 100 μm steps.

The electronic structure of thin layers of SnPc deposited on various GaAs and Ge substrates has previously been studied by both VB-XPS and NEXAFS[145,157]. NEXAFS, in addition to providing information on the orientation of the molecule on the substrate, also probes the partial density of states (PDOS) of the lowest unoccupied molecular orbitals (or LUMO band) while VBXPS (or UPS) measures the total density of states of the highest occupied molecular orbitals (HOMO band). A complementary technique allowing the measurement of the occupied partial density of states on a site- and symmetry-specific ba-

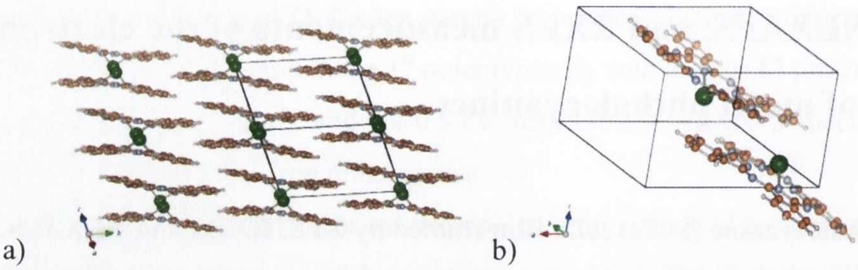

Figure 44 a) Illustration of the columnar stack across the c axis for the triclinic crystal structure of SnPc films after Kubiak et al.[90] b) The projection of concave and convex type arrangement.

sis is that of resonant soft X-ray emission spectroscopy (RXES) which is applied to tin phthalocyanine here.

The non-planar SnPc has a shuttlecock shape and forms a triclinic crystal structure[90]. Individual molecules stack along the *a*-axis, alternating convex and concave sides with all stacks identical (Fig. 44). NEXAFS of thin films of SnPc on Ge and GaAs have shown SnPc molecular planes lying close to parallel to the substrate[145].

In Fig.45 NEXAFS spectra of SnPc films on Si, measured at 20° and 70° angles of incidence at both the C and N *K*-edges, similarly indicate flat lying molecules. In-planar phthalocyanines such as CuPc and ZnPc investigated by NEXAFS, it appears that a transition from lying-down to standing-up configuration occurs after only a few monolayers, whereas in unreactive substrates (passivated Si or HOPG), only the standing-up structure persists in subsequent growth[161-165].

It needs to be noted here that NEXAFS is strictly being a measure of the average azimuthal angular dependence of unoccupied states of molecular arrangements relative to the polarized light. This is particularly important for the bulk like films where arrangements of the molecules following single crystal structures, e.g of β the form ends up with neighbour molecules almost orthogonal. In the case of polycrystallinity there is also the possibility of different orientation, relative to substrate, of the stacking axis of these molecules in different parts of the film.

XES spectra for angular extremes (limited due to experimental geometry[2]) at either the C or N *K*-edge have been recorded with different excitation energies from threshold upwards. These XES spectra represent a measure of the 2*p* PDOS of the selected element,

---

[2] Direct optical pathway of the emitted x-rays to the spectrometer is needed in order to get a decent count rate. These extremes may be considered to be grazing incidence onto the surface or a grazing exit from the surface.

where in the case of the C *K*-edge, a difference in 1*s* binding energy between the pyrrole C site and the ring or aromatic C sites can be exploited near threshold at 285.5 eV (A) and 286.3 eV (B) as shown in Fig. 45.This provides almost separate measurement of their respective local C2*p* PDOS[91]. We also discuss here the angular dependence of the observed SXE spectra measured on resonance and above threshold at both C and N *K*-edges as shown in the left side panels of Fig. 45.

It is seen clearly that the near-normal incidence (70°) spectra shows significantly greater spectral weight at ~282 eV as well as increased weight at ~284 eV in comparison to the grazing incidence spectra. The RXES angular dependence arises as the SnPc molecular planes within the bulk film lie at slight angles to the substrate (see Fig. 45 right top panel) and even if randomly oriented, low angles of incidence onto the surface will have the elec-

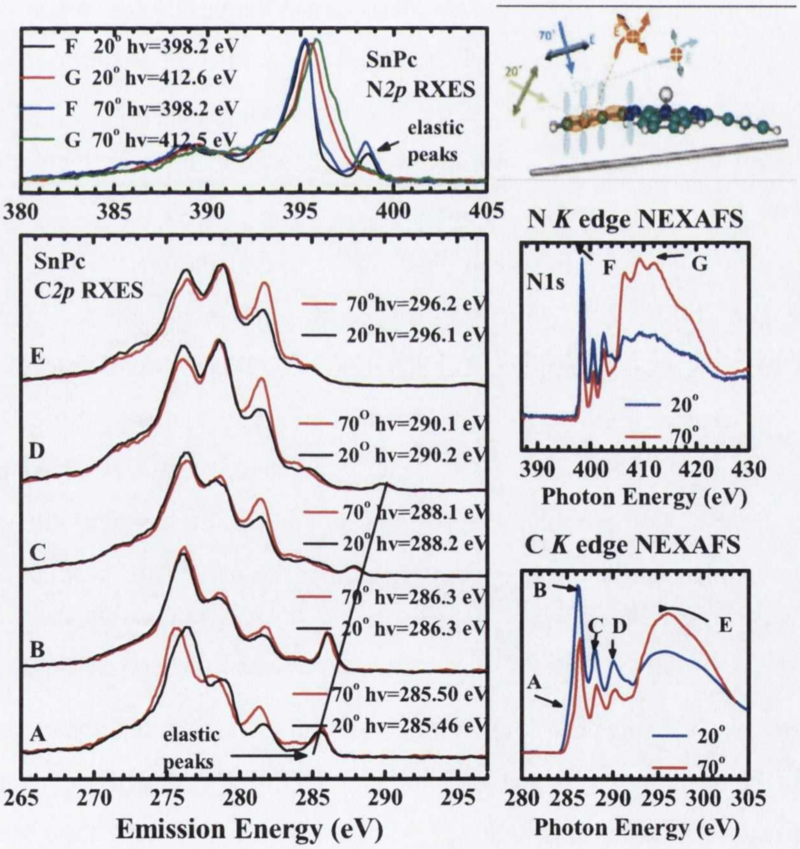

Figure 45 Right side panels: SnPc NEXAFS at N (top) and C (bottom) *K* edges respectively; at 20° and 70° incidence of beam to substrate. Left side panels: C *K* and N *K* SXE spectra at the same angles taken for various resonant energies and in non-resonant mode. Top right panel: Diagram illustrating angular dependence of RXES arising from the various C sites for a single SnPc molecule.

trical field vector Ē predominantly parallel to π* orbitals. Due to the 90° scattering geometry, emission then occurs only from occupied in-plane (σ-like) orbitals[115]. Angles of incidence near to normal to the molecular plane result in emission in a 90° scattering geometry, from both occupied in-plane (σ) and out-of-plane (π) orbitals. As a result we can obtain spatial information of the C and N LPDOS components (states) from the varying chemical sites. Similarly, the N *K*-edge RXES spectra (F) show increased spectral weight for the 70° angles at ~396.5 eV corresponding to the HOMO levels.

At most of the C and N 2*p* emission spectra there is a distinct peak always at the higher emission energy side. This is the resonant elastic X-ray scattering (or Rayleigh scattering) peak and is the participator decay of the excitation where the filling of the core hole occurs from the same excited electron. That means simply that the emitted-photon energy ω′ is the same as that of the incident-photon energy ω (See equation 11).

A full explanation of the observed spectra is supported by comparison to DFT calculations of both the C *2p* and N *2p* PDOS, and further a comparison to the calculated XES spectra which can be emitted from occupied molecular orbitals (σ states) in the plane (strictly the plane defined by the 4 inner Ns) and those occupied molecular orbitals perpendicular to the plane of the molecule or π states.

The StoBe package has been used for these calculations[166]. This package is based on the DeMon DFT code[167], but with a specific implementation for inner-shell spectroscopies. The StoBe calculation was a calculation of a relaxed SnPc molecule in C_{4v} symmetry where the x-ray emission spectra were calculated as a property of the ground state. The calculation employed the double zeta valence polarisable (DZVP) and A1 orbital basis set. In each case presented here the total XES per molecular site is strictly the sum of all possible core molecular orbitals and is thus representative of the non-resonant, non-symmetry selective XES arising from that atomic site. These calculations have been carried out in TCD by Dr. C. McGuinness.

Figure 46a depicts the total occupied and unoccupied density of states of SnPc by the StoBe DFT package. Together with the total DOS the *2p* PDOS on each of the N and C atomic sites within the molecule are presented, where the spectra have been resolved into the orbital components projected along the *z*-axis, perpendicular to the molecular plane, (π-states) and those within the xy plane, which correspond to the molecular plane (σ-states).

However, it should be noted that the non-planar shuttlecock shape of the SnPc distorts the isoindoline arms, and consequently the orbitals related to these, away from the xy plane, therefore such a global orbital basis cannot be exact in describing the local bonding.

Figure 46b presents the calculated X-ray emission spectra arising from a *1s* core hole on each of the C and N atomic sites within the SnPc molecule. In the case of the carbon sites there are three different sites for the benzene ring named link (C2), elbow (C3), outer (C4) and one site for the pyrrole carbons (C1) as shown in sketch at Fig. 46. In the case of N there are two different sites named aza or bridging nitrogens (N1) and inner ni-

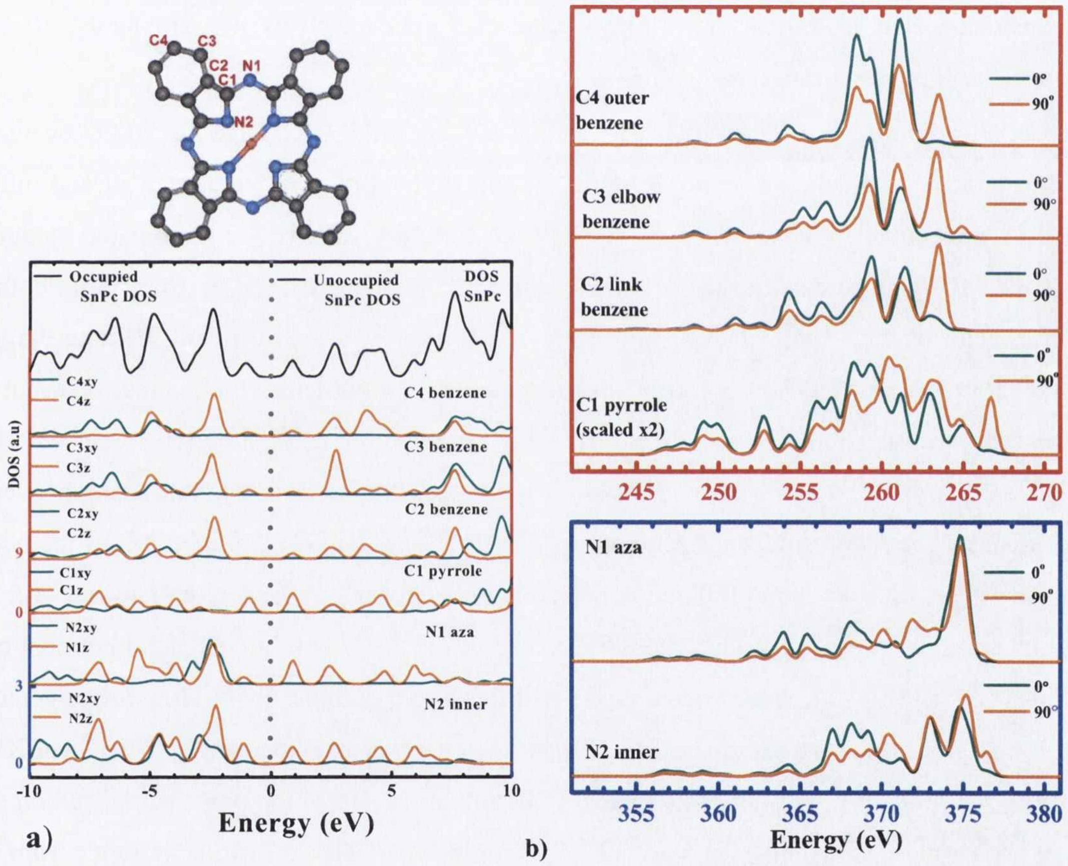

Figure 46 Top left: Sketch illustrating the various atomic C and N sites for a single SnPc molecule. Bottom left (a): At the top the total occupied and unoccupied DOS of SnPc. Subsequent panels: Each subsequent panel shows the *2p* PDOS of the atomic sites where we progress from the outermost carbon site (C4) to the innermost (pyrrole) carbon site (C1) and the two nitrogen sites, the meso-bridging or aza nitrogen (N1) and the inner nitrogen (N2). Each PDOS is shown broken into the *2p* projection (p_z) perpendicular to the molecular plane (*xy* plane) defined by the four inner Ns and the sum of the projections (p_x+p_y) within that plane. The zero in energy is chosen to be exactly between the HOMO and LUMO. Right panel (b): Shown for each C and N atomic site in SnPc are the calculated XES spectra derived from the *2p* PDOS for two differing measurement geometries, measuring the emission from a SnPc molecule face-on (0°) or edge-on (90°). The energy scale is the calculated transition energy.

trogens (N2). The calculation of the XES spectra has been done in the ground state approximation as this is most appropriate for these spectra[168]. The calculated transition energies are in practice rigidly shifted to match the experimental spectra. The calculated XES spectra are broken down into two components corresponding to the measurement of the XES spectrum of a single molecule face-on (0°) and edge-on (90°). The 0° XES spectrum is the sum of all polarisations propagating perpendicular to the plane of the molecule, and effectively sums over the *x* and *y* projections within that plane or from the occupied σ-states only. The 90° XES spectra are calculated as the average of the sum of all polarisations along the differing directions from the centre within the plane of the molecule and can thus be thought of as the sum of the *x*, *y* projection and the *z* projection, or equally, the sum of the occupied σ and π states.

In conjunction with the DFT calculations of SnPc, the PDOS for the C occupied and unoccupied states (Fig. 46a) show a well defined spatial orientation in and out of plane molecular orbitals (MO) with the LUMO, LUMO+1, LUMO+2 dominated by out of plane MO. It appears that the LUMO is distributed mainly between pyrrole C and both N sites. The HOMO and HOMO-1 appear to have a prominent out of plane character largely being located on the C sites and N sites respectively. In particular the angular distribution of the *2p* components of the MOs attributed to the different C sites (chemical environments) is presented in the lower panels of Figure 46a. It appears that the differing benzene-like or ring carbons contribute slightly differently to the total density of states of the occupied HOMO levels, though there are some clear differences in the region between -4-5 eV and again between -6-8 eV particularly as a result of the H bonding on the outermost carbons (C3 and C4). It should be noted that all these ring carbons, as in all non-halogenated phthalocyanines, have very similar C *1s* binding energies as evidenced by core level XPS. Whereas, they have a distinctly separated binding energy from the pyrrole-like carbon site (C1)[3]. As a result, in the calculated XES spectra the calculated transition energies from the occupied MOs to the *1s* hole span the same emission energy range. When one then examines the calculated XES spectra, shown in Figure 46b, originating from these ring carbons there is a very striking effect as regards the geometrical dependence to be seen.

Shown in Figure 47 are the valence band XPS spectra of SnPc, the NEXAFS spectra of SnPc at the C and N *K* edges, the resonant XES (RXES) and non-resonant XES

(NRXES) spectra at the C and N *K* edges, and also the comparison with the calculated XES spectra from the differing atomic sites. For presentation purposes the three benzene carbon calculated XES sites have been summed together. The energy scale is presented relative to the Fermi edge. This is achieved by subtracting the experimental XES spectra emission energy from the experimental 1*s* binding energy for each atomic core site (benzene ring C: 284.62 eV, pyrrole C: 286.03 eV and nitrogen N: 398.82 eV) as extrapolated by fitting of the XPS spectra (see section 3.1.1). Similarly, subtraction of the calculated XES spectra from the calculated 1*s* binding energy for each atomic site has been applied.

The three (benzene ring carbons) exhibit a strong angular dependence for the HOMO-2 levels with strong weight at the 90° calculated X-ray emission which coincides well with the measured XES emission spectra at 70° (Fig. 47). The elbow carbon (C3) has a small contribution to the XES for 90° to the HOMO-1 level, which helps enhance the HOMO-1 level as it appears in the NRXES in Fig. 45 and 47. The deeper VB levels of the outer carbons (C4) differ substantially from the other two (C2 and C3) producing a strong angular dependence which is also observable in the XES spectra. The pyrrole carbon PDOS appears to have contribution at HOMO and HOMO-1 levels, with the π-like HOMO contributing mainly in the 90° emission or edge-on emission.

The N PDOS DFT calculations follow a similar behaviour where LUMO, LUMO+1 and LUMO+2 have mainly, an out of plane π^* orbital distribution for the inner N and the aza N. The HOMO has an out of plane orbital distribution (π-state) and it is mainly found located on the inner N, whereas the HOMO-1 gets contributions from both N sites, with aza and inner N having contributions in both angles. There is a shift at the inner N calculated X-ray emission (Fig. 47) and projected PDOS (Fig. 46a) of the HOMO-1 between the two extreme emission angles (0° and 90°) normal to the plane of the molecule and perpendicular to the plane, which is reproduced well in the measured XES N *K*-edge spectra at the experimental extreme angles of 20° and 70°. The N *K*-edge RXES spectra (F) (Fig. 47) show increased spectral weight for the 70° angles at ~396.5 eV corresponding to the HOMO levels and is in coincidence with that calculated at 90°.

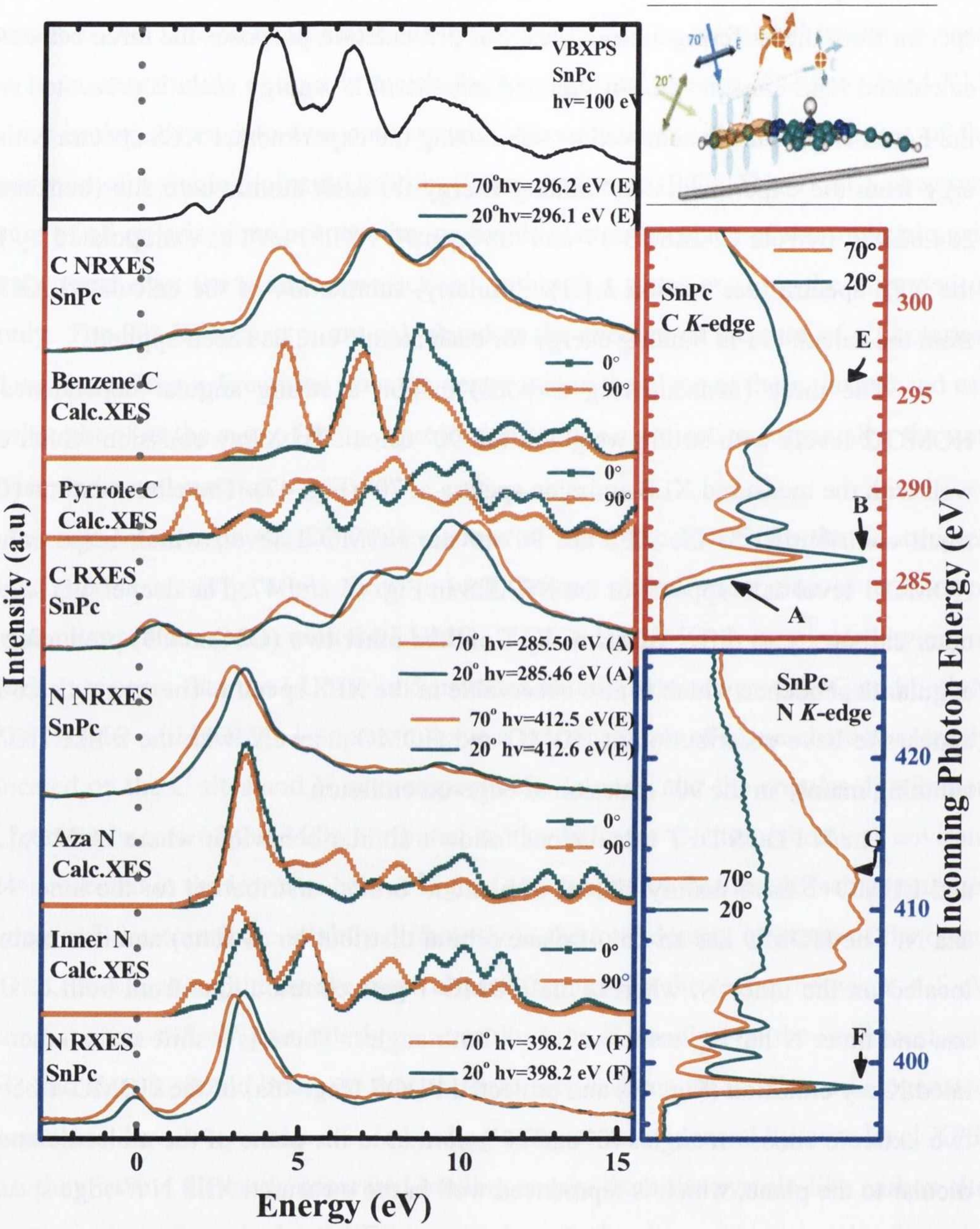

Figure 47 Right: The SnPc NEXAFS at the C (upper panel) and the N (lower panel) *K* edges respectively. The NEXAFS are measured at 20° and 70° incidence of beam to substrate. Left: Shown at the top is a valence band XPS of a 10 ML film of SnPc on Ag(111). Below this C *K*-edge RXES and NRXES spectra are shown here in comparison to the calculated XES spectra arising from the C-C bonded or benzene like Cs and the C-N bonded or pyrrole like C. In the bottom of this panel N k-edge RXES and NRXES spectra are shown here in comparison to the calculated XES spectra arising from the inner N or aza (meso-bridging) N respectively. In each case the XES spectra are measured at the same angles as the NEXAFS.

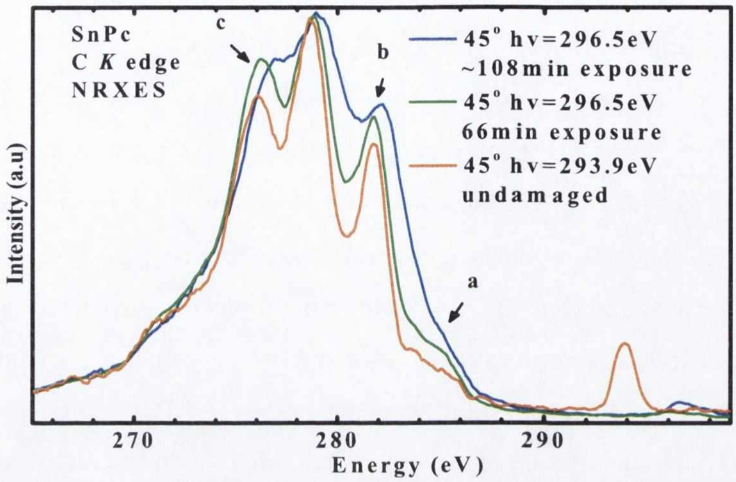

Figure 48 Non-resonant x-ray emission spectra (NRXES) of SnPc. The first spectrum (Orange) has been taken by translating the sample in front of the beam and is considered as undamaged. The other spectra have been taken in a fresh spot with sample kept stationary in the beam with total X-rays exposure of 66 min (Green) and a total estimated x-rays exposure of ~108 min (Blue).

RXES spectra and above threshold XES spectra can be considered as one-step or two-step processes respectively with a relaxation of selection rules for the latter[115,169]. Consider the N *K*-edge non-resonant XES spectra (G): in these, at both angles, a much greater spectral weight from 396 eV and to higher emission energy is observed which arises almost exclusively from the out of plane inner N sites, where this is suppressed in the RXES spectrum (F) due to symmetry considerations. In both C and N RXES spectra it seems that symmetry selection suppresses emission from the HOMO which is distinctive only in the non-resonant emission.

In Figure 48 a non-resonant C *K*-edge x-ray emission spectrum (NRXES) of SnPc, thus measuring the C 2*p* PDOS, is shown in comparison with spectra that are considered as damaged. The first spectrum (orange) has been taken by translating the sample in from of the beam every 350 msec and is considered undamaged. At this time the sample is approximately moved by 100 μm which is twice the FWHM of the beam spot. Typically acquisition time for a XES spectrum is 1-2 hours depending on the count rate. The second spectrum (green) has been taken in a previously unexposed spot, but with the sample kept stationary in the beam with a total X-ray exposure of 66 min during acquisition. The final spectrum (blue) has been taken in a pre-exposed spot, again with the sample kept stationary, now with a total estimated X-ray exposure of ~108 min. All spectra were obtained with the same spectrometer slit. Also they have been normalised with their intensities between 0 and 1. The flux is approximately 2.4×10^{16} $photons\cdot sec^{-1}\cdot mm^{-2}$.

There are observable changes in the HOMO region (labelled as **a** on the graph) which is seen as an enhancement in spectral weight and a slight shift towards higher emission energy. This coincides with the discussion in section 3.1.2 of the damaged VB-XPS spectrum of MPcs. There, it was speculated as arising from an excitonic splitting of HOMO states due to increased interference of neighbouring molecules. There are also changes observable in the HOMO-2 region (labelled as **b** on the graph) noted previously (Fig. 45) as being highly sensitive to the emission geometry and to the deeper VB level (labelled as **c** on the graph). These changes are a strong indication that upon radiation exposure the local crystal structure of the SnPc film is deformed and has as a result changed the geometrical orientation of the molecule to substrate and hence to the polarisation of the beam light. The peak appearing at 294eV in the orange spectrum is the resonant elastic X-ray scattering (or Rayleigh scattering) peak and is the participator decay of the excitation where the filling of the core hole occurs from the same excited electron as described previously.

It is more difficult to say conclusively whether the resultant emission spectra reflects undamaged molecules in a more disordered or modified crystalline structure or whether it reflects an increasing proportion of damaged molecules in the same crystalline arrangement, but evidence suggests the former.

It should be noted that there is a tendency for the beam damaged spectra from a variety of differing organic aromatic based molecules to become broadly similar to each other with a blending and broadening of features and loss of apparent structure[98]. Thus a combination of the two, i.e. a proportion of damaged molecules in an increasingly damaged or disordered structure is likely.

4.1.2 Lead phthalocyanine (PbPc) solid film studied by XPS, RXES and NEXAFS

The same experimental set up as the one used in the case of the measurement of the electronic structure of SnPc has been used for RXES and NEXAFS spectra measurements on PbPc. Instrumental resolutions for NEXAFS C and N *K* edges is an estimated 0.11 eV, and the RXES spectra of the excited C and N *K* edges were obtained with nominal combined instrumental resolutions of 0.53 eV and 0.45-1.85 eV, respectively. The presented valence band XPS were taken from a ~20 ML film grown on a Ge (001) substrate (as described in 3.1.2) at the I511-1 surface branch beamline at MAX-lab using a Scienta R4000 electron analyzer with an estimated total instrumental resolution of 0.08 eV. For the RXES spectra, a PbPc thick film of unknown thickness (due to faulty quartz crystal monitor), was deposited by sublimating from a Knudsen cell at $< 1\times10^{-7}$ Torr onto the native oxide of a Si(100) substrate held at room temperature. The substrate had been degassed for 2 hours at 330 °C in the chamber which had a base pressure of 5×10^{-9} Torr. The sample was translated during acquisition to avoid beam damage as described in the previous section.

Two different crystal structures have been reported so far for PbPc films, monoclinic[87] and triclinic[88] (Fig. 26). There is extensive literature related to the growing of PbPc films on several substrates describing orientation of the molecule and crystal structure that is best summarised by Kadish et al.[85], and references within. There is a variation in the crystal structure formed based on the temperature of the substrate, sublimation rates and annealing of the films. However, no clear boundaries are reported on the exact phase produced. The PbPc film under investigation here is believed to be a mixture between triclinic and monoclinic with the triclinic crystal structure as the dominant phase as concluded by Cabailh et al.[136] where angular dependence diagrams of the π^* intensity peak measured with NEXAFS indicate a mixture of molecular orientation due to the different crystal structures. It should be noted that the current films investigated here are prepared in exactly the same procedure and conditions as Cabailh et al[136]. Further the fact that the films as created are coloured dark blue and not green-dark green confirms this argument according to Collins et al[170]. This is based on XRD studies of differently prepared PbPc films, where films coloured blue have crystallites of the triclinic form and traces of monoclinic form.

The electronic structure of thin layers of PbPc deposited on various Ge substrates has previously been studied by both valence band photoemission spectroscopy (VB-XPS) and near edge X-ray absorption fine structure (NEXAFS) with the NEXAFS of these thin films showing that the molecular planes lie close to parallel to the substrate [136]. Holland[114] and Cabailh[136] examined the angular dependence of the π^* peak as observed by NEXAFS to study the orientation of the molecule. These works have shown that monolayer films and films of several layers of PbPc have the molecules inclined with an average angle tilt of 21° and 45° to the substrate, respectively. The angular dependence of the NEXAFS of the PbPc on Ge(001) is broadly similar to that observed for the data from the films presented here deposited on Si and its native oxide.

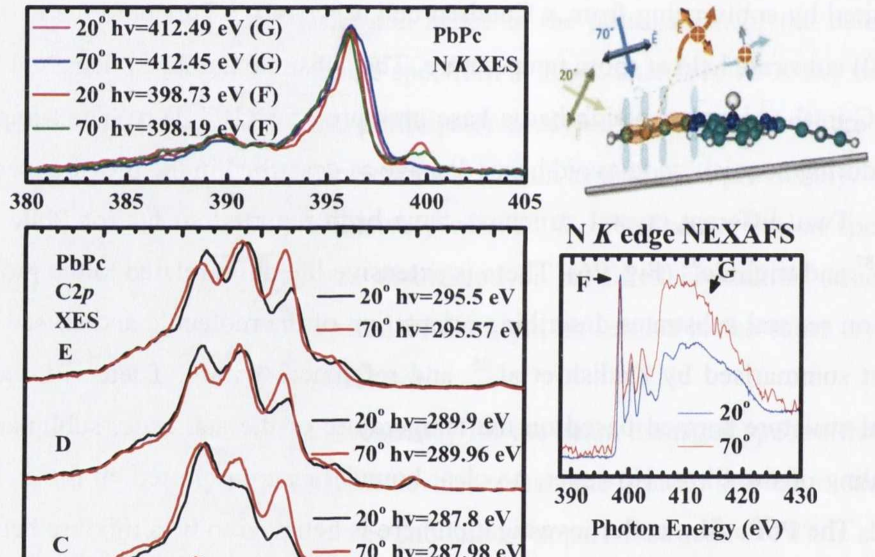

Figure 49 Right side panels: PbPc NEXAFS at N (top) and C (bottom) *K* edges respectively. Measurements taken at 20° and 70° incidence of beam to substrate are shown. Left side panels: C *K* and N *K* XES spectra at the same angles at various resonant excitation energies and in non- resonant mode. Top right panel: Diagram illustrating the angular dependence of RXES arising from the various C sites for a single PbPc molecule.

For the thick film, the crystal structure obtained is believed to be the same as the films presented here, where the same conditions of growth have been applied, albeit on a differing substrate.

In Fig. 49 NEXAFS spectra of PbPc films on Si and its native oxide, measured at 20° and 70° angles of incidence at both the C and N *K*-edges, show a similar angular dependence to SnPc. XES spectra for these angular extremes (limited due to geometry) at either the C or N *K*-edge have been recorded with different excitation energies from threshold upwards, with the angular dependence of the observed XES spectra progressing in a similar fashion to the case of SnPc.

The near-normal incidence (70°) spectrum clearly shows significantly greater spectral weight at ~282 eV as well as increased weight at ~284 eV in comparison to the grazing incidence spectrum. Significant difference is also seen for the deeper VB level at ~276 eV between the two angles near threshold (A) relating to excitation primarily arising from benzene C core holes. The same emission geometry with the small angles to the substrate, as for the case of the SnPc, gives emission (see Fig. 49 right top panel) only from occupied in-plane (σ-like) orbitals[115]. Angles of incidence near normal to the molecular plane (σ^* absorption) result in emission (edge-on) from both occupied in-plane (σ) and out-of-plane (π) orbitals giving information on the spatial distribution of the C and N LPDOS components (states). Furthermore, there is a distinctive difference in the HOMO and HOMO-1 levels between the two emission angles and between the various different resonant spectra. It appears that the HOMO-1 levels appear in the 70° incidence of light which indicates the presence of emission from out-of-plane states, even in the resonant spectra B. The HOMO level is slightly suppressed in the resonant spectra A and B but it starts to gain spectral weight from C, D and E respectively. Similarly, the N *K*-edge RXES spectra (F) show increased spectral weight for the 70° angles at ~397 eV corresponding to the HOMO-2 levels.

DFT calculations of both the C *2p* and N *2p* PDOS and calculated XES spectra from use of the StoBe package are presented here in order to fully understand and explain the observed experimental spectra.

Figure 50a depicts the total occupied and unoccupied density of states of PbPc. The total occupied destiny of states is in very good agreement with the one presented by Papageorgiou et al[137]. Together with the total DOS we present the *2p* partial density of states (PDOS) on each of the N and C atomic sites within the molecule, where we have resolved into the orbital components perpendicular to the molecular plane (π-states) projected along the *z*-axis and those within the molecular plane (σ-states), or in the *x-y* pane. Note that similarly to the SnPc, the PbPc calculation is for a single molecule in the C_{4V} symmetry

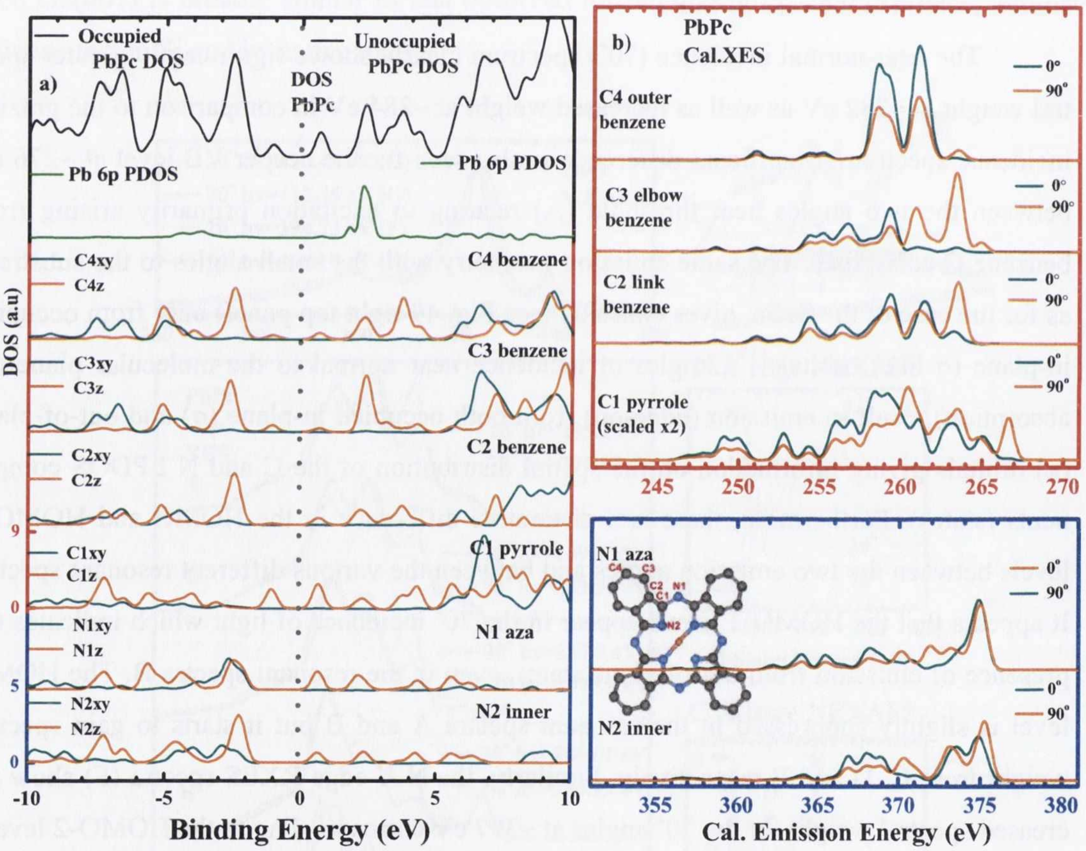

Figure 50 Left panel (a): At the top the total occupied and unoccupied DOS of PbPc. Subsequent panels: Second from the top is the contribution of Pb 6p states on the occupied and unoccupied PDOS. Each subsequent panel shows the *2p* PDOS of the atomic sites where we progress from the outermost carbon site (C4) to the innermost (pyrrole) carbon site (C1) and the two nitrogen sites, the meso-bridging or aza nitrogen (N1) and the inner nitrogen (N2). Each PDOS as presented is broken into the *2p* projection (p_z) perpendicular to the molecular plane (*xy* plane) defined by the four inner Ns and the sum of the projections (p_x+p_y) within that plane. The zero in energy is chosen to be exactly between the ÿOMO and LUMO. Right panel (b): Shown for each C and N atomic site in PbPc are the calculated XES spectra derived from the *2p* PDOS for two differing measurement geometries, measuring the emission from a PbPc molecule face-on or edge-on. The energy scale is the calculated transition energy. Inset: Sketch illustrating the various atomic C and N sites for a single PbPc molecule.

with optimized coordinates.

Figure 50b presents the calculated x-ray emission spectra arising from a *1s* core hole on each of the C and N atomic sites within the PbPc molecule. The calculation of the XES spectra has been done in the ground state approximation as this is most appropriate for these spectra[168]. The calculated XES spectra are broken down into two components corresponding to the measurement of the XES spectrum of a single molecule face-on (σ-only) or edge-on ($\sigma+\pi$), as have been described previously for SnPc.

In conjunction with the DFT calculations of PbPc, the PDOS for the C occupied an unoccupied states (Fig. 50a) show a well defined spatial orientation of in- and out-plane molecular orbitals (MO) with the LUMO, LUMO+1, LUMO+2 dominated by out of plane MO. It appears that LUMO is distributed mainly between pyrrole C and both N sites with marginal contribution of the benzene carbons. Substantial though is the contribution of the 6*p* Pb states on the LUMO+1. This calculated PDOS on the first unoccupied levels seems to be in agreement with previous DFT calculations by Zhang *et al*[139]. The HOMO and HOMO-1 appear to have a prominent out-of-plane character. The HOMO largely is sited on the C-sites in agreement with the case of Zhang *et al*[139] and Papageorgiou et al[137]. HOMO-1 is sited mainly to the benzene ring Cs and to both N (N1& N2) in agreement with Papageorgiou *et al*[137]{benzene ring Cs, N-sites and Pb-sites (6*s*, 6*p*)}, where in the case of Zhang *et al* it is sited on the N-sites and Pb 6*s* sites. In particular the angular distribution of the *2p* components of the MOs attributed to the different C sites (chemical environments) is presented in the lower panels of Figure 50a. It appears that the differing benzene-like or ring carbons contribute slightly differently to the total density of states of the occupied HOMO levels as in the case of SnPc, although they have very similar C *1s* binding energies (in the limits of the XES resolution range), as evidenced by core level XPS, as distinct from the pyrrole-like carbon site (C1). The calculated XES spectra have similar calculated transition energies from the occupied MOs to the 1*s* hole, spanning the same emission energy range as for the SnPc calculations.

When one then examines the calculated XES spectra, shown in Figure 50b, originating from these ring carbons there is a very striking effect as regards the geometrical dependence to be seen, more so than for SnPc (Fig. 46). It needs to be noted here that the PbPc is similar to the SnPc with C_{4V} molecular symmetry (non-planar Pc), but with the metal ion projecting further out of plane than is the case for the SnPc, i.e the distrortion of the phthalocyanine back bone is greater.

Shown in Figure 51 are the valence band XPS spectra of PbPc, the NEXAFS spectra of PbPc at the C and N *K* edges, the resonant XES (RXES) and non-resonant XES (NRXES) spectra at the C and N *K* edges, and also the comparison with the calculated XES spectra from the differing atomic sites, in similar fashion to SnPc, where spectra are adjusted to a common binding energy scale.

The three of them (benzene carbons) prossess a strong angular dependence at HOMO-2 levels with a strong weight at 90° in the calculated X-ray emission which coincides well with the XES emission spectra at 70° (Fig. 43), similarly to the case of SnPc. The contribution of the pyrrole C at HOMO and HOMO-1 at 90° emission seen in the calculated XES seems to be well reproduced by the NRXES C spectrum. Also the HOMO-1 level gets a slight contribution from the outer C3, which helps in the enhancement of the HOMO-1 level as it appears on the NRXES on the Fig. 49 and 51.

The deeper VB levels of the outer carbon (C4) differ substantially from the other two producing a strong angular dependence which is also observable in the XES spectra.

Following the graphs at the lower panels of Fig. 51 it is easy to see the contribution from both N-sites in the calculated emission spectra to the HOMO-1 mostly at 90° (edge-on) for inner N, where this is observable in the 70° NRXES experimental spectrum of N as an enhancement of the elbow (of the main peak) on the lower energy side.

This could possibly be due to the fact that the two different N-sites (aza-inner) transitions to their respective 1*s* core holes with different binding energies, occur at differing transition energies, hence cause a shift between them where the convolution of the two gives a broader spectrum. This shift is easily seen in Fig. 50 between the inner (N2) and aza (N1) calculated emission spectra and this is also the reason that the NRXES N *K*-edge spectrum get more spectral weight (~398 eV) at 70°, since the 90° calculated emission spectrum from the inner N also see an increase in spectral weight. There is no contribution by the HOMO from the N-sites in the calculated spectra and this is reproduced on both N *K*-edge RXES and NRXES as presented inFig. 51.

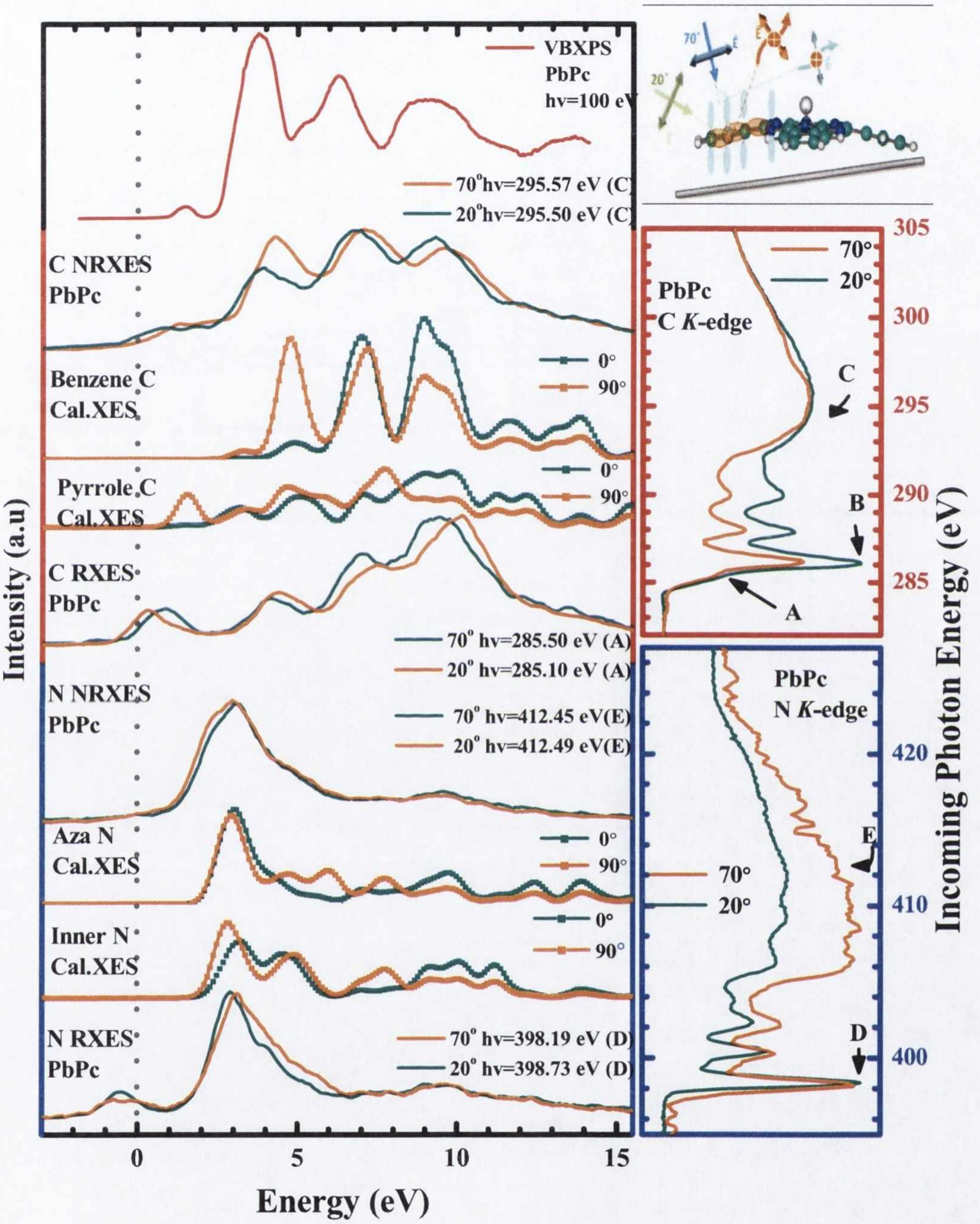

Figure 51 Right: The PbPc NEXAFS at the C (upper panel) and the N (lower panel) *K* edges respectively; the NEXAFS are measured at 20° and 70° incidence of beam to substrate. Left top: Shown at the top is a valence band XPS of a thin (20ML) film of PbPc on Ge(001). Left upper: C *K*-edge RXES and NRXES spectra are shown here in comparison to the calculated XES spectra arising from the C-C bonded or benzene like Cs and the C-N bonded or pyrrole like C. Left lower: N k-edge RXES and NRXES spectra are shown here in comparison to the calculated XES spectra arising from the inner N or aza (meso-bridging) N respectively. In each case the XES spectra are measured at the same angles in resonant and non- resonant mode as the NEXAFS.

In RXES spectra symmetry selection rules may suppress emission from the HOMO which can then be distinguished only in the non resonant emission. A detailed discussion of symmetry selection rules in the cases of RIXS/RXES is given by Ågren and Gelmukhanov[115]. In the RXES C *K*-edge spectra the HOMO, mainly situated on the pyrrole C (and partly on the benzene ring Cs), is starting to have increased spectra weight on going from the C to E spectra (as presented on the Fig. 49). This occurs as the pyrrole core hole is excited and activation of the transition element at this site.

4.1.3 Zinc phthalocyanine (ZnPc) solid film studied by XPS, RXES and NEXAFS spectroscopies.

The same experimental set up as the one used in the case of the SnPc and PbPc has been used for RXES and NEXAFS spectra measurements on ZnPc. ZnPc, unlike the previous cases, is a planar molecule with the Zn in plane with the four surrounding nitrogens and has D_{4h} symmetry. Instrumental resolutions for NEXAFS C and N *K* edges are kept at 0.11 eV, where the RXES spectra of the excited C and N *K* edges were obtained with nominal combined instrumental resolutions of 0.53 eV and 0.45 eV respectively. For the RXES spectra, a ZnPc thick film of ~200 nm thickness, as measured by quartz crystal microbalance, was deposited by sublimating from a Knudsen cell at $<1x10^{-7}$ Torr onto the native oxide of a Si (100) substrate held at room temperature. The substrate had been degassed for several hours at ~300 °C in the chamber which had a base pressure of $5x10^{-9}$ Torr. Translation of the sample by 100 μm steps every 300 ms has been used to obtain a fresh unexposed surface, avoiding beam damage. No core level XPS measurements have been taken for this phthalocyanine[3]. For the analysis purposes a VB XPS spectrum and core level XPS spectra have been taken from Zhang *et al*[171] .

The planar ZnPc is monoclinic and appears as the β-crystalline form where the an-

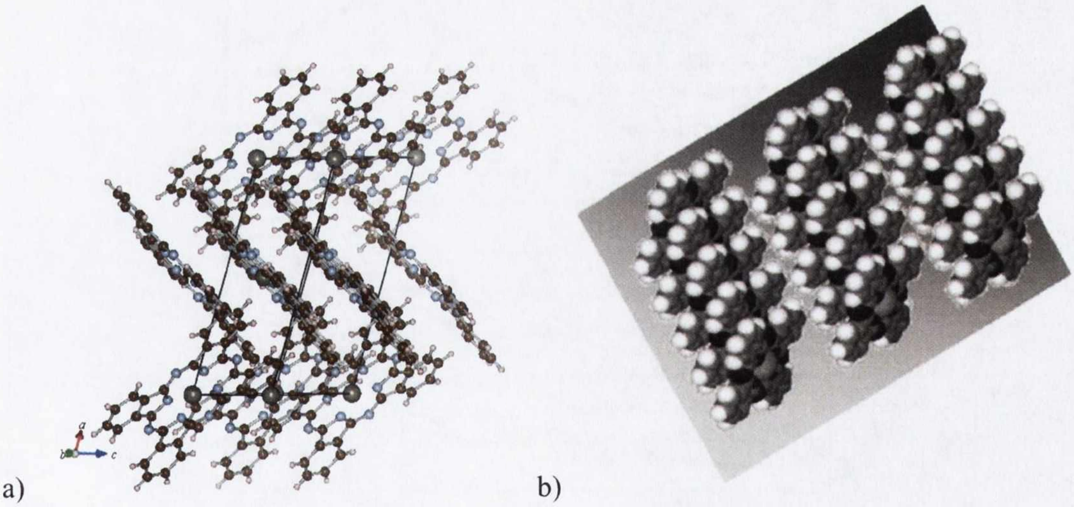

Figure 52 a) Illustration of the columnar stack across the c axis for the monoclinic crystal structure of ZnPc films after Scheidet al[172] with the herringbone arrangement of the following stacks. b) A three dimensional filled body model of ZnPc monolayer on HOPG by Naitoh et al[164]: molecules stand up relative to substrate.

---

[3] At the time of measurement, the end station used at X1B was different, without the Scienta SES100.

gle between the neighbouring stacks is almost orthogonal creating a herringbone arrangement[172] (Fig. 52a). STM images on HOPG show that the molecule stands up on non-interacting substate at 1 ML coverage, and a β crystalline form develops after a few layers [164] (Fig 52b).

The electronic structure of thin layers of ZnPc deposited on Si and ZnS substrates has previously been studied byvalence band photoemission spectroscopy (VBXPS), photoemission spectroscopy (XPS) and near edge X-ray absorption fine structure (NEXAFS)[171,173]. NEXAFS of these films show that the molecular planes are inclined at a big angle to the substrate on non-interacting substrates (SiO_2[163], HOPG[164]).

In Fig. 53 NEXAFS spectra of ZnPc films on Si and its native oxide, measured at

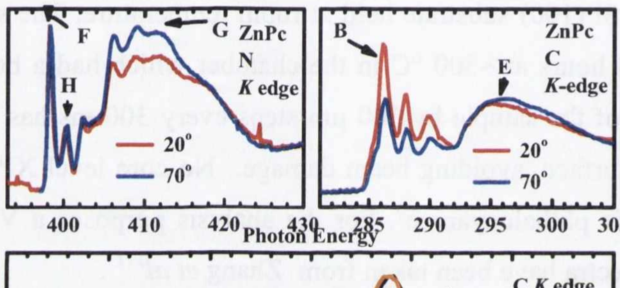

Figure 53 Top panels: ZnPc NEXAFS at N (left) and C (right) *K* edges respectively; at 20° and 70° incidence of beam to substrate. Bottom panels: C *K* and N *K* SXE spectra at the same angles at various resonant excitation energies and non- resonant mode. In the C *K*-edge spectra near resonance, the elastically scattered peak is truncated.

20° and 70° angles of incidence at both the C and N *K*-edges, show an angular dependence that supports an inclined angle to substrate and the herringbone arrangement of the β – polymorph where the almost orthogonal neighbour columns do not allow for a significant angular variation to be measured from the spectra of a thick film. XES spectra at the same angles at either the C or N *K*-edge have been recorded with different excitation energies, both resonant and non resonant. The angular dependence of the observed XES spectra, progresses in almost the opposite fashion from that observed in both SnPc and PbPc.

This time the grazing incidence (20°) spectrum is the one that shows greater spectral weight at ~282 eV as well as increased weight at ~284 eV. The emission geometry this time for ZnPc is different due to the inclined angle between neighbouring columns of the β - polymorph crystal structure, and as a result for any given angle to the substrate, emission occurs (see Fig. 55 right top panel) from both occupied in-plane (σ-like) and out of plane π orbitals. It would appear that the grazing angles of incidence to the substrate result in slightly more emission from the out of molecular plane π orbitals. The HOMO levels appear suppressed in the resonant spectra (B), similarly to SnPc, perhaps due to selection rules. Similarly, the N *K*-edge XES spectra show increased spectral weight on the non-resonant spectra (G) at ~397 eV corresponding to the HOMO-1 levels.

In a similar fashion with the previous phthalocyanines, DFT calculations of both the C *2p* and N *2p* PDOS and calculated XES spectra based on the StoBe package are going to be presented here in order to fully understand and explain the observed experimental spectra.

Figure 54a depicts the total occupied and unoccupied density of states of ZnPc. Together with the total DOS we present the *2p* partial density of states (PDOS) on each of the N and C atomic sites within the molecule, where we have resolved the orbital components perpendicular to the molecular plane (π states along *z*-axis) and those within the molecular plane (σ states within the *x*-*y* plane).

Figure 54b presents the calculated x-ray emission spectra arising from a *1s* core hole on each of the C and N atomic sites within the ZnPc molecule. The calculation of the XES spectra has been done in the ground state approximation as this is most appropriate for these spectra[168]. The calculated XES spectra are broken down into two components corresponding to the measurement of the XES spectrum of a single molecule face-on (σ emis-

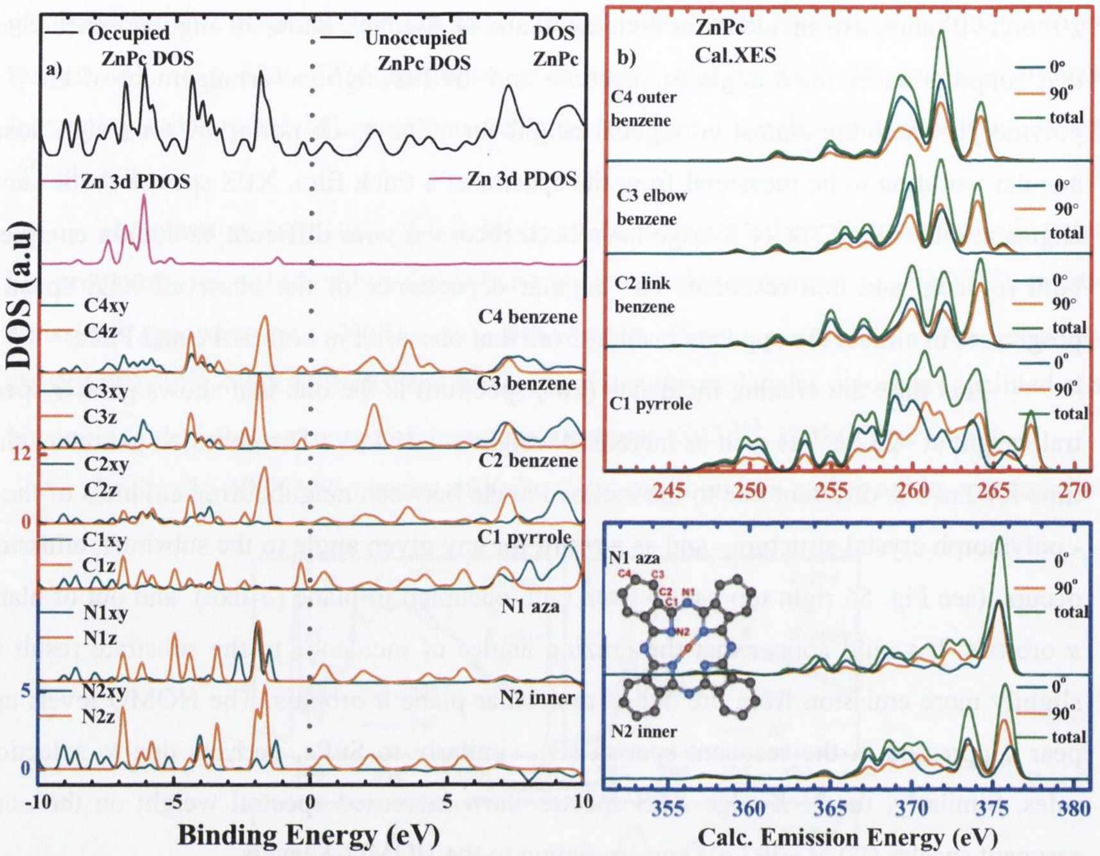

Figure 54 Left panel (a): At the top the total occupied and unoccupied DOS of ZnPc. Subsequent panels: Second from the top is the contribution of Zn 3d states on the occupied and unoccupied PDOS. Each subsequent panel shows the *2p* PDOS of the atomic sites where we progress from the outermost carbon site (C4) to the innermost (pyrrole) carbon site (C1) and the two nitrogen sites, the meso-bridging or aza nitrogen (N1) and the inner nitrogen (N2). Each PDOS as presented is broken into the *2p* projection (p_z) perpendicular to the molecular plane (*xy* plane) defined by the four inner Ns and the sum of the projections (p_x+p_y) within that plane. The zero in energy is chosen to be exactly between the □□□□□Ĝ□µ□□□□□MO. Right panel (b): Shown for each C and N atomic site in ZnPc are the XES spectra derived from the *2p* PDOS for two differing measurement geometries, measuring the emission from a ZnPc molecule face-on or edge-on. The energy scale is the calculated transition energy. Inset: Sketch illustrating the various atomic C and N sites for a single ZnPc molecule.

sion) or edge-on (σ+π emission), as have been described previously on SnPc. The total calculated XES spectra also presented here is the sum of the two different emission components and might prove more useful in the case of ZnPc since the emission in any measured angle combine both in plane and out of plane states, much more so than for the previous instances.

It appears that the main characteristic of the calculated DOS is similar to the previous phthalocyanines, describing a delocalised distribution of charge across the macromolecule. The ZnPc PDOS for the C occupied and unoccupied states (Fig. 54a) shows a well defined spatial orientation, in and out of plane molecular orbitals (MO) with the LUMO, LUMO+1, LUMO+2 dominated by out of plane MO. It appears that LUMO is distributed mainly between pyrrole C and both N sites with small contribution from benzene ring carbons. The HOMO appears to have a prominent out of plane character largely being sited on the pyrrole (C1) and with less contribution from outer benzenes (C3, C4) C-sites. The HOMO-1 appears to gain significant contribution from inner N (N2) sites with in plane 2*p* MO and also from the Zn 3d states which is in good agreement with previous DFT calculations by Liao et al[92]. The Zn 3d states have a substantial contribution also to the deeper VB levels on the 5.5-8 eV range.

It should be remarked that the planar phthalocyanine ZnPc shows in the calculations substantially narrower features for both σ and π states, than the distorted non-planar SnPc and PbPc shown previously, particularly for the higher HOMO levels. This may in part be due to a mixing of the px, py and pz bases, which may no longer be locally orthogonal to the bond directions in the isoindoline arms, bent as they are from the center of the macromolecule.

As a result of the planar structure of the ZnPc molecule, crystal structures no longer favour the stacking of the molecules side by side, where molecules in the neighbouring stacks are nearly parallel. Instead we have an orthogonal herringbone stacking arrangement.

Shown in Figure 55 are the valence band XPS spectra of ZnPc, the NEXAFS spectra of ZnPc at the C and N *K* edges, the resonant XES (RXES) and non-resonant XES (NRXES) spectra at the C and N *K* edges, and also the comparison with the calculated XES spectra from the differing atomic sites. For presentation purposes the three benzene carbon sites calculated XES have been summed. The energy scale is presented relative to the Fermi edge, on a common binding energy scale, in similar fashion to SnPc. Experimental binding energies for each atomic site have been taken from Zhang *et al*[171] where benzene ring sets at C: 285.07 eV, pyrrole C: 286.43 eV and nitrogen N: 398.6 eV.

Benzene carbons produce a strong angular dependence at HOMO-2 levels with a strong spectral weight at 90° (edge-on) from the X-ray emission calculated in similar way to the previous phthalocyanines, due to an out-of-plane *π* MO. Here due to different molecular stacking, (see right top panel Fig. 55) this *π* MO can be probed for both emission angles of the NRXES spectra with slightly more weight on the NRXES emission spectra at 20° (Fig. 55).

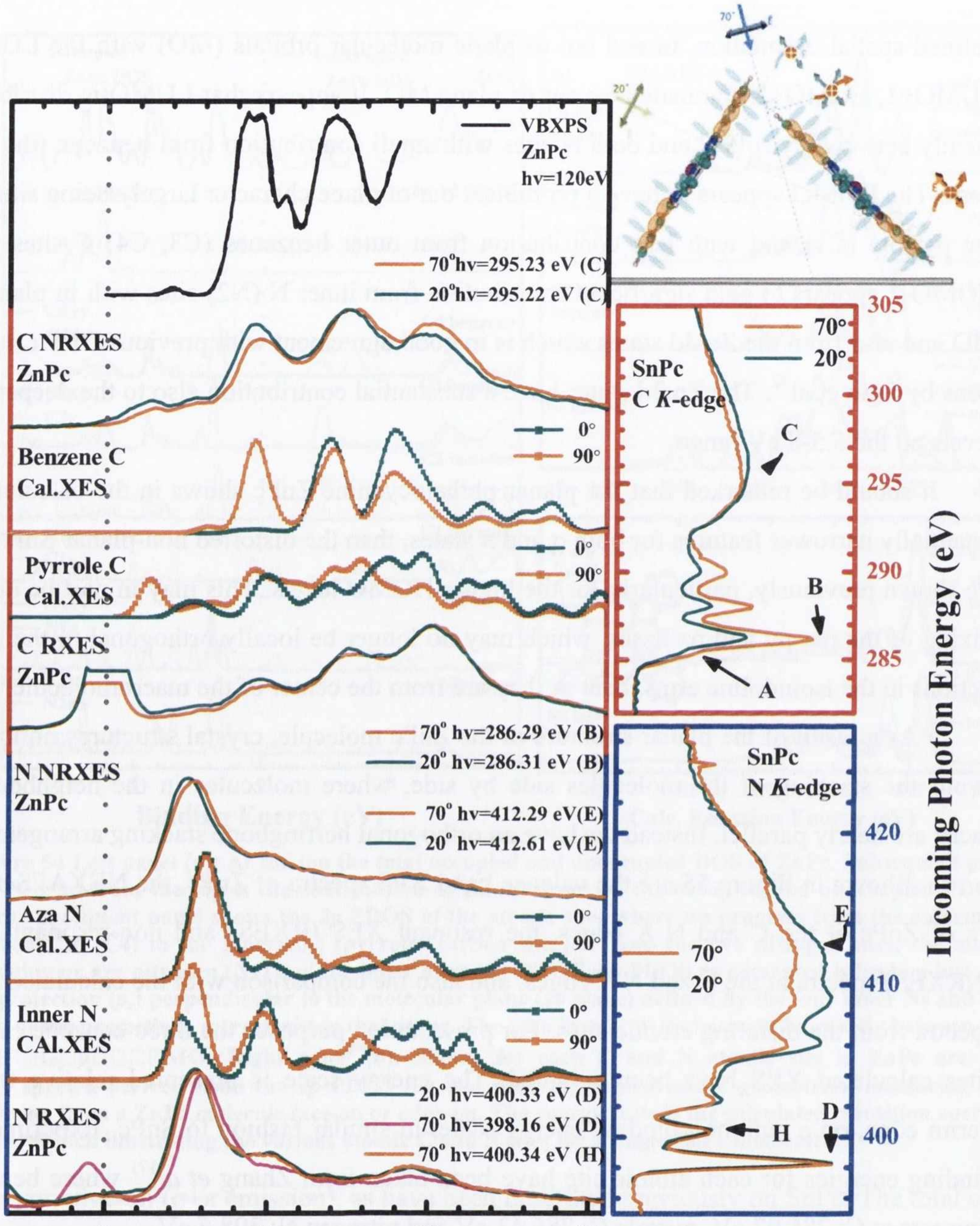

Figure 55 Right: The ZnPc NEXAFS at the C (upper panel) and the N (lower panel) *K* edges respectively; the NEXAFS are measured at 20° and 70° incidence of beam to substrate. Left top: Shown at the top is a valence band XPS of a thin (23 ML) film of ZnPc on ZnS[171]. Left upper: C *K*-edge RXES and NRXES spectra are shown here in comparison to the calculated XES spectra arising from the C-C bonded or benzene like Cs and the C-N bonded or pyrrole like C. Left lower: N *K*-edge RXES and NRXES spectra are shown here in comparison to the calculated XES spectra arising from the inner N or aza (meso-bridging) N respectively. In each case the XES spectra are measured at the same angles in resonant and non-resonant mode as the NEXAFS. Top right panel: Sketch illustrating angular dependence of RXES arising from the various C and N sites for ZnPc herringbone crystal structure.

The elbow (C3) benzene carbon has a small contribution at 90° (edge-on) to the HOMO-1 level, which helps enhance the emission from the HOMO-1 level, as it appears in the NRXES in the Fig. 53 and 55.

The deeper VB levels of the outer carbons differ substantially from the other two, as they exhibit a strong angular dependence which is also observable on the XES spectra. The pyrrole carbons PDOS contribute to both at HOMO and HOMO-1 levels, with the π-like HOMO mainly contributing to the 90° (edge-on) emission spectrum.

The N PDOS (DFT calculations) follows a similar behaviour with LUMO, LUMO+1 and LUMO+2 having mainly out of plane π^* orbital distribution from both inner N and the aza N. There is no N contribution at the HOMO level. HOMO-1 gets contributions from the inner N (N2), where it contributes to in-plane σ orbitals. There is a shift for the inner N calculated X-ray emission (Fig. 55) and projected PDOS (Fig. 54a) of the HOMO-1 between the two extreme emission angles (0° and 90° face and edge-on), normal to the plane of the molecule and perpendicular to the plane, which is reproduced quite well in the NRXES N *K*-edge spectra at the experimental extreme angles of 20° and 70°. The N *K*-edge RXES spectra (D) (Fig. 55) seems to coincide more with the aza calculated XES spectrum, possibly indicating a preferential filling of the aza core hole. This core hole should be at a smaller binding energy than the inner N.

RXES spectra and above threshold XES spectra can be considered as one-step or two-step processes respectively with a relaxation of selection rules for the latter[115,169]. In both C and N RXES spectra it seems that symmetry selection suppresses the HOMO and HOMO-1 which is distinctive only in the non resonant emission. It needs to be noted here that the high symmetry point group D_{4h} for the planar ZnPc gives symmetry distict states α_{1u} and $2e_g$ for HOMO and LUMO, respectively according to Liao et al[92]. The transitions to (or from) these states dictated by the dipole selection rules. This simply means that transition of a core hole to the unfilled LUMO MO that has *g* (gerade) symmetry can occur only from an *u* (ungerade) symmetry core hole and thus filling of the core hole can occur only from occupied MOs of *g* symmetry. This in the case of ZnPc means that in the resonant excitation to the LUMO ($2e_g$) the optical transition from the HOMO state (α_{1u}) to the core hole is forbitten and the HOMO signal appears suppressed in the spectra.

4.1.4 Zinc hexadecafluorophthalocyanine ($F_{16}ZnPc$) solid film studied by XPS, RXES and NEXAFS spectroscopies.

The same experimental set up as the one used in the case of the previous phthalocyanines has been used for RXES and NEXAFS spectra measurements on $F_{16}ZnPc$. Instrumental resolutions for NEXAFS C and N *K* edges kept on 0.11 eV, where in the RXES spectra of the excited C and N *K* edges were obtained with nominal instrumental resolutions of 0.7-2 eV and 0.9-1.8 eV respectively. We also obtained valence band x-ray photoemission spectrum taken from the same sample using the Scienta SES100 hemispherical electron analyzer of the end station at X1B with an estimated total instrumental resolution of 0.3 eV, and C 1s, N 1s core levels XPS spectra with total instrumental resolution of 0.3 eV and 0.5 eV, respectively. A $F_{16}ZnPc$ thick film of ~200 nm thickness measured by quartz crystal microbalance, was deposited by sublimating from a Knudsen cell at $<8\times10^{-8}$ Torr onto a Ge (001) substrate held at ~100 °C. This was previously obsered to improve the crystallinity of the film[174]. The substrate had been sputtered with argon and annealed at 550 °C for approximately 1/2 hour and afterwards cooled down slowly to retrieve 2x1 reconstruction at base pressure of 3×10^{-9} Torr. LEED pattern shows that the surface reconstruction wasn't fully successful. As XES measurements require long accumulation times, sample exposure was limited to avoid beam damage by vertically translating the sample every 300 ms to obtain a fresh unexposed surface. This time XES measurements have been taken with only one incidence angle (45°) of the beam, and hence polarisation, to substrate.

To the best of our knowledge there is no known crystal structure published for the $F_{16}ZnPc$. Bao et al[175] based on XRD measurements, proposed an α-form with lattice planes similar to that of the α-CuPc but in an expanded unit cell for the $F_{16}CuPc$. They also concluded that the $F_{16}CuPc$ molecules are standing, and are essentially perpendicular to the SiO_2 surface where they had been deposited. Schlettwein *et al*[174] seems to support this stacking arrangement (standing molecules to substrate) for $F_{16}ZnPc$ thick films grown on a glass substrate, based on conductivity measurements. He also proposed a model of lattice parameters and crystal structure based on preliminary XRD measurements. This has been combined with molecular dynamics geometry optimisation and a molecular arrangement that best explained the optical absorption spectra (band splitting) that were obtained due to dipole transition moments arising from intermolecular interaction. According to this, an in-plane rather than a dense packing square lattice, is formed with an intermolecular distance of 1.32 nm (Fig. 56a). The molecules in the next layer are shifted by half a lattice constant in the two directions of the square lattice. Such an arrangement would lead to a position of the central metal of the adjacent layer right on top of the free space in the centre of the square as is often observed in crystalline Pc thin films, which have axial ligands[176] (Fig. 56b).

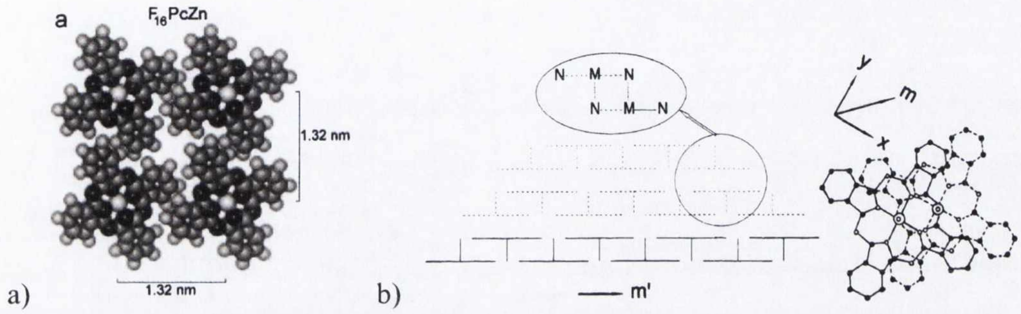

Figure 56 a) Space-filling model of F_{16}PcZn as concluded from XRD and UV-vis analysis by Schlettwein et al[174] b) Left: A cross sectional view of the stacking of Pcs in the first *6* equivalent monolayers of an epitaxial deposit and a close-up view of the stacking of two back-to-back Pcs in adjacent bilayers. Right: A top view of the close-up of the stacking of two back-to-back Pcs in adjacent bilayers. Sketch referring to ClGaPc and ClAlPc stacking as presented by Chau et al[176], which is believed to be similar for F_{16}ZnPc as outlined in the text.

An investigation by Kawabe et al[177] based on NEXAFS and ARUPS measurements of F_{16}ZnPc monolayer on GeS (001) shows that molecules take nearly flat-lying but slightly tilted orientation which is estimated as 12±2.5° to substrate.

Further, the molecular orientations of F_{16}ZnPc vacuum-deposited films (~10 ML) on Au and Mg substrates studied by Ikame et al[178] using NEXAFS spectroscopy, show that the molecular planes of F_{16}ZnPc deposited on Au and Mg substrates were found to be nearly parallel (~35°) and vertical (~80°) to the substrate surface, respectively. In the same work thicker films on both substrates appeared to lose the perfect orientation and an inclined molecular angle of 55° to substrate has been estimated.

In Fig. 57 NEXAFS spectra of F_{16}ZnPc films on Ge, measured at 45° angle of incidence at both the C and N *K*-edges, show a similar angular dependence to that presented by Ikame et al[178] for thicker films (estimates an incline angle of 55°) where the preferential orientation of the thin films is lost. XES spectra at the same incidence angle of the beam at either the C or N *K*-edge have been recorded with different excitation energies from

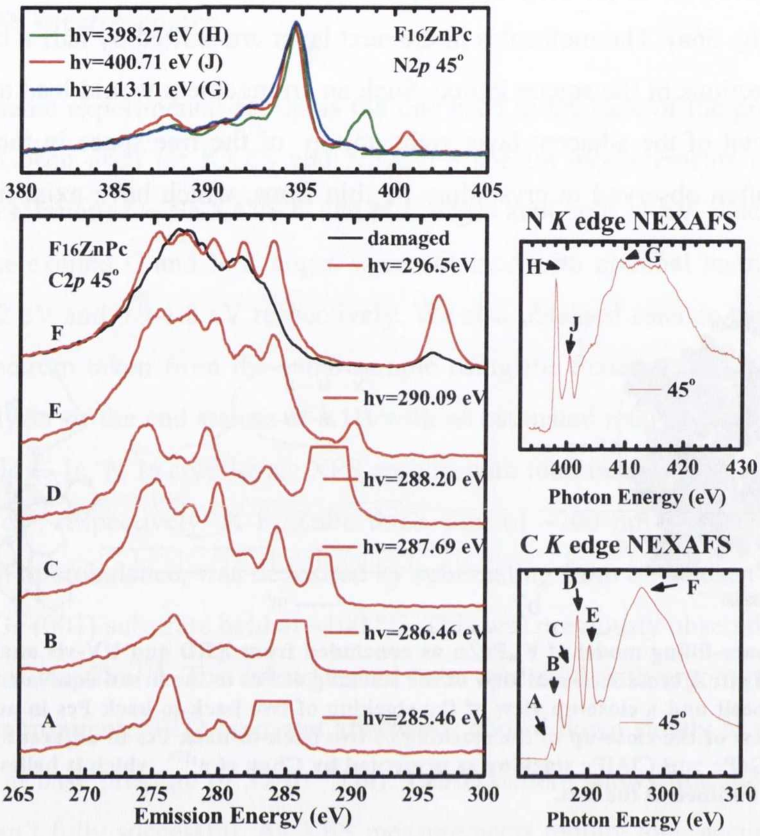

Figure 57 Right side panels: F_{16}ZnPc NEXAFS at N (top) and C (bottom) *K* edges respectively; at 45° incidence of beam to substrate. Left side panels: C *K* and N *K* XES spectra at the same angles in various resonant excitation energies and non- resonant mode.

threshold upwards, going from resonant mode as depicted from NEXAFS spectra to non resonant excitation.

The substitution of hydrogen by fluorine on the benzene ring carbon atoms has, as a result, altered substantially the C 1*s* core-level XPS as presented in Fig. 58a. The highly electronegative fluorine upon the formation of the C-F bond, works to withdraw electronic charge from the macromolecule. As a result, a decrease in screening is responsible for all the core levels being shifted to higher binding energies, with the most substantial shift for the fluorine substituted benzene carbons (~1.8 eV), to the less extent at pyrrole carbons (~0.5 eV) and nitrogens (~0.4 eV) compare to ones for the un-substituted ZnPc[171].

This alteration in the span of binding energies for the C 1s could be one of the reasons for the dramatic difference observed between F_{16}ZnPc and ZnPc XES spectra, resulting in a broadening of the XES spectrum, due to a larger range of valence band to C 1*s*

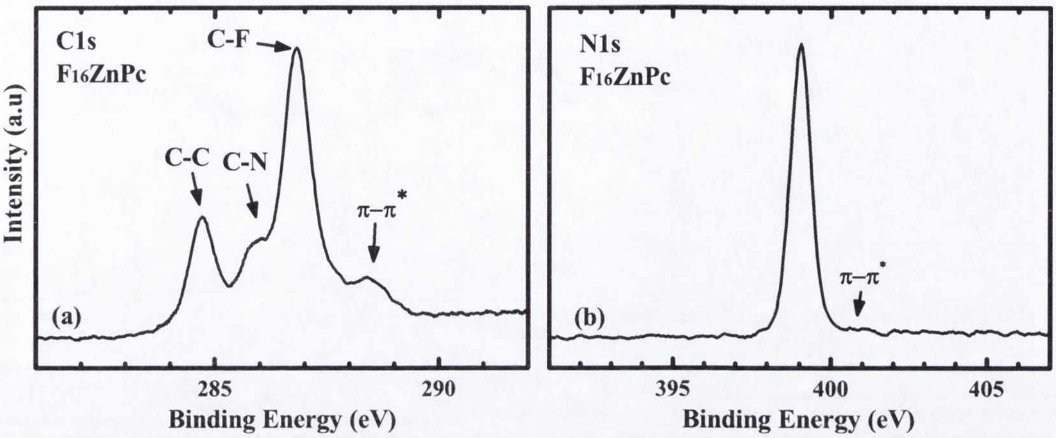

Figure 58 a) C1s core level spectrum of F16ZnPc at RT, where the different chemical environments labelled as C-C the link carbons (C2), C-N the pyrrole carbons (C1) and C-F the fluorinated benzene carbons (C3, C4). The shake up features are denoted as π-π^*. b) N1s core level of F16ZnPc with the accompanied π-π^* resonances.

core-level transitions possible. Additional sharp features are clearly observed in $F_{16}ZnPc$ which are absent for ZnPc.

Further information can be gleaned with resonant x-ray emission spectroscopy (RXES). There is a stark difference between the two first resonant spectra relative (A and B) to threshold, where only the C-C (C2) and C-N (C1) core holes maybe created, respectively, to spectra C and D where the C-F (C3 and C4) core holes are created and participate in the de-excitation, due to the transition matrix element of their C1s core holes with the VB DOS.

In the case of the N XES spectra there is a no shift of the main peak between the resonant (H) and non-resonant XES (G) spectra (Fig. 57 & Fig. 60) although there is difference in the binding energy between the inner (N2) and aza (N1) nitrogen (~0.35 eV) as estimated from the DFT calculation that follows. Also, for the resonant spectrum (H) the elastic peak appears broad and with a highly asymmetric shape. It is speculated that this asymmetry might be caused from losses by intra-molecular excitonic transitions due to atomic vibrations as described in the case of ethylene and benzene by Hennies et al[179,180].

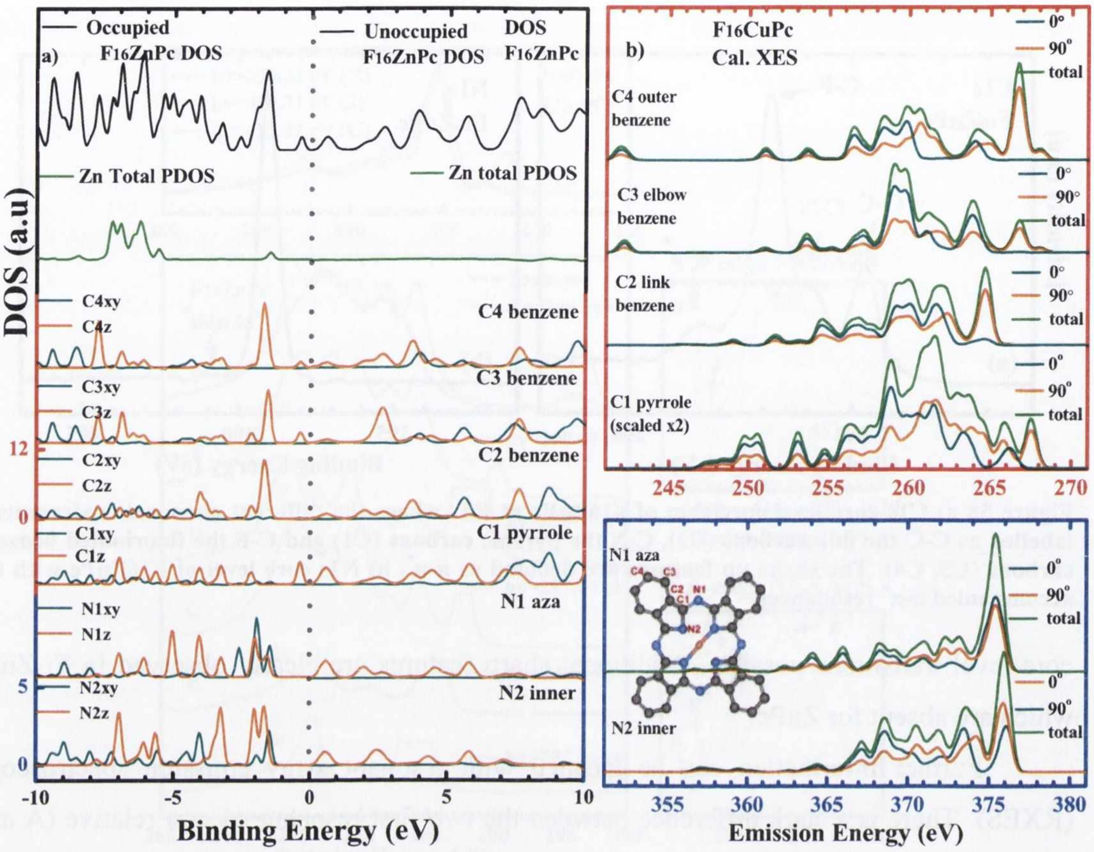

Figure 59 Left panel (a): At the top the total occupied and unoccupied DOS of F_{16}ZnPc. Subsequent panels: Second from the top is the contribution of Zn 3d states on the occupied and unoccupied PDOS. Each subsequent panel shows the *2p* PDOS of the atomic sites where we progress from the outermost carbon site (C4) to the innermost (pyrrole) carbon site (C1) and the two nitrogen sites, the meso-bridging or aza nitrogen (N1) and the inner nitrogen (N2). Each PDOS as presented is broken into the *2p* projection (p_z) perpendicular to the molecular plane (*xy* plane) defined by the four inner Ns and the sum of the projections (p_x+p_y) within that plane. The zero in energy is chosen to be exactly between the HOMO and LUMO. Right panel (b): Shown for each C and N atomic site in F_{16}ZnPc are the calculated XES spectra derived from the *2p* PDOS for two differing measurement geometries, measuring the emission from a F_{16}ZnPc molecule face-on or edge-on. The total emission from each atomic site is presented in green colour. The energy scale is the calculated transition energy. Inset: Sketch illustrating the various atomic C and N sites for a single F_{16}ZnPc molecule.

In a similar fashion with the previous phthalocyanines, DFT calculations of both the C *2p* and N *2p* PDOS and calculated XES spectra based on the StoBe package are presented here in Fig. 59.

Figure 59a depicts the total occupied and unoccupied density of states of F_{16}ZnPc. Together with the total DOS we present the *2p* partial density of states (PDOS) on each of the N and C atomic sites within the molecule, where we have resolved the PDOS into the orbital components perpendicular to the molecular plane (π-states) and those within the molecular plane (σ-states).

Figure 59b presents the calculated x-ray emission spectra arising from a *1s* core hole on each of the C and N atomic sites within the F_{16}ZnPc molecule. The calculated XES spectra are broken down into two components corresponding to the measurement of the XES spectrum of a single molecule face-on (σ-states) or edge-on (σ+π states), as has been described previously for SnPc. The total calculated XES spectra is also presented here which is the sum of the two different emission components and is more useful, as in the case of ZnPc, due to the 45° incident angle of the beam on the substrate and the 90° scattering geometry of the emission. As a result the measured spectra are a combination of emission from both in plane and out of plane states.

There is a delocalised distribution of charge across the macromolecule here too. It appears that LUMO is distributed across all the C and N sites, similarly to the case of ZnPc (see Fig. 54a). The LUMO+1 appears distributed between the outer benzene carbon (C4), the benzene carbon (C2) and the aza N (N1), whereas in ZnPc it is located at both N sites, pyrrole carbon (C1) and benzene carbon (C2). The HOMO appears to have a prominent out of plane π character as expected, largely being sited on the pyrrole (C1) site and with a lesser contribution from the outer benzene C-sites (C3, C4), similarly to ZnPc. The HOMO-1 appears to have a significant contribution from both N sites with in plane *2p* σ MO, whereas in ZnPc only the inner N (N2) appears to contribute, and also from the Zn states as in ZnPc. The Zn states have substantial contribution to the deeper VB levels on the 6-8 eV range.

Shown in Figure 60 are the valence band XPS spectra of F_{16}ZnPc, the NEXAFS spectra of F_{16}ZnPc at the C and N *K* edges, the resonant XES (RXES) and non-resonant XES (NRXES) spectra at the C and N *K* edges, and also the comparison with the calculated XES spectra from the differing atomic sites. For our presentation purposes the total emission (summation of both emission angles) calculated for each site has been used. The energy scale is presented relative to the Fermi edge, on a common binding energy scale as before.

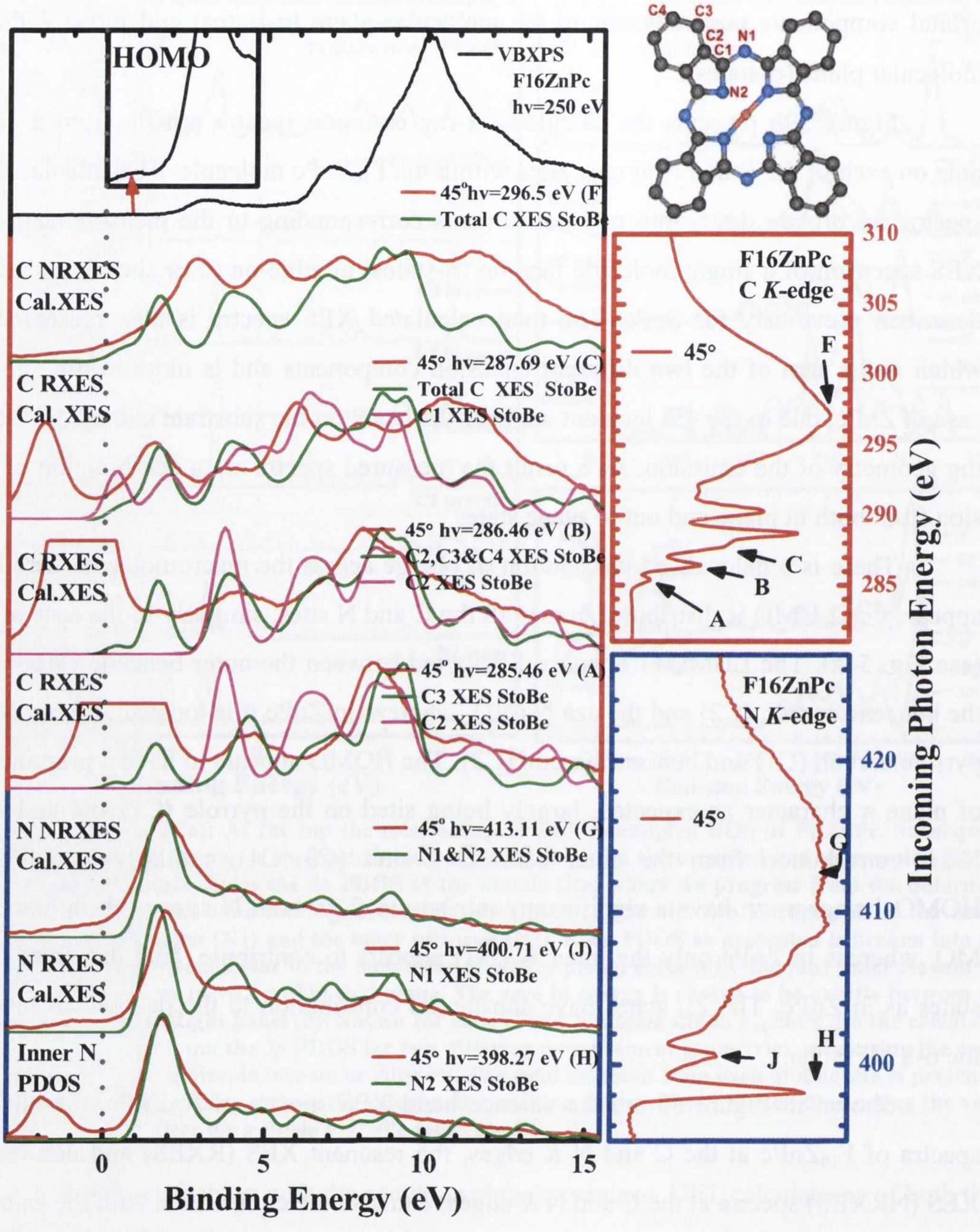

Figure 60 Right: The F$_{16}$ZnPc NEXAFS at the C (upper panel) and the N (lower panel) *K* edges respectively; the NEXAFS are measured at 45° incidence of beam to substrate. Left top: Shown at the top is a valence band XPS of F$_{16}$ZnPc thick (~200 nm) film on Ge (001). Left upper: C *K*-edge RXES and NRXES spectra are shown here in comparison to the calculated XES spectra arising from the C-C bonded or benzene like Cs and the C-N bonded or pyrrole like C. Left lower: N *K*-edge RXES and NRXES spectra are shown here in comparison to the calculated XES spectra arising from the inner N or aza (meso-bridging) N respectively. In each case the XES spectra are measured at the same angle in r><RecNum>70</RecNum><MDL><REFERENCE_TYPE>0</REFTop right panel: Sketch cyanine macromolecule labelled with each different chemical atomic site under investigation.

At the resonant XES spectrum A in Figure 60, the excited core electron in the LUMO and the excited energy is enough to create core holes only on the link benzene carbons (C2) as can be concluded from the XPS spectra (Fig. 58). Fitting of the XPS spectra results binding energy for the link benzene C 1s (C-C or C2): 284.71 eV, pyrrole C 1s (C-N or C1): 285.87 eV, benzene outer and elbow C 1s (C-F or C4 and C3): 286.82 eV and N 1s: 399.05 eV. Comparing the fingerprint of this spectrum A with the various site-specific calculated XES spectra, the best match is with the spectrum from the elbow benzene carbon (C3). It should be expected that the link benzene carbon (C2) calculated emission spectrum would be the most suitable choice however.

It is speculated that the transition matrix element for refilling this core hole includes a contribution of VB electrons from both neighbour carbons (C2-C3). This transition although forbidden seems to get weight through an unknown mechanism, but with a possible candidate a vibronic coupling of the neighbour atoms. It needs to be noted that the HOMO-1 is greatly despersed along all the benzene Cs (C2-C3-C4). Similarly, on the second resonant spectra B where the excitation energy is enough to create pyrrole carbon (C1) core holes and the LUMO+1 still delocalised mainly between the C4-C2 benzene carbons, the summation of the benzene ring carbons (C2-C3-C4) calculated XES spectrum gave the best match with the contribution of the link carbon (C2) revealed.

In the resonant XES spectra C the picture change dramatically. This time the excitation energy is enough to create the fluorinated benzene carbons (C3, C4) core holes and the LUMO+2 is still delocalised on all the carbon sites. The broad span of the core binding energies and the multiplicity of transitions to the different core holes, causing relaxation of selection rules and all the possible transitions are revealed. This spectrum looks similar to the non-resonant (F). The spectrum resembles the total calculated carbon emission spectrum.

In the case of N the resonant XES spectrum (H) to the LUMO is in good agreement with the calculated XES spectrum for the inner nitrogen (N2). The binding energy of the inner nitrogen found to be ~0.35 eV smaller that the inner nitrogen from the DFT calculation and thus for this resonant excitation it is believed that the energy is sufficient to create only a core hole on this site. The next resonant XES spectra (J) to the LUMO+1 has excitation energy to create core holes on both sites but the LUMO+1 is mainly distributed only to the aza (N1) nitrogens (Fig. 59a). Thus it should be the case that this emission spectrum gets more weight due to aza (N1) core holes although a smaller contribution from the inner (N2) should be expected as well. The broadening of the main peak, on or near the Fermi level of the experimental spectrum, could be explained from the difference in the binding energy of the N-sites (see Fig. 59b) and thus the higher transition energy for emission from the HOMO to the inner (N2) 1s core hole. The non-resonant N XES spectrum (G) is in good agreement with the sum of the calculated XES spectra from both N sites.

Finally the HOMO is reproduced quite well by the calculated XES spectrum following the same distribution as the DFT PDOS shown in Fig. 59a and the VB spectrum presented at the Fig. 60.

4.2 Summary

In summary we have measured the electronic structure of planar and non-planar closed shell metal phthalocyanines ZnPc, SnPc and PbPc, as well the fluorinated counterpart of ZnPc, F_{16}ZnPc.

The non-planar SnPc and PbPc thick films have a molecular arrangement with a shallow inclination to the substrate compared to the planar ZnPc as concluded from NEXAFS spectra taken with a highly polarised light source.

Calculated PDOS and calculated XES show that the HOMO level of the non-planar phthalocyanines (SnPc and PbPc) is located across all the phthalocyanine ligand (C, N atoms) whereas in the case of the planar phthalocyanines (ZnPc, F_{16}ZnPc), it is still on the phthalocyanine ligand but is located mostly on the C atoms. This is in good agreement and has been confirmed from the XES experimental spectra. Also the calculated PDOS shows that the LUMO is dispersed across all of the macromolecule in the phthalocynines under examination.

It should be remarked that the planar phthalocyanine ZnPc shows in the calculations substantially narrower features for both σ and π-states than the distorted non-planar SnPc and PbPc shown previously, particularly for the higher HOMO levels. This may in part be due to a mixing of the px, py and pz bases which are no longer be locally orthogonal to the bond directions in the isoindoline arms, bent as they are from the centre of the macromolecule.

Angular resolved XES spectra are in relatively good agreement with calculated XES at face-on (0°) and edge-on (90°) single molecule emission. This is the first time that experimentally a spatial distribution of PDOS states of these systems has been revealed. Thus the SnPc, PbPc and ZnPc have π-states (out-of-plane of the molecule) on HOMO levels with a strong angular dependence of the HOMO-2 in particular.

Selection rules seem to be dominant in the resonant emission spectra and seem to affect the optical transitions such that the signal of the HOMO level gets suppressed in the resonant spectra. This appears to be the case on the ZnPc and F_{16}ZnPc where inversion symmetry is present in the molecule.

ZnPc and F_{16}ZnPc appear to have very similar NEXAFS and XES on the N K-edge but the picture is different for the C K-edge where the highly electronegative fluorine appears to withdraw substantial charge from the C atoms, affecting all the XPS, NEXAFS and XES spectra as a result of changed binding energies.

5. Electronic and Optical Properties of Magnesium Phthalocyanine (MgPc) Solid Films Studied by Soft X-Ray Excited Optical Luminescence (XEOL) and X-Ray Absorption Spectroscopies (XAS).

In addition to the two principal themes investigating beam damage and electronic structure in phthalocyanine organic molecular semiconductors, a relatively new synchrotron based spectroscopy, x-ray excited optical luminescence (XEOL), is applied here to the organic semiconductor MgPc. This is an attempt to focus on trying to locate chromophore sites across the macromolecule, which are critical for OLED optical transitions.

The electronic and optical properties of MgPc were investigated using XEOL and XAS measurements at the MPW6.1 Phoenix beamline station at the Daresbury Synchrotron Radiation Source (UK). MPW6.1 ("PHOENIX") is based on a multi-pole wiggler insertion device, providing about 10 times the flux output, as compared with traditional bending magnets at Daresbury. The energy range covered is from 40-400 eV (nominally), but there is significant flux available to 500 eV. This is achieved at good resolution across the whole energy range. Typical applications are photo-electron analysis, optical absorption and fluorescence emission detection. More details of beamline MPW6.1 can be obtained in the literature[181].

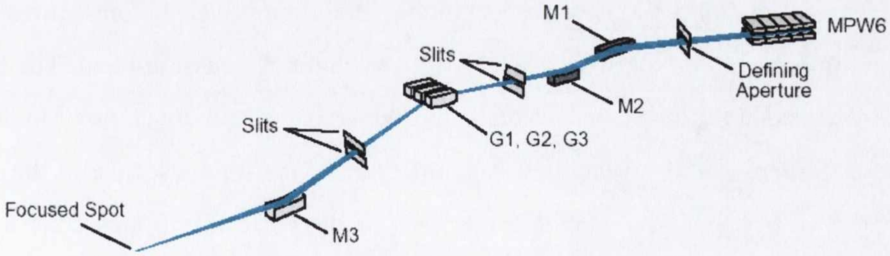

Figure 61 The MPW6.1 Phoenix beamline station layout is shown below in a schematic representation[182].

For the purpose of this investigation the MoLES apparatus[183] and the ARUPS10 UHV end station have been used. This allowed the in-situ study of epitaxial thick films (~900 nm) of MgPc grown on clean GaAs(001) in a growth chamber attached to the ARUPS10 end station which had a base pressure of ~1×10^{-8} mbar. It should be noted that all x-ray absorption, optical and photoelectron spectroscopy measurements were obtained in situ in vacuum in the ARUPS10 endstation, where the base pressure was ~9×10^{-10} mbar, after sample transfer from the growth chamber.

The GaAs(001) surface, with substrate dimensions of 7×7 mm, was prepared by sputtering and annealing and checked for contamination by photoemission and LEED until a clean well-prepared surface was available[184]. The Knudsen cell used to evaporate the MgPc was thoroughly outgassed for several hours prior to deposition at a temperature just below the deposition temperature of ~360 °C, during which the pressure in the growth chamber was ~1×10^{-7} mbar. The rate of deposition was monitored before, during and after by a quartz crystal thickness monitor where after the initial 5 monolayers were created a deposition rate of ~2 nm/min was used to create a film with a thickness of ~900 nm. Subsequently ex-situ measurements of the thickness by spectroscopic ellipsometry were carried out confirming a thickness of ~906±62 nm. The first and later stages of growth were confirmed by comparison of valence band photoemission of MgPc and x-ray absorption spectra.

X-ray absorption near-edge structure (XANES) spectra at the C and N *K* edges of MgPc presented here were recorded in total electron yield (TEY) and by photoluminescence yield (PLY), with estimated monochromator resolutions of 0.17 eV at 280 eV and 0.24 eV at 400 eV. The TEY was recorded by the drain current method, while PLY was obtained in a total optical yield (zero order) mode, integrating over the optical response of the photomultipliers and then also at a selected wavelength or emission band. The luminescence was recorded at 90° to the incoming x-rays which had a grazing angle of incidence to the substrate surface of ~30° to facilitate the collection of the luminescence of the films by the attached MoLES apparatus. Apart from some of the collecting optics consisting of a lens within the UHV chamber, this was situated outside the vacuum but attached to the chamber.

For the OD-XAS and XEOL measurements Hamamatsu R2949 and R758P photomultiplier tubes have been used with optical ranges of 185-900 nm and 160-930 nm respectively. Optical emission spectra were recorded using the low and medium energy gratings of a Jobin-Yvon optical spectrograph that is installed on MoLES with a nominal optical resolution ~6 nm and a spectral range spanning the visible/NIR between 400-930 nm. Samples were cooled down to liquid N_2 temperatures with an open cycle cryostat.

Optical properties of metal phthalocyanines, among them the luminescence, are strongly related to the valence band electronic configuration and the excitation de-excitation process between highest occupied molecular orbitals (HOMO) and lowest unoccupied molecular orbitals (LUMO). There is quite extensive literature on the determination of the optical electronic transitions of these materials based on optical absorption and magnetic circular dichroism (MCD) spectroscopy mainly in the monomeric form of vapor phase and in solutions using various solvents[29,185-189]. Traditional methods for increasing spectral resolution by measuring data from crystals or thin films at cryogenic temperatures fail because strong intermolecular interactions result in exciton coupling. The spectra of solid-state species as in thin films are extremely broad and very poorly resolved compared with data recorded from solutions[190].

Interpretation of these spectra has been aided by theoretical analysis from calculated electronic configurations. Early calculations made use of semi empirical methods which are of questionable accuracy. The simple model of Gouterman and co-workers[191-193] has been widely used and provides a reasonable description of the experimental spectra of main group porphyrin and phthalocyanine complexes. The model employs a four-orbital linear combination of atomic orbitals LCAO-MO (Hückel) in a theoretical treatment that includes a 16-atom, 18-π-electron cyclin polyene model to take into account the structure of the porphyrin ring[194]. The main optical transitions of this model are usually referred to as the Q and B (Soret) transitions respectively. Recently, density functional theory (DFT) methods were used by Liao *et al.* in a systematic study of a series of first row transition-metal phthalocyanines (M-Pc) that included MgPc[92]. This calculation of their electronic structure has resolved doubts on the determination of some M-Pc ground states, and has resulted in accurate calculations of their band gaps. Liao and Scheiner found differing molecular point group symmetries in the neutral and radical forms (D_{4h}, D_{2h} respectively), which can result in the better determination of optical transitions and spectra for the free molecule. The rapid introduction of these materials as thin layers in OLEDs, among many other applications, brought the need for further investigation of the optical transitions in the crystalline form. Works of Hollebone[195] and Sharp[196] gave the first absorption and MCD spectra of CH_2Pc, CoPc, NiPc, CuPc and H_2Pc in crystal form and band shape analysis based on Davydov splitting in both the Q and B bands have given rise to good agreement with these observed spectra.

A recently developed synchrotron based spectroscopy, X-ray Excited Optical Luminescence (XEOL)[197], is employed here in order to explore the optical transitions in films of MgPc and assign them to luminescence centers. Furthermore, through Optically Detected X-ray Absorption Spectroscopy (OD-XAS), it is possible to relate luminescence to particular core sites, though this remains a challenge in such delocalized electronic system.

XAS involves the absorption of an X-ray photon to excited or ionized states resulting in emission of photoelectrons, Auger electrons and further secondary electrons; typically detected by total electron yield (TEY) methods. The decay of these core-hole excited states may, through interactions of the Auger or secondary electrons with the valence states, result in energy being transferred to luminescent centres or chromophores through inelastic or shake-up processes. Thus, this can result in creation of holes in valence band and electrons in conduction band for example in semiconductors, or in the occupied and unoccupied molecular orbital (MO) of organic molecular semiconductors. In OD-XAS the radiative recombination of these holes and electrons is measured. In XEOL the spectral distribution of these photons is measured and both can be a probe of the core electronic structure that is related to luminescence.

5.1 XEOL of MgPc

X-ray excited optical luminescence spectra of MgPc have been taken at several excitation energies below and above thresholds of C and N *K* edges. Luminescence is obtained in the visible/NIR range (400-930 nm) at ~100K and results in one significant broad optical emission at 860 nm which is most prominent for excitations below C *K* edge threshold (280 eV). This is ascribed to the Q-band in MgPc, normally the strongest emission feature (Fig. 62). Above the C *K* edge threshold the emission is substantially suppressed.

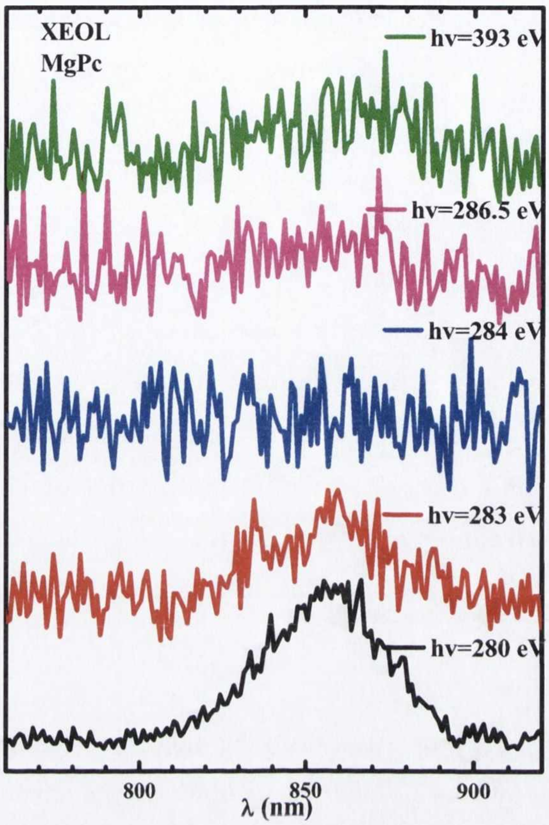

Figure 62 X-ray excited optical luminescence of MgPc at different excitation energies below and above threshold at C *K*-edge and below threshold at *N*-edge. Luminescence appears to be suppressed above the threshold excitation energies.

At the N *K* edge a broad, weak signal has been obtained in the same range around 860 nm at excitation energies below threshold but similarly the optical emission is further suppressed at excitations above threshold. This suppression of intensity relates to the luminescent yield from these core levels as well as the attenuation length for the incoming x-rays within the film and is discussed later. Previous optical absorption measurements of MgPc in solution place the Q band transition from the HOMO a_{1u} to the degenerate (in D_{4h} point symmetry) $2e_g$ LUMO[92] at ~670 nm (fluorescence at 683 nm[198]) whereas the B, N, L, S bands mainly lie below 400 nm[190]. This substantial difference between solution (monomer) and crystal (polymeric) form have been previously reported in measurements on CH_2Pc, CoPc, NiPc, CuPc, H_2Pc[195,196] and have been attributed to Davydov splitting in both the Q and the B (Soret) bands[195]. Davydov splitting arises from molecular exciton coupling which occurs due to the excited state resonance interaction in loosely bound molecular systems.

Recent photoluminescence measurements from vacuum-deposited MgPc films have shown the Q-band to peak at ~1.45 eV or 855 nm at room temperature consistent with our own observations[199]. The observed emission was ascribed to the two Davydov components of the first singlet exciton band corresponding to the Q absorption band. Thus the luminescence from the Q band is measured in our XEOL spectra. When the transition dipole appears on the molecule upon excitation, the resonance interaction arises due to transition dipoles in translationally equivalent or inequivalent molecules[200]. The molecular point group symmetry, e.g. D_{4h}, is lowered from consideration of the unit cell, the space group symmetry, and the positioning of the neighbouring molecules in the cell. Furthermore, intermolecular cohesive forces in the crystal may result in distortion of the molecule from the planar free-space form, with a consequent reduction in the molecular point group symmetry, all of which has an effect on the dipole moments of the molecule[201-203]. This has long been established as having a significant effect on the optical spectra from organic molecular crystals[204,205].

Mizuguchi et al[203] proposes a distorted molecule in the MgPc crystal with the Mg atom projected out of the plane of the four central nitrogen atoms by about 0.45 Å, forming a pyramidal structure which has been confirmed by Janczak et al[202]. The molecular symmetry is C_1 in contrast to D_{4h} usually assumed for MgPc in the free space; the excited state of the metal phthalocyanine is doubly degenerate so the molecular distortion upon crystallization can remove the degeneracy to cause band splitting. Mizuguchi calculated that in the optimized geometry (D_{4h}) there is a degenerate absorption band at 711 nm whereas for the C_1 there are two bands at 712.9 nm and 699.5 nm; however, the splitting is too small to observe two distinguishable broad absorption bands in experiment. Moreover, he predicts an interplanar spacing along the *b*-axis of 3.19 Å which is considerably smaller compared with that of the other planar phthalocyanines. The distance between the Mg atom and the nitrogen atom in the upper layer is quite small and amounts to 2.70 Å. It is suggested that the Mg atom is in a position to accept an electron lone pair of the nitrogen atom from the upper molecule to form a five-coordinate complex in the solid state. As a result strong exciton coupling with spectra displacement and energy shifts may be expected. Calculations and absorption reflection suggested that the two bands should be around 625 nm and 829 nm. Similar measurements presented in Janczak et al[201] are in agreement showing two broad bands with the lower energy one more intense. We only observed an emission peak at 860 nm (Figure 62), which could be attributed to the calculated 829 nm band taking into account the Stokes shift (i.e singlet to triplet). The photoluminescence spectra of Wojdyla et al[199] are in agreement with these measurements with a similarly large Stokes shift. A possible reason for not observing the first band is due to that fast vibronic modes may cause this excited state relax radiationlessly and then decay through the lower energy transition[206].

5.2 OD-XAS of MgPc

X-ray Absorption Near edge Structure (XANES) were recorded in total electron yield (TEY) mode and photoluminescence yield (PLY) at both C and N *K*-edges. These were measured at liquid N_2 temperatures.

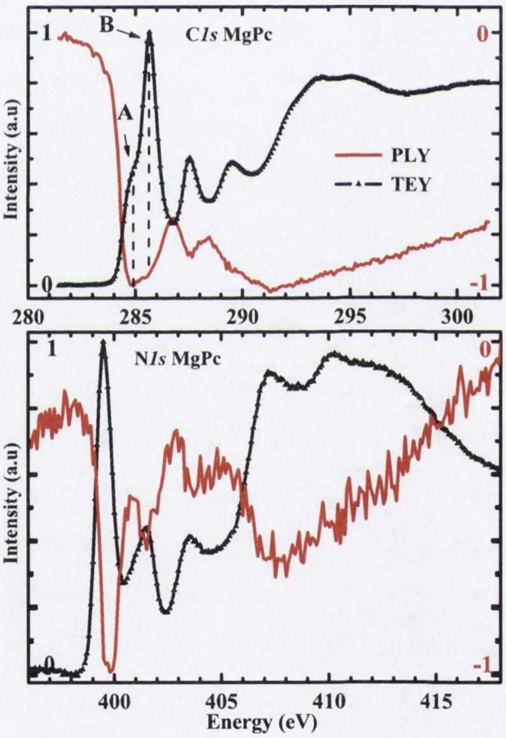

Figure 63 The top panel shows the x-ray absorption spectra (XAS) of MgPc C *K*-edge in TEY and zero-order PLY mode. The bottom panel shows the XAS spectra at the N *K*-edge in TEY and in zero order PLY mode. In both cases PLY spectra show inversion or a negative edge jump as compared to the TEY.

In Figure 63 the C and N *K* edge XAS spectra in TEY and zero order PLY are shown. The zero order PLY at both edges is inverted with respect to the TEY specifically showing a decrease in luminescence upon reaching the 1s→ π^* transition, but clearly reflects many of the same spectral features in both instances. This anticorrelation between the PLY and TEY is a well known phenomenon in optical luminescence yield spectra[206] and has been thoroughly analysed by Emura et al[120,207]. Essentially, the negative edge jump seen in the PLY spectrum arises due to competition between different excitation-luminescence channels, each having different luminescence yields. In x-ray absorption below both the C and N *K* shell thresholds, all the shallow core levels of C, N and Mg are excited and will participate in producing e–h pairs. Upon reaching the C *K* shell threshold the *1s* transition is turned on and the absorption cross section of C increases abruptly, particularly at the π^* resonance. As all elements and all accessible levels are competing for photons, if the luminescence yield for the C *1s* excitation is less than from the shallower levels, then a reduction in the total luminescence PLY can be expected for a thick film. This is unlike the case of photoemission which underlies the electron yield method where the electron escape depth is limited and the absorption channels do not compete. (Thinner films may still exhibit positive edge jumps because there is no longer the additional absorption from shallower levels deeper in the film.) This lower luminescence yield at the *K* edge may arise through a less effective coupling of the 1s core-hole excited state to the luminescence chromosphere.

The 1s-π^* resonance of MgPc at the C *K* edge shows two prominent features which we denote as A and B, where the first is a shoulder of the main second peak as seen in TEY. These may be attributed to the 1s to π^* transitions of nonequivalent benzene (C-C) and pyrrole carbons (C-N) in the MgPc molecule where the aromatic carbons are less tightly bound with a lower C 1s binding energy[208]. On that basis it might be expected that the ratio A:B is the same ratio as C-C:C-N but this is not the case as the projected C 2p partial density of states on the pyrrole C site may be higher while the feature B may also consist of the ring C 1s to LUMO+1 transitions. Pyridine exhibits a similar anomalous ratio in the XAS spectrum[155,209] where this is explained through inclusion of vibrational excitations leading to asymmetric line shapes with a tail on the high energy sides for each 1s-π^* excitation and this is also applicable to phthalocyanine systems[210]. It should be noted that in the zero-order PLY this observed ratio is reversed from that observed in TEY wherein the A peak (C-C) is more efficient at reducing the luminescence than the B peak (C-N). Possibly, the pyrrole site (C-N) 1s-π* excited state couples more effectively to luminescence due to a faster transition of the electron to the chromosphore in comparison to the decay rate of the core hole than is the case for 1s-π* excitation on the aromatic C site (C-C). The pyrrole C is bonded with the bridging N_{bg} where one of the chromosphore sites (n→π*)[206,211,212]of the Q band is located and the proximity with this neighbouring site may enhance the coupling of the luminescence from this particular core level excitation in contrast to the C-C sites.

Another noticeable point is the loss of features in PLY after excitation around 288.5 eV, where the transition from C 1s to σ* quasi bound states starts and the electron can tunnel out into the continuum. Luminescence resulting from the C 1s hole is further suppressed[213] because the participator Auger electrons are no longer involved in the decay of the core hole and the accompanied secondary processes leading to recombination of hole-electrons on the luminescence centers are absent. At the N *K* edge, the PLY shows the same inversion of the TEY with a monotonic increase of signal towards high energies consistent with observed increase of the luminescent quantum yield with higher excitation energies[214].

The inset in Figure 64 is the x-ray excited optical luminescence (XEOL), which is seen as a band centered at 860 nm, obtained with excitation energy just below the C *K* threshold. It is this band at 860 nm that is attributed to the Q band transition. Wavelength specific photoluminescence yield (PLY) spectra were obtained at the C and N *K* edges with the optical spectrometer centered on this band which is the strongest of the emission bands. Note that the zero-order PLY spectra include higher energy optical transitions such as the B (Soret) bands, which lie within the range of spectral response of the phomotomultiplier tubes as noted above. Thus the zero-order PLY spectra include emission from the Q and B, and N, L and S bands. Note that the optical emission can be confirmed as being from the organic film and not from the substrate from consideration of the attenuation lengths of the x-rays in the organic film, the ratios of the observed intensity of the XEOL before and after the C and N *K* edges respectively (not shown), as well as the reversal of the ratio of features A and B in the OD-XAS at the C *K* edge.

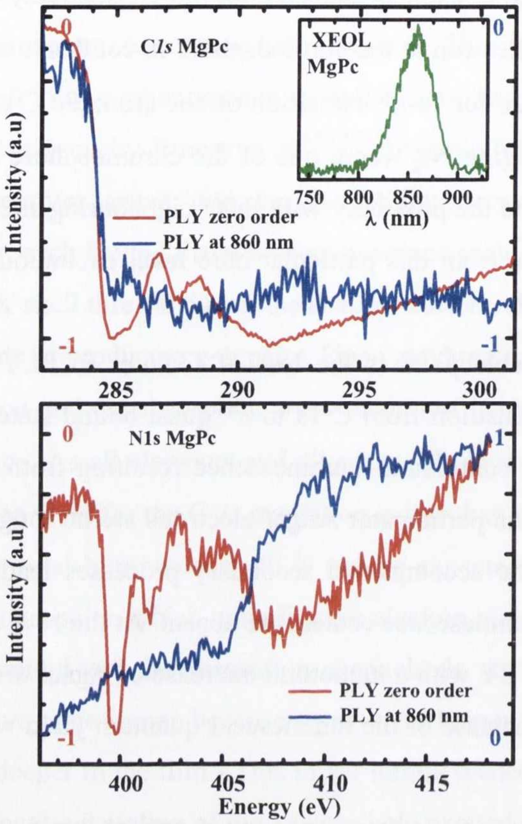

Figure 64 The top panel shows x-ray absorption spectra (XAS) of MgPc C *K*-edge at zero-order PLY and wavelength specific (860 nm) PLY. The bottom panel shows the N *K*-edge at zero-order PLY and wavelength specific (860 nm) PLY. A positive jump on the partial PLY (860 nm) of N *K*-edge is attributed to a site (bridging nitrogen N_{bg}) and state (n→π*) selective luminescence channel. Inset shows the x-ray excited optical luminescence (XEOL) spectrum of MgPc excited at 280 eV, below the C *K*-edge absorption threshold.

Shown in Figure 64 are wavelength-specific PLY spectra obtained at 860 nm for both the C *K* and N *K* edges. The wavelength-specific PLY spectrum from the C *K* edge shows a negative edge jump at the threshold as the zero order PLY does but with no distinguishable features. This lack of features is indicative that there is more than one emission center and that the Q-band is not C *K* edge site related. On the other hand interesting results emerge from the 860 nm wavelength partial PLY spectrum at the N *K* edge where a significant increase in luminescence is observed as the N *1s*-σ* range begins. Clearly, a site-specific and state specific excitation channel that couples to the Q-band luminescence has been opened in this instance. This could be related to a σ-like molecular orbital derived from the *2p* lone pair of the bridging nitrogen $(N_{bg})^{206,211,212}$. The n→π* optical transition, previously assigned to N_{bg} sites has a significant vibronic coupling with the $\pi \rightarrow \pi^*$ optical transition from which the optical emission of the Q-band is derived[206,211,212]. This should mean that the Q band contains a substantial contribution of this ($n \rightarrow \pi^*$) band which is localized on the lone pair of N_{bg}. The difference in wavelength between these two optical transitions was ~70 nm (or ~0.2 eV)[206,211,212] which is halved in ClAlPc where an electronegative axial ligand is present.[206] As Mizuguchi points out, the Mg atom in the MgPc crystal structure effectively becomes five-fold coordinated, and this may be relevant to our case where this intermolecular Mg-N_{bg}. interaction appears.

5.3 Summary

Thus XEOL can be used in the case of phthalocyanines as a probe, not simply of the molecular origin of the luminescence, but also of the intermolecular interactions in organic crystalline solids which may influence these.

Several other phthalocyanines or other porphyrin based materials could be investigated in similar studies

6. XPS, NEXAFS, RXES and XEOL measurements on metal chelates, revealing the electronic structure.

The electronic structure of metal chelate organic semiconductors is the theme of investigation in this chapter. These investigations have proceeded by synchrotron radiation based x-ray spectroscopic measurements of thick (bulk-like) and thin films. The results presented here are mainly XPS, NEXAFS, XES and XEOL measurements that took place in National Synchrotron Light Source (Brookhaven National Laboratory, USA).

The same experimental set up as the one used in the case of the phthalocyanines has been used for RXES and NEXAFS spectra measurements on Zinc(II) bis(8-hydroxyquinoline) Znq2 and Aluminium [tris-(8, hydroxyquinoline)] Alq3.

Znq2: Instrumental resolutions for NEXAFS C, N and O *K* edges is kept at 0.15 eV, where in the RXES spectra of the excited C, N and O *K* edges were obtained with nominal instrumental resolutions of 0.7-2 eV(resonant vs non-resonant), 0.95-1.8 eV(resonant vs non-resonant) and 0.82-1.9 eV (resonant vs non-resonant), respectively. We also obtained valence band x-ray photoemission spectrum taken from the same sample using the Scienta SES100 hemispherical electron analyzer of the end station at X1b with an estimated total instrumental resolution of 0.3 eV, and C 1s, N 1s and O 1s core levels XPS spectra with total instrumental resolution of ~0.8 eV, respectively. A Znq2 thick film of ~500 nm thickness measured by quartz crystal microbalance, was deposited by sublimating from a Knudsen cell at $<1\times10^{-7}$ Torr onto the native oxide of a Si (001) substrate. The substrate had been degassed for several hours at ~300 °C in the chamber which had a base pressure of 5×10^{-9} Torr.

Alq3: The energy resolution for XES spectra presented here was approximately 0.4 eV near the C *K*-edge, and 0.6 eV near the N and O *K*-edges. The energy resolution for XAS is approximately 0.2 eV at the carbon and nitrogen *K*-edges, and 0.3 eV at the oxygen *K*-edge. Thin films of Alq3 were grown *in situ* on native oxide covered Si (001) substrates which ultrasonically cleaned in acetone before introduction into the vacuum. Once in vacuum, the substrates were heated to 800 °C for 2 min. The thickness of deposited films used in RXES was approximately 100 nm estimated by quartz crystal microbalance.

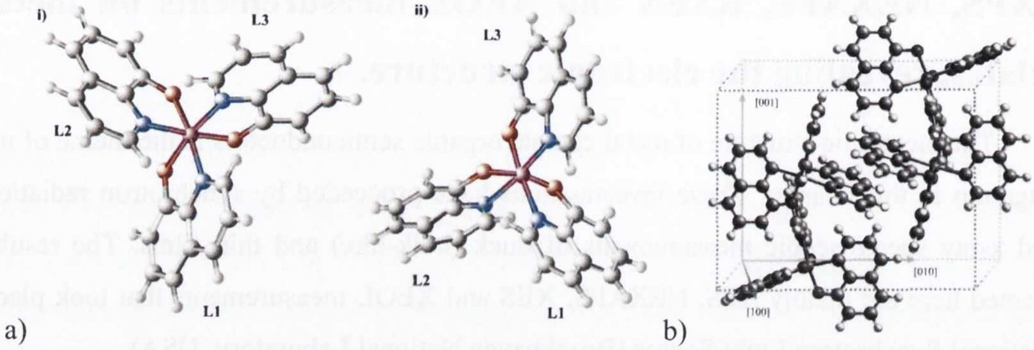

Figure 65 a) Structure of the two isomers: (i) facial and (ii) meridianal. L1, L2, and L3 denote the three ligands. Color code: nitrogen (blue), oxygen (red), aluminum (purple), carbon (dark gray), hydrogen (light gray)[216]. b) Crystal structure of Alq3[217]. Arrows indicate the direction of the reciprocal lattice basis vectors.

As XES measurements require long accumulation times, sample exposure was limited to avoid beam damage by vertically translating the sample a distance of 100 μm every 300 ms to obtain a fresh unexposed surface. All XES measurements have been taken with an incidence angle (45°) of the beam at the substrate.

Alq3 is a tris-chelate organometallic complex in which the metal atom (Al) has a distorted octahedral coordination. It can exist in either of the two geometrical isomers, the "meridianal" (C1 symmetry) isomer or the "facial" (C3 symmetry) isomer, which differ in the relative position of the oxygens and nitrogens of the metal coordination shell[215]. Both geometrical isomers are chiral and thus correspond to two different optical isomers.

Alq3 thin films are amorphous and their morphology is quite complex. Recent experimental studies have provided evidence of the presence of different phases[218]. There are three different crystal phases, two of them contain only the meridianal isomer, with different relative orientations, and the third is not well identified[218].

The meridianal isomer is the more energetically favourable form, and it will be especially dominant in films produced by evaporation onto a substrate, such as those in this study[216].

The XPS, NEXAFS and XES measurements of Alq3 have been taken in collaboration with the Boston University group of Kevin Smith and they will be presented and analysed elsewhere[219,220]. Here they are going to be used only in a comparison to the Znq2 data.

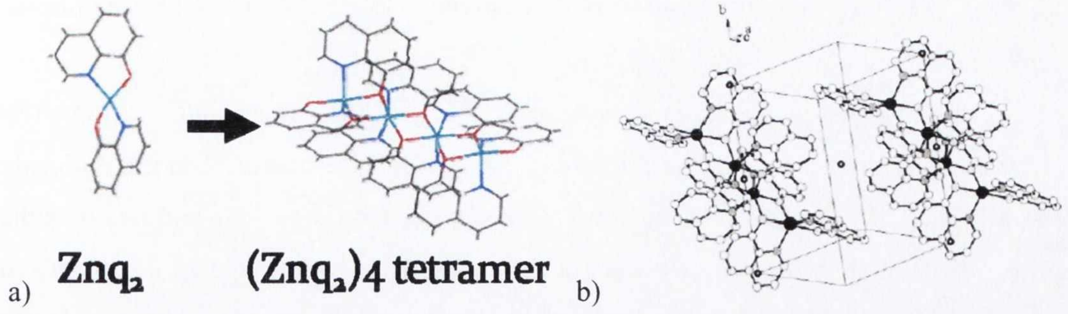

Figure 66 a) (Znq2)*x* supramolecular structures formed by thermodynamically favourable oligomerization reactions leading to the tetramer formation[226] (Colour code: nitrogen (blue), oxygen (red) Zinc (cyan), carbon (dark gray)) . b) $(Znq2)_4$ unit cell with Zn atoms (black), O atoms (light gray), N atoms (dark gray), and C atoms (white). Important symmetry inversion centres are indicated with small, empty black circles[46].

It appears that the crystal films of Znq2 occur in dehydrated and anhydrous form. Molecular modeling studies of anhydrous Znq2 predict distorted planar or distorted tetrahedral geometries depending on the theoretical method used[221]. The crystal structure of Znq2 dihydrate has been reported and shows that the 8-hydroxyquinoline ligands were planar[222,223]. In contrast, Kai et al.[224] shows that anhydrous Znq2 crystals grown from the vapour phase have a tetrameric structure $(Znq2)_4$ with two distinct Zn^{2+} ion centres with six- and five-coordinate geometry, respectively.

The suggestion that Znq2 existed as a tetramer in solid films was also raised by Hopkins et al[225], who suggested that "oligomeric" purity must be taken in to account. Sapochak et al[46,226] through a combination of theoretical modeling of oligomerization energetics leading to supramolecular structures and experimental size-exclusion chromatography studies, investigated the stability and purity of Znq2. The existence of the tetrameric phase in Znq2 purified by temperature gradient sublimation is demonstrated by using powder X-ray diffraction. Theoretical calculations of the total energies of the $(Znq2)_n$ series ($n = 1, 2, 4$) show that the tetramer is energetically preferred over both the monomer and the dimer. Differential scanning calorimetry (DSC) supports the existence of this phase as the sole phase present in both single crystals and amorphous, vacuum-deposited thin films[46].

The X-ray diffraction pattern for Znq2 films prepared in situ at high vacuum temperature by sublimation show good correspondence to the calculated pattern for the tetramer $(Znq2)_4$ suggesting a single crystalline phase for this material[46]. Films used for this study have been prepared with similar conditions, where Znq2 has been sublimated from a well degassed Knudsen cell at <1x10^{-7} Torr.

Unlike *mer*-Alq3, which lacks symmetry, $(Znq2)_4$ has a more highly symmetrical structure belonging to space group $P\bar{1}$. In the triclinic crystal structure $(Znq2)_4$ molecules are arranged so that one inversion centre is located at the tetramer centre and two on either end of the tetrameric unit between terminal, bridging 8-hydroxyquinoline ligands of neighboring $(Znq2)_4$ molecules (see Figure 66b). The former results in inversion symmetry for the $(Znq2)_4$ molecule (point group $\bar{1}$), and the latter arises from the parallel arrangement of the bridging, terminal ligands on adjacent tetrameric units, resulting in a close intermolecular π-π interaction with a distance of 3.37 Å[46].

6.1 XPS of $(Znq2)_4$

To the best of our knowledge there are no published data presenting the electronic structure of $(Znq2)_4$ by XPS, NEXAFS and XES spectroscopy.

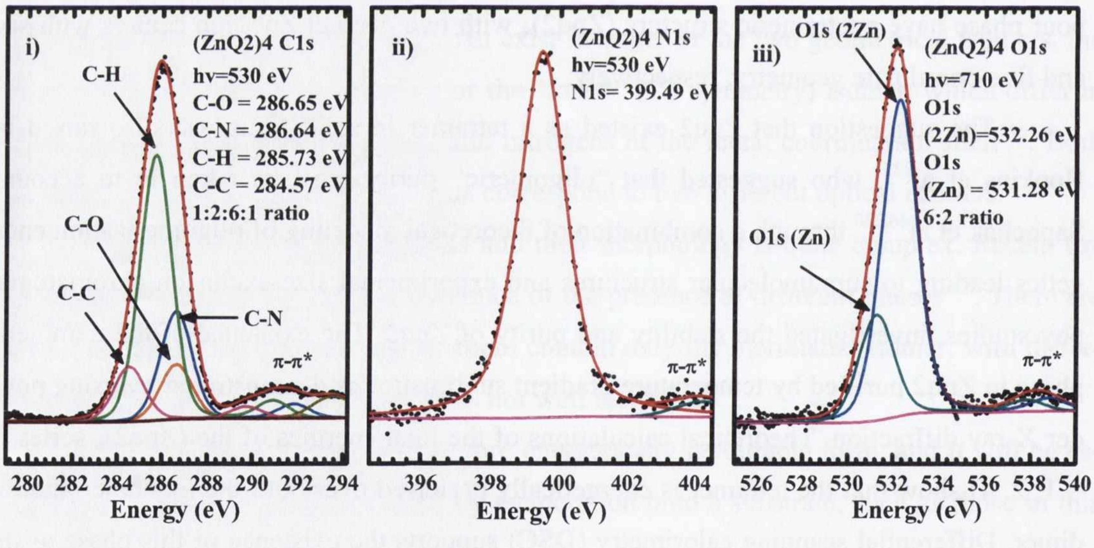

Figure 67 i) C1s core level spectrum of tetrameric form of Znq2 [$(Znq2)_4$] fitted with pseudo-Voigt peaks by keeping the stoichiometric ratio 1:2:5:1, where the different chemical environments labelled as C-C a bridged carbon connected to only other carbons (pink colour); C-N inner carbons attached to nitrogen (blue colour); C-O inner carbon attached to the oxygen (orange colour) and C-H outer carbons that bonds to both carbon and hydrogen (green colour). The shakes up features are denoted as π-π*. ii) N1s core level of $(Znq2)_4$ with the accompanied π-π* resonances. iii) O1s core level spectrum of $(Znq2)_4$ fitted with two pseudo-Voigt peaks describing the two different bondings of O to the Zn. These are the two outer O of the tetramer that are bonded only to one Zn (labelled Zn2 & Zn2′ see Fig. 68) and six O that there are bonded to two Zn (2Zn) (labelled Zn1 & Zn1′ see Fig. 68).

Figure 67 displays the C 1*s*, N 1*s* and O1*s* core-level spectra with excitation energies 530, 530 and 710 eV, respectively. The energies are chosen to enhance x-ray absorption and maximise the energy resolution, by picking the lowest possible excitation energies that also have sufficient flux to minimize the monocromator slits and as such maximise the instrumental resolution. The experimental data are plotted as dotted curves. To derive detailed information, we analyse each spectrum, fitting it and display the results as solid curves in Fig. 67. Each component is represented with a pseudo Voigt doublet function with adjustable line position, intensity, Gaussian width and lifetime width, and the background function with a Shirley form. The doublet accounts for the shake up features in a constant and independent manner for each atomic site by varying a shift from the main peak that best fit the data.

The C 1*s* core levels comprise four main components accompanied by their own shake-up satellite structures. All the peaks have been fitted with the same fitting parameters (width, mixing ratio Gaussian-Lorenzian). The overall width is 1.65 eV where the natural lifetime width Γ_L is 239 meV full width at half maximum (FWHM) as extrapoled from the fitting. This magnitude is larger than that estimated for Alq3[227] but is similar to that of graphite, 178–210 meV[228,229].

According to the best fit, binding energies of the four components are 284.57 eV, 285.73 eV, 286.64 eV and 286.65 eV which are in good correspondence with values for C1*s* of Alq3[227]. These four components originate from four bonding environments for carbon in the structure of the 8-quinolinol ligand: A bridged carbon connected to only other

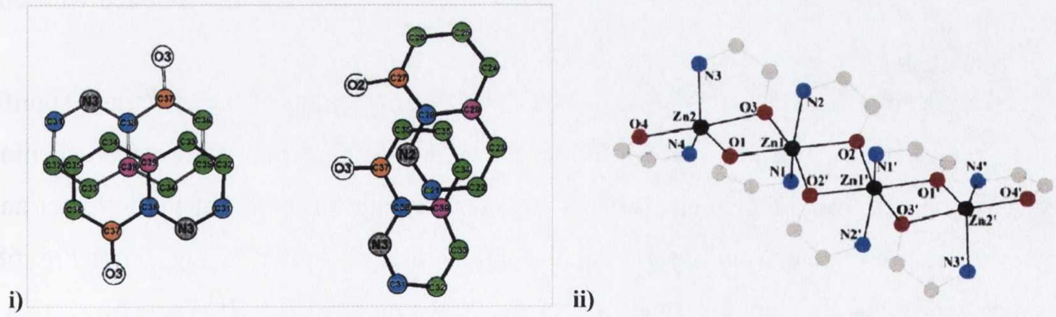

Figure 68 i) Pyridyl/phenolato ring overlap is shown for (left) intermolecular interactions of bridging, terminal ligands and (right) intramolecular interactions between bridging, terminal ligands and central ligands46. Also colouring have been added marking the carbons of different chemical environment. ii) Structures showing the coordination geometry and atomic labelling about the Zn ions in the tetramer for Znq2. The full 8-quinolinolate ligands are not shown for clarity[226].

carbons called the C–C bond (coloured pink in Fig. 67i), an outer carbon that bonds to both carbon and hydrogen called the C–H bond (coloured green in Fig. 67i), an inner carbon attached to nitrogen called C-N bond (coloured blue in Fig. 67i) and an inner carbon attach to oxygen called the C–O bond (coloured orange in Fig. 67i). The area ratio for the C–C, C–H, C–N and C-O components is roughly 1:5:2:1, in agreement with their numbers in an 8-quinolinol ligand. It needs to be noted here that on the fitted areas for each site the individual shake up area also included.

The N 1*s*, core-level XPS spectrum, has been fitted with only one main component with overall width of 1.9 eV at 399.49 eV, which does not necessarily reflect only one bonding configuration of these atoms. An attempt to fit it with two equal area peaks involving nitrogens that bonded with the inner zincs (labelled Zn1 & Zn1' at Fig. 68ii) and outer zincs (labelled Zn2 & Zn2' at Fig. 68ii) which are in different atomic coordination specially on bonding with O, did not improve significantly the χ^2 and the energy difference was only 0.5 eV which is less than the instrumental resolution of 0.8 eV and thus could not be resolved and confirmed.

The O 1*s* core level spectrum of $(Znq2)_4$ have been fitted with two pseudo-Voigt peaks describing the two different bondings of O to the Zn. There are the two outer O of the tetramer that are bonded only to one Zn (labelled Zn2 & Zn2′) and six O that there are bonded to two Zn (labelled Zn1 & Zn2′). The area ratio of the two fitted curves is in good agreement with this atomic stoichiometric ratio (including shake up area). Both curves have been fitted with the same width of 1.83 eV and Gaussian-Laurenzian mixing ratio of 0.82 (dominant Gaussian). The binding energy for the inner oxygens bonded with two zincs [O1*s* (2Zn)] is 532.26 eV and for the outer oxygens of the tetramer bonded with one zinc [O1*s* (Zn)] is 531.28 eV.

In all three cases (C1*s*, N1*s*, O1*s*) the FWHM broadening of the spectra is significant larger than the instrumental resolution and expected core hole lifetime broadening most likely due to inhomogeneous broadening cause by the formation of the tetramer and the various intramolecular and intermolecular interactions as shown in Fig. 66 & Fig. 68. Tabulated fitting parameters for these spectra are shown in Appendix III, Table 6.

6.2 XES of $(Znq2)_4$

In Figure 69 NEXAFS spectra of $(Znq2)_4$ films on native oxide covered Si, measured at a 45° angle of incidence of the beam to the substrate at both the C and N *K*-edges are presented. In the case of the C *K*-edge peaks A and B may be attributed to the 1s π^* transitions of nonequivalent phenyl ring C-C, C-H and C-N, C-O carbons in the $(Znq2)_4$ molecule where the C-C and C-H carbons are less tightly bound with a lower C *1s* binding energy as shown from the XPS spectra. XES spectra at the same incidence angle of the beam at either the C or N *K*-edge have been recorded with different excitation energies from threshold upwards, going from resonant mode as depicted from NEXAFS spectra to non resonant excitation and are in the lower panel of Fig. 69.

In Figure 69a the spectra A, B and C considered as resonant emission and are com-

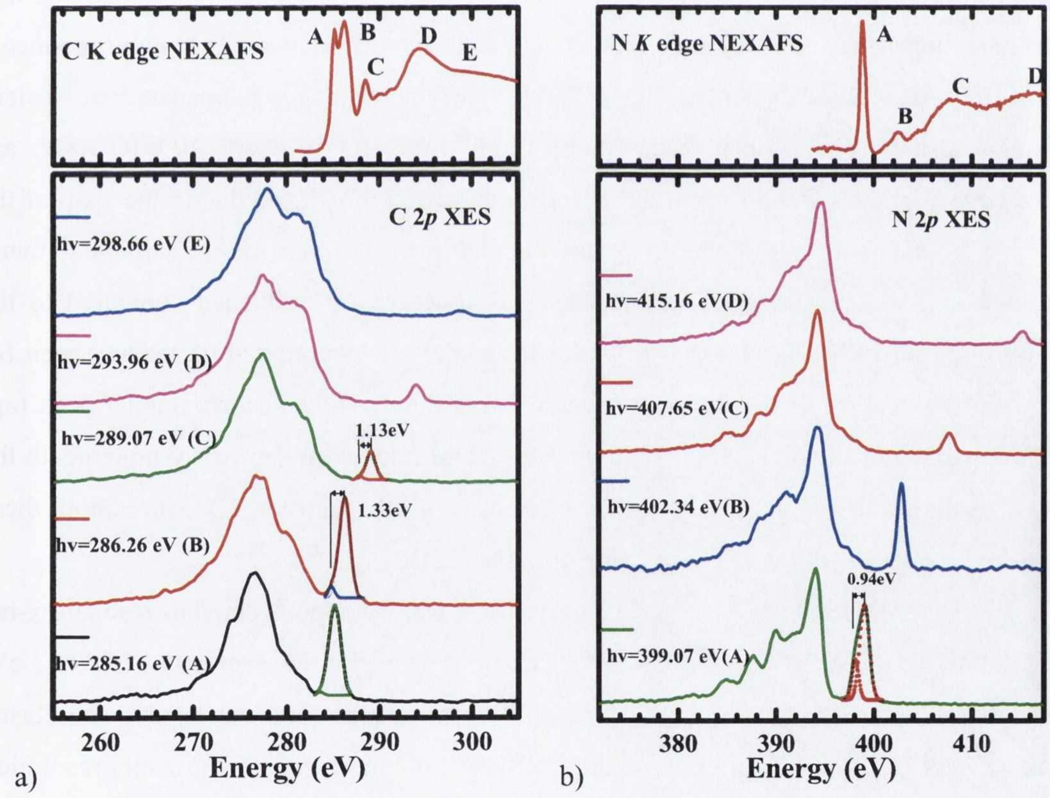

Figure 69 a) Top panel: $(Znq2)_4$ NEXAFS at C *K* edge at 45° incidence of beam to substrate. Bottom side panels: C *K* edge XES spectra at the same angles at various resonant energies and non- resonant energy. b) Top panel: $(Znq2)_4$ NEXAFS at N *K* edge at 45° incidence of beam to substrate. Bottom side panels: N *K* edge XES spectra at the same angles in various resonant sites and non- resonant excitation energy. Elastic peaks on both C and N edges appear broadened, in some cases asymmetrically, and have been fitted with two peaks.

ing with the same overall shape but with some distinct differences. The resonant emission spectrum A excited with 285.16 eV is only capable of creating core holes on the C-C carbons, an atomic site that does not seem to have contributions from the LUMO and HOMO levels, according to the ab initio Hartree-Fock (HF) calculations by Sapochak et al[46]. The filling of this core hole ($2p \rightarrow 1s$) most likely does not include HOMO states which may suppressed by stricter RXES selection rules, based on the fact that the tetrameric form of Znq2 has an inversion centre (highly symmetric) where only $g \rightarrow u$ transitions are allowed. Spectrum B excited at 286.26 eV involves emission transitions from the C-H atomic sites. There is only an enhancement of the same features as those which appeared in spectrum A. The broadening is most likely attributed to the span in binding energies of the core holes. In spectrum C, excited at 289.07 eV, from this point on all core holes from the different carbon sites are involved and the HOMO level is observable due to transitions from the sites with the highest 1s core level binding energies, the C-N and C-O sites. The fact that the main shape of the spectrum (C) looks similar to the earlier two (A & B) pronounce a completely delocalised system to HOMO and LUMO levels as the Sapochak et al[46] calculations are shown. In the non resonant spectrum E, the HOMO-1 and HOMO levels are more clearly observed and the overall spectrum has been broadened due to the span of the different binding energies of core holes and the multiplicity of transitions available to them. The elastic peaks of the three resonant spectra appear over broadened compared to the natural lifetime width combined with the instrumental broadening and these have been fitted with two peaks. For the first two spectra it is not clear if the second smaller peak (appearing as inelastic loss) is associated with the HOMO level hidden partly underneath the elastic peak, but this is definitely not the case in the third spectrum (C). More about these inelastic losses will follow in conjunction with the N XES spectra.

In Figure 69b the N *K*-edge RXES spectra A and B are considered as resonant x-ray emission spectra. The resonant emission spectrum A is excited with energy of 399.07 eV, and appears with relatively sharp features, but no observable HOMO levels. The elastic peak appears broader, beyond the natural life time combined with instrumental resolution broadening. Further it is asymmetric and has been fitted with two peaks. It is speculated that this asymmetry might been caused from losses by intra-molecular excitonic transitions due to atomic vibrations as described in the case of ethylene and benzene by Hennies et al[179,180], something that is more susceptible to happen in a 3D super-molecule like the $(Znq2)_4$ specially on the pyridyl/phenolato ring.

The second resonant emission spectrum B excited at 402.34 eV appeared with the same features broadened this time and with observable HOMO levels. It is not clear if the broadening on the second spectra has to do with the speculation of the slightly different binding energies between outer and inner nitrogen of the tetramer. In that case the first emission spectrum A creates a core hole only on the outer nitrogens where part of the HOMO is allocated (Sapochak et al[46]) and in the second spectrum core holes from both (outer, inner) nitrogens are created and the multiplicity of transitions from the VB states creates broadening.

In Figure 70 O *K*-edge NEXAFS spectrum of $(Znq2)_4$ films on native oxide cov-

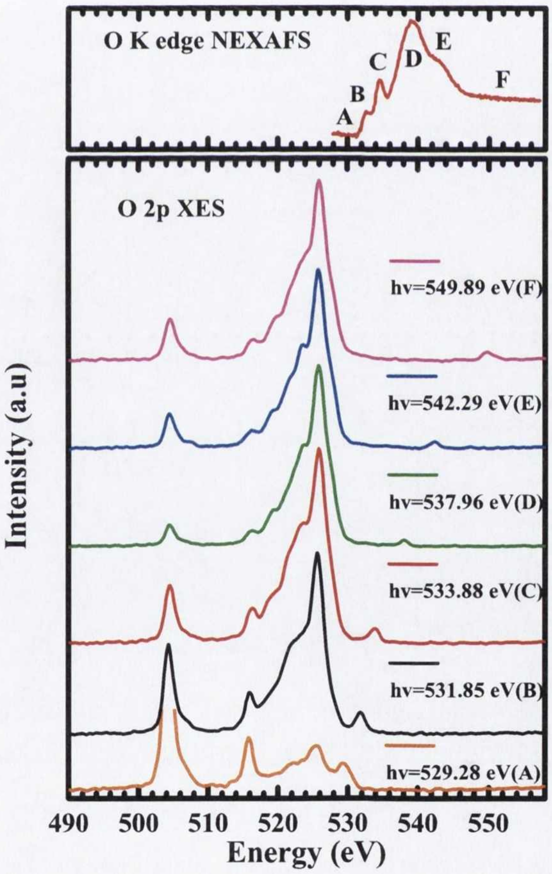

Figure 70 Top panel: $(Znq2)_4$ NEXAFS at O *K* edge at 45° incidence of beam to substrate. Bottom panels: C *K* edge XES spectra at the same angle at various resonant excitation energies and non-resonant excitation energy.

ered Si, measured at 45° angle of incidence in conjunction with XES spectra at the same incidence angle of the beam have been recorded with different excitation energies from threshold upwards, going from resonant mode as depicted from NEXAFS spectra to non resonant excitation.

Spectra B and C of the XES panel in Fig. 70 are considered to be resonant x-ray emission spectra. Spectrum A excited at 529.28 eV is just at the absorption threshold but, as can be seen, a weak signal due to the O *2p-1s* emission is observable. This weak signal is largely due to a small proportion of second order light in the beamline contributing to both creation of 1s core holes and Zn 2*p* core holes, hence the significant Zn *3d-2p* emission spectra seen in this spectrum recorded by the x-ray emission spectrometer in second order. Thus, the O2*p* component of the XES observed here should be considered to be NRXES, excited as it is by photons of 1058 eV energy. Dominant features of this spectrum are a set of doublet peaks at ~505 eV and ~516 eV. These peaks are a second order light signal belonging to Zn $2p_{3/2}$ and Zn $2p_{1/2}$ state transitions (L_α /L_β emission lines) with

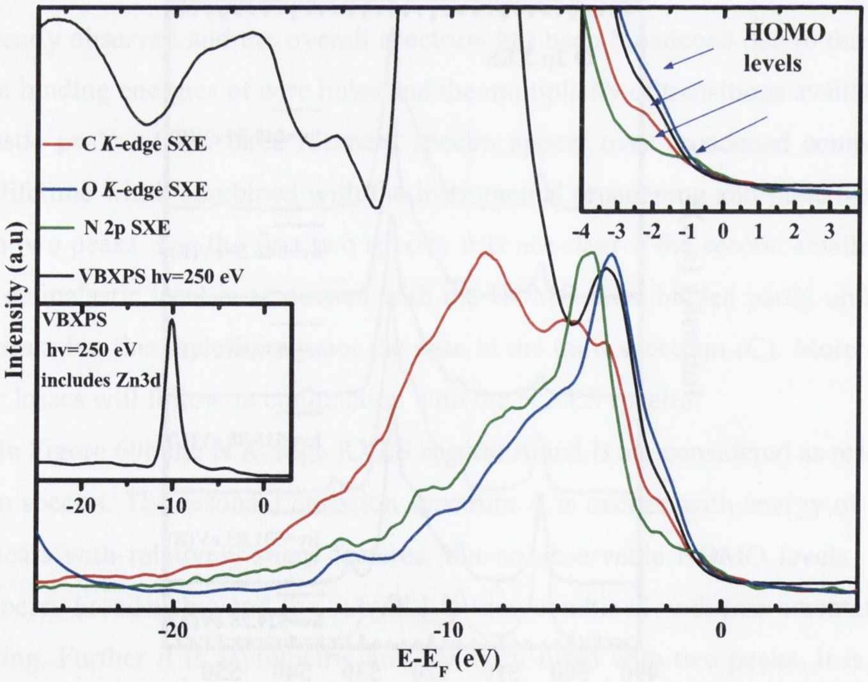

Figure 71 Valence band XPS spectrum taken with excitation energy of hv=250 eV superimposed with the C, N and O *K* edges non resonant XES spectra of the (Znq2)$_4$. Energies have been scaled relative to the Fermi edge. Inset on the left hand side shows the valence band spectrum including the Zn3d peak. Inset on the top right side shows in magnification the HOMO levels from the VB and XES spectra.

emission energies at 1011.7 eV and 1034.7 eV, respectively[230]. Resonant emission spectrum B excited with 531.85 eV at the π^* state appears with a relative sharp main emission feature where the HOMO only weakly appears as a shoulder on the high emission energy side. Although the excitation energy appears to be smaller than the binding core hole energy for outer oxygens (532.26 eV) it is believed that core holes are likely to have been created at both oxygen sites due to the uncertainty in the energy imposed by the combined instrumental resolution of 0.8 eV. Resonant emission spectrum C appears with the same features which are slightly broadened and is similar to the non-resonant emission spectrum F.

In Figure 71 valence band spectrum taken with hv=250 eV excitation energy is shown in a direct comparison with the non resonant C, N and O *K* edges XES spectra. All the energies are presented relative to the Fermi level. The valence band spectrum is dominated by the Zn 3d peak at ~10 eV (inset on the right side of Fig. 71) which obscures a large part of the other valence band states. The valence band XPS spectrum appears to be insensitive to the detail of the HOMO levels, although the combined instrumental resolution is ~0.3 eV, as compared to the XES spectra which exhibit more distinct features. This coincides well with the character of the HOMO levels on the pyridyl/phenolato ring as cal-

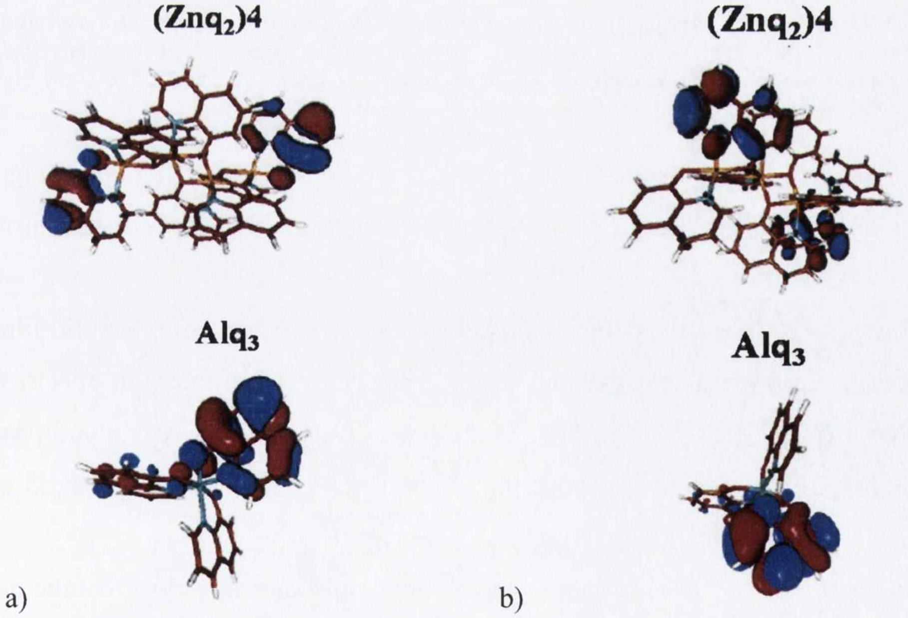

Figure 72 a) Orbital density plots of the HOMO for (Znq2)$_4$ on the top and *mer*-Alq3 on bottom panel. b) Orbital density plots of the LUMO for (Znq2)$_4$ on the top and and *mer*-Alq3 on bottom panel. Representation based on ab initio Hartree-Fock (HF) calculations by Sapochak et al[46].

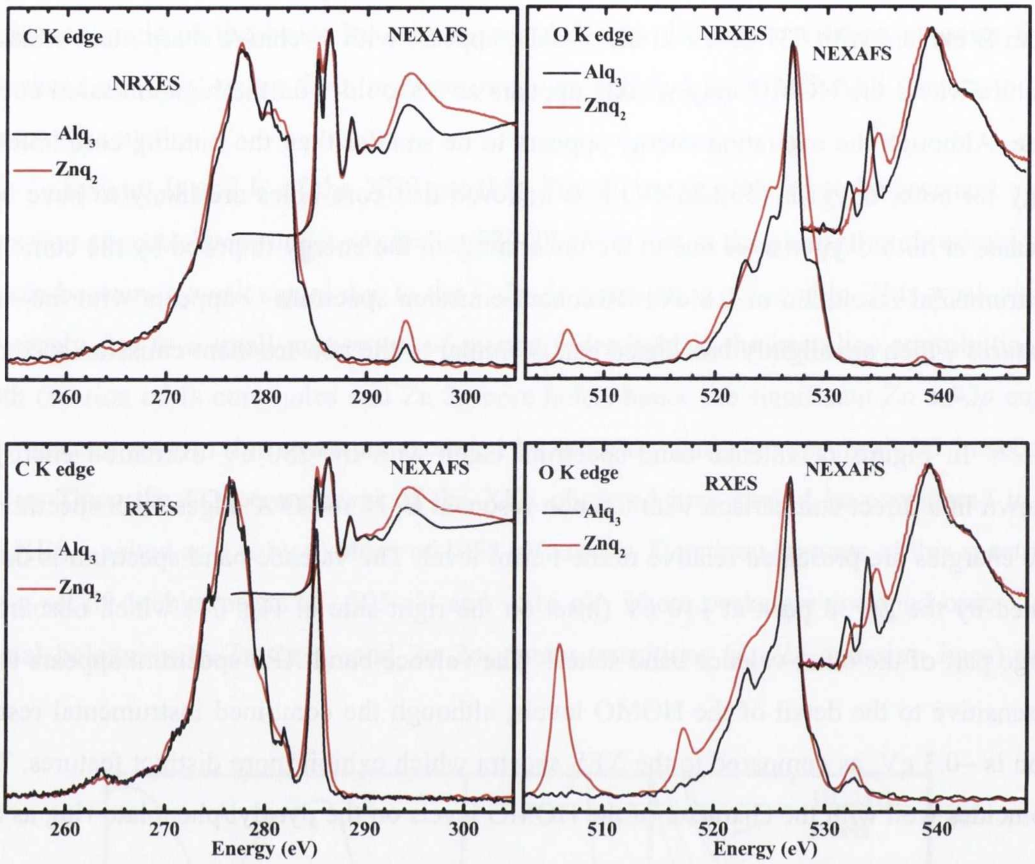

Figure 73 Left panels shows comparison between *mer*-Alq3 and $(Znq2)_4$ C *K*-edge NEXAFS and *C K*-edge *x*-ray emission spectra at resonant (bottom) and non resonant mode (top), respectively. Right panels in the same fashion show the comparison on O *K*-edge NEXAFS and O *K*-edge x-ray emission spectra.

culated by Sapochak et al[46] based on ab initio Hartree-Fock (HF) calculations (Fig. 72). Possibly the high excitation energy, of the specific valence band XPS spectrum contributes to this.

In Figures 73 and 74 the comparison between *mer*-Alq3 and $(Znq2)_4$ solid films by near edge x-ray absorption spectroscopy (NEXAFS) and x-ray emission spectroscopy (XES) is presented. In particular in Fig. 73 the C and O *K* edge NEXAFS and resonant (Fig. 73 bottom panel) and non resonant (Fig.73 top panel) C and O *K*-edges XES of the two metal chelates are compared directly.

Looking at the NEXAFS spectra of these two atomic sites it is clear that the overall shapes are very similar, as should be expected since both chelates are based on the same pyridyl/phenolato ring. In the case of the O *K* edge of the $(Znq2)_4$, features appear much

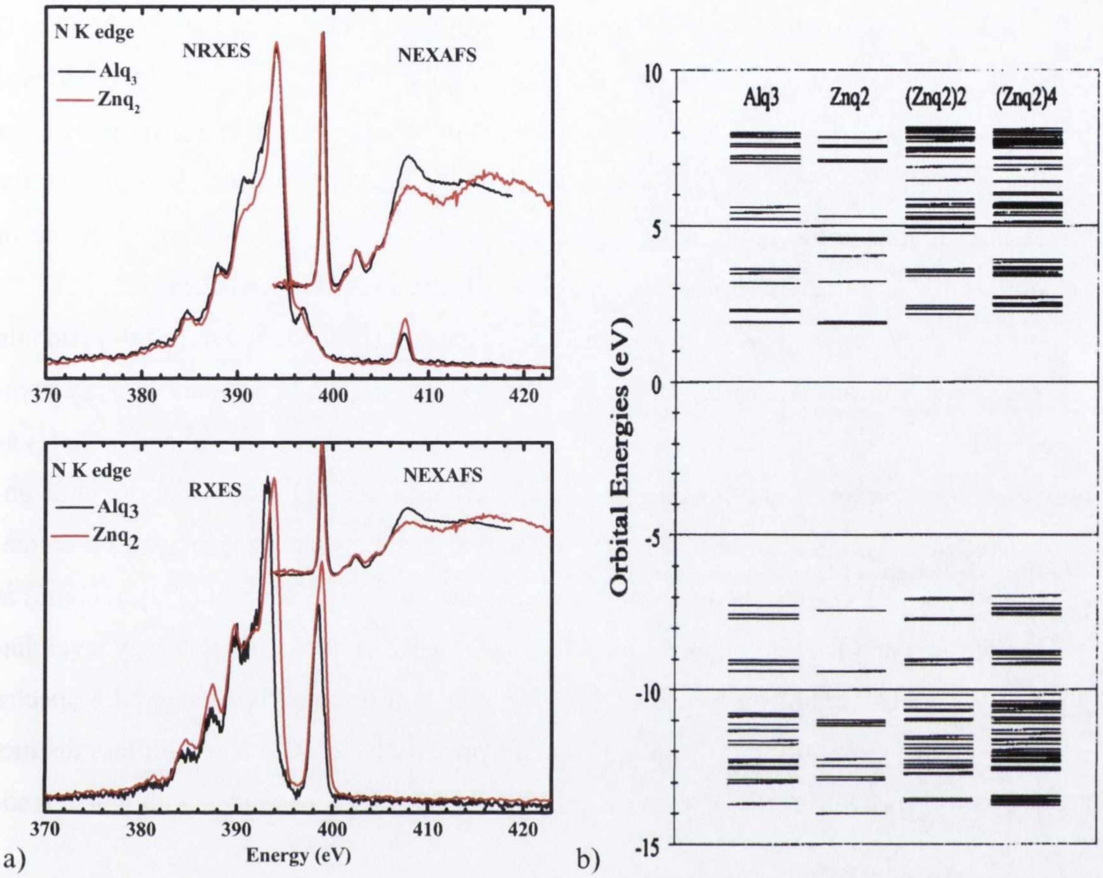

Figure 74 a) Comparison between *mer*-Alq3 and (Znq2) N *K*-edge NEXAFS and *N K*-edge *x*-ray emission spectra at resonant (bottom) and non resonant mode (top), respectively b) Calculated orbital energy level diagram for *mer*-Alq3 and the (Znq2)*n* oligomer series as presented by Sapochak et al[46].

broadened in comparison to the *mer*-Alq3 because of the multiplicity of states created in the tetrameric form (see Fig. 74b). This is a result of the increase in the number of atoms and unoccupied non-degenerate electronic states, which is consistent with a tetrameric structure for Znq2.

Also the π^* resonance describing the lowest unoccupied molecular orbital (LUMO) at these sites for the $(Znq2)_4$ is at a higher energy as compared to that of the *mer*-Alq3 and corresponds well with the calculated orbital energy level diagram based on Hartree-Fock eigenvalues presented by Sapochak et al[46] for the two molecules (Fig. 74b).

The fact that the ratio between π^* and σ^* states is very similar can most likely be attributed to the three dimensional structure of these molecules in conjunction with the amorphous crystal structure as has been reported previously[46,218].

The C *K* edge XES spectra both resonant and non-resonant are looking almost identical for the two metal chelates, with slightly less features in the case of the $(Znq2)_4$. The O *K* edge XES spectra follows the same trend with a similar overall shape but with broadened features in the case of $(Znq2)_4$. It should be noted that the instrumental broadening is higher in the case of the Znq2 spectra thatn for the Alq3 spectra and thus it is not clear whether the broadening is due to the multiplicity of states (tetramer) as has been described before or because of the instrumental resolution, though the N spectra indicate the former.

In Figure 74a the N *K* edge NEXAFS and resonant (Fig. 74a bottom panel) and non resonant (Fig. 74a top panel) N *K* edge XES of the two metal chelates are directly compared. NEXAFS spectra look identical following the same ratio between π^* and σ^* states as previously noticed for C and O *K* edges. The LUMO appeared to be almost at the same energy. The N *K* edge resonant XES spectra of the two metal chelates appears with a noticeable difference at HOMO-2 level where the main peak on the spectrum of $(Znq2)_4$ comes at a higher energy and is in good correspondence with the calculated orbital energy level diagram by Sapochak et al[46] presented on Fig. 74b. The non resonant N *K* edge XES spectra is in good agreement with the $(Znq2)_4$, just being slightly broadened and with less distinct HOMO and HOMO-1 levels. Also in this case the $(Znq2)_4$ has been taken with worse resolution.

The HOMO and LUMO levels as extrapolated from the C, O, N *K*-edge XES and NEXAFS spectra (shown at appendix IV) reveal a much smaller band gap for the Alq3 and $(Znq2)_4$ than the presented calculated orbital energy level diagram by Sapochak et al[46] on Fig. 74. The failure of Hartee-Fock eigenvalues to calculate accurate energy levels for the band gap in combination with excitonic states might contribute on this mismatch.

6.3 XEOL of $(Znq2)_4$

A first attempt to explore the optical luminescence of $(Znq2)_4$ films by x-ray excited optical luminescence (XEOL) spectroscopy was attempted.

Measurements took place on the X1B beam line end station with an experimental set up used for the first time at this end station (Fig. 75). A focusing lens (a UV grade collimator) was connected to a fibre cable (UV grade 400 μm fibre) and mounted to a retractable z stage manipulator inserted in the main chamber in close proximity to the sample to maximise the luminescent light collection. Optical light through the fibre optic was measured with an optical detector USB2000, which is supplied with Sony ILX511B linear silicon CCD array detector. It is configured with a 600 mm^{-1} grating, blazed for 400 nm, and a 25 μm entrance slit which can deliver 1.3 nm (FWHM) resolution. The detector has useful sensitivity range of 200 – 850 nm.

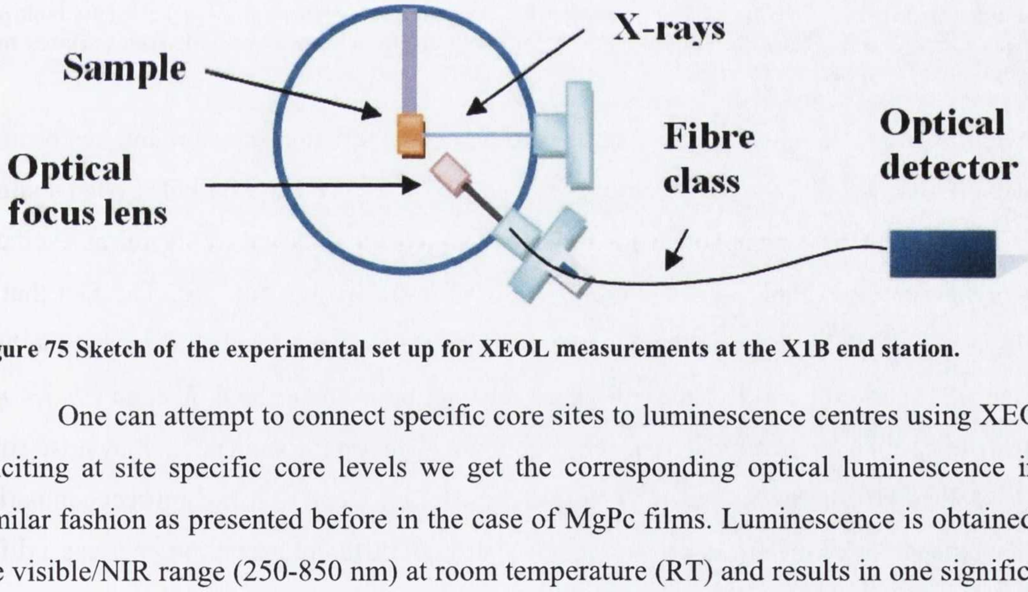

Figure 75 Sketch of the experimental set up for XEOL measurements at the X1B end station.

One can attempt to connect specific core sites to luminescence centres using XEOL. Exciting at site specific core levels we get the corresponding optical luminescence in a similar fashion as presented before in the case of MgPc films. Luminescence is obtained in the visible/NIR range (250-850 nm) at room temperature (RT) and results in one significant broad optical emission at 546 nm which is most prominent for excitations below the C *K* edge threshold (280 eV). This emission feature has been reported before, and is red shifted relative to Znq2 in solution[231,232], and in agrees with other thin film photoluminescence investigations[232,233]. Above the C *K* edge threshold the emission is substantially suppressed (310 eV). This suppression of intensity relates to the luminescent yield from this core level

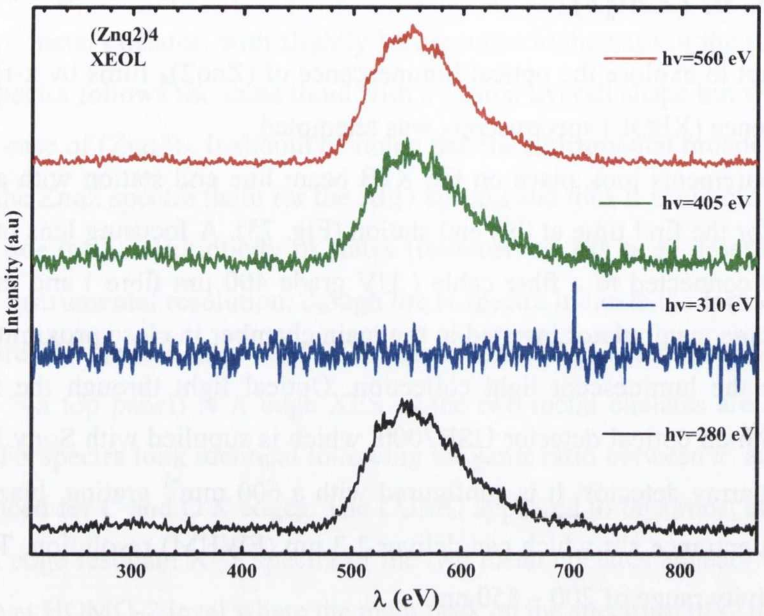

Figure 76 An attempt to connect specific core sites to luminescence centres using XEOL. Exciting at site specific core levels we get the optical luminescence correspondence. From the bottom to the top, spectra excited before the C *K* edge absorption threshold, above the C absorption threshold, above the N *K* edge threshold above the O *K* edge absorption threshold are presented. Measurements took place at room temperature, thus the optical signal most likely originates from excitonic states related to the chromophore and the crystal structure.

as well as the attenuation length for the incoming x-rays within the film and has been extensively discussed at the MgPc case (see at chapter 5.1). At the N and O *K* edge a similar XEOL signal has been obtained in same range, with peak around 546 nm at excitation energies above threshold at 405 eV and 560 eV, respectively (Fig. 76). The fact that we still get substantial emission above threshold for these two core levels means that the luminescence (quantum) yield of these two are relative higher than the C *K* edge ($\eta_{C1s} < \eta_{N1s}$, η_{O1s}) and could be indicative that the chromophore is not on the C-sites but may arise solely from optical transitions on N and O atomic sites. It is difficult to make a direct comparison of the intensities of the emission peaks, since between different excitation energies a different focal position for the optical lens was required.

The fact that measurements took place at room temperature could possibly involve conformational changes due to strong exciton phonon coupling which may cause the excited state to relax radiationlessly and decay through the lowest energy transition[206,234]. Excitonic states and electron traps below the LUMO are common in such films, as has been shown for other chelates[234]. The bridging and terminal ligands not only exhibit intramolecular π–π stacking interactions with center ligands of the tetrameric unit, but also involve strong intermolecular π–π stacking as described by Sapochak et al[46] . The inter- and intra-molecular π–π interactions result in an extended network of overlapping phenolato and pyridyl moieties, which create a band like electronic structure (Fig74b) and thereby could lower LUMO level energy and give a narrower band gap than in Alq3. Extended intermolecular orbitals could not be excluded and could be responsible for a red-shifted or blue-shifted spectra displacement caused by exciton coupling effects[203].

These are possible reasons for the broad PL red shifted spectrum relative to the one obtained from Znq2 molecules in solution. Also there is no sign of atomic core site related chromophore states since at room temperature luminance effects due to the crystal structure as appear dominant.

6.4 Summary

In conclusion, the electronic structure of Znq2 thin films, as measured by NEXAFS, RXES, XPS and XEOL was compared to measurements of Alq3. Evidence was found to support the conclusion that a tetrameric form of these films was studied with differences observed in particular in the O and N *K*-edge XES spectra.

7. Conclusions

7.1 Conclusions

At the outset I indicated that there were two themes of study. These were investigations of phththalocyanines materials specifically looking at beam damage in OMS MPcs and the electronic structure of MPcs.

Synchrotron radiation induced damaged to the organic semiconductor family of metal phthalocyanines solid films has been under investigation through photoemission and NEXAFS spectroscopies. Themes of investigation included comparison between non-planar and planar phthalocyanines, temperature dependence and thick versus thin films.

Two major damage processes have been indentified: a) Degradation or alteration of the crystal structure of the films and b) molecular damage, that is scissioning of bonds, observed mainly though XPS and NEXAFS studies of thick PbPc films.

Temperature seems to slow down these two processes, as has been proved to be the case at liquid nitrogen temperature with XPS studies on PbPc thick film.

Comparison between non-planar (PbPc) and planar (MgPc) metal phthalocyanines under the same time of exposure and the same energy and flux, shows that the planar MgPc is more robust compared to the non-planar PbPc.

Similar to this is the comparison between thin films (~1 ML) of non-planar PbPc and planar MgPc, investigated through core level and VB photoemission spectroscopy, where MgPc appeared to be intact even after prolonged exposure to synchrotron radiation.

In the case of PbPc thin films, prolonged exposure seems to alter the way the non planar molecule faces the substrate. The molecule is sitting flat with the Pb atom facing the substrate (facing down) and the Pb atom facing away of the substrate (facing up) in a ratio 1:7. Synchrotron radiation seems to flip substantial numbers of molecules and alter this ratio to 1:2.

The electronic structure of planar and non-planar closed shell metal phthalocyanines ZnPc, SnPc and PbPc, as well the fluorinated counterpart of ZnPc F_{16}ZnPc, was investigated in the second theme of this thesis, where NEXAFS, XES and VBXPS measurements were used.

The non-planar SnPc and PbPc thick films have a molecular arrangement with a shallow inclination to the substrate compared to the planar ZnPc as concluded from NEXAFS spectra taken with the highly polarised light source.

Calculated PDOS and calculated XES shows that the HOMO level of the non-planar phthalocyanines (SnPc & PbPc) is located across all the phthalocyanine ligand (C, N atoms) whereas in the case of the planar phthalocyanines (ZnPc, F_{16}ZnPc), though it is still on the phthalocyanine ligand, it is located mostly on the C atoms. This is shown to be in good agreement with observations such as the XES experimental spectra at the C and N K edges. Further the calculated PDOS shows that the LUMO is dispersed across the whole macromolecule in the phthalocyanines under examination.

This appears to be the case with the ZnPc where inversion symmetry is present in the molecule.

ZnPc and F_{16}ZnPc appear to have very similar NEXAFS and XES on the N *K*-edge, but the picture is different for the C *K*-dege where the highly electronegative fluorine appears to withdraw substantial charge from the C atoms that affect the XPS, NEXAFS and XES spectra signficantly.

In addition x-ray excited optical luminescence and optically detected x-ray absorption spectroscopy, two relatively new synchrotron based spectroscopies, were used on (MgPc) and Zinc(II) bis(8-hydroxyquinoline) (Znq$_2$) molecular films. The scope was to reveal luminescence chromophore centres in the atomic sites of these optically active molecular semiconductors. Results from MgPc indicate that a non-bonding nitrogen state is actively involved on the main optical luminescence band of this molecule. Furthermore, the intermolecular interference appears to play a large role in this kind of transition on such solid films. Thus XEOL and OD-XAS can be used in the case of phthalocyanines as a probe, not simply of the molecular origin of the luminescence, but also of the intermolecular interactions in organic crystalline solids which may influence these.

Lastly, the electronic structure of Znq2 thin films, as measured by NEXAFS, RXES, XPS and XEOL was compared to measurements of Alq3. Evidence was found to support the conclusion that a tetrameric form of these films was studied. The tetrameric form of Znq2, with the multiplicity of states but also the extensive intamolecular and intermolecular interference of π-π quiline bonds, has a lower band gap compared to the Alq3 and this seems to be supported by the direct comparison of the XES spectra.

7.2 Intentions

It had been hoped that a third theme would have been possible through my investigations, which would have been investigations of the electronic structure of thin films of MPcs through XES and their correspondence with XPS. However experiments to this end were frustrated by equipment problems over several years at MAXlab I511-1 where it was intended that these investigations take place.

7.3 Future work

Advances in spectrometers have already allowed acquisition of XES spectra in seconds where hours were necessary before[235,236]. This has the advantage of minimising the radiation exposure of such organic films and giving much better signal to noise spectra, especially on very thin films. Thus extended investigation on thin films of the same molecular semiconductors could be worthwhile where accurate determination of the electronic structure across an interface is crucial for the performance of several devices based on these materials.

Since XES is a photon-in/photon-out spectroscopy, organic thin films under bias can be easily measured, providing an alternative and perhaps more accurate method of investigating electrical parameters governing charge transport across semiconductor interfaces (valence band offset, interface dipole, bandbending). Electron affinity and ionisation potential relative to the anode and cathode contacts could be explored through this method and accurate values for the energy barriers mismatch between semiconductor-conductor interfaces, extracted.

In metal chelates, such as Znq2, the asymmetry in elastic peaks can be studied further with higher resolution RIXS. Already, such high resolution RIXS is being applied to small molecules[179,180]. An extensive high resolution RIXS could retrieve more information about the geometry of such 3D macromolecules and also the vibrationally activated optical transitions.

8. Publications

- "Preliminary results from resonant soft x-ray emission and beam damage studies of the phthalocyanine family of organic molecular semiconductors" N. Peltekis, B. Holland, S. Krishnamurthy, C. Stephens, G. Cabailh, I.T. McGovern, L. Kjeldgaard, J. E. Downes, H. J. Trodahl, S. Wang, K. E. Smith and C. McGuinness.
  Poster at Zuoz summer school (2005)

- "Preliminary results from soft x-ray beam damage studies of phthalocyanine organic molecular semiconductors." N. Peltekis, B. Holland, S. Krishnamurthy, C. Stephens, G. Cabailh, I.T. McGovern, L. Kjeldgaard and C.McGuinness. MaxLab report (2004)

- "Preliminary results from Optical Detected – X-ray Absorption Spectroscopy and X-ray Excited Optical Luminescence on phthalocyanine organic molecular semiconductors." N. Peltekis, B. Holland, S. Krishnamurthy, C. McGuinness S. Patel, N. Poolton.
  Daresboury SRS report (2005)

- "Electronic structure of HfO_2- a d^0 ferromagnet." S. Krishnamurthy, N. Peltekis, C. McGuinness, J.M.D. Coey, C.B. Fitzgerald, M. Venkatesan, J.G. Lunney, and T. Schmitt.
  MaxLab report (2005-06)

- "NEXAFS on metal phthalocyanines on Ge (111)" B.N. Holland, N. Peltekis, C.McGuinness, I.T. McGovern.
  MaxLab report (2007)

- "Interface effects on NEXAFS spectra of MPc" B.N. Holland, N. Peltekis, C.McGuinness, I.T. McGovern.
  MaxLab report (2008)

- "Arrangement of metal phthalocyanines on Ge (0 0 1) 2 × 1 surfaces". B.N. Holland, G. Cabailh, N. Peltekis, C. McGuinness, A.A. Cafolla, I.T. McGovern.
  Applied Surface Science, 255,775-777, 2008

- "The local electronic structure of tin phthalocyanine studied by resonant soft X-ray emission spectroscopies". N. Peltekis, B.N. Holland, L.F.J. Piper, A. DeMasi, K.E. Smith, J.E. Downes, I.T. McGovern, C. McGuinness.
  Applied Surface Science, 255, 764-766, 2008

- “Electronic and Optical Properties of Magnesium Phthalocyanine (MgPc) Solid Films Studied by Soft X-Ray Excited Optical Luminescence and X-Ray Absorption Spectroscopies”. N. Peltekis, B. N. Holland, S. Krishnamurthy, I. T. McGovern, N. R. J. Poolton, S. Patel and C. McGuinness.
  Journal of American Chemical Society 130 (39), 13008–13012, 2008. 10.1021/ja803063b
- “Electronic Structure of the Organic Semiconductor Alq3 (aluminum tris-8-hydroxyquinoline) from Soft X-ray Spectroscopies and Density Functional Theory Calculations”. A. DeMasi, L. F. J. Piper, Y. Zhang, I. Reid, S. Wang, K. E. Smith, J. E. Downes, N. Peltekis, C. McGuinness, and A. Matsuura.
  Journal of Chemical Physics, 129 ,224705, 2008
- “STM and synchrotron studies of the adsorption of MPc on the Ge(001)-2x1 surface”. B. N. Holland, N. Peltekis, G. Cabailh, C. McGuinness, A. A. Cafolla, I. T. McGovern.
  Surface Science submitted
- “NEXAFS studies of copper phthaloyanine on Ge(001)-2x1 and Ge(111)-c(2x8) surfaces”. B. N. Holland, N. Peltekis, T. Farrelly, R. G. Wilks, G. Gavrila, D. R. T. Zahn, C. McGuinness, and I. T. McGovern,
  Physica Status Solidi B 246 ,1546, 2009

Publications (other)

- "Gold film with gold nitride - a conductor but harder than gold" L. Siller, N. Peltekis, S. Krishnamurthy, Y. Chao, S. J. Bull, and M. R. C. Hunt. Applied Physics Letters 86, 221912 (2005)

- *"Electronic and Optical properties of Gold nitride"*N. Peltekis M.Phil Thesis, Newcastle Upon Tyne University (2005)

- "Potassium intercalation of carbon onions 'opened' by carbon dioxide treatment". Yu.V. Butenko, Amit K. Chakraborty, N. Peltekis, S. Krishnamurthy, V.R. Dhanak, M.R.C. Hunt, L. Šiller.
  Carbon, Volume 46, Issue 8, July 2008, Pages 1133-1140

9. References

[1] S. R. Forrest, "The path to ubiquitous and low-cost organic electronic appliances on plastic," Nature **428** (6986), 911-918 (2004).

[2] T.W. Kelley, P.F. Baude, C. Gerlach *et al.*, "Recent Progress in Organic Electronics: Materials, Devices, and Processes," Chem. Mater. **16** (23), 4413-4422 (2004).

[3] Y. Alfredsson, B. Brena, K. Nilson *et al.*, "Electronic structure of a vapor-deposited metal-free phthalocyanine thin film," Journal of Chemical Physics **122** (21), 214723 (2005).

[4] Kathleen.M.Vaeth, in *Information Display SID* (2003), Vol. 19, pp. 12-17.

[5] C. W. Tang and S. A. VanSlyke, "Organic electroluminescent diodes," Appl. Phys. Lett. **51** (12), 913-915 (1987).

[6] D.J. Gundlach, Y.Y. Lin, T.N. Jackson *et al.*, "Pentacene organic thin-film transistors-molecular ordering and mobility," Electron Device Letters, IEEE **18** (3), 87-89 (1997).

[7] Y.Y. Lin, D.J. Gundlach, and T.N. Jackson, presented at the Device Research Conference, 1996. Digest. 54th Annual Device Research Conference, 1996. Digest. 54th Annual VO -, 1996 (unpublished).

[8] Y.-Y. Lin, A. Dodabalapur, R. Sarpeshkar *et al.*, presented at the Device Research Conference Digest, 1999 57th Annual Device Research Conference Digest, 1999 57th Annual VO -, 1999 (unpublished).

[9] Y.Y. Lin, D.J. Gundlach, S.F. Nelson *et al.*, presented at the Device Research Conference Digest, 1997. 5th Device Research Conference Digest, 1997. 5th VO -, 1997 (unpublished).

[10] Max Shtein, Jonathan Mapel, Jay B. Benziger *et al.*, "Effects of film morphology and gate dielectric surface preparation on the electrical characteristics of organic-vapor-phase-deposited pentacene thin-film transistors," Appl. Phys. Lett. **81** (2), 268-270 (2002).

[11] C. J. Drury, C. M. J. Mutsaers, C. M. Hart *et al.*, "Low-cost all-polymer integrated circuits," Appl. Phys. Lett. **73** (1), 108-110 (1998).

[12] M. Granstrom, K. Petritsch, A.C. Arias *et al.*, "Laminated fabrication of polymeric photovoltaic diodes," Nature **395** (6699), 257-260 (1998).

[13] P. Peumans and S. R. Forrest, "Very-high-efficiency double-heterostructure copper phthalocyanine/C[sub 60] photovoltaic cells," Appl. Phys. Lett. **79** (1), 126-128 (2001).

[14] Peter Peumans, Soichi Uchida, and Stephen R. Forrest, "Efficient bulk heterojunction photovoltaic cells using small-molecular-weight organic thin films," Nature **425** (6954), 158-162 (2003).

[15] Sean E. Shaheen, Christoph J. Brabec, N. Serdar Sariciftci *et al.*, "2.5% efficient organic plastic solar cells," Appl. Phys. Lett. **78** (6), 841-843 (2001).

[16] C. W. Tang, "Two-layer organic photovoltaic cell," Appl. Phys. Lett. **48** (2), 183-185 (1986).

[17] Gilles Horowitz, "Organic Semiconductors for new electronic devices," Advanced Materials **2** (6-7), 287-292 (1990).

[18] A. R. Vearey-Roberts and D. A. Evans, "Modification of GaAs Schottky diodes by thin organic interlayers," Applied Physics Letters **86** (7), 072105 (2005).

[19] W Brütting, *Physics of Organic Semiconductors*. (WILEY-VCH, Weinheim, 2005).

[20] A.P. Kulkarni, C.J. Tonzola, A. Babel *et al.*, "Electron Transport Materials for Organic Light-Emitting Diodes," Chem. Mater. **16** (23), 4556-4573 (2004).

[21] W. Helfrich and W. G. Schneider, "Recombination Radiation in Anthracene Crystals," Physical Review Letters **14** (7), 229 - 231 (1965).

[22] S. Singh and B. P. Stoicheff, "Double-Photon Excitation of Fluorescence in Anthracene Single Crystals," The Journal of Chemical Physics **38** (8), 2032-2033 (1963).

[23] M. Pope, H. P. Kallmann, and P. Magnante, "Electroluminescence in Organic Crystals," The Journal of Chemical Physics **38** (8), 2042-2043 (1963).

[24] J. H. Burroughes, D. D. C. Bradley, A. R. Brown *et al.*, "Light-emitting diodes based on conjugated polymers," **347** (6293), 539-541 (1990).

[25] Andrew C. Grimsdale Arno Kraft, Andrew B. Holmes, "Electroluminescent Conjugated Polymers - Seeing Polymers in a New Light," Angewandte Chemie International Edition **37** (4), 402-428 (1998).

[26] C. W. Tang, S. A. VanSlyke, and C. H. Chen, "Electroluminescence of doped organic thin films," J. Appl. Phys. **65** (9), 3610-3616 (1989).

[27] Stephen R. Forrest, "Ultrathin Organic Films Grown by Organic Molecular Beam Deposition and Related Techniques," Chemical Reviews **97** (6), 1793-1896 (1997).

[28] Peter Peumans, Aharon Yakimov, and Stephen R. Forrest, "Small molecular weight organic thin-film photodetectors and solar cells," Journal of Applied Physics **93** (7), 3693-3723 (2003).

[29] J. Mack and M. J. Stillman, in *The Porphyrin Handbook* (Elsevier, 2003), Vol. 16.

[30] H. Grennberg and J. E. Backvall, "Iron Phthalocyanine as a Catalyst for the Aerobic Oxidation of Hydroquinone to 1,4-Benzoquinone - a Simple Test for Catalytic Oxidase Activity," Acta Chemica Scandinavica **47** (5), 506-508 (1993).

[31] Sylvie Faizon Helena Grennberg, Jan-E. Bäckvall, "Cobalt Tetra(hydroquinone)porphyrin: An Efficient Electron Transfer Reagent in Aerobic Pd-Catalyzed 1,4-Diacetoxylation of 1,3-Cyclohexadiene," Angewandte Chemie International Edition in English **32** (2), 263-264 (1993).

[32] Jan-E. Bäckvall Jens Wöltinger, Ágnes Zsigmond, "Zeolite-Encapsulated Cobalt Salophen Complexes as Efficient Oxygen-Activating Catalysts in Palladium-Catalyzed Aerobic 1,4-Oxidation of 1,3-Dienes," Chemistry - A European Journal **5** (5), 1460-1467 (1999).

[33] Fethi Bedioui, "Zeolite-encapsulated and clay-intercalated metal porphyrin, phthalocyanine and Schiff-base complexes as models for biomimetic oxidation catalysts: an overview," Coordination Chemistry Reviews **144**, 39-68 (1995).

[34] J Simon and P Bassoul, in *Design of molecular materials : supramolecular engineering* (Chichester : John Wiley & Sons, New York, 2000).

[35] N. R. Armstrong, "Phthalocyanines and porphyrins as materials," J. Porphyr. Phthalocyanines **4** (4), 414-417 (2000).

[36] D. Campbell and R. A. Collins, "The effect of surface topography on the sensitivity of lead phthalocyanine thin films to nitrogen dioxide," Phys. Status Solidi A-Appl. Res. **152** (2), 431-442 (1995).

[37] V. R. Zakamov, V. A. Panteleev, L. G. Pakhomov *et al.*, "Ion beam doping of chlorinated copper phthalocyanine thin films," High Energy Chem. **36** (2), 80-84 (2002).

[38] G.L. Pakhomov, L.G. Pakhomov, D.E. Pozdnyaev *et al.*, "Irradiation assisted preparation of gas sensitive layers based on halogen substituted phthalocyanines,"

1st International Seminar on Semiconductor Gas Sensors - SGS'98, Sep 22-Sep 25 1998 Electron Technology (Warsaw) **33** (1-2), 136-144 (2000).

[39] Il'yushonok I.P, Pochtennyi A.E, and Dolgiy V.K, Vacuum Technique Technol.(Russia) **3**, 48 (1993).

[40] Nguyen and Khe C., "Composite organic photoconductor having particulate charge transport layer," US-patent (5821019) (1998).

[41] Y. Shirota, "Organic materials for electronic and optoelectronic devices," Journal of Materials Chemistry **10** (1), 1-25 (2000).

[42] K.O. Sylvester-Hvid, "Two-Dimensional Simulations of CuPc-PCTDA Solar Cells: The Importance of Mobility and Molecular π Stacking," J. Phys. Chem. B **110** (6), 2618-2627 (2006).

[43] P. E. Burrows, L. S. Sapochak, D. M. McCarty *et al.*, "Metal ion dependent luminescence effects in metal tris-quinolate organic heterojunction light emitting devices," Appl. Phys. Lett. **64** (20), 2718-2720 (1994).

[44] B. J. Chen, X. W. Sun, and Y. K. Li, "Influences of central metal ions on the electroluminescene and transport properties of tris-(8-hydroxyquinoline) metal chelates," Appl. Phys. Lett. **82** (18), 3017-3019 (2003).

[45] C. C. Wu, J. K. M. Chun, P. E. Burrows *et al.*, "Poly(p-phenylene vinylene)/tris(8-hydroxy) quinoline aluminum heterostructure light emitting diode," Appl. Phys. Lett. **66** (6), 653-655 (1995).

[46] L.S. Sapochak, F.E. Benincasa, R.S. Schofield *et al.*, "Electroluminescent Zinc(II) Bis(8-hydroxyquinoline): Structural Effects on Electronic States and Device Performance," J. Am. Chem. Soc. **124** (21), 6119-6125 (2002).

[47] Stephen R. Forrest, "Ultrathin Organic Films Grown by Organic Molecular Beam Deposition and Related Techniques doi:10.1021/cr941014o," Chemical Reviews **97** (6), 1793-1896 (1997).

[48] S. Kera, M.B. Casu, K.R. Bauchspieß *et al.*, "Growth mode and molecular orientation of phthalocyanine molecules on metal single crystal substrates: A NEXAFS and XPS study," Surface Science **600** (5), 1077-1084 (2006).

[49] Alfred Cho and American Institute of Physics., *Molecular beam epitaxy*. (AIP Press, New York, 1994), pp.xiii, 570.

[50] S. R. Forrest, M. L. Kaplan, and P. H. Schmidt, "Organic-on-inorganic semiconductor contact barrier diodes. I. Theory with applications to organic thin films and prototype devices," J. Appl. Phys. **55** (6), 1492-1507 (1984).

[51] Masahiko Hara, Hiroyuki Sasabe, Akira Yamada *et al.*, "Epitaxial Growth of Organic Thin Films by Organic Molecular Beam Epitaxy," Jpn. J. Appl. Phys. **28** (Part 2, No. 2), L306 LP - L308 (1989).

[52] F. F. So, S. R. Forrest, Y. Q. Shi *et al.*, "Quasi-epitaxial growth of organic multiple quantum well structures by organic molecular beam deposition," Appl. Phys. Lett. **56** (7), 674-676 (1990).

[53] F. F. So and S. R. Forrest, "Evidence for exciton confinement in crystalline organic multiple quantum wells," Physical Review Letters **66** (20), 2649 LP - 2652 (1991).

[54] Atsushi Koma, "New epitaxial growth method for modulated structures using Van der Waals interactions," Surface Science **267** (1-3), 29-33 (1992).

[55] M. Möbus, N. Karl, and T. Kobayashi, "Structure of perylene-tetracarboxylic-dianhydride thin films on alkali halide crystal substrates," Journal of Crystal Growth **116** (3-4), 495-504 (1992).

[56] P. E. Burrows, Y. Zhang, E. I. Haskal *et al.*, "Observation and modeling of quasiepitaxial growth of a crystalline organic thin film," Appl. Phys. Lett. **61** (20), 2417-2419 (1992).

[57] J. A. Venables, G. D. T. Spiller, and M. Hanbucken, "Nucleation and growth of thin films," Reports on Progress in Physics **47** (4), 399-459 (1984).

[58] Y. Zhang and S. R. Forrest, "Mechanisms of quasiepitaxial ordering at organic molecular thin film interfaces," Physical Review Letters **71** (17), 2765 LP - 2768 (1993).

[59] P. Fenter, P. Eisenberger, P. Burrows *et al.*, "Epitaxy at the organic--inorganic interface," Physica B: Condensed Matter Proceedings of the Fourth International Conference on Surface X-ray and Neutron Scatterin **221** (1-4), 145-151 (1996).

[60] P. Fenter, P. E. Burrows, P. Eisenberger *et al.*, "Layer-by-layer quasi-epitaxial growth of a crystalline organic thin film," Journal of Crystal Growth **152** (1-2), 65-72 (1995).

[61] Eliav I. Haskal, Franky F. So, Paul E. Burrows *et al.*, "Evolution of quasi-epitaxial growth of a crystalline organic semiconductor on graphite," Appl. Phys. Lett. **60** (26), 3223-3225 (1992).

[62] S. R. Forrest and P. E. Burrows, "Growth modes of organic semiconductor thin films using organic molecular beam deposition: epitaxy, van der Waals epitaxy, and quasi-epirtaxy," Supramolecular Science **4** (1-2), 127-139 (1997).

[63] Aleksander Isaakovich Kitaigorodsky, *Molecular crystals and molecules*. (Academic Press, New York ; London, 1973), pp.xiii,553.

[64] Neil W. Ashcroft and N. David Mermin, *Solid state physics*. (Holt Rinehart and Winston, New York ; London [etc.], 1977), pp.xxi,826.

[65] J.W. Matthews and A.E. Blakeslee, "Defects in epitaxial multilayers: I. Misfit dislocations," Journal of Crystal Growth **27**, 118-125 (1974).

[66] Anthony J. Dann, Hajime Hoshi, and Yusei Maruyama, "The structure and properties of phthalocyanine films grown by the molecular beam epitaxy technique. I. Preparation and characterization," J. Appl. Phys. **67** (3), 1371-1379 (1990).

[67] Hajime Hoshi, Anthony J. Dann, and Yusei Maruyama, "The structure and properties of phthalocyanine films grown by the molecular-beam epitaxy technique. II. Ultraviolet/visible spectroscopic study," J. Appl. Phys. **67** (4), 1845-1849 (1990).

[68] Hajime Hoshi, Anthony J. Dann, and Yusei Maruyama, "The structure and properties of phthalocyanine films grown by the molecular beam epitaxy technique. III. Preparation and characterization of lutetium diphthalocyanine films," J. Appl. Phys. **67** (11), 6871-6875 (1990).

[69] Hajime Hoshi, Shaoli Fang, and Yusei Maruyama, "Epitaxial growth of lead phthalocyanine film on KI crystal," J. Appl. Phys. **73** (6), 3111-3113 (1993).

[70] Hajime Hoshi and Yusei Maruyama, "Epitaxial growth of chloroaluminum and vanadyl phthalocyanine films on alkali halide single crystals by the molecular-beam-epitaxy technique," J. Appl. Phys. **69** (5), 3046-3052 (1991).

[71] Hajime Hoshi, Yusei Maruyama, Hideki Masuda *et al.*, "A new type of epitaxial growth in lithium phthalocyanine film on KBr(100) prepared by the molecular-beam epitaxy," J. Appl. Phys. **68** (3), 1396-1398 (1990).

[72] H. Tada, T. Morioka, and A. Koma, "Epitaxial growth of ultrathin vanadyl-naphthalocyanine films on RbI, KI and KBr," Journal of Physics: Condensed Matter **6** (10), 1881-1892 (1994).

[73] Hirokazu Tada, Koichiro Saiki, and Atsushi Koma, "Structural analysis of lead phthalocyanine ultrathin films grown on cleaved faces of alkali halides by reflection high energy electron diffraction," Surface Science **268** (1-3), 387-396 (1992).

[74] J. C. Buchholz and G. A. Somorjai, "The surface structures of phthalocyanine monolayers and vapor-grown films: A low-energy electron diffraction study," The Journal of Chemical Physics **66** (2), 573-580 (1977).

[75] Takafumi Kawaguchi, Hirokazu Tada, and Atsushi Koma, "Structural analysis of epitaxial films of metal phthalocyanines on hydrogen-terminated Si(111) surfaces," J. Appl. Phys. **75** (3), 1486-1492 (1994).

[76] Hideki Yamamoto, Hirokazu Tada, Takafumi Kawaguchi *et al.*, "Epitaxial growth of metal-phthalocyanines on selenium-terminated GaAs(111) surfaces," Appl. Phys. Lett. **64** (16), 2099-2101 (1994).

[77] Hirokazu Tada, Takafumi Kawaguchi, and Atsushi Koma, "Epitaxial growth of vanadyl-phthalocyanine ultrathin films on hydrogen-terminated Si(111) surfaces," Appl. Phys. Lett. **61** (17), 2021-2023 (1992).

[78] Karl M. Kadish, Kevin M. Smith, and Roger Guilard, *The porphyrin handbook.* (Academic, San Diego, Calif. ; London, 2000), pp.xxvi, 405.

[79] Michael K. Engel, "Single-Crystal and Solid-State Molecular Structures of Phthalocyanine Complexes," Reports of Kawamura Institute Chemical Research/Kawamura Rikagaku Kenkyusho Hokoko -1996., 11-54 (1997).

[80] Joel Bernstein and International Union of Crystallography., *Polymorphism in molecular crystals.* (Oxford University Press, New York ; Oxford, 2002), pp.xiv, 410.

[81] J.D. Dunitz, "Phase changes and chemical reactions in molecular crystals," New Trends in Small Moiety Crystallography, 26 June-1 July 1994 Acta Crystallographica, Section B (Structural Science) **B51**, 619-631 (1995).

[82] G. Susich, "Identification of organic dyestuffs by X-ray powder diffraction," Analytical Chemistry **22** (3), 425-430 (1950).

[83] Andrea Birgit; Scherhag Schutze, Frank; Klopp, Ingo; Hartmann, Anette., U.S. Patent No. 5,932,723 (1999).

[84] Kock Yee. Law, "Organic photoconductive materials: recent trends and developments doi:10.1021/cr00017a020," Chemical Reviews **93** (1), 449-486 (1993).

[85] Karl M. Kadish, Kevin M. Smith, and Roger Guilard, in *The porphyrin handbook* (Academic, San Diego, Calif. ; London, 2000), Vol. 17, pp. 49,52.

[86] Peter Erk, Heidi Hengelsberg, Mairi F. Haddow *et al.*, "The innovative momentum of crystal engineering.," CrystEngComm **6** (78), 475-484 (2004).

[87] K. Ukei, "Lead phthalocyanine," Acta Crystallographica Section B **29** (10), 2290-2292 (1973).

[88] Y. Iyechika, K. Yakushi, I. Ikemoto *et al.*, "Structure of lead phthalocyanine (triclinic form)," Acta Crystallographica Section B **38** (3), 766-770 (1982).

[89] Friedel M. K. , Hoskins B. F. , and R. L. Martin and S. A. Mason, "A new metal(II) phthalocyanine structure: X-ray and Mössbauer studies of the triclinic tin(II) phthalocyanine," Journal of the Chemical Society D: Chemical Communications, 400 - 401 (1970).

[90] R. Kubiak and J. Janczak, "X-Ray-Analysis of Phthalocyanines Formed in the Reaction of Au-Cu and Au-Sn Alloys with 1,2-Dicyanobenzene," J. Alloy. Compd. **189** (1), 107-111 (1992).

[91] J. E. Downes, C. McGuinness, P. A. Glans *et al.*, "Electronic structure near the Fermi level of the organic semiconductor copper phthalocyanine," Chemical Physics Letters **390** (1-3), 203-207 (2004).

[92] Meng-Sheng Liao and S. Scheiner, "Electronic structure and bonding in metal phthalocyanines, Metal=Fe, Co, Ni, Cu, Zn, Mg," Journal of Chemical Physics **114** (22), 9780-9791 (2001).

[93] Hans Agren, Yi Luo, Faris Gelmukhanov *et al.*, "Screening in resonant X-ray emission of molecules," Journal of Electron Spectroscopy and Related Phenomena **82** (1-2), 125-134 (1996).

[94] E. Z. Kurmaev, M. I. Katsnelson, A. Moewes *et al.*, "Spectroscopic observation of polaron-lattice band structure in the conducting polymer polyaniline," Journal of Physics-Condensed Matter **13** (17), 3907-3912 (2001).

[95] W. R. K. Clark, J. N. Chapman, and R. P. Ferrier, "Structure of Alpha'-Copper Phthalocyanine and Its Susceptibility to Radiation-Damage," Nature **277** (5695), 368-370 (1979).

[96] N. Ohta and M. Gomi, "Photochemical decomposition of Co phthalocyanine films using ultraviolet excimer lamp," Japanese Journal of Applied Physics Part 1-Regular Papers Short Notes & Review Papers **39** (7A), 4195-4197 (2000).

[97] E.Z. Kurmaev, S.N. Shamin, V.R. Galakhov *et al.*, "Electronic structure of thiophenes and phtalocyanines," Physical Review B (Condensed Matter and Materials Physics) **64** (4), 045211/045211-045217 (2001).

[98] E. Tegeler, M. Iwan, and E.-E. Koch, "Electronic structure of the valence bands of H_2-, Mg- and Pt-phthalocyanine derived from soft X-ray emission and photoelectron emission spectra," Journal of Electron Spectroscopy and Related Phenomena **22** (3-4), 297-307 (1981).

[99] G. Cabailh, J. W. Wells, I. T. McGovern *et al.*, "Synchrotron radiation studies of the growth and beam damage of tin-phthalocyanine on GaAs(001)-1x6 substrates," Applied Surface Science **234** (1-4), 144-148 (2004).

[100] A. Nilsson, "Applications of core level spectroscopy to adsorbates," Journal of Electron Spectroscopy and Related Phenomena **126** (1-3), 3-42 (2002).

[101] Jens Als-Nielsen and Des McMorrow, *Elements of modern X-ray physics*. (Wiley, New York ; Chichester, 2001), pp.xi, 318.

[102] A. C. Thompson, *X-ray Data Booklet*, 2nd ed. (Lawrence Berkeley National Laboratory,University of California,CA 94720, Berkeley, 2001).

[103] M. O. Krause, "Atomic radiative and radiationless yields for K and L shells," J. Phys. Chem. Ref. Data **8** (2), 307-327 (1979).

[104] Anne Thorne, Ulf Litzen , and Sveneric Johansson, *Spectrophysics: Principles and Applications*. (Springer-Verlag Berlin and Heidelberg GmbH & Co. K, Berlin, 1999), p.447.

[105] P. van der Straten, R. Morgenstern, and A. Niehaus, "Angular dependent post-collision interaction in auger processes," Zeitschrift fur Physik D Atoms, Molecules and Clusters **8** (1), 35-45 (1988).

[106] L. J. Medhurst, P. A. Heimann, M. R. F. Siggel *et al.*, "Vibrationally Resolved Threshold Photoemission of N2 and Co at the N-K Edge and C-K Edge," Chemical Physics Letters **193** (6), 493-498 (1992).

[107] J. E. Downes, *Soft x-ray spectroscopic studies of the electronic structure of organic molecular superconductors and semiconductors*. (PhD thesis Boston University, Boston, 2004), p.170.

[108] Joachim Stöhr, *NEXAFS Spectroscopy*. (Springer, Berlin, 1992).

[109] F. Sette, J. Stohr, and A. P. Hitchcock, "Determination of intramolecular bond lengths in gas phase molecules from K shell shape resonances," The Journal of Chemical Physics **81** (11), 4906-4914 (1984).

[110] N.R.J. Poolton, A.E.R. Malins, F.M. Quinn *et al.*, "Luminescence excitation characteristics of Ca-, Na- and K-aluminosilicates," Journal of Physics D: Applied Physics **36** (9), 1107-1114 (2003).

[111] N.R.J. Poolton, L. Botter-Jensen, P.M. Denby *et al.*, "High-sensitivity instrumentation for spectrally-resolved optically detected X-ray absorption spectroscopy," Nuclear Instruments and Methods in Physics Research, Section B: Beam Interactions with Materials and Atoms **225** (4), 590-598 (2004).

[112] Barbara Brena, *First principles modeling of soft X-ray spectroscopy of complex systems*. (Royal Institute of Technology, Stockholm, 2005), p.15.

[113] E. Hückel, "Zur Quantentheorie der Doppelbindung," Zeitschrift für Physik **60**, 423-580 (1930).

[114] B.N. Holland, *An experimental investigation of metal phthalocyanine-germanium interfaces*. (PhD thesis Trinity College, Dublin, 2009), p.138.

[115] F. Gel'mukhanov and H. Agren, "Resonant X-ray Raman scattering," Phys. Rep.-Rev. Sec. Phys. Lett. **312** (3-6), 87-330 (1999).

[116] A. Kotani and S. Shin, "Resonant inelastic x-ray scattering spectra for electrons in solids," Reviews of Modern Physics **73** (1), 203-246 (2001).

[117] A. Föhlisch, J. Hasselström, P. Bennich *et al.*, "Ground-state interpretation of x-ray emission spectroscopy on adsorbates: CO adsorbed on Cu(100)," Phys. Rev. B J1 - PRB **61** (23), 16229 - 16240 (2000).

[118] Hans Ågren, Yi Luo, Faris Gelmukhanov *et al.*, "Screening in resonant X-ray emission of molecules," Journal of Electron Spectroscopy and Related Phenomena **82** (1-2), 125-134 (1996).

[119] F. Gel'mukhanov and H. Agren, "Resonant X-ray Raman scattering," Physics Reports-Review Section of Physics Letters **312** (3-6), 91 (1999).

[120] Shuichi Emura, Toshihiro Moriga, Jun Takizawa *et al.*, "Optical-luminescence yield spectra produced by x-ray excitation," Phys Rev B **47** (12), 6918 - 6930 (1993).

[121] G. L. Pakhomov, L. G. Pakhomov, V. I. Shashkin *et al.*, "Implantation and annealing effects in molecular organic films," Nuclear Instruments and Methods in Physics Research Section B: Beam Interactions with Materials and Atoms **194** (3), 269-280 (2002).

[122] H. U. Muller, M. Zharnikov, B. Volkel *et al.*, "Low-Energy Electron-Induced Damage in Hexadecanethiolate Monolayers," The Journal of Physical Chemistry B **102** (41), 7949-7959 (1998).

[123] S. Nagamatsu, M. Ono1, S. Kera *et al.*, "Multiple Scattering Approach to Polarization-Dependent F K-edge XANES Spectra of Polytetrafluoroethylene," Proc. Int. Symp. Super-Functionality Organic Devices IPAP Conf. Series **6**, 84-87 (2005).

[124] J. R. Fryer, "Molecular arrays and molecular structure in organic thin films observed by electron microscopy," Journal of Physics D: Applied Physics **26** (8B), B137-B144 (1993).

[125] Y. Murata, J.R. Fryer, T. Baird *et al.*, "Radiation damage of an organic crystal," Acta Crystallographica, Section A (Crystal Physics, Diffraction, Theoretical and General Crystallography) **A33**, 198-200 (1977).

[126] J.R. Fryer and F. Holland, "High resolution electron microscopy of molecular crystals. III. Radiation processes at room temperature," Proceedings of the Royal Society of London, Series A (Mathematical and Physical Sciences) **393** (1805), 353-369 (1984).

[127] Ralf Muller, Edgar Weckert, Johannes Zellner *et al.*, "Investigation of radiation-dose-induced changes in organic light-atom crystals by accurate d-spacing measurementsPresented at the `Second International Workshop on Radiation Damage to Crystalline Biological Samples' held at Advanced Photon Source, Chicago, USA, in December 2001.," Journal of Synchrotron Radiation **9** (6), 368-374 (2002).

[128] W. R. K. Clark, J. N. Chapman, A. M. MacLeod *et al.*, "Radiation damage mechanisms in copper phthalocyanine and its chlorinated derivatives," Ultramicroscopy **5** (1-3), 195-208 (1980).

[129] Rudolf Slota and Gabriela Dyrda, "UV Photostability of Metal Phthalocyanines in Organic Solvents," Inorganic Chemistry **42** (18), 5743-5750 (2003).

[130] John R. Helliwell, *Macromolecular crystallography with synchrotron radiation*. (Cambridge Universitry Press, 1992), p.[480].

[131] Martyn C.R. Symons, "Chemical aspects of electron-beam interactions in the solid state," Ultramicroscopy **10** (1-2), 15-23 (1982).

[132] J.R. Fryer, C.H. McConnell, F. Zemlin *et al.*, "Effect of temperature on radiation damage to aromatic organic molecules," Ultramicroscopy **40** (2), 163-169 (1992).

[133] A.E. Dray, R. Rachel, W.O. Saxton *et al.*, "Beam damage in a transition-metal-containing poly-yne," Ultramicroscopy **41** (1-3), 83-88 (1992).

[134] R. Denecke, P. Vaterlein, M. Bassler *et al.*, "Beamline I511 at MAX II, capabilities and performance," Vacuum Ultraviolet Radiation Physics. 12th International Conference, 3-7 Aug. 1998 Journal of Electron Spectroscopy and Related Phenomena **101-103**, 971-977 (1999).

[135] J.-H. Guo, N. Wassdahl, P. Skytt *et al.*, "End station for polarization and excitation energy selective soft x-ray fluorescence spectroscopy," Rev. Sci. Instrum. **66**, 1561-1563 (February 00, 1995).

[136] Grégory Cabailh, *Synchrotron radiation studies of organic/inorganic semiconductor interfaces*. (PhD thesis Trinity College, Dublin, 2005), p.1v.

[137] N. Papageorgiou, Y. Ferro, E. Salomon *et al.*, "Geometry and electronic structure of lead phthalocyanine: Quantum calculations via density-functional theory and photoemission measurements," Phys Rev B **68** (23), 235105 (2003).

[138] Fabrizio Evangelista, Vincenzo Carravetta, Giovanni Stefani *et al.*, "Electronic structure of copper phthalocyanine: An experimental and theoretical study of occupied and unoccupied levels," The Journal of Chemical Physics **126** (12), 124709-124710 (2007).

[139] Xue Cai Yuexing Zhang, Xianxi Zhang, Hui Xu, Zhongqiang Liu, Jianzhuang Jiang,, "Time-dependent density functional theory studies of the electronic absorption spectra of metallophthalocyanines of group IVA," International Journal of Quantum Chemistry **107** (4), 952-961 (2007).

[140] S.P. Keizer, J. Mack, B.A. Bench *et al.*, "Spectroscopy and Electronic Structure of Electron Deficient Zinc Phthalocyanines," J. Am. Chem. Soc. **125** (23), 7067-7085 (2003).

[141] V.Yu. Aristov, O.V. Molodtsova, V. Maslyuk *et al.*, "Electronic structure of pristine CuPc: Experiment and calculations," Applied Surface Science Proceedings of the 13th International Conference on Solid Films and Surfaces - ICSFS 13 **254** (1), 20-25 (2007).

[142] B. Brena, S. Carniato, and Y. Luo, "Functional and basis set dependence of K-edge shake-up spectra of molecules," Journal of Chemical Physics **122** (18) (2005).

[143] B. Brena, Y. Luo, M. Nyberg *et al.*, "Equivalent core-hole time-dependent density functional theory calculations of carbon 1s shake-up states of phthalocyanine," Phys. Rev. B J1 - PRB **70** (19) (2004).

[144] B. Brena and Y. Luo, "Time-dependent DFT calculations of core electron shake-up states of metal-(free)-phthalocyanines," Radiation Physics and Chemistry Proceedings of the 20th International Conference on X-ray and Inner-Shell Processes - 4-8 July 2005, Melbourne, Australia, Proceedings of the 20th International Conference on X-ray and Inner-Shell Processes **75** (11), 1578-1581 (2006).

[145] G. Cabailh, J. W. Wells, I. T. McGovern *et al.*, "Synchrotron radiation studies of the growth and beam damage of tin-phthalocyanine on GaAs(0 0 1)-1 × 6 substrates," Applied Surface Science, The Ninth International Conference on the Formation of Semiconductor Interfaces, **234** (1-4), 144-148 (2004).

[146] Peter O'Neill, David L. Stevens, and Elspeth F. Garman, "Physical and chemical considerations of damage induced in protein crystals by synchrotron radiation: a radiation chemical perspective," Presented at the `Second International Workshop on X-ray Damage to Crystalline Biological Samples' held at the Advanced Photon Source, Chicago, USA, in December 2001. Journal of Synchrotron Radiation **9** (6), 329-332 (2002).

[147] X. Crispin, J. Cornil, R. Friedlein *et al.*, "Electronic Delocalization in Discotic Liquid Crystals: A Joint Experimental and Theoretical Study," J. Am. Chem. Soc. **126** (38), 11889-11899 (2004).

[148] V. Lemaur J. Cornil, J.-P. Calbert, J.-L. Brédas,, "Charge Transport in Discotic Liquid Crystals: A Molecular Scale Description," Advanced Materials **14** (10), 726-729 (2002).

[149] E.F. Valeev, V. Coropceanu, D.A. daSilvaFilho *et al.*, "Effect of Electronic Polarization on Charge-Transport Parameters in Molecular Organic Semiconductors," J. Am. Chem. Soc. **128** (30), 9882-9886 (2006).

[150] H. Yamane, H. Honda, H. Fukagawa *et al.*, presented at the Ninth International Conference on Electronic Spectroscopy and Science - ICESS 9, 30 June-4 July 2003 Journal of Electron Spectroscopy and Related Phenomena, Netherlands, 2004 (unpublished).

[151] A. Miyamoto, K. Nichogi, A. Taomoto *et al.*, "Structural control of evaporated lead-phthalocyanine films," Thin Solid Films **256** (1-2), 64-67 (1995).

[152] W.Y. Tong, A.B. Djurisic, M.H. Xie *et al.*, "Metal Phthalocyanine Nanoribbons and Nanowires," J. Phys. Chem. B **110** (35), 17406-17413 (2006).

[153] Z. G. Ji, K. W. Wong, M. Wang *et al.*, "X-ray photoemission study of low-energy ion beam induced changes on copper phthalocyanine film," Nuclear Instruments and Methods in Physics Research Section B: Beam Interactions with Materials and Atoms **174** (3), 311-316 (2001).

[154] M. Bader, J. Haase, K. -H. Frank *et al.*, "Orientational Phase Transition in the System Pyridine/Ag(111): A Near-Edge X-Ray-Absorption Fine-Structure Study," Physical Review Letters **56** (18), 1921 LP - 1924 (1986).

[155] C. Kolczewski, R. Puttner, O. Plashkevych *et al.*, "Detailed study of pyridine at the C 1s and N 1s ionization thresholds: The influence of the vibrational fine structure," Journal of Chemical Physics **115** (14), 6426-6437 (2001).

[156] K. Ukei, K. Takamoto, and E. Kanda, "Lead Phthalocyanine: A one-dimensional conductor," Physics Letters A **45** (4), 345-346 (1973).

[157] G. Cabailh, B.N. Holland, C. Stephens *et al.*, "Soft X-ray photoelectron spectroscopy of metal-phthalocyanines on the (001) surface of GaAs and Ge," ICFSI-10 - 10th International Conference on the Formation of Semiconductor Interfaces, Jul 3-8 2005. Journal De Physique. IV **132**, 11-15 (2006).

[158] K.J. Randall, J. Feldhaus, W. Erlebach *et al.*, "Soft X-ray spectroscopy beam line on the NSLS X1 undulator: optical design and first performance tests," 4th International Conference on Synchrotron Radiation Instrumentation, 15-19 July 1991 Review of Scientific Instruments **63** (1), 1367-1370 (1992).

[159] J. Nordgren, G. Bray, S. Cramm *et al.*, "Soft x-ray emission spectroscopy using monochromatized synchrotron radiation (invited)," INTERNATIONAL CONFER-

ENCE ON SYNCHROTRON RADIATION INSTRUMENTATION Rev. Sci. Instrum **60** (7), 1690-1696 (1989).

[160] J. Nordgren, G. Bray, S. Cramm *et al.*, "Soft x-ray emission spectroscopy using monochromatized synchrotron radiation (invited)," INTERNATIONAL CONFERENCE ON SYNCHROTRON RADIATION INSTRUMENTATION Rev. Sci. Instrum. **60** (7), 1690-1696 (1989).

[161] Li Wang, Dongchen Qi, Lei Liu *et al.*, "Molecular Orientation and Ordering during Initial Growth of Copper Phthalocyanine on Si(111)," The Journal of Physical Chemistry C **111** (8), 3454-3458 (2007).

[162] Indro Biswas, Heiko Peisert, Mathias Nagel *et al.*, "Buried interfacial layer of highly oriented molecules in copper phthalocyanine thin films on polycrystalline gold," The Journal of Chemical Physics **126** (17), 174704-174705 (2007).

[163] T. Okajima, H. Fujimoto, M. Sumitomo *et al.*, "Soft x-ray absorption spectra of the lithium phthalocyanine radical," Thirteenth International Conference on Vacuum Ultraviolet Radiation Physics, 23-27 July 2001 Surface Review and Letters **9** (1), 441-446 (2002).

[164] Yasuhisa Naitoh, Takuya Matsumoto, Ken-ichi Sugiura *et al.*, "Self-assembled stripe structure of zinc-phthalocyanine on graphite surfaces," Surface Science **487** (1-3), L534-L540 (2001).

[165] A. C. Brieva, T. E. Jenkins, D. G. Jones *et al.*, "Internal structure of copper(II)-phthalocyanine thin films on SiO_2/Si substrates investigated by grazing incidence x-ray reflectometry," J. Appl. Phys. **99** (7), 073504-073503 (2006).

[166] K. Hermann, L.G.M. Pettersson, M.E. Casida *et al.*, *StoBe-deMon version 3.0.* (2007).

[167] A.St-Amant, *http://www.demon-software.com*. (Universit'e de Montreal, Montreal, 1992).

[168] Luciano Triguero, Yi Luo, Lars G. M. Pettersson *et al.*, "Resonant soft-x-ray emission spectroscopy of surface adsorbates: Theory, computations, and measurements of ethylene and benzene on Cu(110)," Phys Rev B **59** (7), 5189 - 5200 (1999).

[169] Y. Luo, H. Agren, and F. Gelmukhanov, "Polarization anisotropy in resonant x-ray emission from molecules," Phys. Rev. A **53** (3), 1340-1348 (1996).

[170] R.A. Collins and A. Belghachi, "Structural properties of lead phthalocyanine thin films," Materials Letters **8** (9), 349-352 (1989).

[171] L. Zhang, H. Peisert, I. Biswas *et al.*, "Growth of zinc phthalocyanine onto ZnS film investigated by synchrotron radiation-excited X-ray photoelectron and near-edge absorption spectroscopy," Surface Science **596** (1-3), 98-107 (2005).

[172] W. Robert Scheidt and W. Dow, "Molecular stereochemistry of phthalocyanatozinc(II)," Journal of the American Chemical Society **99** (4), 1101-1104 (1977).

[173] Weiying Gao and Antoine Kahn, "Electronic structure and current injection in zinc phthalocyanine doped with tetrafluorotetracyanoquinodimethane: Interface versus bulk effects," Organic Electronics **3** (2), 53-63 (2002).

[174] D. Schlettwein, H. Graaf, J.-P. Meyer *et al.*, "Molecular Interactions in Thin Films of Hexadecafluorophthalocyaninatozinc (F16PcZn) as Compared to Islands of N,N'-Dimethylperylene-3,4,9,10-biscarboximide (MePTCDI)," The Journal of Physical Chemistry B **103** (16), 3078-3086 (1999).

[175] Zhenan Bao, Andrew J. Lovinger, and Janelle Brown, "New Air-Stable n-Channel Organic Thin Film Transistors," Journal of the American Chemical Society **120** (1), 207-208 (1998).

[176] Lai Kwan Chau, Craig D. England, Siying Chen *et al.*, "Visible absorption and photocurrent spectra of epitaxially deposited phthalocyanine thin films: interpretation of exciton coupling effects," The Journal of Physical Chemistry **97** (11), 2699-2706 (1993).

[177] Eiji Kawabe, Daisuke Yoshimura, Kaname Kanai *et al.*, "Epitaxial growth of hexadecafluorozincphthalocyanine (F16ZnPc) film deposited on GeS(0 0 1)," Surface Science **602** (7), 1328-1336 (2008).

[178] T. Ikame, K. Kanai, Y. Ouchi *et al.*, "Molecular orientation of F16ZnPc deposited on Au and Mg substrates studied by NEXAFS and IRRAS," Chemical Physics Letters **413** (4-6), 373-378 (2005).

[179] F. Hennies, S. Polyutov, I. Minkov *et al.*, "Nonadiabatic Effects in Resonant Inelastic X-Ray Scattering," Physical Review Letters **95** (16), 163002 (2005).

[180] F. Hennies, S. Polyutov, I. Minkov *et al.*, "Dynamic interpretation of resonant x-ray Raman scattering: Ethylene and benzene," Physical Review A (Atomic, Molecular, and Optical Physics) **76** (3), 032505-032513 (2007).

[181] M. Bowler, J.B. West, F.M. Quinn *et al.*, presented at the Thirteenth International Conference on Vacuum Ultraviolet Radiation Physics, 23-27 July 2001 Surface Review and Letters, Singapore, 2002 (unpublished).

[182] SRS, *MPW6.1 Phoenix beamline overview http://srs.dl.ac.uk/XUV-VUV/science/mpw6.1/images/image10.gif.* (Synchrotron Radiation Source, Daresbury Laboratory,Warrington).

[183] F. Quinn, N. Poolton, A. Malins *et al.*, "The Mobile Luminescence End-Station, MoLES: a new public facility at Daresbury Synchrotron," Journal of Synchrotron Radiation **10**, 461-466 (2003).

[184] G. Cabailh, B. N. Holland, C. Stephens *et al.*, "Soft X-ray photoelectron spectroscopy of metal-phthalocyanines on the (001) surface of GaAs and Ge," J. Phys. IV **132**, 11-15 (2006).

[185] P. C. Minor, M. Gouterman, and A. B. P. Lever, "Electronic spectra of phthalocyanine radical anions and cations," Inorg. Chem. **24** (12), 1894-1900 (1985).

[186] John Mack, Scott Kirkby, Edward A. Ough *et al.*, "Ground-state and optical spectrum of metallophthalocyanine radical anions from low-temperature magnetic circular dichroism spectroscopy," Inorg. Chem. **31** (9), 1717-1719 (1992).

[187] Tebello Nyokong, Zbigniew Gasyna, and Martin J. Stillman, "Analysis of the absorption and magnetic circular dichroism spectra of zinc phthalocyanine and the .π-cation-radical species $[ZnPc(1-)]^+$." Inorg. Chem. **26** (7), 1087-1095 (1987).

[188] Edward Ough, Zbigniew Gasyna, and Martin J. Stillman, "Photochemical, electrochemical, and chemical formation of the π-cation-radical species of magnesium phthalocyanine. Analysis of the absorption and MCD spectra of $[MgPc(-1)]^+$." Inorg. Chem. **30** (10), 2301-2310 (1991).

[189] Edward A. Ough and Martin J. Stillman, "Analysis of the absorption and magnetic circular dichroism spectra of low spin (S = 1/2) iron(III) phthalocyanine," Inorg. Chem. **34** (17), 4317-4325 (1995).

[190] Edward Ough, Tebello Nyokong, Katherine A. M. Creber *et al.*, "Electrochemistry and spectroscopy of magnesium phthalocyanine. Analysis of the absorption and magnetic circular dichroism spectra," Inorg. Chem. **27** (15), 2724-2732 (1988).

[191] Charles Weiss, Hiroshi Kobayashi, and Martin Gouterman, "Spectra of porphyrins : Part III. Self-consistent molecular orbital calculations of porphyrin and related ring systems," Journal of Molecular Spectroscopy **16** (2), 415-450 (1965).

[192] A.J. McHugh, M. Gouterman, and C. Weiss, Jr., "Porphyrins XXIV. Energy, oscillator strength, and Zeeman splitting calculations (SCMO-CI) for phthalocyanine, porphyrins, and related ring systems," Theoretica Chimica Acta **24** (4), 346-370 (1972).

[193] Martin Gouterman, Georges H. Wagniere, and Lawrence C. Snyder, "Spectra of porphyrins : Part II. Four orbital model," Journal of Molecular Spectroscopy **11** (1-6), 108-127 (1963).

[194] John Mack and Martin J. Stillman, "Assignment of the optical spectrum of metal porphyrin and phthalocyanine radical anions," J. Porphyr. Phthalocyanines **5** (1), 67-76 (2001).

[195] B.R. Hollebone and M.J. Stillman, "Assignment of absorption and magnetic circular dichroism spectra of solid, α phase metallophthalocyanines," Journal of the Chemical Society Faraday Transactions II **74**, 2107-2127 (1978).

[196] James H. Sharp and Marcel Lardon, "Spectroscopic characterization of a new polymorph of metal-free phthalocyanine," J. Phys. Chem. **72** (9), 3230-3235 (1968).

[197] T.K. Sham, D.T. Jiang, I. Coulthard *et al.*, "Origin of luminescence from porous silicon deduced by synchrotron-light-induced optical luminescence," Nature **363** (6427), 331 (1993).

[198] P. S. Vincett, E. M. Voigt, and K. E. Rieckhoff, "Phosphorescence and Fluorescence of Phthalocyanines," The Journal of Chemical Physics **55** (8), 4131-4140 (1971).

[199] M. Wojdyla, W. Bala, B. Derkowska *et al.*, "The temperature dependence of photoluminescence and absorption spectra of vacuum-sublimed magnesium phthalocyanine thin films," Opt. Mater. **30** (5), 734-739 (2008).

[200] A. Endo, S. Matsumoto, and J. Mizuguchi, "Interpretation of the Near-Infrared Absorption of Magnesium Phthalocyanine Complexes in Terms of Exciton Coupling Effects," J. Phys. Chem. A **103** (41), 8193-8199 (1999).

[201] J. Janczak and Y. M. Idemori, "Synthesis, crystal structure and characterisation of aquamagnesium phthalocyanine-MgPc(H2O). The origin of an intense near-IR absorption of magnesium phthalocyanine known as 'X-phase'," Polyhedron **22** (9), 1167-1181 (2003).

[202] Jan Janczak and Ryszard Kubiak, "X-ray single crystal investigations of magnesium phthalocyanine. The 4+1 coordination of the Mg ion and its consequence," Polyhedron **20** (24-25), 2901-2909 (2001).

[203] J. Mizuguchi, "Crystal Structure of Magnesiumphthalocyanine and Its Polarized Reflection Spectra," J. Phys. Chem. A **105** (7), 1121-1124 (2001).

[204] Aleksandr Sergeevich Davydov, *Theory of molecular excitons*. (New York,, 1962).

[205] D. P. Craig and P. C. Hobbins, "The Polarized Spectrum of Anthracene .1. The Assignment of the Intense Short Wave-Length System," Journal of the Chemical Society, 539-548 (1955).

[206] T.-H. Huang, K. E. Rieckhoff, and E. M. Voigt, "Shpol'skii effect and vibronic spectra of the phthalocyanines," The Journal of Chemical Physics **77** (7), 3424-3441 (1982).

[207] D. A. Evans, A. R. Vearey-Roberts, and N. R. J. Poolton, "Locating hexagonal and cubic phases in boron nitride using wavelength-selective optically detected x-ray absorption spectroscopy," Appl. Phys. Lett. **89** (16), 161107-161103 (2006).

[208] Y. Niwa, Kobayash.H, and T. Tsuchiya, "X-Ray Photoelectron-Spectroscopy of Tetraphenylporphin and Phthalocyanine," Journal of Chemical Physics **60** (3), 799-807 (1974).

[209] C. Kolczewski, R. Puttner, O. Plashkevych *et al.*, "Detailed study of pyridine at the C 1*s* and N 1*s* ionization thresholds: The influence of the vibrational fine structure," The Journal of Chemical Physics **115** (14), 6426-6437 (2001).

[210] S. Kera, M. B. Casu, A. Scholl *et al.*, "High-resolution inner-shell excitation spectroscopy of H-2-phthalocyanine," Journal of Chemical Physics **125** (1), 014705 (2006).

[211] Thomas C. Van Cott, Janna L. Rose, G. Christian Misener *et al.*, "Magnetic circular dichroism and absorption spectrum of zinc phthalocyanine in an argon matrix between 14700 and 74000 cm-1," J. Phys. Chem. **93** (8), 2999-3011 (1989).

[212] Tzer-Hsiang Huang, Klaus E. Rieckhoff, and Eva M. Voigt, "New singlets in the phthalocyanines," J. Phys. Chem. **85** (22), 3322-3326 (1981).

[213] P.-S. Kim, T.-K. Sham, P. Zhang *et al.*, "X-ray Excited Optical Luminescence Studies of Tris-(2,2'-bipyridine)ruthenium(II) at the C, N K-edge and Ru $L_{3,2}$-edge," J. Am. Chem. Soc. **123** (36), 8870-8871 (2001).

[214] A. Bianconi, D. Jackson, and K. Monahan, "Intrinsic luminescence excitation spectrum and extended x-ray absorption fine structure above the K edge in CaF_{2}," Phys Rev B **17** (4), 2021 LP - 2024 (1978).

[215] C. H. Chen and Jianmin Shi, "Metal chelates as emitting materials for organic electroluminescence," Coordination Chemistry Reviews Twelfth International Symposium on Photochemistry and Photophysics of Coordination Compounds **171**, 161-174 (1998).

[216] Alessandro Curioni, Mauro Boero, and Wanda Andreoni, "Alq3: ab initio calculations of its structural and electronic properties in neutral and charged states," Chemical Physics Letters **294** (4-5), 263-271 (1998).

[217] A. Curioni and W. Andreoni, "Computer simulations for organic light-emitting diodes," IBM Journal of Research and Development **45** (1), 101-113 (2001).

[218] Martin Brinkmann, Gregory Gadret, Michele Muccini *et al.*, "Correlation between Molecular Packing and Optical Properties in Different Crystalline Polymorphs and Amorphous Thin Films of mer-Tris(8-hydroxyquinoline)aluminum(III)," Journal of the American Chemical Society **122** (21), 5147-5157 (2000).

[219] A. DeMasi, *Electronic properties of organic semiconductors investigated by RXES, NEXAFS and XPS studies (to be published)*. (Boston University, Boston, 2009).

[220] A. DeMasi, L. F. J. Piper, Y. Zhang *et al.*, "Electronic structure of the organic semiconductor Alq[sub 3] (aluminum tris-8-hydroxyquinoline) from soft x-ray spectroscopies and density functional theory calculations," The Journal of Chemical Physics **129** (22), 224705-224707 (2008).

[221] Dan V Nicolau and Susumu Yoshikawa, "Molecular modelling of Me2+- (8-hydroxy-quinolinate)2 complexes using ZINDO and ESSF methods," Journal of Molecular Graphics and Modelling **16** (2), 83-96 (1998).

[222] L. L. Merritt, R. T. Cady, and B. W. Mundy, "The crystal structure of zinc 8-hydroxyquinolinate dihydrate," Acta Crystallographica **7** (6-7), 473-476 (1954).

[223] G. Palenik, "The structure of coordination compounds. III. A refinement of the structure of zinc 8-hydroxyquinolinate dihydrate 8," Acta Crystallographica **17** (6), 696-700 (1964).

[224] Y. Kai, Morita, M. ,Yasuoka, N., Kasai, N., "The Crystal and Molecular Structure of Anhydrous Zinc 8-Quinolinolate Complex, [Zn(C9H6NO)2]4," Bulletin of Chemical Society Japan **58**, 1631-1635 (1985).

[225] T. A. Hopkins, K. Meerholz, S. Shaheen *et al.*, "Substituted Aluminum and Zinc Quinolates with Blue-Shifted Absorbance/Luminescence Bands:Synthesis and Spectroscopic, Photoluminescence, and Electroluminescence Characterization," Chemistry of Materials **8** (2), 344-351 (1996).

[226] L.S. Sapochak, A. Falkowitz, K.F. Ferris *et al.*, "Supramolecular Structures of Zinc (II) (8-Quinolinolato) Chelates," J. Phys. Chem. B **108** (25), 8558-8566 (2004).

[227] T. W. Pi, T. C. Yu, C. P. Ouyang *et al.*, "Electronic structure of tris(8-hydroxyquinolato) aluminum at room temperature and during annealing," Phys Rev B **71** (20), 205310 (2005).

[228] K. C. Prince, I. Ulrych, M. Peloi *et al.*, "Core-level photoemission from graphite," Phys Rev B **62** (11), 6866 - 6868 (2000).

[229] F. Sette, G. K. Wertheim, Y. Ma *et al.*, "Lifetime and screening of the C 1s photo-emission in graphite," Phys. Rev. B J1 - PRB **41** (14), 9766 - 9770 (1990).

[230] J. A. Bearden, "X-Ray Wavelengths," Reviews of Modern Physics **39** (1), 78 - 124 (1967).

[231] Vasilis P. Barberis and John A. Mikroyannidis, "Synthesis and optical properties of aluminum and zinc quinolates through styryl subsituent in 2-position," Synthetic Metals **156** (11-13), 865-871 (2006).

[232] T.A. Hopkins, K. Meerholz, S. Shaheen *et al.*, "Substituted Aluminum and Zinc Quinolates with Blue-Shifted Absorbance/Luminescence Bands: Synthesis and Spectroscopic, Photoluminescence, and Electroluminescence Characterization," Chem. Mater. **8** (2), 344-351 (1996).

[233] Xu Bing-she, Hao Yu-ying, Wang Hua *et al.*, "The effects of crystal structure on optical absorption/photoluminescence of bis(8-hydroxyquinoline)zinc," Solid State Communications **136** (6), 318-322 (2005).

[234] P. E. Burrows, Z. Shen, V. Bulovic *et al.*, "Relationship between electroluminescence and current transport in organic heterojunction light-emitting devices," J. Appl. Phys. **79** (10), 7991-8006 (1996).

[235] O. Fuchs, L. Weinhardt, M. Blum *et al.*, Review of Scientific Instruments, (to be published) (2009).

[236] L. Weinhardt, O. Fuchs, A. Fleszar *et al.*, "Resonant inelastic soft x-ray scattering of CdS: A two-dimensional electronic structure map approach," Physical Review B (Condensed Matter and Materials Physics) **79** (16), 165305-165305 (2009).

[237] Xiaobo Chen, Per-Anders Glans, Xiaofeng Qiu *et al.*, "X-ray spectroscopic study of the electronic structure of visible-light responsive N-, C- and S-doped TiO2," Journal of Electron Spectroscopy and Related Phenomena **162** (2), 67-73 (2008).

Appendix I

Tabulate fitting parameters for the C 1s, N 1s, Pb 5d and VB phtoemission spectra for the 5min synchrotron radiation exposure of the thick PbPc film (Fig. 30).

Table 2 Fitting parameters of C 1s and N1s, Pb 5d and VB photoemission spectra of 5 min synchrotron radiation exposure of PbPc thick film (Fig. 30).

	E_{bind} (eV)	FWHM	% shake up	E_{split} (shake up) (eV)	Integrated Area
1A: benzene ring C 1s sp^2+2p_z	284.58	0.66	8.0	1.87	240.3
2A: benzene ring C 1s sp^2	284.81	0.66	8.0	1.87	118.3
3A: pyrrole C 1s	285.93	0.66	16	1.91	122.1
1B: benzene ring C 1s sp^2+2p_z	284.37	0.66	8.0	1.87	115.3
2B: benzene ring C 1s sp^2	284.64	0.66	12	1.87	56.2
3B: pyrrole C 1s	285.52	0.66	11.9	1.91	52.8
A: N 1s	398.66	0.69	3.9	1.72	145.5
B: N 1s	398.37	0.69	4.3	1.72	67.0
A: VB HOMO	1.60	0.74	-	-	193.1
B: VB HOMO	1.05	0.74	-	-	109.9
A: Pb 5d 5/2	19.7	0.93	-	-	7651.7
B: Pb 5d 5/2	19.94	0.93	-	-	1272.8

Tabulate fitting parameters for the C 1s, N 1s, Pb 5d and VB phtoemission spectra for the 10min synchrotron radiation exposure of the thick PbPc film (Fig. 32).

Table 3 Fitting parameters of C 1s and N1s, Pb 5d and VB photoemission spectra of 10 min synchrotron radiation exposure of PbPc thick film (Fig. 32).

	E_{bind} (eV)	FWHM	% shake up	E_{split} (shake up) (eV)	Integrated Area
1A: benzene ring C 1s sp^2+2p$_z$	284.57	0.68	20.3	1.76	117.8
2A: benzene ring C 1s sp^2	285.1	0.68	23.3	1.87	137.4
3A: pyrrole C 1s	285.93	0.68	10.0	1.93	48.3
1B: benzene ring C 1s sp^2+2p$_z$	284.35	0.68	7.6	1.76	167.1
2B: benzene ring C 1s sp^2	284.73	0.68	21.6	1.77	95.6
3B: pyrrole C 1s	285.57	0.68	23.0	1.83	80.7
C: C 1s	283.88	0.68	13.0	1.76	45.8
A: N 1s	398.65	0.69	3.0	1.90	61.0
B: N 1s	398.23	0.69	5.8	1.90	91.9
C: N 1s	397.71	0.69	11.5	1.90	34.0
D: N 1s	399.25	0.69	13.6	1.90	11.2
A: VB HOMO	1.60	0.74	-	-	74.1
B: VB HOMO	1.06	0.74	-	-	66.9
A: Pb 5d 5/2	19.94	0.98	-	-	1139.3
B: Pb 5d 5/2	19.65	0.98	-	-	8233.7

Tabulate fitting parameters for the C 1s, N 1s and Pb 5d photoemission spectra for 1ML pristine thin film of PbPc (Fig. 38).

Table 4 Fitting parameters of C 1s and N1s and Pb 5d photoemission spectra for 1 ML pristine thin film of PbPc (Fig. 38).

	E_{bind} (eV)	FWHM	% shake up	E_{split} (shake up) (eV)	Integrated Area	Ratio D/U	
1D: benzene ring C 1s sp^2+2p_z	284.54	0.79	10.6	1.87	5.4	10.6	1.7
2D: benzene ring C 1s sp^2	284.98	0.79	10.6	1.87	2.7		
3D: pyrrole C 1s	285.85	0.79	10.6	1.87	2.5		
1U: benzene ring C 1s sp^2+2p_z	283.95	0.79	10.6	1.87	1.7	6.1	
2U: benzene ring C 1s sp^2	284.32	0.79	10.6	1.87	2.9		
3U: pyrrole C 1s	285.22	0.79	10.6	1.87	1.5		
D: N 1s	398.58	0.93	7.9	2.3	5.0		
U: N 1s	398.11	0.93	7.9	2.3	2.9		
D: Pb 5d 5/2	19.8	0.98	-	-	420.1		1.75
U: Pb 5d 5/2	20.55	0.98	-	-	239.6		

Tabulate fitting parameters for the C 1s, N 1s and Pb 5d photoemission spectra for 1ML beam damaged thin film of PbPc (Fig. 38).

Table 5 Fitting parameters of C 1s and N1s and Pb 5d photoemission spectra for 1ML beam damaged thin film of PbPc (Fig. 38).

	E_{bind} (eV)	FWHM	% shake up	E_{split} (shake up) (eV)	Integrated Area	Ratio D/U	
1D: benzene ring C 1s sp^2+$2p_z$	284.44	0.84	9.2	2.14	4.5	8.9	1.17
2D: benzene ring C 1s sp^2	284.78	0.84	9.2	2.14	2.6		
3D: pyrrole C 1s	285.83	0.84	9.2	2.14	1.8		
1U: benzene ring C 1s sp^2+$2p_z$	283.84	0.84	9.2	2.14	2.1	7.6	
2U: benzene ring C 1s sp^2	284.14	0.84	9.2	2.14	3.6		
3U: pyrrole C 1s	285.20	0.84	9.2	2.14	1.85		
D: N 1s	398.55	0.89	5.8	1.9	3.3		
U: N 1s	398.10	0.89	5.8	1.9	2.6		
C: N 1s	399.07	0.89	5.8	1.9	1.3		
D: Pb 5d 5/2	19.84	1.06	-	-	414.4		1.26
U: Pb 5d 5/2	20.53	1.06	-	-	327.0		

Appendix II

Notes on calibration of energy scales

The energy scale of the C *K*-edge emission spectra was calibrated with 3rd order Ni L_α / L_β metal emission, while the N *K*-edge emission spectra were calibrated with 2nd order Co L_α / L_β emission, and the O *K*-edge spectra with 2nd order Zn L_α / L_β[102]. These are clean reference samples that kept constantly under vaccum on the neck of the sample holder, at X1B endstation.

XAS spectra were normalized to current from a reference Au coated mesh. Also in XAS measurements at MAXLAB II at I511-1, background correction to the absorption cross section of the Ge substrate needed to be applied. This happened by recording the background signal from a clean Ge substrate with the same beam incidence angle as the one used for the MPcs films measurements. Then subtraction of this reference spectrum after scaling to a pre-threshold point of the main spectrum is applied.

C *K* edge photon energy has been calibrated to an absorption dip in the Au coated mesh due to accumulation of amorphous carbon on it. The energy scale of the N and O *K* edges XAS measurements was calibrated using known absorption features of rutile TiO_2[237]. The calibration methods for XES and XAS at X1B, are consistent with each other, and confirmed by the agreement between the XES elastic peaks and the positions of chosen excitation energies on the XAS spectra

Calibration of the XPS binding energies measurements took place in MAXLAB II I511-1 end station based on the the measurement of XPS background signal obtained at the same time from well know Ge 3d states or by using a reference clean Au foil sample measuring the well known Au 4f states. In XPS measurements that took place at X1B Au foil that was held attached to the measured sample has been used measuring the Au 4f states.

Appendix III

Tabulate fitting parameters for the C 1s, N 1s and O1s photoemission spectra for $(Znq2)_4$ film (Fig. 67).

Table 6 Fitting parameters of C 1s and N1s and O1s photoemission spectra for a $(Znq2)_4$ film (Fig. 67).

	E_{bind} (eV)	FWHM	% shake up	E_{split} (shake up) (eV)	Integrated Area
C-C: Pyridyl/phenolato ring C 1s	284.57	1.65	21.6	5.20	38.2
C-H: Pyridyl/phenolato ring C 1s	285.73	1.65	6.5	5.20	163.1
C-N: Pyridyl/phenolato ring C 1s	286.64	1.65	12.9	5.20	70.3
C-O: Pyridyl/phenolato ring C 1s	286.65	1.65	4.2	5.20	32.7
N 1s: Pyridyl/phenolato ring N 1s	399.49	1.62	-	4.73	48.4
O 1s (2Zn): Pyridyl/phenolato ring O 1s	532.26	1.83	3.9	6.55	29.1
O 1s (Zn): Pyridyl/phenolato ring O 1s	531.28	1.83	8.2	6.55	10.34

Appendix IV

Tabulate HOMO and LUMO levels for Alq3 and (Znq2)4 as have been extrapolated from the C 1s, N 1s and O1s XES and NEXAFS spectra at figures 73 and 74.

Table 7 HOMO and LUMO levels of Alq3 and $(Znq2)_4$ as extrapolated from C, N and O *K*-edge XES and NEXAFS spectra.

	K-edge	HOMO (eV)	LUMO (eV)	Band gap (eV)
Alq3	C	282.42	284.74	2.32
	N	396.98	398.92	1.94
	O	529.30	531.84	2.54
(Znq2)4	C	283.49	285.16	1.67
	N	396.11	398.76	2.65
	O	528.78	532.72	3.94